UNIVERSITY OF CALIFORNIA,
IRVINE

Fundamental Investigations of Metal-Metal Oxide Model Catalysts and the Liquid/Vapor Interface of Aqueous Solutions

DISSERTATION

submitted in partial satisfaction of the requirements
for the degree of

DOCTOR OF PHILOSOPHY

in Physical Chemistry

by

Amanda R. Haines

Dissertation Committee:
Professor John C. Hemminger, Chair
Professor Reginald M. Penner
Professor Wilson Ho

2021

DEDICATION

To

My family and friends

For their endless support

In loving memory of
Rosella Adelsberg
1933 – 2020
Thank you for always supporting my ambitions

"And once the storm is over you won't remember
how you made it through … But one thing is certain.
When you come out of the storm
you won't be the same person that walked in.
That's what this storm's all about"
- Haruki Murakami, Kafka on the Shore

TABLE OF CONTENTS

LIST OF FIGURES

LIST OF TABLES

ACKNOWLEDGEMENTS

I would like to thank Professor John Hemminger for allowing me to join his group and being a great advisor. I truly appreciate his guidance and support throughout my Ph.D. studies and he has been crucial to my development as a scientist. He has been an amazing role model and taught me so much both in and outside of the lab and helped me grow as an independent researcher. I'm so thankful for his sense of humor and optimistic attitude whenever things didn't go as planned. Working in your group has been a pleasure and thank you for your understanding, support, and encouragement. I truly could not have asked for a better advisor. I would also like to thank my other committee members, Professors Reginald Penner and Wilson Ho for their support throughout this process. Thank you to Prof. Mecartney for her suggestion to use AFM for stability studies. I also would like to thank Drs. Robert Seidel, Bernd Winter, Ira Waluyo, Adrian Hunt, and Hendrik Bluhm for all of their help at the various synchrotron facilities.

I want to extend a huge thank you to my parents and family members for their constant love and support throughout this process. I'd also like to thank the California Haines family; I'm not sure how well the move across the country would have gone without having family out here to keep me sane, provide endless entertainment, and have someone that understands my Dinosaurs references. I love and appreciate you all so much. Also I appreciate my niece and nephews: Henry, Phillip, Harlyn, and Wesley for bringing so much fun and joy to my life.

I am forever grateful for the amazing friends I made in my life who have stood by me through everything, despite being across the country. I could write an entire page thanking each person individually but that's excessive so I will try to limit myself. To my very best friends Kim, Grace, and Robyn, I truly don't know if any of this would be possible without you guys. They have wholeheartedly supported me in everything I've done, kept me grounded, offered valuable advice, and are absolute amazing people. Marg, I am so thankful to have you out in California and for your friendship. I appreciate our life discussions and all of the fun times we had.

I was fortunate enough to have met some wonderful, supportive people in my graduate class that have made my grad school experience enjoyable. Hayley, Bronte, Melvin, Jess, Wyeth, Glynis, Jeff, and Sierra – thank you guys for being amazing friends since the very beginning. I'll always appreciate your support and commiserating over alcohol and board games. Thank you to the Penner lab members for their friendship, allowing me to follow them around, and all of their help learning electrochemistry. I'd also like to thank the Law lab members for their friendship and allowing me the use of their equipment.

Finally, I would like to thank the past Hemminger lab members: Drs. Anthony Babore, Jared Bruce, Randima Galhenage, Djawhar Ferrah, and Joel Langford. Thank you for all of your help and scientific discussions that have educated me and helped me become a better scientist. I have enjoyed all of our interactions, beamline trips, and fruitful conversations. Thank you to Anthony for introducing me to the wonderful world of soldering and power tools. I want to thank Djawhar for helping me when I first joined the group, teaching me everything she knew, and all of her guidance and support. Thank you to Jared for helping me with the liquid jet studies and all of our conversations about life. It has been a pleasure to work with you all.

CURRICULUM VITAE

Amanda R. Haines

EDUCATION

Doctor of Philosophy in Chemistry **2021**
University of California, Irvine *Irvine, California*
Concentration: Physical Chemistry

Bachelor of Science in Chemistry **2013**
Temple University *Philadelphia, Pennsylvania*

RESEARCH EXPERIENCE

University of California, Irvine **Feb 2017-Jun 2021**
Advisor: Prof. John C. Hemminger *Irvine, California*
Graduate Student Researcher

Dow Chemical Company **Dec 2015-Jul 2016**
Dow Coating Materials **Feb 2014-Apr 2015**
Lab Technologist *Collegeville, Pennsylvania*

Henry Company **May 2015-Sept 2015**
Chemist *Kimberton, Pennsylvania*

FujiFilm Imaging Colorants **Jun 2013-Feb 2014**
Quality Control Technician *New Castle, Delaware*

TEACHING EXPERIENCE

Graduate Teaching Assistant **Jan-Mar 2018**
General Chemistry Lecture **Apr-Jun 2017**
University of California, Irvine *Irvine, California*

Graduate Teaching Assistant **Apr-Jun 2019**
General and Analytical Chemistry Lab **Sept 2016-Mar 2017**
University of California, Irvine *Irvine, California*

PUBLICATIONS AND PRESENTATIONS

1. Ferrah, D., **Haines, A. R**., Galhenage, R., Bruce, J., Babore, A., Hunt, A., Waluyo, I., Hemminger, J. C. Wet chemical growth and thermo-catalytic activity of Cu-based nanoparticles supported on TiO_2 nanoparticles/HOPG: In situ ambient pressure XPS study of CO_2 hydrogenation reaction. *ACS Catalysis* **2019**, 9, 6783-6802
2. **Haines, A.R.**, Hemminger, J. C. Stability of Cu/TiO_2 nanoparticle model catalysts under electrochemical CO_2 reduction conditions. *ACS Catalysis* **2021,** 11, 6960-6970.
3. Bruce, J. P., Zhang, K., Balasubramani, S. G., **Haines, A. R.**, Galhenege, R.P., Voora, V.K., Furche, F., Hemminger, J. C. Exploring the solvation of acetic acid in water using liquid jet X-ray photoelectronspectroscopy and core level binding energy calculations. Submitted, **2021**.
4. **Haines, A.R**., Bruce, J.P., Seidel, R., Winter, B., Hemminger, J.C. Depth dependent changes in the solvation of small molecules in aqueous solution at the liquid/vapor interface probed by liquid-jet X-ray photoelectron spectroscopy. In preparation, **2021**.
5. **Haines, A.R.**, Bruce, J.P., Seidel, R., Winter, B., Hemminger, J.C. Investigating the solvation of organic solutes in aqueous solution at the liquid/vapor interface using liquid-jet X-ray photoelectron spectroscopy. In preparation, **2021**.
6. **American Vacuum Society International Meeting,** Long Beach, CA; October 21-26, 2018; Oral presentation. "Synthesis and Characterization of Metals Supported on TiO_2 Nanoparticles"

PROFESSIONAL MEMBERSHIPS

American Chemical Society	2019-present
American Vacuum Society	2018-present

ABSTRACT OF THE DISSERTATION

Fundamental Investigations of Metal-Metal Oxide Model Catalysts
and the Liquid/Vapor Interface of Aqueous Solutions

By

Amanda R. Haines

Doctor of Philosophy in Physical Chemistry

University of California, Irvine, 2021

Professor John C. Hemminger, Chair

Fundamental surface science investigations are primarily concerned with understanding the chemistry that occurs at the interface of phases, such as the solid/gas, solid/liquid, and liquid/vapor interface. Surface science investigations have led to breakthroughs in understanding chemisorption and physisorption on heterogeneous catalysts, reactions that occur at the interface of electrodes, and hydrogen bonding in aqueous solutions. Fundamental understanding of the chemistry that occurs on surfaces can lead to better material design, such as more efficient catalysts, and insight into complex chemical processes that are not well understood, such as how a solvent affects the electronic properties of solutes.

The work presented in this thesis includes fundamental studies on both solid/gas and liquid/vapor interfaces. Chapter 1 discusses the synthesis and characterization of a Cu/TiO_2 nanoparticle model catalyst system supported on a highly oriented pyrolytic graphite (HOPG) substrate. Supporting the nanoparticles on an inert HOPG substrate allows for the rigorous characterization of this model catalyst using advanced surface science techniques. Further reactivity and stability studies were then conducted on this system.

Chapter 2 investigates the thermal reduction of CO_2 over the Cu/TiO_2/HOPG model catalyst through the use of ambient pressure X-ray photoelectron spectroscopy (AP-XPS) at a synchrotron light source. The Cu/TiO_2/HOPG sample was heated in an atmosphere of CO_2 and H_2 reactant gases and AP-XPS measurements were taken in an effort to observe formation of intermediates on the catalyst surface. Using the synchrotron, we are able to obtain information at the near surface and bulk of the catalyst in order to elucidate fundamental information on the CO_2 hydrogenation reaction mechanism.

The electrochemical reactivity and stability of the Cu/TiO_2/HOPG catalyst is discussed in Chapter 3. Differential electrochemical mass spectrometry (DEMS) measurements showed that this catalyst forms methane as its major product under electrochemical CO_2 reduction conditions. The stability of the Cu and TiO_2 nanoparticles were investigated using cyclic voltammetry and chronoamperometry.

In an effort to fundamentally study the Cu/ZnO system, similar to the Cu/TiO_2 system, the synthesis of ZnO nanoparticles on HOPG was attempted using PVD. The synthesis of these nanoparticles is discussed in Chapter 4, which details the various parameters that were adjusted in order to optimize the PVD process. Photodeposition and stability studies of the synthesized ZnO/HOPG samples were also investigated.

The study of liquid interfaces using liquid-jet ambient-pressure X-ray photoelectron spectroscopy (LJ-APXPS) is discussed in Chapter 5. Various solutes in aqueous solutions were investigated using synchrotron radiation in order to study the solvation induced changes in the electronic structure of solutes from the surface to the bulk of the solution and as a function of pH. These investigations provide insight into the solvent effects for molecular solutes that reside at or near the liquid/vapor interface in solution.

Chapter 1

Synthesis and Characterization of Cu-based Nanoparticles on TiO_2 Nanoparticles Supported on HOPG

1.1 Introduction

Heterogeneous catalysts are widely used industrially in various sectors such as oil refining, organic synthesis or pollution control.[1–6] There has been significant research into improving the reaction rate and selectivity of heterogeneous catalysis products but atomic level understanding of these materials still remains a challenge due to the complex nature of the catalytic materials.[7] Modern surface science techniques have been used in order to understand these materials at the atomic scale but there still exists several gaps between catalysis and surface science: (1) materials gap, (2) pressure gap and (3) complexity gap.[8] Early studies in this field focused on single crystal surfaces, which provided useful information on the role of surface defects and gas adsorption, but these surfaces do not accurately reflect the complexity of real industrial catalysts.[7,9] To overcome this materials gap between fundamental studies and real catalysts, model heterogeneous catalysts are used that are based on metal oxides on single crystal surfaces or oxide supported metal particles.[9–12]

In this context, a model catalyst consisting of Cu-based nanoparticles on metal oxide nanoparticles, specifically titanium dioxide (TiO_2), has been fabricated and characterized in this Chapter. The majority of industrial catalysts consist of small metal nanoparticles dispersed onto a high surface area solid, usually a metal oxide.[11] The model system described here consists of 2-5 nm Cu-based nanoparticles supported on 15-20 nm TiO_2 nanoparticles, thus increasing the surface area of these catalysts and helping to bridge the materials gap.

It is well established that copper is an important metal for CO_2 reduction reactions, specifically the thermocatalytic reduction into methanol and the electrochemical reduction into methane.[2,13,22,23,14–21] However, there remains a debate as to whether copper metal or Cu^+ species is responsible for its high catalytic activity.[24–27] Under CO_2 reduction conditions, both electrochemical and thermocatalytic, it is not thought that copper would remain as an oxide and would be subsequently reduced to copper metal. It has been found that metal oxide supports play a role in supplying oxygen to copper and may stabilize the Cu^+ species under reduction conditions.[26,28]

TiO_2 is a reducible metal oxide that is capable of having multiple oxidation states which, when used as a support for copper, may also be relevant to surface-catalyzed reactions. TiO_2 has several adsorption sites which include oxygen vacancies and undercoordinated Ti and O atoms, which may help to stabilize the CuO_x species.[29,30] In this Chapter, the synthesis of a model catalyst consisting of CuO_x nanoparticles on TiO_2 nanoparticles is realized using photodeposition and physical vapor deposition (PVD). One advantage of such a catalyst is that, in addition to reaction studies, the catalyst structure and composition can be studied using advanced surface science methods of nanoscale imagery and spectroscopy.

1.2 Experimental

1.2.1 Physical Vapor Deposition (PVD)

TiO_2 nanoparticles were grown on a highly oriented pyrolytic graphite substrate (HOPG) (HOPG/ZYB/DS/1-1, 8^o mosaic spread, MikroMasch) by PVD on a commercial evaporator (Edwards 306A Coating System) under high vacuum (10^{-6} Torr). The HOPG substrate is cleaved using the “Scotch tape” method and either placed directly into the evaporator or treated with low

energy plasma and fixed between two copper rods. The HOPG substrate is resistively heated to 770^{o}C to remove any surface contamination prior to the deposition and is held at a constant temperature throughout the deposition in order to induce Ti atom mobility on the surface.

The TiO_2 nanoparticles were prepared by the thermal evaporation of a titanium (Ti) metal source (1.0 mm dia., hard, 99.99% metals basis, Alfa Aesar) in a tungsten crucible. The tungsten crucible containing the Ti rod is resistively heated above the evaporation temperature of Ti in order to sublimate into the vapor phase. The Ti atoms are readily oxidized by residual oxygen in the chamber to form TiO_2 nanoparticles under high vacuum (10^{-6} Torr). The growth rate and amount of TiO_2 deposited is monitored by a quartz crystal microbalance (QCM). The sample is then annealed for 2.5 hours at 770^{o}C after deposition in order to obtain highly crystalline rutile TiO_2 NPs.

1.2.2 Photodeposition

The TiO_2/HOPG sample is placed in a photo-electrochemical cell and submerged in an aqueous $CuCl_2$ (99.99% trace metal basis, Sigma-Aldrich) solution where the $CuCl_2$ salt was dissolved in HPLC grade water (Sigma-Aldrich). The solution is bubbled with Ar gas for 20 minutes prior to irradiation in order to degas oxygen, as it is thought to compete as an electron scavenger, and improve photoreduction.[31] The inert Ar gas purge continued throughout the duration of the deposition. The TiO_2/HOPG sample in the aqueous $CuCl_2$ solution was irradiated with ultraviolet (UV) light (mercury xenon arc lamp) with a wavelength of 365 nm for 6 hours. Samples were washed in HPLC grade water, dried using nitrogen gas, and stored in a desiccator prior to characterization.

1.2.3 Characterization

X-ray photoelectron spectroscopy (XPS) measurements were performed using an AXIS Supra photoelectron spectrometer (Kratos Analytical) equipped with a monochromatic Al Kα source (1486.6 eV). High resolution C1s, O1s, Cu2p and Ti2p core level spectra were recorded with an analyzer pass energy of 20 eV. All survey spectra were recorded with a pass energy of 160 eV. All recorded spectra were calibrated to the C1s peak appearing at 284.4 eV, corresponding to graphitic carbon of HOPG.[32,33] Scanning electron microscopy (SEM) measurements were performed using a FEI Magellan 400 XHR SEM equipped with a monochromated FEG source at an acceleration voltage of 10 kV, probe current of 50 pA and working distance of ~4 mm. Prior to SEM imaging, all samples were plasma treated using an in situ plasma cleaner that uses an ambient air plasma to lay down oxygen radicals on the sample surface in order to prevent the formation of hydrocarbon contamination during imaging.[34] Local chemical state analysis was performed using the energy-dispersive X-ray spectrometer (EDS) (Oxford silicon drift detector, 80 mm^2) in the SEM at an acceleration voltage of 25 kV, probe current of 0.2 nA, and a working distance of ~4 mm. Atomic force microscopy (AFM) measurements were performed on an Anton-Paar Tosca 400 AFM in tapping mode using commercially available silicon cantilevers (Arrow-NCR-10, NanoWorld) with a spring constant of 42 N/m and a resonance frequency of 285 kHz.

1.3 Results and Discussion

1.3.1 Fabrication and characterization of TiO_2 nanoparticles

The TiO_2 nanoparticles grown using PVD can have either a high or low density of nanoparticles depending on the pretreatment of the HOPG substrate. For a low density of nanoparticles, the HOPG substrate is placed directly into the PVD chamber after cleaving. In this

instance, the TiO_2 nanoparticles grow preferentially along the naturally occurring step edges of HOPG to form linear arrays (Figure 1.1 A,B). Upon substrate heating, the Ti adatoms become mobile and move towards defect sites on the HOPG substrate, in this case the step edges, in order to nucleate.[35]

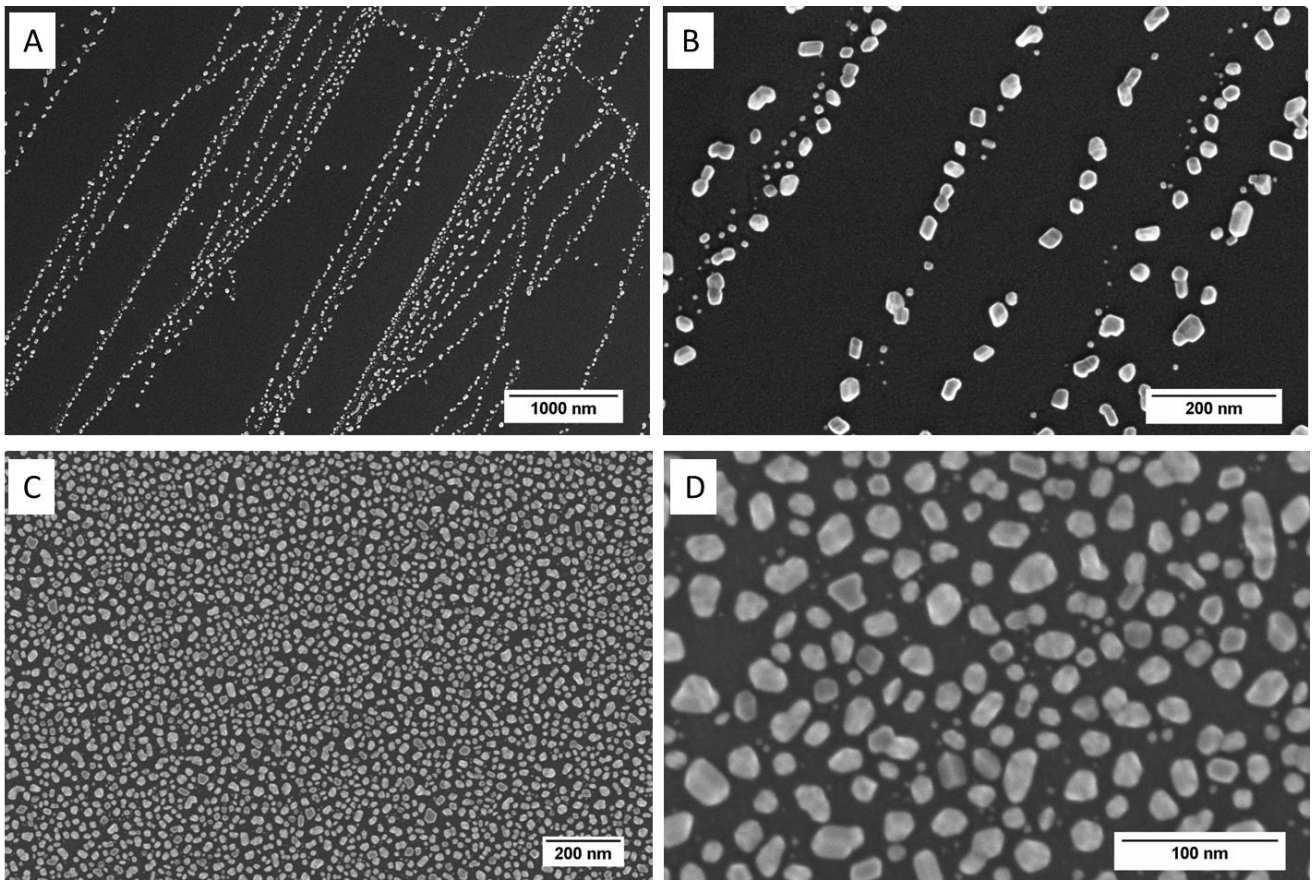

Figure 1.1: SEM image of TiO_2 nanoparticles (A) at the step edges of HOPG with (B) magnified image and (C) at a high density of nanoparticles with (D) magnified image.

To obtain a high density of TiO_2 nanoparticles, the HOPG substrate is plasma treated using a low energy Ar plasma (8 W, 160 mTorr) for 20 minutes using either a Tergeo Plasma Cleaner (PIE Scientific) or a PC 2000 plasma cleaner (South Bay Technology, Inc.) after cleaving. This plasma treatment creates multiple defects on the HOPG substrate that act as nucleation sites for the mobile Ti atoms. It is presumed that the step edges of the HOPG substrate

are broken up by the Ar plasma as the TiO_2 nanoparticles don't appear to align in any particular order on the plasma treated substrate. The plasma treatments results in a high density of TiO_2 nanoparticles that are 15-20 nm in diameter on the surface of HOPG (Figure 1.1 C,D).

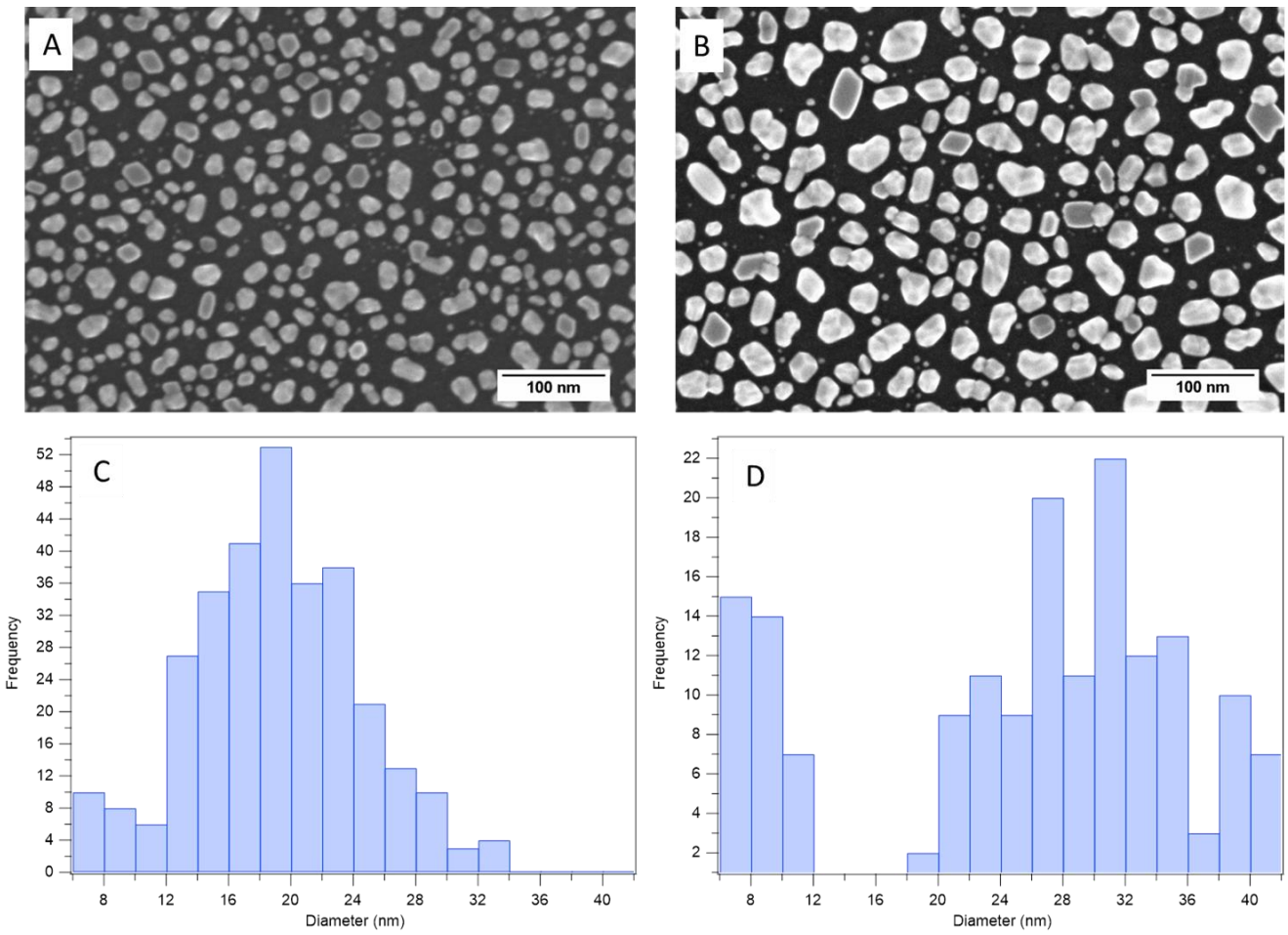

Figure 1.2: SEM image of TiO_2 nanoparticles at a QCM deposition of (A) 6.2 nm and (B) 11.8 nm. Histograms (C) and (D) are the nanoparticle diameter distribution for the SEM images in (A) and (B) respectively.

The size of the nanoparticles deposited can be controlled relatively well by adjusting the amount of TiO_2 deposited. In Figure 1.1, the QCM recorded that the amount of TiO_2 deposited was 9.2 nm and the average nanoparticle diameter was between 25-40 nm for the linear arrays, as measured from the SEM images using ImageJ. The high density nanoparticles that had 6.2 nm

and 11.8 nm amount of TiO_2 deposited, as measured by QCM, had corresponding average nanoparticle diameters of 17 and 24 nm, respectively. The SEM images comparing the nanoparticle size and corresponding histograms are shown in Figure 1.2, where the diameter measurements and histograms were recorded from the SEM images using ImageJ. Adjusting the

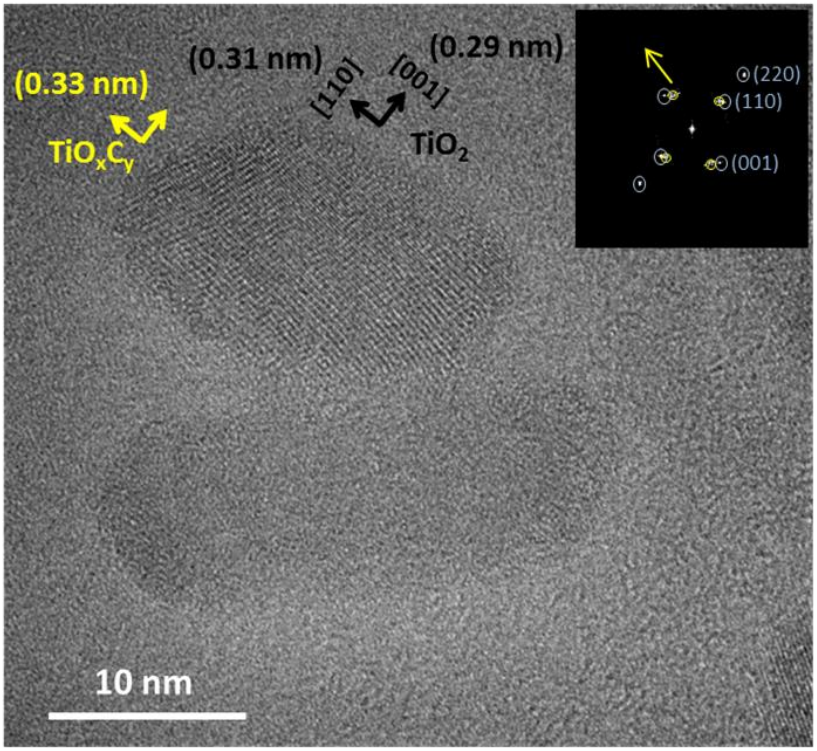

Figure 1.3: TEM image of TiO_2 nanoparticles on a carbon TEM grid showing rutile TiO_2 nanoparticles. Inset is the fast Fourier Transform (FFT) patterns of TiO2 nanoparticle.[36]

parameters during PVD, such as substrate temperature and amount of deposited material, allows us to control the size and crystallinity of the TiO_2 nanoparticles. The HOPG substrate was held at 770^{o}C throughout the deposition and the sample was further annealed for 2.5 hours after deposition in order to form rutile TiO_2 nanoparticles. The crystallinity of the nanoparticles was confirmed via transmission electron microscopy (TEM) (Figure 1.3) where the inset of the 2D-FFT shows diffraction spots indicating distances of 0.29 and 0.31 nm, which corresponds to the (001) and (110) interplanar spacing of rutile TiO_2 (110), respectively.[36]

The chemical composition of the synthesized TiO_2 nanoparticles was analyzed using X-ray photoelectron spectroscopy. The high resolution Ti2p spectra in Figure 1.4 shows the

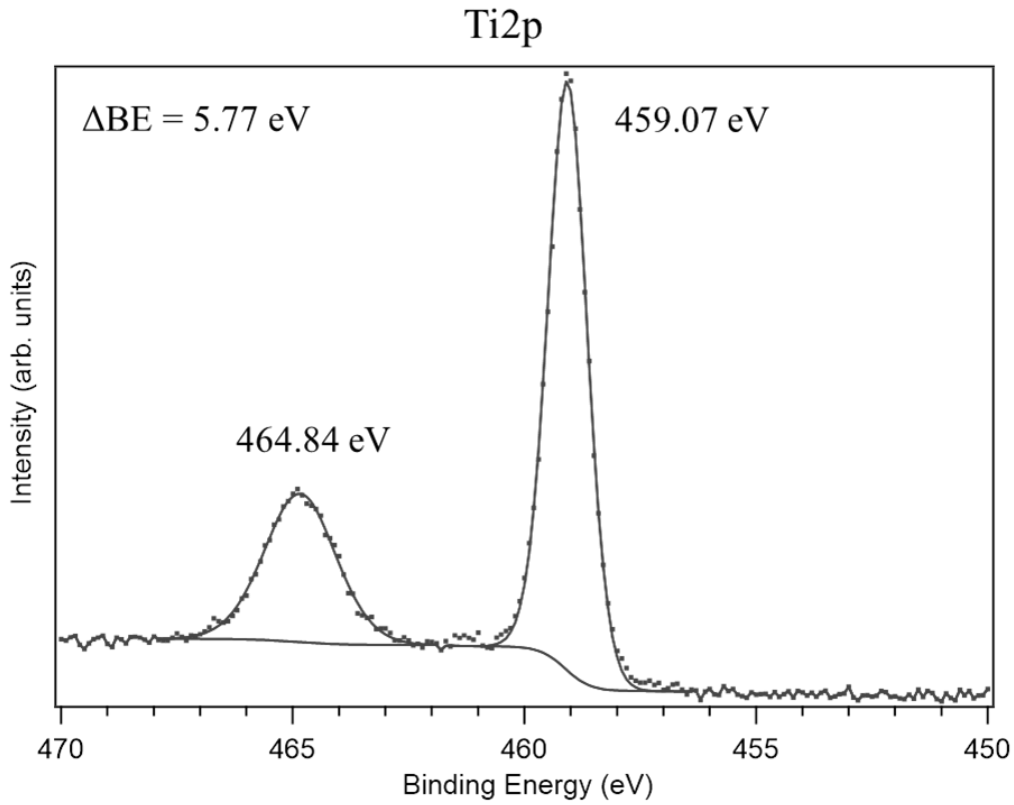

Figure 1.4: Ti2p XPS spectra of TiO_2 nanoparticles showing the formation of stoichiometric TiO2 with the Ti2p3/2 peak located at 459.07 eV.

formation of stoichiometric TiO_2 nanoparticles with the $Ti2p_{3/2}$ and $Ti2p_{1/2}$ peaks located at 459.07 and 464.84 eV, respectively. The $Ti2p_{3/2}$ binding energy is characteristic of TiO_2 which can range from 458.5 and 459.2 eV and the splitting (ΔBE) between the $Ti2p_{3/2}$ and $Ti2p_{1/2}$ peak is 5.77 eV, where TiO_2 is reported to have a peak splitting value of 5.54 eV.[37,38] Figure 1.5 shows the AFM images of the linear and high density TiO_2 nanoparticles and corresponding line scan profiles. The linear and high density TiO_2 nanoparticles were found to have average heights of 18 and 6 nm, respectively.

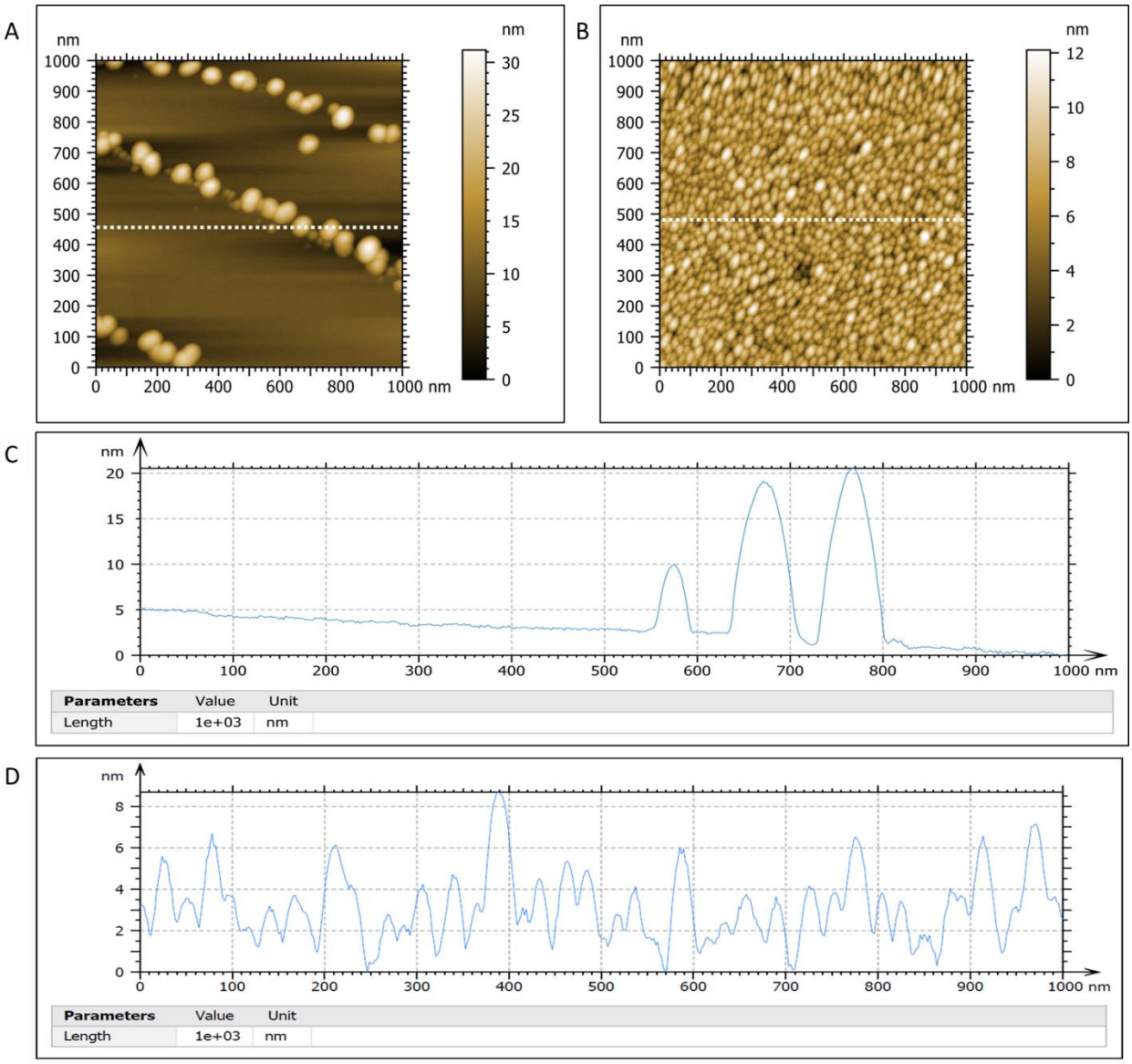

Figure 1.5: AFM image of (A) linear TiO_2 nanoparticles with (C) corresponding line scan and (B) high density of TiO_2 nanoparticles with (D) corresponding line scan.

1.3.2 Photodeposition and characterization of Cu-based nanoparticles on TiO_2 nanoparticles

The TiO_2/HOPG sample was then submerged in a 3 mM aqueous $CuCl_2$ solution and irradiated with UV light for 6 hours in order to selectively deposit small, Cu-based nanoparticles onto the TiO_2 nanoparticles. Previous studies have shown that 3 mM $CuCl_2$ in aqueous solution at a pH of ~3 results in selective deposition of 2-5 nm CuO_x nanoparticles on TiO_2

nanoparticles.[36,39] At more neutral pH, the hydrolysis of $Cu(OH)_2$ is predominant and results in the deposition of large $Cu(OH)_2$ particles on the surface. The wavelength of UV light used to irradiate the sample is 365 nm, corresponding to a photon energy of 3.4 eV, which is greater than the band gap of rutile TiO_2 of 3.0 eV. This allows for the promotion of an electron (e^-) from the valence band to the conduction band of TiO_2 where the electron in the conduction band will bind with the metal ions that are in solution, as shown in the scheme in Figure 1.6. The promotion of an electron leaves behind a hole (h^+) in the valence band. During photodeposition, it has been found that a sacrificial agent can be used as a hole scavenger that will occupy the holes in the valence band, suppress recombination of the electrons and holes, and improve photoreduction.[40,41]

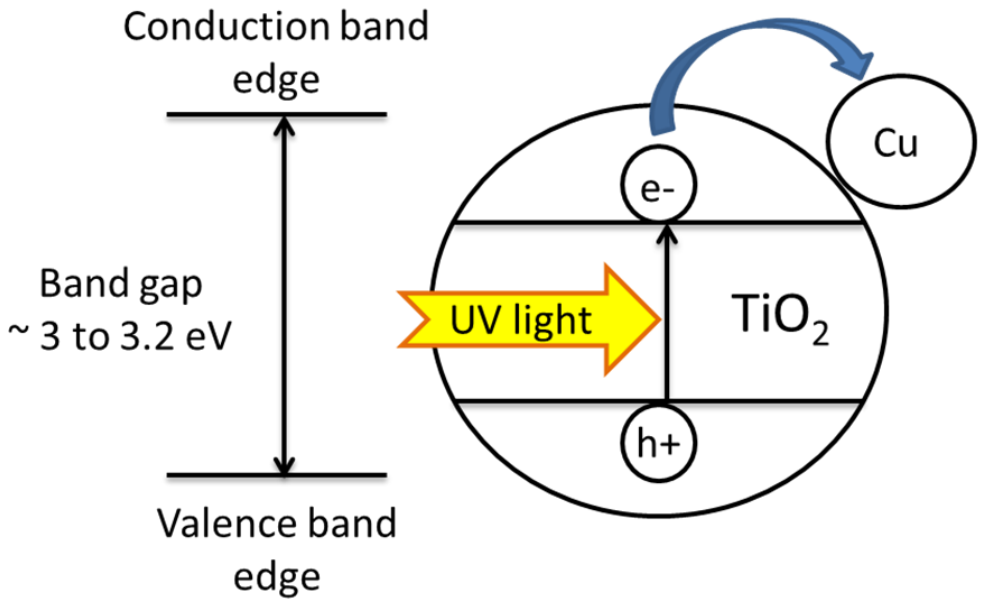

Figure 1.6: Schematic of photodeposition reaction for the band gap of TiO_2. An electron (e^-) is promoted from the valence band to the conduction band leaving behind a hole (h^+) in the valence band. The promoted e^- can then bind with the metal ion in solution.

The addition of various sacrificial agents to the aqueous $CuCl_2$ solution studied here were the following: methanol, acetic acid, formic acid, oxalic acid, sodium acetate, sodium formate,

and sodium oxalate. The addition of 1% by volume of methanol was used as a standard as previous studies revealed an increase in the rate and amount of Cu-based nanoparticles deposited with its addition.[36] Studies have investigated these particular organic hole scavengers and found that the addition of formate results in faster photodeposition.[41] Our experimental results revealed that the addition of small amounts of the sacrificial agents added to the $CuCl_2$ solution resulted in significant copper photodeposition. For these solutions, the addition of liquids was 1% by volume and the solids were added in order to reach a final solution concentration of 3 mM.

Table 1.1: Description of additives used in the aqueous 3 mM $CuCl_2$ solutions for photodeposition.

Solution	Additives
1	1% vol. methanol
2	1% vol. acetic acid
3	1% vol. formic acid
4	3 mM oxalic acid
5	3 mM sodium acetate
6	3 mM sodium formate
7	3 mM sodium oxalate

For all of these solutions, the pH was kept at ~3 in order to minimize the hydrolysis of $Cu(OH)_2$ formation and the competitive reduction reaction that occurs between Cu^{2+} with H^+ ions.[40,41] The summary of the solutions with the amount of sacrificial agent added are recorded in Table 1.1. The TiO_2/HOPG samples were illuminated for 3 hours in all six of the $CuCl_2$ solutions described in Table 1.1, except for the solution with 1% methanol, which was illuminated for 6 hours. For solutions 2-7, the addition of the organic hole scavenger resulted in an increase in the rate and amount of Cu-based nanoparticles deposited onto the TiO_2 nanoparticles. Figure 1.7 shows a representative Cu2p XPS spectrum for the 3 mM $CuCl_2$ solution containing 3 mM

sodium oxalate. Initially, the Cu2p spectrum had a large Cu2p peak located at 932.53 eV, corresponding to Cu_2O and smaller peaks located at 933.63 and 934.83 eV,

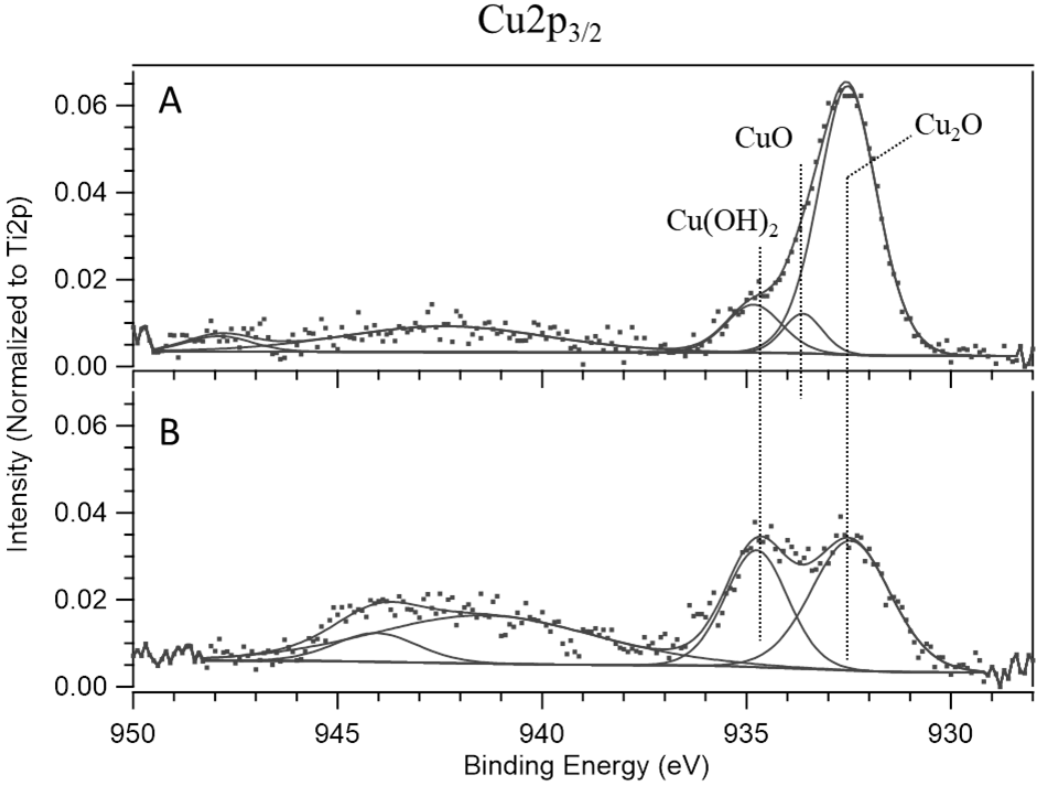

Figure 1.7: $Cu2p_{3/2}$ XPS spectrum of Cu nanoparticles on TiO_2 nanoparticles using a photodeposition solution of aqueous 3 mM $CuCl_2$ solution with 3 mM sodium oxalate (A) initially and (B) after SEM imaging. The y axis is normalized to the $Ti2p_{3/2}$ peak in order to compare the amount of Cu present on the TiO_2 nanoparticles.

corresponding to CuO and $Cu(OH)_2$, respectively (Figure 1.7 A). However, after exposure to X-rays and SEM imaging, the amount of Cu_2O nanoparticles decreased significantly (seen in Figure 1.7 B) and relatively equal amounts of Cu_2O and $Cu(OH)_2$ were observed. The shake-up peaks characteristic of Cu^{2+} species, located at 941.39 and 944.05 eV, were more pronounced in the spectrum in Figure 1.7 B, indicating oxidation of the Cu_2O species.[42]

As stated in the Experimental section, the CuO_x/TiO_2/HOPG samples were exposed to an in situ plasma treatment in the SEM prior to imaging. The exposure to this plasma treatment,

which is air based plasma, results in the oxidation of Cu_2O nanoparticles on the surface of the CuO_x/TiO_2/HOPG substrate. The Cu2p spectrum was normalized to the $Ti2p_{3/2}$ peak and it was found that the initial Cu2p/Ti2p amount for Cu_2O was 0.065 and was reduced to 0.035 after SEM imaging. The XPS data for Solutions 2-7 before and after SEM imaging, is recorded in Tables 1.2 for the acids and Table 1.3 for the bases.

Table 1.2: Cu2p XPS data for the photodeposition of Cu on TiO_2 nanoparticles with 3 mM $CuCl_2$ solution and the addition of various acids. The addition of acetic, formic and oxalic acids correspond to Solutions 2-4.

		Acetic Acid		Formic Acid		Oxalic Acid	
Species	**Ratio**	**Initial**	**After SEM/XPS**	**Initial**	**After SEM/XPS**	**Initial**	**After SEM/XPS**
Cu_2O	Cu2p/Ti2p	0.043	0.029	0.045	0.033	0.063	0.037
$Cu(OH)_2$	Cu2p/Ti2p	0.021	0.016	0.016	0.022	0.010	0.033
Total	Cu2p/Ti2p	0.101	0.073	0.062	0.054	0.119	0.130

Table 1.3: Cu2p XPS data for the photodeposition of Cu on TiO_2 nanoparticles with 3 mM $CuCl_2$ solution and the addition of various bases. The addition of sodium acetate, formate and oxalate acids correspond to Solutions 5-7.

		Sodium Acetate		Sodium Formate		Sodium Oxalate	
Species	**Ratio**	**Initial**	**After SEM/XPS**	**Initial**	**After SEM/XPS**	**Initial**	**After SEM/XPS**
Cu_2O	Cu2p/Ti2p	0.131	0.103	0.137	0.067	0.116	0.071
$Cu(OH)_2$	Cu2p/Ti2p	0.100	0.094	0.032	0.009	0.019	0.051
Total	Cu2p/Ti2p	0.382	0.341	0.220	0.233	0.193	0.212

While the rate and amount of Cu-based nanoparticles increased with the addition of the organic hole scavengers (Solutions 2-7), the addition of these sacrificial agents resulted in the growth of 200-400 nm Cu-based structures on the surface of the samples (Figure 1.8). These large structures were not found to be stable as the plasma treatment in the SEM or reduction by the X-rays produced through XPS analysis resulted in a significant decrease in the amount of Cu_2O on the samples. For these sacrificial agents, the amount of Cu did not result in selective deposition onto the TiO_2 nanoparticles.

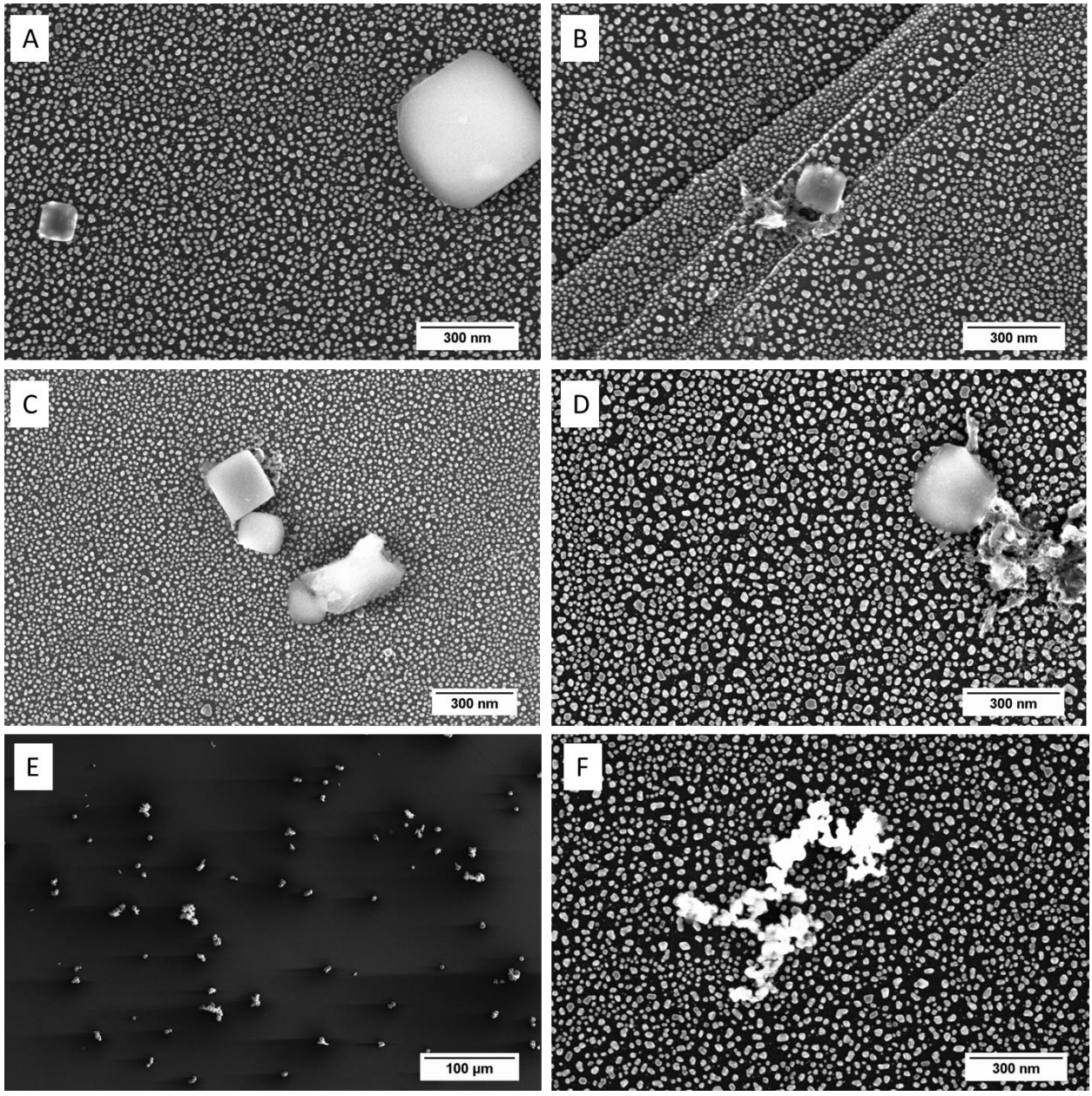

Figure 1.8: SEM images of $Cu/TiO_2/HOPG$ samples after photodeposition of a 3 mM $CuCl_2$ solution with (A) acetic acid, (B) sodium acetate, (C) formic acid, (D) sodium formate, (E) oxalic acid and (F) sodium oxalate. The deposition of Cu onto the TiO_2 nanoparticles resulted in the growth of large, Cu-based structures.

Solution 1, containing 1% by volume of methanol, was the only solution that resulted in the growth of small, Cu-based nanoparticles that were selectively deposited onto the TiO_2 nanoparticles, however this solution required longer illumination times of 6 hours. Figure 1.9

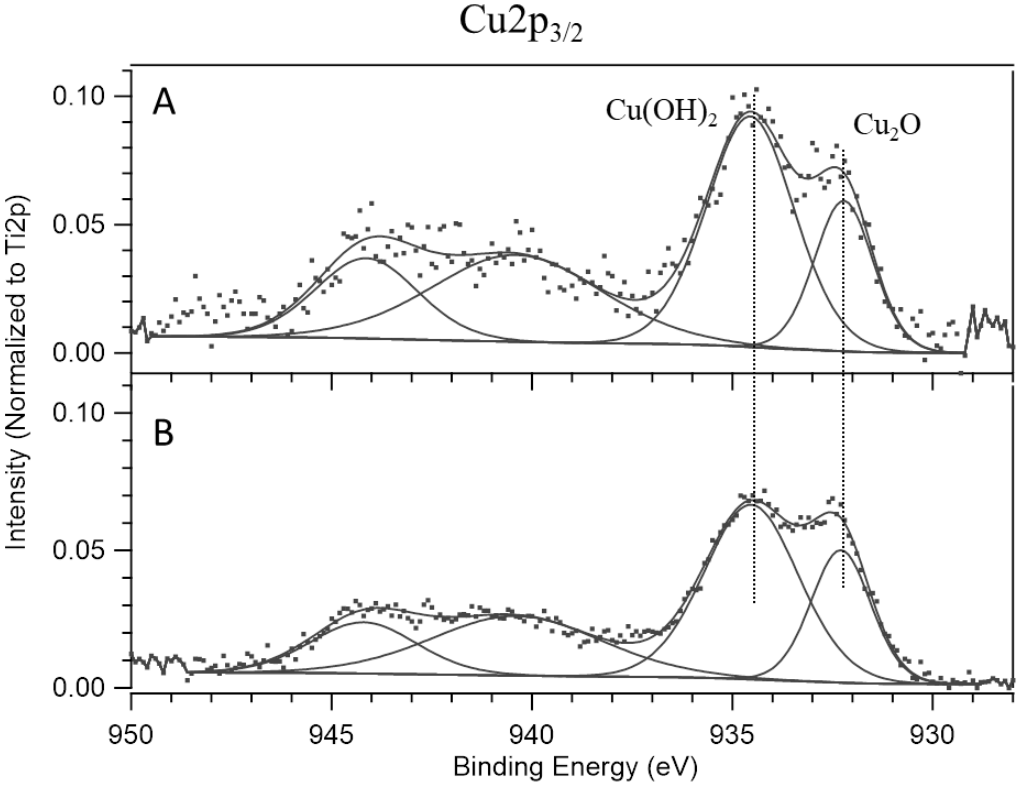

Figure 1.9: $Cu2p_{3/2}$ XPS spectrum of Cu nanoparticles on TiO_2 nanoparticles using a photodeposition solution of 3 mM $CuCl_2$ with 1% methanol (A) initially and (B) after SEM imaging. The y axis is normalized to the $Ti2p_{3/2}$ peak in order to compare the amount of Cu present on the TiO_2 nanoparticles.

shows the Cu2p XPS spectrum before and after SEM imaging when Solution 1 is used for photodeposition. The spectrum has two main Cu2p peaks located at 932.20 and 934.51 eV corresponding to Cu_2O and $Cu(OH)_2$, respectively. Initially, the $Cu(OH)_2$ species was more prevalent with a Cup/Ti2p ratio of 0.092 but, after SEM imaging, was reduced and has a Cu2p/Ti2p ratio of 0.066. It is thought that the exposure to the plasma treatment in the SEM or the X-rays during XPS analysis resulted in the removal of some of the $Cu(OH)_2$ nanoparticles if

they were adhered to the surface by electrostatic interactions. It has been shown that the deposition of $Cu(OH)_2$ particles occurs on a bare HOPG substrate in a 3 mM $CuCl_2$ solution with 1% by volume of methanol which confirms the hydrolysis of $Cu(OH)_2$ in solution and subsequent deposition. It is thought that during photodeposition, the Cu_2O species is obtained by photoreduction of the $Cu(OH)_2$ species.

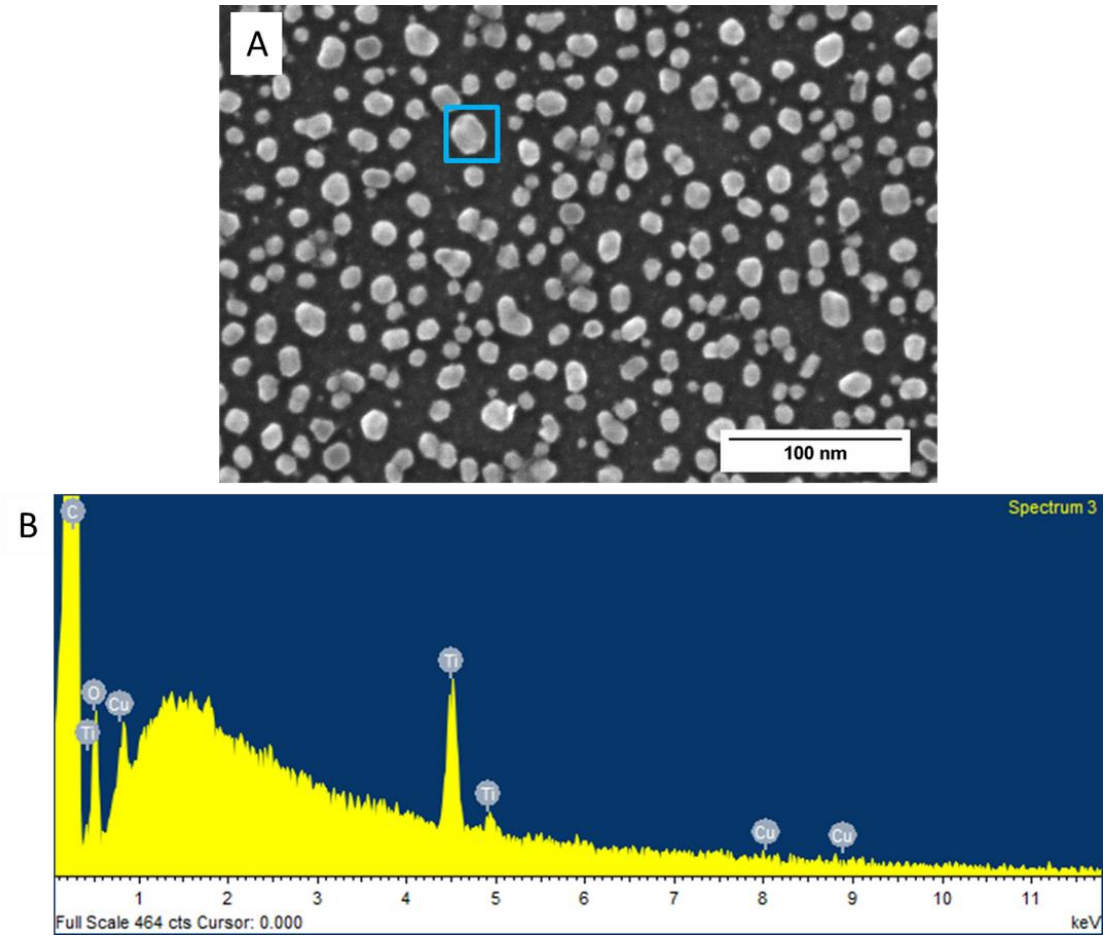

Figure 1.10: (A) SEM image of Cu/TiO_2/HOPG sample using a photodeposition solution of 3 mM $CuCl_2$ with 1% methanol. (B) EDS spectra of Cu/TiO_2 nanoparticle, marked with the blue box in the SEM image, which confirms the presence of Cu nanoparticles on TiO_2 nanoparticles.

SEM imaging of the CuO_x/TiO_2/HOPG sample did not show the formation of large, Cu-based structures on the surface (Figure 1.10 A). Since both Cu and Ti have similar atomic

numbers, it is difficult to differentiate between the two species visually by SEM as the two species have similar contrast. Local chemical analysis by EDS was performed to confirm the presence of Cu material on individual TiO_2 nanoparticles (Figure 1.10 B). The Cu Lα peak is observed at 0.93 keV and the Ti Kα and Kβ peaks are located at 4.51 and 4.95 keV, respectively. TEM imaging was also performed in order to determine the size of the Cu-based nanoparticles that were selectively deposited onto the TiO_2 nanoparticles. TEM imaging shows that initially (Figure 1.11 A) a thin, amorphous layer of Cu-based material (combination of Cu_2O and $Cu(OH)_2$) is formed over the TiO_2 nanoparticle. After a few minutes of exposure to the TEM beam, the de-wetting of the film is observed and results in the formation of 2-5 nm sized Cu_2O nanoparticles (Figure 1.11 B) that are selectively located on the TiO_2 nanoparticles.[36]

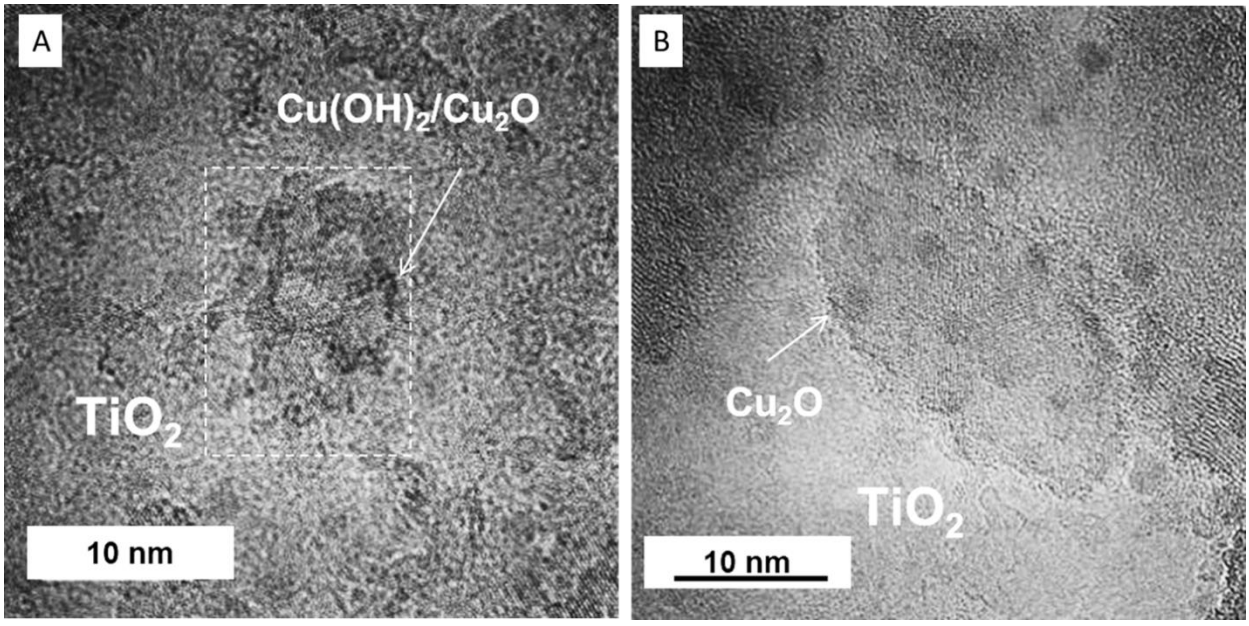

Figure 1.11: TEM image of the (A) as obtained Cu/TiO_2 nanoparticles showing an amorphous thin layer of $Cu_2O/Cu(OH)_2$ on TiO_2 nanoparticles and (B) after a few minutes of exposure to the electron beam showing the formation of 2 nm sized Cu_2O nanoparticles on TiO_2 nanoparticles.[36]

1.4 Conclusion

The fabrication of TiO_2 nanoparticles at both high and low densities has been realized using PVD. The size and crystallinity of the nanoparticles is able to be relatively controlled by adjusting the HOPG substrate temperature and amount of material deposited via QCM. The PVD parameters used here result in the formation rutile TiO_2 nanoparticles that are 25-40 nm in diameter for the low density nanoparticles, or linear arrays, and 15-20 nm in diameter for the high density nanoparticles. The selective deposition of Cu_2O and $Cu(OH)_2$ species onto the TiO_2 nanoparticles was realized using photodeposition. Various hole scavenging agents were tested and it was found that the addition of 1% methanol to the aqueous $CuCl_2$ solution resulted in an improved deposition rate with the formation of 2-5 nm diameter Cu-based nanoparticles. This model catalyst system is able to be rigorously characterized and used in reactivity studies, which will be discussed later.

1.5 References

(1) Bagheri, S.; Julkapli, N. M.; Bee Abd Hamid, S. Titanium Dioxide as a Catalyst Support in Heterogeneous Catalysis. *Sci. World J.* **2014**, 1–21.

(2) Porosoff, M. D.; Yan, B.; Chen, J. G. Catalytic Reduction of CO_2 by H_2 for Synthesis of CO, Methanol and Hydrocarbons: Challenges and Opportunities. *Energy Environ. Sci.* **2016**, *9*, 62–73.

(3) Liu, X.-M.; Lu, G. Q.; Yan, Z.-F.; Beltramini, J. Recent Advances in Catalysts for Methanol Synthesis via Hydrogenation of CO and CO_2. *Ind. Eng. Chem. Res.* **2003**, *42* (25), 6518–6530.

(4) Abdullah, H.; Khan, M. M. R.; Ong, H. R.; Yaakob, Z. Modified TiO_2 Photocatalyst for CO_2 Photocatalytic Reduction: An Overview. *J. CO_2 Util.* **2017**, *22*, 15–32.

(5) Shibasaki-kitakawa, N.; Honda, H.; Kuribayashi, H.; Toda, T. Biodiesel Production Using Anionic Ion-Exchange Resin as Heterogeneous Catalyst. *Bioresour. Technol.* **2007**, *98*, 416–421.

(6) Leng, Y.; Liu, J.; Jiang, P.; Wang, J. Organometallic-Polyoxometalate Hybrid Based on V-Schiff Base and Phosphovanadomolybdate as a Highly Effective Heterogenous Catalyst for Hydroxylation of Benzene. *Chem. Eng. J.* **2014**, *239*, 1–7.

(7) Gao, F.; Goodman, D. W. Model Catalysts: Simulating the Complexities of Heterogeneous Catalysts. *Annu. Rev. Phys. Chem.* **2012**, *63* (1), 265–286.

(8) Freund, H. J.; Kuhlenbeck, H.; Libuda, J.; Rupprechter, G.; Baumer, M.; Hamann, H. Bridging the Pressure and Materials Gaps between Catalysis and Surface Science: Clean and Modified Oxide Surfaces. *Top. Catal.* **2001**, *15* (2–4), 201–209.

(9) Libuda, J.; Schauermann, S.; Laurin, M.; Schalow, T.; Freund, H. J. Model Studies in Heterogeneous Catalysis. From Structure to Kinetics. *Monatshefte fur Chemie* **2005**, *136* (1), 59–75.

(10) Rodriguez, J. A.; Liu, P.; Graciani, J.; Senanayake, S. D.; Grinter, D. C.; Stacchiola, D.; Hrbek, J.; Fernández-Sanz, J. Inverse Oxide/Metal Catalysts in Fundamental Studies and Practical Applications: A Perspective of Recent Developments. *J. Phys. Chem. Lett.* **2016**, *7* (13), 2627–2639.

(11) Bell, A. T. The Impact of Nanoscience on Heterogeneous Catalysis. *Science.* **2003**, *299*, 1688–1691.

(12) Bahruji, H.; Bowker, M.; Hutchings, G.; Dimitratos, N.; Wells, P.; Gibson, E.; Jones, W.; Brookes, C.; Morgan, D.; Lalev, G. Pd/ZnO Catalysts for Direct CO_2 Hydrogenation to Methanol. *J. Catal.* **2016**, *343*, 133–146.

(13) Saeidi, S.; Amin, N. A. S.; Rahimpour, M. R. Hydrogenation of CO_2 to Value-Added Products - A Review and Potential Future Developments. *J. CO_2 Util.* **2014**, *5*, 66–81.

(14) Nomura, N.; Tagawa, T.; Goto, S. Titania Supported Copper Catalysts for Methanol Synthesis from Carbon Dioxide. *React. Kinet. Catal. Lett.* **1998**, *63* (1), 9–13.

(15) Chen, C. S.; Chen, T. C.; Chen, C. C.; Lai, Y. T.; You, J. H.; Chou, T. M.; Chen, C. H.; Lee, J. F. Effect of Ti^{3+} on TiO_2-Supported Cu Catalysts Used for CO Oxidation. *Langmuir* **2012**, *28* (26), 9996–10006.

(16) Xiao, J.; Mao, D.; Guo, X.; Yu, J. Effect of TiO_2, ZrO_2, and TiO_2-ZrO_2 on the Performance of CuO-ZnO Catalyst for CO_2 Hydrogenation to Methanol. *Appl. Surf. Sci.* **2015**, *338*, 146–153.

(17) Kattel, S.; Ramírez, P. J.; Chen, J. G.; Rodriguez, J. A.; Liu, P. Active Sites for CO_2

Hydrogenation to Methanol on Cu / ZnO Catalysts. *Science.* **2017**, *355*, 1296–1299.
(18) Raciti, D.; Wang, C. Recent Advances in CO_2 Reduction Electrocatalysis on Copper. *ACS Energy Lett.* **2018**, *3* (7), 1545–1556.
(19) Kas, R.; Kortlever, R.; Milbrat, A.; Koper, M. T. M.; Mul, G.; Baltrusaitis, J. Electrochemical CO_2 Reduction on Cu_2O-Derived Copper Nanoparticles: Controlling the Catalytic Selectivity of Hydrocarbons. *Phys. Chem. Chem. Phys.* **2014**, *16* (24), 12194–12201.
(20) Kuhl, K. P.; Hatsukade, T.; Cave, E. R.; Abram, D. N.; Kibsgaard, J.; Jaramillo, T. F. Electrocatalytic Conversion of Carbon Dioxide to Methane and Methanol on Transition Metal Surfaces. *J. Am. Chem. Soc.* **2014**, No. 136, 14107–14113.
(21) Peterson, A. A.; Nørskov, J. K. Activity Descriptors for CO_2 Electroreduction to Methane on Transition-Metal Catalysts. *J. Phys. Chem. Lett.* **2012**, *3*, 251–258.
(22) Hori, Y.; Murata, A.; Takahashi, R. Formation of Hydrocarbons in the Electrochemical Reduction of Carbon Dioxide at a Copper Electrode in Aqueous Solution. *J. Chem. Soc., Faraday Trans. 1* **1989**, *85* (8), 2309–2326.
(23) Kuhl, K. P.; Cave, E. R.; Abram, D. N.; Jaramillo, T. F. New Insights into the Electrochemical Reduction of Carbon Dioxide on Metallic Copper Surfaces. *Energy Environ. Sci.* **2012**, *5*, 7050–7059.
(24) Herman, R. G.; Klier, K.; Simmons, G. W.; Finn, B. P.; Bulko, J. B.; Kobylinski, T. P. Catalytic Synthesis of Methanol from COH_2. *J. Catal.* **1979**, *56* (3), 407–429.
(25) Sheffer, G. R.; King, T. S. Differences in the Promotional Effect of the Group IA Elements on Unsupported Copper Catalysts for Carbon Monoxide Hydrogenation. *J. Catal.* **1989**, *116* (2), 488–497.
(26) Gao, D.; Zegkinoglou, I.; Divins, N. J.; Scholten, F.; Sinev, I.; Grosse, P.; Cuenya, B. R. Plasma-Activated Copper Nanocube Catalysts for Efficient Carbon Dioxide Electroreduction to Hydrocarbons and Alcohols. *ACS Nano* **2017**, *11*, 4825–4831.
(27) Li, C. W.; Kanan, M. W. CO_2 Reduction at Low Overpotential on Cu Electrodes Resulting from the Reduction of Thick Cu_2O Films. *J. Am. Chem. Soc.* **2012**, *134* (17), 7231–7234.
(28) Wang, Y.; Chen, Z.; Han, P.; Du, Y.; Gu, Z.; Xu, X.; Zheng, G. Single-Atomic Cu with Multiple Oxygen Vacancies on Ceria for Electrocatalytic CO_2 Reduction to CH_4. *ACS Catal.* **2018**, *8* (8), 7113–7119.
(29) Jupille, J.; Thornton, G. *Defects at Oxide Surfaces*, Vol. 58.; Springer, 2015.
(30) Guo, Q.; Zhou, C.; Ma, Z.; Ren, Z.; Fan, H.; Yang, X. Elementary Photocatalytic Chemistry on TiO_2 Surfaces. *Chem. Soc. Rev.* **2016**, *45*, 3701–3730.
(31) Mahlamvana, F.; Kriek, R. J. Photocatalytic Reduction of Platinum (II and IV) from Their Chloro Complexes in a Titanium Dioxide Suspension in the Absence of an Organic Sacrificial Reducing Agent. *Appl. Catal. B Environ.* **2014**, *148–149*, 387–393.
(32) Wu, C. H.; Eren, B.; Bluhm, H.; Salmeron, M. B. Ambient-Pressure X-Ray Photoelectron Spectroscopy Study of Cobalt Foil Model Catalyst under CO, H_2, and Their Mixtures. *ACS Catal.* **2017**, *7* (2), 1150–1157.
(33) Kruse, N.; Chenakin, S. XPS Characterization of Au/TiO_2 Catalysts: Binding Energy Assessment and Irradiation Effects. *Appl. Catal. A Gen.* **2011**, *391*, 367–376.
(34) Levesque, T.; Leckenby, J. Application of Plasma Cleaning Technology in Microscopy. XEI Scientific, Inc.
(35) Taing, J.; Cheng, M. H.; Hemminger, J. C. Photodeposition of Ag or Pt onto TiO_2 Nanoparticles Decorated on Step Edges of HOPG. *ACS Nano* **2011**, *5* (8), 6325–6333.

(36) Ferrah, D.; Haines, A. R.; Galhenage, R. P.; Bruce, J. P.; Babore, A. D.; Hunt, A.; Waluyo, I.; Hemminger, J. C. Wet Chemical Growth and Thermocatalytic Activity of Cu-Based Nanoparticles Supported on TiO_2 Nanoparticles/HOPG: In Situ Ambient Pressure XPS Study of the CO_2 Hydrogenation Reaction. *ACS Catal.* **2019**, *9*, 6783–6802.
(37) Wagner, C. D.; Riggs, W. M.; Davis, L. E.; Moulder, J. F. Handbook of X-Ray Photoelectron Spectroscopy. 1979, p 190.
(38) Jackman, M. J.; Thomas, A. G.; Muryn, C. Photoelectron Spectroscopy Study of Stoichiometric and Reduced Anatase TiO_2 (101) Surfaces: The Effect of Subsurface Defects on Water Adsorption at near-Ambient Pressures. *J. Phys. Chem. C* **2015**, *119* (24), 13682–13690.
(39) Ferrah, D.; Tieu, P. Controllable Growth of Copper on TiO_2 Nanoparticles by Photodeposition Based on Coupled Effects of Solution Viscosity and Photoreduction Rate for Catalysis-Related Applications. *ACS Appl. Nano Mater.* **2020**, *3*, 5855–5861.
(40) Wenderich, K.; Mul, G. Methods, Mechanism, and Applications of Photodeposition in Photocatalysis: A Review. *Chem. Rev.* **2016**, *116* (23), 14587–14619.
(41) Foster, N. S.; Lancaster, A. N.; Noble, R. D.; Koval, C. A. Effect of Organics on the Photodeposition of Copper in Titanium Dioxide Aqueous Suspensions. *Ind. Eng. Chem. Res.* **1995**, *34*, 3865–3871.
(42) Biesinger, M. C. Advanced Analysis of Copper X-Ray Photoelectron Spectra. *Surf. Interface Anal.* **2017**, *49*, 1325–1334.

Chapter 2

Thermocatalytic Reactivity of CO_2 over CuO_x/TiO_2/HOPG and TiO_2/Cu Model Catalysts: Ambient Pressure XPS Study of CO_2 Hydrogenation Reaction

2.1 Introduction

Currently, CO_2 reduction efforts are focused on the development of highly active, selective, and stable catalysts in three categories: (1) electrochemical, (2) photocatalytic, and (3) thermal reduction of CO_2.[1,2] The thermal reduction of CO_2 is used industrially where a mixture of synthesis gases ($H_2/CO_2/CO$) is passed over a $Cu/ZnO/Al_2O_3$ catalyst at elevated temperatures and pressures.[3–6] While this catalyst is used on a larger scale for the production of methanol, there lacks a fundamental understanding of the reaction mechanism of CO_2 hydrogenation that occurs over this catalyst, as well as the role of the metal oxide supports and the nature of the copper species.[5,7–10]

It is well established that copper is an important metal for methanol synthesis, however there remains a debate as to whether copper metal (Cu^0) or oxidized copper species (Cu^+, Cu^{2+}) are responsible for the high catalytic reactivity. Some researchers have shown that methanol is formed on a metallic copper surface and is dependent on its surface area[11–13] while others have found that Cu^+ species results in higher catalytic activity.[14,15] For the electrochemical reduction of CO_2, it has been found that subsurface oxygen is key for improving the adsorption and subsequent electroreduction on Cu nanocube catalysts.[16] Since it is thought that at high temperatures, CuO_x species would reduce to copper metal, the incorporation of metal oxide supports could supply oxygen to copper which would stabilize the Cu^+ species and may improve adsorption of intermediates or CO_2 molecules for the thermal reduction process.[17]

Understanding the role of both the metal and reducible metal oxide supports will enable insight into the CO_2 reduction reaction mechanism, as it is likely that CO_2 reduction occurs at the interface of these particles.[5] It is generally thought that hydrogen splitting occurs on the copper species (either Cu^0 or Cu^+) and CO_2 adsorption occurs on the surface of the metal oxide supports, such as TiO_2, ZnO and Ce_2O_3.[1,18–23] The interface of the Cu/metal oxide has also been shown to improve the dispersion of the Cu nanoparticles, which allows for a high density of active sites and higher surface area.[18] The metal oxide supports can act in one or more of the following ways: (1) structural and morphological modifiers, (2) a reservoir for spillover hydrogen atoms, which would occur after H_2 dissociation on Cu, and (3) sites for CO_2 activation, which is achieved through either oxygen vacancies at the interface of the metal/metal oxide or through the encapsulation of Cu nanoparticles by nonstoichiometric oxide.[3,7,30–33,9,10,24–29]

Recent studies using high-resolution transmission electron microscopy (HRTEM) have shown that ZnO_x forms an overlayer on Cu particles for Cu/ZnO catalysts used in methanol synthesis.[24,34,35] This has also been observed for Cu/MoO_x, Rh/TiO_2, Ni/CeO_2, Pt/CeO_x, and Pt/TiO_2 catalysts under reduction in hydrogen atmosphere.[34,36–43] This encapsulation of metal particles may be more common in heterogeneous catalysis than expected as oxides that have low surface free energy exhibit a tendency to cover metals upon partial reduction.[24,35,36,42,44] Investigations of different systems containing metal oxides that are either (1) supports for metal nanoparticles or (2) supported on a metallic substrate will give insight into the role of these nanoparticles for CO_2 reduction.

Here we studied the reactivity of model catalysts consisting of CuO_x/TiO_2/HOPG (discussed in Chapter 1) and TiO_2 nanoparticles on a Cu metal substrate under CO_2 reduction conditions using ambient pressure X-ray photoelectron spectroscopy (AP-XPS) in an attempt to

elucidate the reaction mechanism of CO_2 hydrogenation. The stability and reactivity of these catalysts was studied as a function of increasing temperature in an atmosphere of CO_2 and H_2 reactant gases. Using AP-XPS, we were able to observe the intermediate formation for various systems and gain insight into the mechanism of CO_2 hydrogenation and the importance of the metal oxide supports.

2.2 Experimental

2.2.1 Fabrication of TiO_2/HOPG, CuO_x/TiO_2/HOPG, and TiO_2/Cu samples

The TiO_2 nanoparticles on HOPG were prepared by PVD on a commercial evaporator under high vacuum (10^{-6} Torr). The HOPG substrate was pretreated with low energy Ar plasma in order to achieve a high density of TiO_2 nanoparticles. The HOPG substrate temperature was held at 770 ^{o}C throughout the deposition and further annealed for 2.5 hours after deposition in order to obtain rutile TiO_2 nanoparticles. For the CuO_x/TiO_2/HOPG samples studied here, a photodeposition solution of aqueous 3 mM $CuCl_2$ at a pH of 3 with the addition of 1% by volume of methanol was used. The sample was submerged in this solution and irradiated with UV light for 6 hours in order to selectively deposit CuO_x nanoparticles onto the TiO_2 nanoparticles.

For the inverse model catalyst, TiO_2 nanoparticles are deposited onto a copper metal surface. The Cu metal was sonicated for 15 minutes in separate solutions of acetone, methanol, and acetic acid before it was placed into the PVD chamber in order to remove any hydrocarbons and the native oxide layer. The metal was attached to a piece of HOPG in order to resistively heat the sample during TiO_2 deposition. The Cu metal was then heated to 500 ^{o}C in order to remove any adsorbed water. Three separate samples were prepared and the substrate temperature

during the deposition was reduced to 100, 200 and 300 ^{o}C for each sample. TiO_2 was then deposited for 10 minutes to achieve a QCM reading of 1 nm and subsequently annealed for 30 minutes. The above samples were characterized using scanning electron microscopy (SEM) and X-ray photoelectron spectroscopy (XPS) using an FEI Magellan 400 XHR SEM and Kratos Axis Supra photoelectron spectrometer (Kratos Analytical), respectively, prior to reactivity studies.

2.2.2 Ambient pressure X-ray photoelectron spectroscopy

AP-XPS measurements were performed at the 23-ID-2 (IOS) beamline at the National Synchrotron Light Source II (NSLS-II) at Brookhaven National Laboratory (BNL). Reactant gases of CO_2, H_2, and O_2 were used in this study. The samples were mounted on a pyrolytic boron nitride heater in order to study the reactivity of the samples as a function of temperature. Prior to analysis, the samples were annealed in ultra-high vacuum (UHV) at 275 ^{o}C (550 K) for 15 minutes in order to desorb any water and contamination. The AP-XPS chamber was backfilled with 100 mTorr of CO_2 and H_2 (200 mTorr total) and the samples supported on HOPG were heated in the temperature range of 300-550 K. The photon energies used for this study were 1120, 870, 685 and 450 eV. The C 1s, Ti 2p, O 1s, Cu 2p, and Cu LMM high resolution spectra were recorded with a pass energy of 10 eV. All recorded spectra were calibrated to the C 1s peak appearing at 284.4 eV, corresponding to graphitic carbon of HOPG.[45,46]

For the sample consisting of TiO_2 nanoparticles deposited on a Cu metal substrate, the AP-XPS chamber was backfilled with equal parts CO_2 and H_2 to give a total pressure of 200 mTorr and the substrate was heated in the temperature range of 350-650 K. The high resolution spectra were acquired at a photon energy of 1170 eV with a pass energy of 10 eV.

2.3 Results and Discussion

XPS measurements were obtained at different photon energies of 450, 685, 870, and 1120 eV in order to obtain depth profile information of the sample under reaction conditions. The photon energy (E_P) range corresponds to photoelectron kinetic energies (E_K) of approximately 150, 340, and 590 eV for the C 1s and O 1s orbitals ($E_K = E_P - E_B$, where E_B is the orbital binding energy). The AP-XPS measurements for all the samples were taken under CO_2 reduction conditions by heating the substrate and ramping up the temperature from 300-550 K in an environment of equal parts CO_2 and H_2 reactant gases to give a total pressure of 200 mTorr. The reaction conditions used during this study are described in Table 2.1. Initially, XPS measurements were performed in UHV at 300 K (Condition 1) and with the introduction of CO_2 (Condition 2) before performing the temperature ramp and the addition of H_2 gas (Conditions 3-8). The reactant gases were then pumped out and the substrate temperature returned to 300 K (Condition 9).

Table 2.1: Description of the reaction conditions used in the AP-XPS study of CO_2 hydrogenation for various model catalysts.

Condition	Gas	Substrate Temp. (K)
1	UHV	300
2	100 mTorr CO_2	300
3	100 mTorr CO_2, 100 mTorr H_2	300
4	100 mTorr CO_2, 100 mTorr H_2	350
5	100 mTorr CO_2, 100 mTorr H_2	400
6	100 mTorr CO_2, 100 mTorr H_2	450
7	100 mTorr CO_2, 100 mTorr H_2	500
8	100 mTorr CO_2, 100 mTorr H_2	550
9	UHV	300

The possible intermediates for the reduction of CO_2 with the addition of H_2O or H_2 gases are activated CO_2 ($CO_2^{\delta-}$), methoxy ($O–CH_3$), formate ($HCOO^-$), carbonate (CO_3^{2-}), adsorbed CO (CO^{ad}) and water (H_2O^{ad}), CH_xO, CH_x, and OH^-.[33,47,48] The deconvolution of the O 1s and C 1s spectra were fitted to account for these intermediates, however, the binding energy of these intermediates overlaps with peaks that are already present in both the C 1s and O 1s spectra. In order to account for this, the ratios between the C 1s/Ti 2p and O 1s/Ti 2p peaks are used to identify specific changes that occur throughout the reaction. The O 1s and C 1s ratios are taken with respect to the Ti 2p spectrum as the TiO_2 nanoparticles remain stable under reaction conditions. For instance, if the Ti^{4+} intensity does not change, then the O 1s peak corresponding to TiO_2 should not fluctuate as well and any increase in the intensity of that peak would be indicative of an increase in methoxy ($O–CH_3$) formation.

Table 2.2: Binding energy positions and components used in the deconvolution of the C 1s and O 1s high resolution XPS spectra.

C1s		**O1s**	
Position (eV)	**Component**	**Position (eV)**	**Component**
283.9	C–M	530.4	TiO_2, Cu_2O, $O–CH_3$
284.5	C=C	531.2	–OH
285.0	C–C, $O–CH_3$, CH_x	532.4	carbon contamination, $HCOO^-$, CO_3^{2-}, CO^{ad}
286.1	CH_xO	533.6	H_2O^{ad}
287.1	C=O, $HCOO^-$, CO^{ad}	536.9	CO_2 (g)
288.5	$CO_2^{\delta-}$		
289.7	O–C=O, CO_3^{2-}		
291.2	($\pi \rightarrow \pi^*$) transition		
293.3	CO_2 (g)		

The deconvolution and components for the O 1s and C 1s spectra are listed in Table 2.2.[47–51] Representative O 1s and C 1s spectra at different photon energies with the

deconvolution is shown in Figure 2.1 for a Cu/TiO_2/HOPG sample with a substrate temperature of 350 K in an environment of 200 mTorr equal parts CO_2 and H_2 reactant gases. The CO_2 gas phase peak (Figure 2.1A) is more pronounced at lower photon energy, corresponding to the surface of the nanoparticles, and becomes less prominent at higher photon energies. The C1s spectrum is dominated by the strong signal contribution from the sp^2 hybridized carbon in

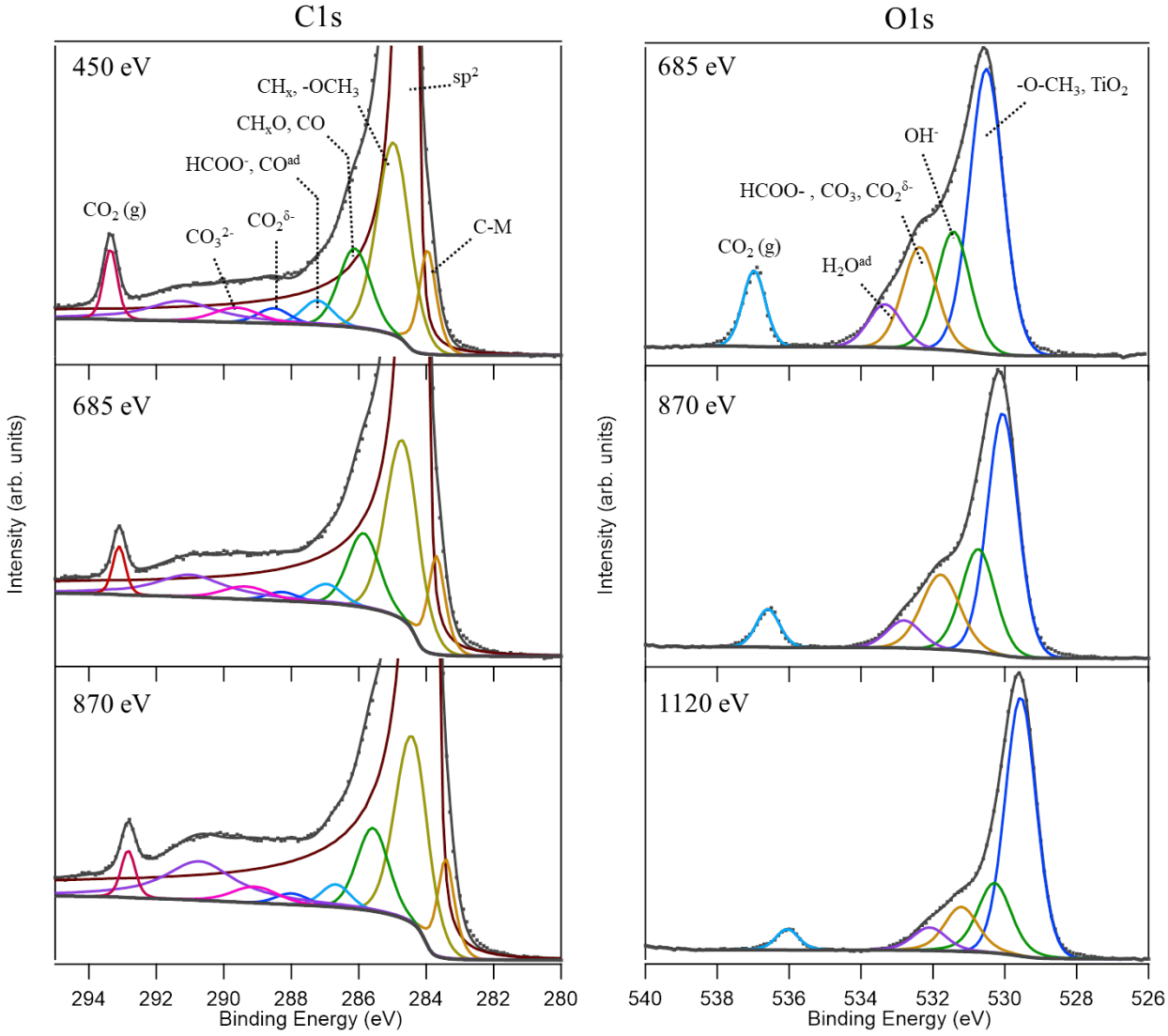

Figure 2.1: (A) C 1s and (B) O 1s spectra recorded at various photon energies during the *in situ* CO_2 reduction reaction on a Cu/TiO_2/HOPG sample with equal parts CO_2 and H_2 (200 mTorr total) at 350 K.

graphite and the contribution from carbon contamination. The C 1s deconvolution was performed by restricting the background, position, energy, and FWHM parameters in order to compare the fluctuations in the signal contributions of these species and ensure accurate analysis.

2.3.1 TiO_2/HOPG sample

The intensity ratio of C 1s(x)/Ti 2p and O 1s(x)/Ti 2p is plotted with respect to the reaction conditions (detailed in Table 2.1) in Figure 2.2 where (x) refers to the specific component that is analyzed as seen displayed on the Figure. Initially, gas phase CO_2 (Figure 2.2A, red curve) is physisorbed on the surface of TiO_2 nanoparticles and the amount of CO_2 gas decreases with increasing substrate temperature and progression of the reaction. While the CO_2 gas component decreases, there is an observed increase in the CO_3^{2-}, $HCOO^-$, CO^{ad}, and $O–CH_3$ and CH_x curves which indicates that the gas phase CO_2 is activated on the TiO_2 nanoparticles. However, the formation of CO_3^{2-} is unstable at high temperatures, as seen in the decrease of the CO_3^{2-} component with progression of the reaction, and may desorb as CO_2 or further hydrogenate to $HCOO^-$.

The green curve in Figure 2.2A corresponding to $HCOO^-$ at binding energy 287.3 eV steadily increases with the progression of the reaction until about 450 K (Condition 6) where it starts to decrease, indicating that the $HCOO^-$ intermediate may hydrogenate further. The formation of $O–CH_3$ steadily increases as the reaction progresses, as seen by tracking the gold curves in Figure 2.2A and B. The slow increase in the O 1s/Ti 2p curve for $O–CH_3$ is likely a result of a lack of significant H_2 dissociation that occurs on the TiO_2 nanoparticles. This results in a slight increase of the intensity ratio as the reaction progresses where it is assumed that, with the addition of more dissociated hydrogen, there would be a sharper increase for this component.

These results show that TiO_2 has the ability to dissociate H_2 however; it is much less prominent compared to the dissociation that occurs on copper nanoparticles, which will be discussed later.

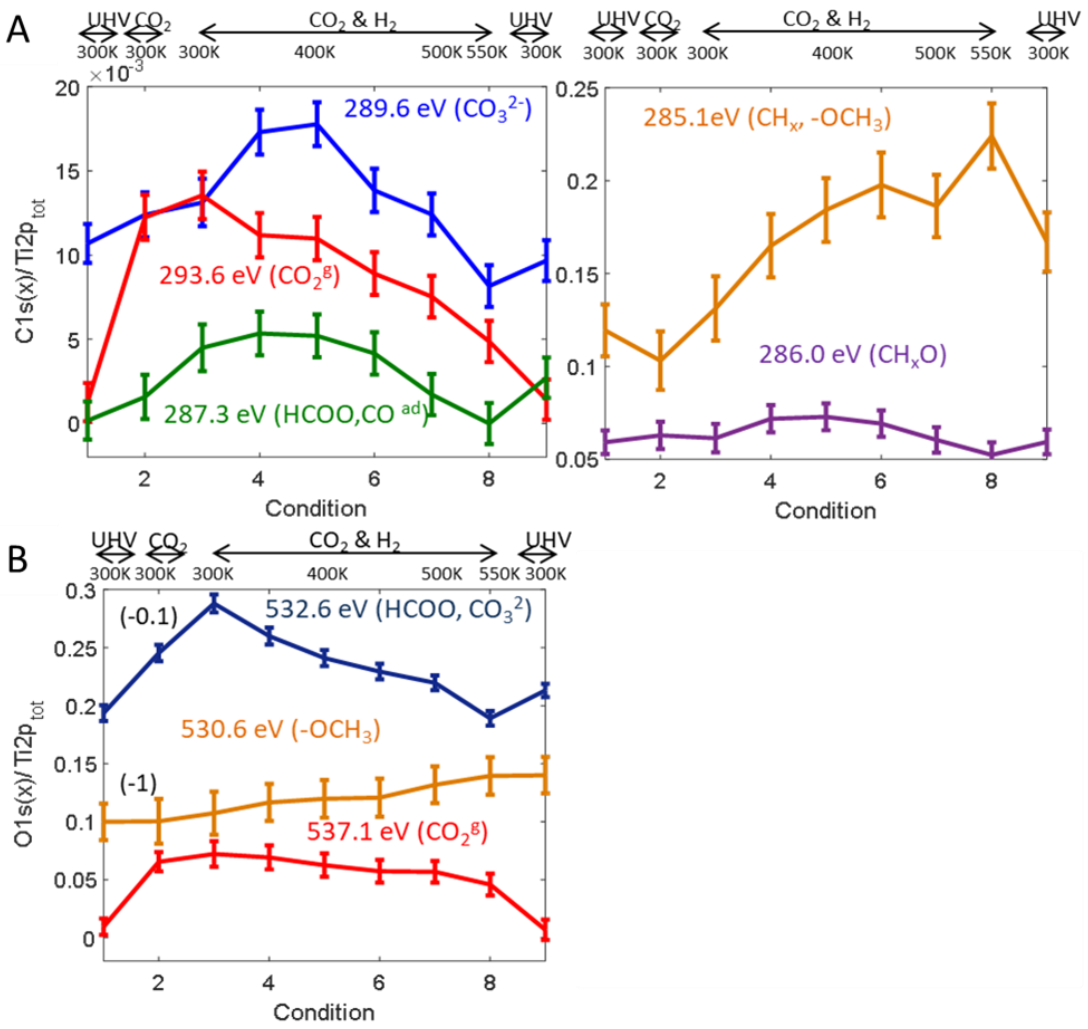

Figure 2.2: (A) C 1s(x)/Ti 2p and (B) O 1s(x)/Ti 2p intensity profile evolution as a function of reaction conditions on TiO_2/HOPG sample.[52] Reprinted with permission from Reference 52. Copyright 2019 American Chemical Society.

The sharp increase in the CH_x and O–CH_3 curve (gold curve in Figure 2.2A) at 285.1 eV is likely a result of carbon contamination that forms on the surface of the sample since, after the reactant gases have been pumped out (Condition 9), there is still a significant intensity of that component that remains. The decrease that is observed is likely a result of the intermediate

formation and subsequent evacuation after the reactant gases have been pumped out. The observed formation of $O–CH_3$ indicates that TiO_2 nanoparticles may be used in the reduction of CO_2 into methanol via the methoxy ($O–CH_3$) pathway, although this reaction is slower compared to the samples that contain copper nanoparticles as a result of less H_2 being dissociated on TiO_2.

XPS spectra of the TiO_2 nanoparticles initially and after the reaction (Figure 2.3A and B) show two Ti $2p_{3/2}$ peaks located at 458.0 and 459.4 eV corresponding to oxygen vacancies (Ti^{3+}) and Ti^{4+} species in TiO_2, respectively. The Ti 2p spectrum shows that the Ti^{3+} species is more prevalent initially and decreases after heating and reaction with CO_2 and H_2 synthesis gases. Figure 2.4 shows the evolution of the intensity ratio of Ti^{3+}/Ti^{4+} species as the reaction progresses and shows a significant decrease upon introduction of CO_2 (Condition 2) which continues to decrease with increasing substrate temperature. It is assumed that the oxygen vacancies are filled with CO_2 and then by the intermediate products that are formed upon introduction of H_2 gas and as the reaction proceeds.

It is well known that TiO_2 (110) has three main stable adsorption sites of (1) oxygen vacancies or surface defects (O_v), (2) 5-fold coordinated Ti (Ti_{5c}), and (3) oxygen bridging sites (O_b).[53] For the samples here, including the ones containing copper nanoparticles, the activation of CO_2 at O_v sites is confirmed by the presence of Ti^{3+} defects of the TiO_2 nanoparticles (Figure 2.3). The formation of the CO_3^{2-} species is likely a result of the bonding of CO_2 molecules to the O_b sites however, CO_3^{2-} is unstable at high temperatures and may desorb as CO_2 or displace to adjacent Ti_{5c} or O_v sites to further hydrogenate. The CO_2 molecules that are bound through either the Ti_{5c} or O_v sites are assumed to be more stable and would further hydrogenate to form $HCOO^-$ and subsequently $O–CH_3$. The dissociation of H_2 on TiO_2 has been suggested to be a result of the O_b sites in TiO_2, however this mechanism is not well understood.[53]

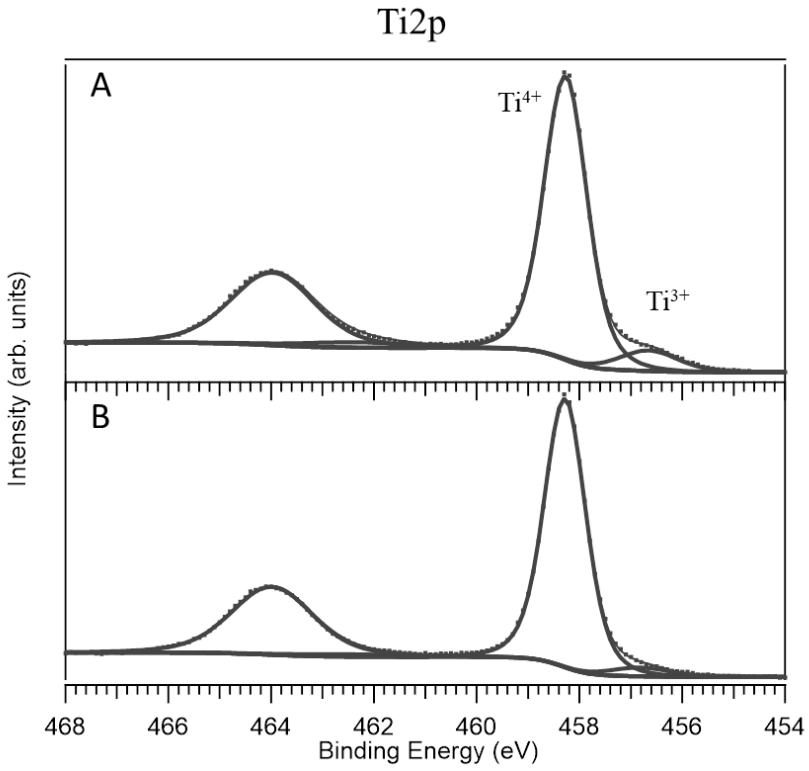

Figure 2.3: Ti 2p XPS spectra of TiO_2 nanoparticles (A) initially and (B) after CO_2 reduction reaction.

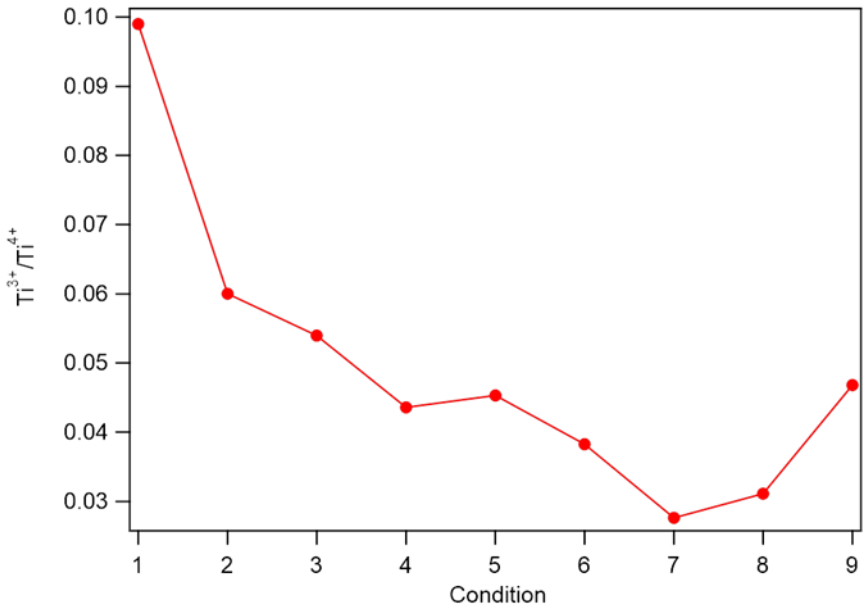

Figure 2.4: Ti^{3+}/Ti^{4+} intensity as a function of the reaction conditions described in Table 2.1. The Ti 2p spectra were recorded at 1120 eV photon energy on a TiO_2/HOPG sample.

2.3.2 Cu/TiO_2/HOPG sample

The Cu-based nanoparticles that are deposited onto the TiO_2 nanoparticles are usually a combination of Cu_2O and $Cu(OH)_2$ species, as discussed in Chapter 1. However, the strong X-rays produced at the synchrotron result in the reduction of the $Cu(OH)_2$ species into Cu_2O so there is only one Cu species present for these samples. In order to obtain reactivity data of copper metal (Cu^0) nanoparticles, the CuO_x/TiO_2/HOPG samples were heated to 690 K in the UHV chamber for 15 minutes. The transition from CuO_x species to Cu^0 was confirmed by the Cu LMM spectrum, as the binding energy of Cu^0 and Cu_2O is essentially the same and the X-ray induced Auger spectrum (Cu LMM) has very specific peak shapes for the Cu^0, Cu^+ and Cu^{2+} species (Figure 2.5).[54]

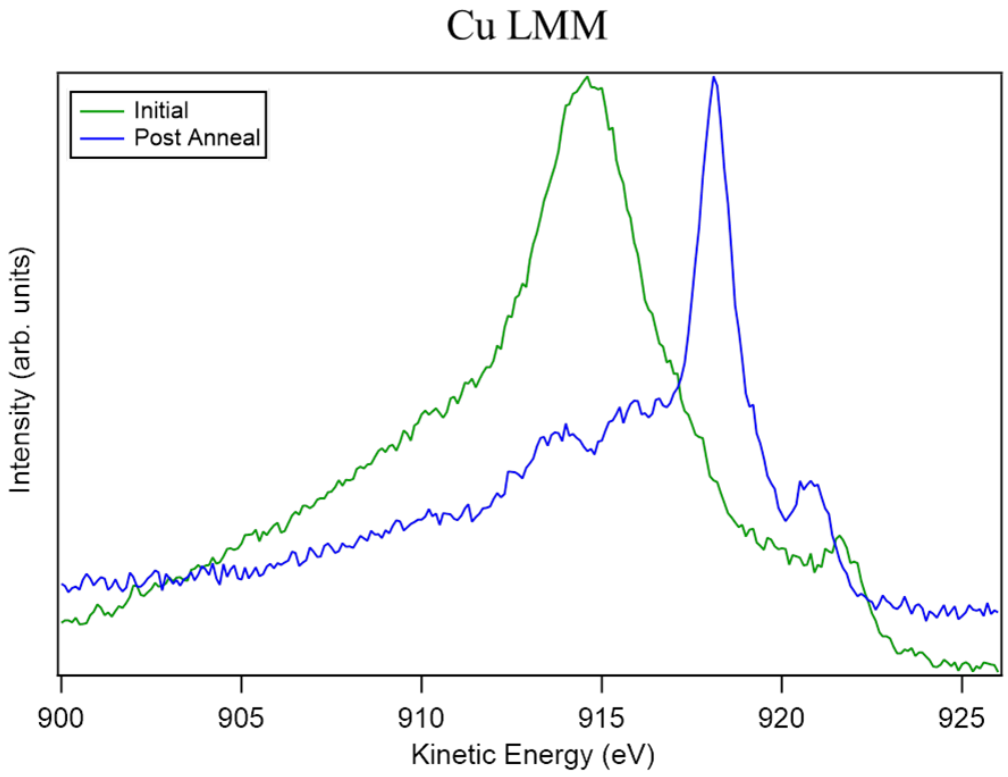

Figure 2.5: Cu LMM spectra of CuO_x/TiO_2/HOPG sample initially (green trace) indicating the presence of Cu_2O. The sample was annealed at 690 K for 15 minutes in the AP-XPS chamber (blue trace) and shows the formation of Cu^0.

The intensity ratio of C 1s(x)/Ti 2p and O 1s(x)/Ti 2p is plotted with respect to the reaction conditions in Figure 2.6. After the introduction of CO_2 and H_2 at 300 K, a small signal arises from $HCOO^-$ (green curve, Figure 2.6A) at 287.1 eV which then decreases with increasing substrate temperature. The activated CO_2 ($CO_2^{\delta-}$) component (teal curve) located at 288.5 eV remains relatively stable with the progression of the reaction. It is assumed that the initial increase in $HCOO^-$ is a result of the spontaneous conversion of $CO_2^{\delta-}$ to $HCOO^-$. At temperatures above 450 K, the $HCOO^-$ signal decreases (Figure 2.6A) which is consistent with studies that

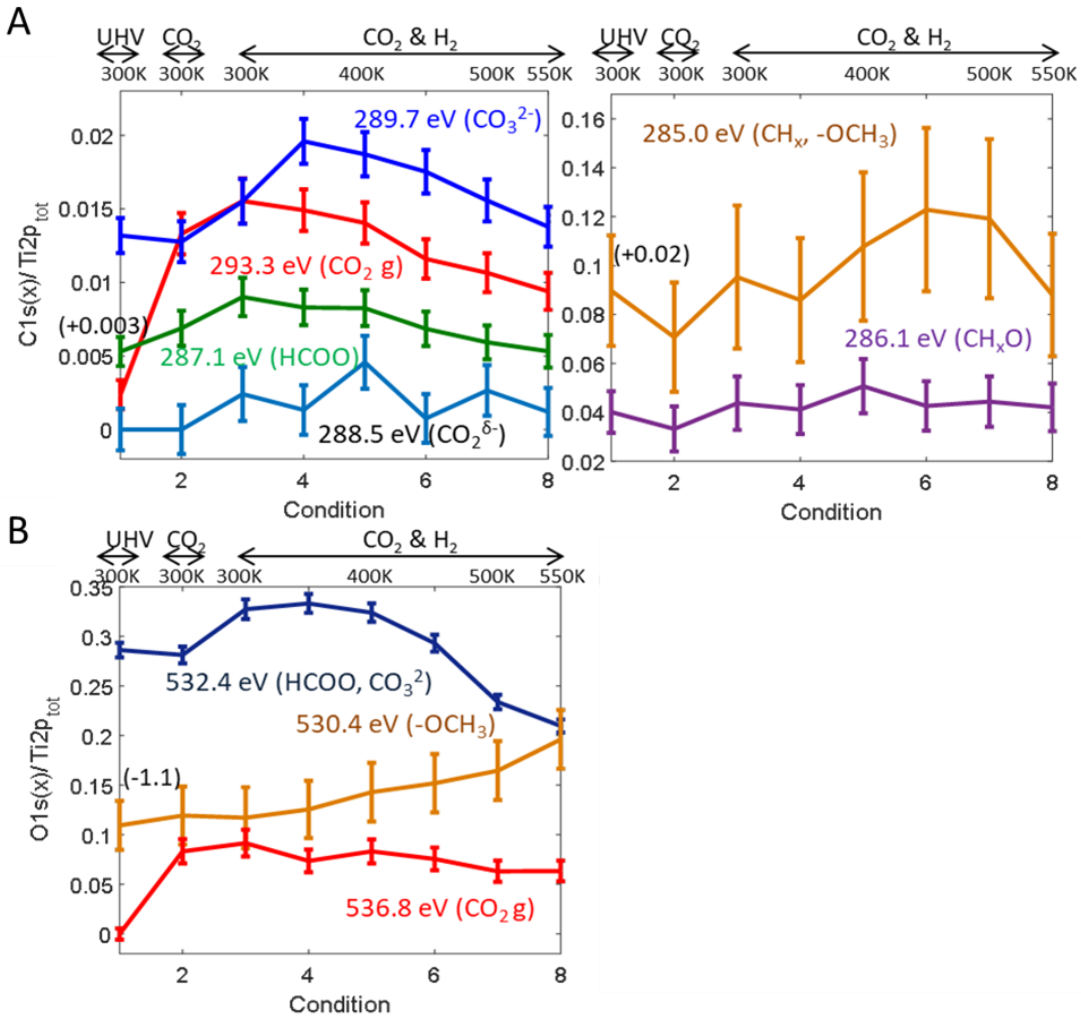

Figure 2.6: (A) C 1s(x)/Ti 2p and (B) O 1s(x)/Ti 2p intensity profile evolution as a function of reaction conditions on Cu/TiO_2/HOPG sample.[52] Reprinted with permission from Reference 52. Copyright 2019 American Chemical Society.

show that $HCOO^-$ is unstable at temperatures above 450 K.[51] $HCOO^-$ and CO^{ad} have the same binding energy and it is expected that the CO^{ad} contribution would increase at temperatures above 350 K but, as that is not observed; it is assumed that there is a lack of CO formation on the Cu/TiO_2/HOPG sample. The decreasing signal of $HCOO^-$ at higher temperatures may be indicative of its subsequent hydrogenation to higher level intermediates, such as CH_x or methoxy ($O–CH_3$).

The formation of CO_3^{2-} (blue curve, Figure 2.6A) located at 289.7 eV reaches a maximum at 350 K and then proceeds to decrease with increasing substrate temperature. As discussed previously, the initial formation of CO_3^{2-} is explained by adsorption of CO_2 to the O_b sites in TiO_2 nanoparticles which are not stable at high temperatures and could either desorb as CO_2 or further hydrogenate to $HCOO^-$. It has been thought that the formation of CO_3^{2-} is associated with CO_2 dissociation into CO and CO_3^{2-} but the working conditions in this experiment are not favorable for this dissociation nor do we observe any CO adsorption in the XPS measurements.[48]

The signal contribution from CH_xO (purple curve, Figure 2.6A) at 286.1 eV is not significant and it is not thought that this intermediate is produced during this reaction. At 285.0 eV, the CH_x and $O–CH_3$ signals overlap and show an increase with increasing temperature (Figure 2.6A). It is thought that this is mostly attributed to the formation of $O–CH_3$ as opposed to CH_x since the $O–CH_3$ O 1s signal increases with increasing reaction temperature as well (Figure 2.6B). These results indicate that CO_2 activation occurs initially through the formation of the $HCOO^-$ intermediate. The $HCOO^-$ is then further hydrogenated to produce methoxy ($O–CH_3$) likely by a complex pathway that would involve OCH and OCH_2 intermediates. However, we did not observe any formation of $O–CH_3$ via mass spectrometry as the chemisorbed methanol is

only stable at the surface at low temperatures[50] and the produced gas phase is likely under the detection limit. The formation of CO, CH_x, and CH_xO, which are related to the synthesis of methane, was also not observed in the mass spectrum as it is likely under the detection limits.

For CO_2 hydrogenation over the Cu/TiO_2/HOPG sample at moderate pressure (< 1 Torr), we suggest that H_2 gas dissociates on the surface of the Cu nanoparticles while CO_2 is activated at the surface of the TiO_2 nanoparticles. The primary spillover of atomic hydrogen (H_a) from the Cu nanoparticles then interacts with activated CO_2 ($CO_2^{\delta-}$) on the surface of TiO_2 which produces $HCOO^-$ and subsequently $O–CH_3$. It is presumed that the methoxy intermediate will further hydrogenate to form methanol (CH_3OH).

2.3.3 Cu@CuO_x/TiO_2/HOPG sample

The Cu-Cu_2O core-shell (Cu@Cu_2O)/TiO_2/HOPG sample was formed by the incomplete annealing of the CuO_x/TiO_2/HOPG sample and subsequent exposure to oxygen gas for 1 minute in order to oxidize the outer layer of the Cu-based nanoparticles. The total percentage of oxygen in these particles in estimated to be below 5%.[52] The intensity ratios of C 1s(x)/Ti 2p and O 1s(x)/Ti 2p as a function of reaction condition is shown in Figure 2.7. As the reaction progresses, there is a significant rise in intensity for the peak attributed to the CH_x and $O–CH_3$ species (gold curve, Figure 2.7A) located at 284.9 eV. This indicates formation of CH_x as the O 1s peak associated with $O–CH_3$ located at 530.5 eV (gold curve, Figure 2.7B) does not show a similar increase in intensity. This is further evidenced by the rapid decline of this species after the reactant gases are pumped out and evacuated from the chamber. The incorporation of small amounts of oxygen at the surface of the Cu nanoparticles leads to a change in reaction selectivity

and favors the formation of CH_4 as opposed to CH_3OH, which is identified by the presence of the potential intermediates of CH_x and $O–CH_3$, respectively.

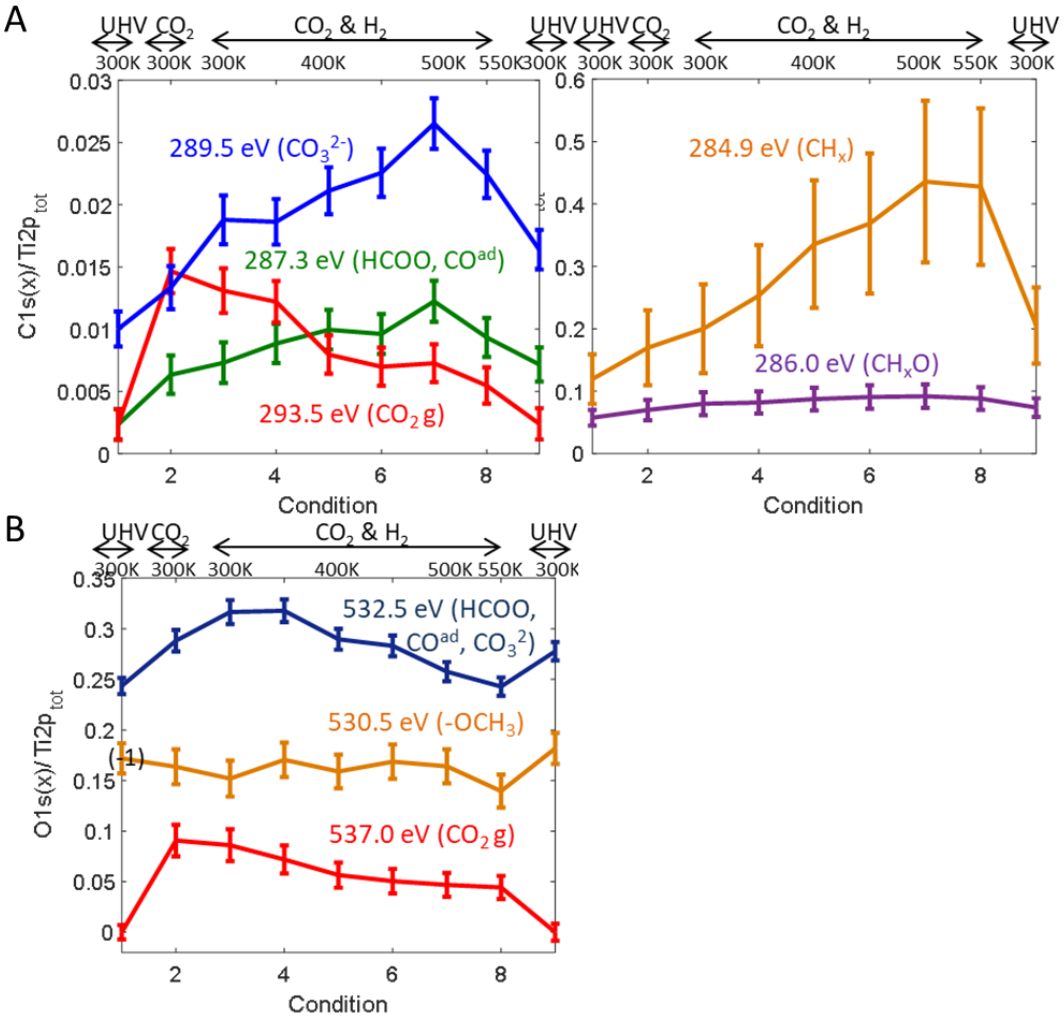

Figure 2.7: (A) C 1s(x)/Ti 2p and (B) O 1s(x)/Ti 2p intensity profile evolution as a function of reaction conditions on $Cu@CuO_x/TiO_2$/HOPG sample.[52] Reprinted with permission from Reference 52. Copyright 2019 American Chemical Society.

The CH_xO species (purple curve, Figure 2.7A) located at 286.0 eV exhibits a similar evolution in intensity as the CH_x species, although on a smaller scale. It is assumed that CH_xO is not very stable and will spontaneously hydrogenate to CH_x under the reaction conditions used here. The curve associated with $HCOO^-$ and CO^{ad} components (green curve, Figure 2.7A)

located at 287.5 eV, show a steady increase with the addition of CO_2 and H_2 and reaches a maximum at 500 K. Since the stability of $HCOO^-$ decreases with increasing temperatures, as discussed previously, it is assumed that the formation of CO occurs at 500 K. The CO_3^{2-} component (blue curve, Figure 2.7A) located at 289.5 eV shows a large increase as the reaction progresses and also reaches a maximum at 500 K. We believe that the TiO_2 nanoparticle surface allows for CO_2 adsorption at oxygen sites, which was discussed previously, resulting in the formation of CO_3^{2-}. The CO_3^{2-} formation may be attributed to the association of atomic oxygen (O_a) and CO_2, which would result in the formation of stable CO_3^{2-} species.[50]

For CO_2 hydrogenation on $Cu@Cu_2O/TiO_2/HOPG$, it is assumed that the surface of the $Cu@CuO_x$ nanoparticles leads to the adsorption and dissociation of both H_2 to H_a and CO_2 to CO and O_a. The dissociation and spillover of H_a and O_a is low at room temperature but increases rapidly with increasing substrate temperature. It is also shown that these nanoparticles are more favorable to the formation of CO_3^{2-} as opposed to $HCOO^-$. It is assumed that further spillover hydrogen allows for the hydrogenation of CO_3^{2-} with increasing temperature to CH_xO and CH_x and subsequently forms CH_4.

2.3.4 Cu_2O/TiO_2/HOPG sample

The investigation of the reactivity on a sample of Cu_2O/TiO_2/HOPG, containing fully oxidized Cu nanoparticles, was carried out under the same reaction conditions as discussed previously. Figure 2.8 shows the C 1s(x)/Ti 2p and O 1s(x)/Ti 2p intensity ratios as a function of change in reaction condition for this sample. The $CO_2^{\delta-}$ species (teal curve, Figure 2.8A) located at 288.5 eV shows a sharp increase upon introduction of CO_2 gas and a decrease in intensity ratio once H_2 gas is added to the reaction. This shows that there is significant physisorption of CO_2 at

300 K which subsequently desorbs in the presence of H_2, likely due to the weak interaction of CO_2 molecules with the surface. However, the CO_2 gas phase (red curve, Figure 2.8A) located at 293.2 eV shows an increase in intensity upon addition of H_2 gas. This further shows that the CO_2 molecules are desorbed and are no longer activated at the surface as they do not go on to form intermediates, as seen in the stationary curves of $HCOO^-$ and CO^{ad}, CO_3^{2-}, CH_xO and O–CH_3 (Figure 2.8A and B). This deactivation of CO_2 is either a result of the little to no activity of Cu_2O nanoparticles and/or the deactivation of TiO_2 upon addition of Cu_2O. The reduction in intensity

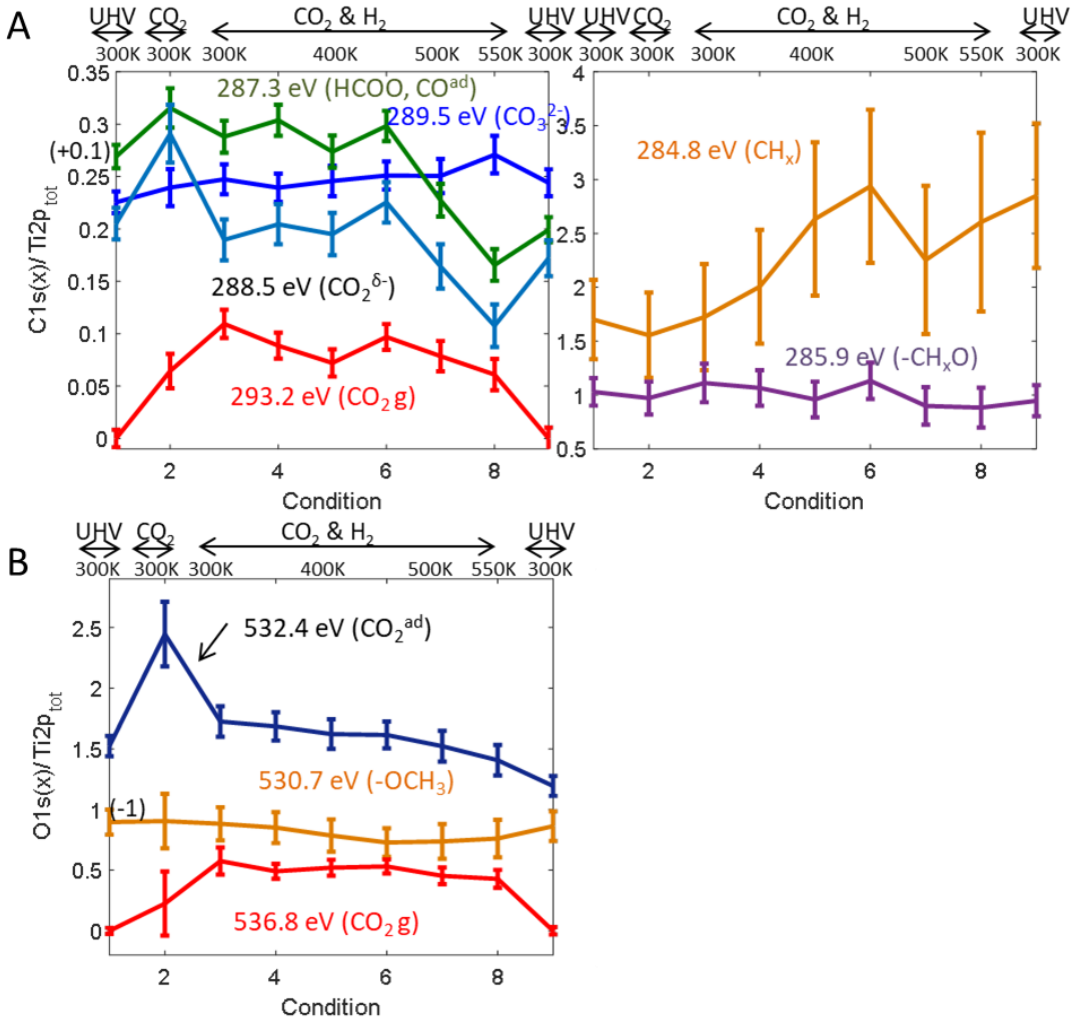

Figure 2.8: (A) C 1s(x)/Ti 2p and (B) O 1s(x)/Ti 2p intensity profile evolution as a function of reaction conditions on Cu_2O/TiO_2/HOPG sample.[52] Reprinted with permission from Reference 52. Copyright 2019 American Chemical Society.

that is observed in some of the curves above 500 K is likely due to the reduction in contamination in the H_2 atmosphere.

These results indicate the absence of CO_2 activation and subsequent hydrogenation at the surface of the TiO_2 nanoparticles when Cu_2O nanoparticles are added. Experiments made on Cu_2O nanoparticles supported on HOPG (with no TiO_2 nanoparticles present) indicates little to no adsorption of CO_2, suggesting that CO_2 is physisorbed at the surface of TiO_2 nanoparticles in the Cu_2O/TiO_2/HOPG sample. This may be due to a lack of charge transfer to the physisorbed CO_2 molecules at the TiO_2 surface where, instead, the charge transfer occurs between the TiO_2 and Cu_2O nanoparticles which lead to a weak catalyst. The intensity of the CH_x species located at 284.8 eV (Figure 2.8A) shows an increase with increasing substrate temperature in a CO_2 and H_2 atmosphere. However, this is likely due to the formation of carbon at the surface of the sample as the intensity of this species does not change when the reactant gases are pumped out of the chamber and the substrate temperature returns to 300 K. The formation of this carbon layer may be from CO_2 decomposition or graphene displacement at the surface of the TiO_2 nanoparticles as a result of the reaction conditions.

The results from the reaction study indicate that the Cu_2O/TiO_2/HOPG catalyst is inactive for CO_2 hydrogenation, mostly as a result of the introduction of Cu_2O nanoparticles. We suggest that Cu_2O does not have the ability to dissociate CO_2 or H_2 due to the lack of electron transfer between the molecules. The activation of CO_2 at the surface of TiO_2 is also not observed which is possibly due to low surface charge densities as a result of charge transfer that occurs between TiO_2 and Cu_2O nanoparticles.

2.3.5 TiO_2/Cu metal sample

SEM analysis of the TiO_2/Cu samples prepared with substrate temperatures of 100, 200 and 300 ^oC are shown in Figure 2.9D, E, and F. These SEM images display different morphologies for the various samples. At 100 ^oC, the deposited titanium appears to have formed

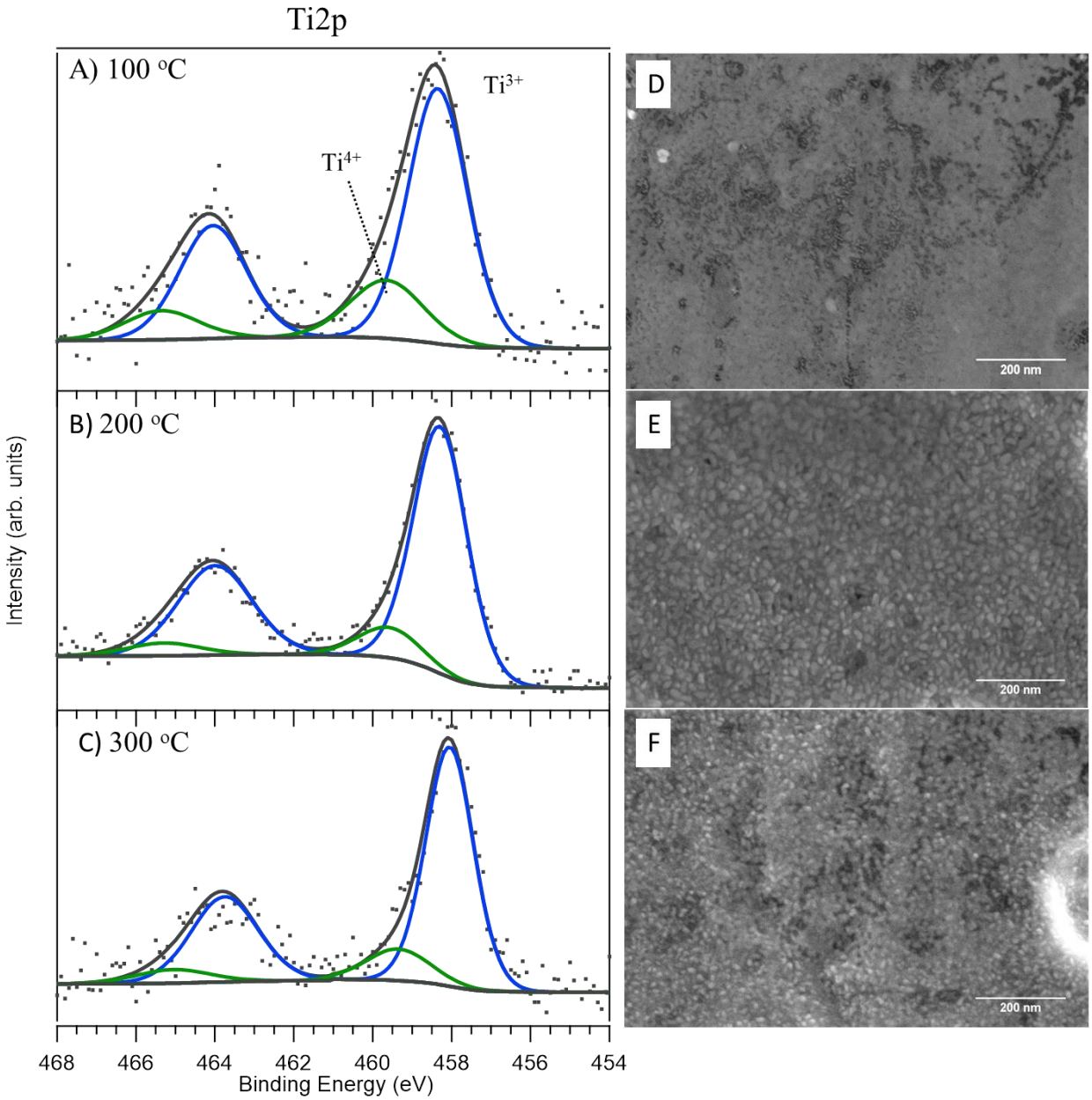

Figure 2.9: Ti 2p XPS spectra and SEM images of TiO_2 nanoparticles on Cu with substrate temperatures of (A, D) 100 ^oC, (B, E) 200 ^oC, and (C, F) 300 ^oC during PVD.

a thin film across the Cu substrate and individual particles were not able to be identified whereas at 200 and 300 ^{o}C, distinct particles were able to be observed. At 300 ^{o}C, the particles are not as pronounced as they are on the 200 ^{o}C substrate which may be a result of diffusion of the nanoparticles into the Cu substrate at higher temperatures or a result of the inconsistency of the deposition during the PVD process. However, the diffusion of TiO_2 into metallic substrates is observed for TiO_2 on a Cu (111) substrate where the formation of a $CuTiO_x$ monolayer film was observed even at 350 K.[55] The diffusion of the TiO_2 into the Cu metal substrate would likely happen faster at higher temperatures and could lead to the observation of less pronounced TiO_2 nanoparticles seen at 300 ^{o}C (Figure 2.9F).

The high resolution Ti 2p XPS spectra of the TiO_2/Cu samples prepared with substrate temperatures of 100, 200, and 300 ^{o}C are shown in Figure 2.9A, B, and C. The Ti $2p_{3/2}$ peaks located at 458.3 and 459.6 eV correspond to Ti^{3+} and Ti^{4+} species (TiO_2), respectively. The Ti^{3+} component is more prominent in the spectra indicating the formation of non-stoichiometric TiO_x. This is likely a result of the strong interaction between TiO_x and the Cu substrate which may result in the formation of a $CuTiO_x$ alloy.[34,56] The presence of Ti^{4+} indicates the full oxidation of some of the Ti species to form TiO_2, likely located on the surface as opposed to interacting with the Cu substrate.

The sample prepared with a substrate temperature of 200 ^{o}C was taken to perform ambient pressure X-ray photoelectron spectroscopy studies. The chamber was backfilled with equal parts CO_2 and H_2 to give a total pressure of 200 mTorr and the substrate was heated from 350-650 K. The Ti 2p spectra (Figure 2.10A) show that at 350 K, the particles were mostly Ti^{3+} species but at 650 K, the majority of the Ti^{3+} species is oxidized to form Ti^{4+} species in the form of TiO_2. This indicates a separation of the $CuTiO_x$ alloy that may occur at high temperatures.

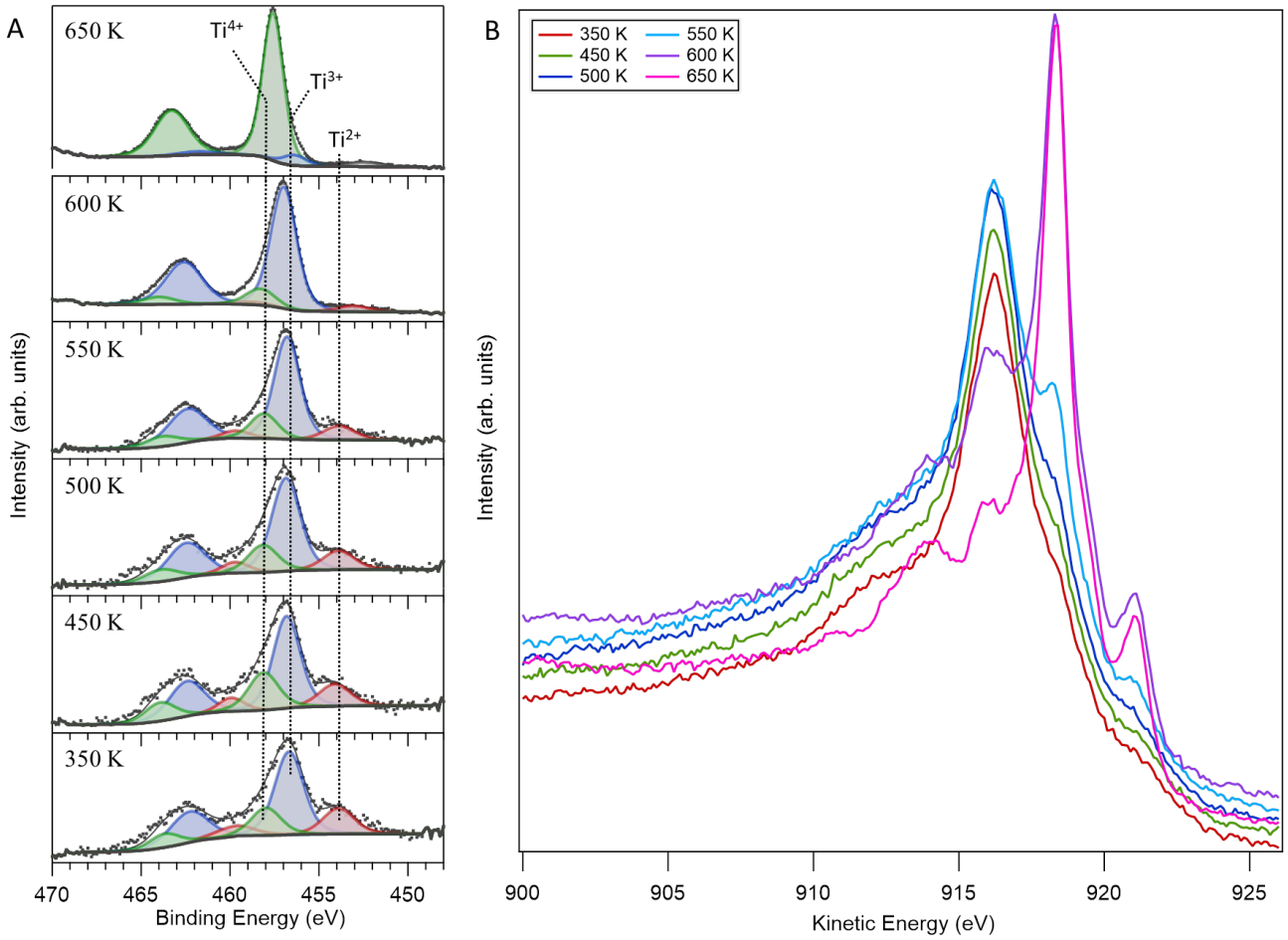

Figure 2.10: (A) Ti 2p and (B) Cu LMM XPS spectra for TiO_x/Cu sample during reaction with CO_2 and H_2 with increasing temperature.

In order to investigate this, the Cu LMM Auger peaks were analyzed as the binding energy of Cu^0 is similar to Cu_2O, as discussed earlier.[54] The Cu LMM peak at 350 K has the distinct shape of Cu_2O species and changes peak shape with increasing temperature (Figure 2.10B). At 650 K, the Cu LMM peak is representative of Cu^0, indicating the full reduction of the Cu substrate at high temperatures. Kim et al. stated that TiO_2 deposited on a Cu (111) substrate is reduced due to an electronic effect interaction with Cu_2O (111) and forms a $CuTiO_x$ layer.[57] The formation of a $CuTiO_x$ alloy was observed at low temperatures, seen by the presence of the Ti^{3+} species, and at higher temperatures there may be a separation in this alloy as the formation of

TiO_2 and Cu^0 is observed. The mechanism of this separation is still being investigated but similar results have been observed for alloys in reactive environments.[56] Figure 2.11 shows SEM images before and after the reaction with CO_2 and H_2 reactant gases and shows changes in the TiO_2 particle size and shape, which is likely a result of restructuring of the surface that occurs upon reduction of the $CuTiO_x$ alloy.

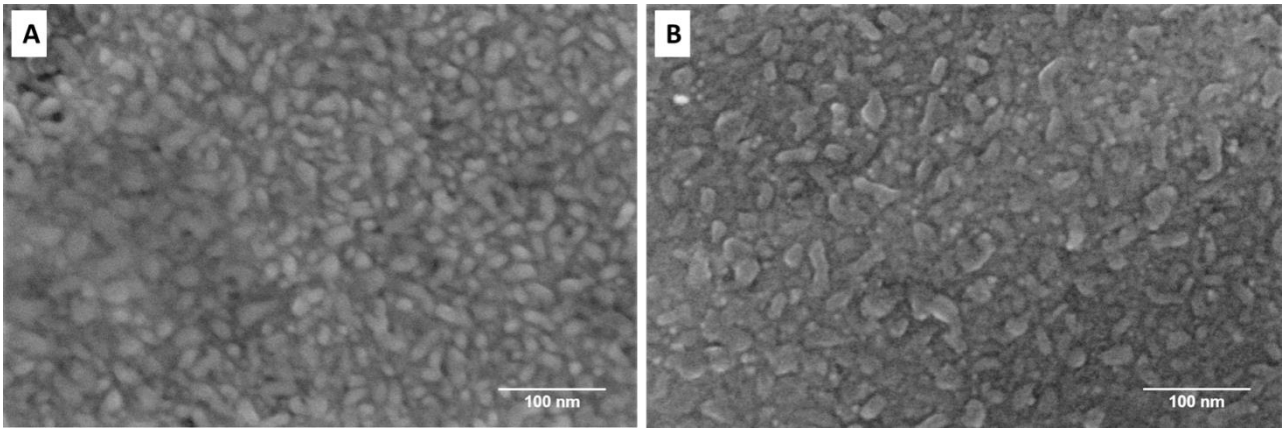

Figure 2.11: SEM images of TiO_x nanoparticles on Cu metal substrate (A) initially and (B) after reaction with CO_2 and H_2 with increasing temperature in the range of 350-650 K.

2.4 Conclusion

In this Chapter, AP-XPS was used to study various samples consisting of Cu-based nanoparticles on TiO_2 nanoparticles on HOPG under CO_2 reduction conditions by increasing the substrate temperature and the addition of CO_2 and H_2 synthesis gases. It was found that TiO_2 nanoparticles on HOPG are capable of producing methanol (CH_3OH), as we observed the formation of $O–CH_3$ intermediates in low amounts. The addition of Cu^0 nanoparticles results in more significant $O–CH_3$ formation as the Cu^0 nanoparticles promote the dissociation of hydrogen which further reacts with activated CO_2 ($CO_2^{\delta-}$). When the Cu^0 nanoparticles are exposed to oxygen gas, the formation of a CuO_x shell over the metallic particles is assumed. The addition of oxygen leads to a change in the reaction mechanism and the $Cu@CuO_x/TiO_2$/HOPG sample is

active for methane (CH_4) formation as we observed the formation of CH_x intermediates. Fully oxidized Cu-based nanoparticles (Cu_2O) on TiO_2 were not found to be catalytically active.

TiO_2 nanoparticles on a Cu substrate revealed a formation of a $CuTiO_x$ alloy at low temperatures that eventually separated into TiO_2 and Cu^0 species at 650 K. The TiO_2 nanoparticles underwent restructuring during this reaction that affected the size and shape of the TiO_2 nanoparticles however; this sample did not exhibit any interesting CO_2 hydrogenation reactivity.

2.5 References

(1) Porosoff, M. D.; Yan, B.; Chen, J. G. Catalytic Reduction of CO_2 by H_2 for Synthesis of CO, Methanol and Hydrocarbons: Challenges and Opportunities. *Energy Environ. Sci.* **2016**, *9*, 62–73.

(2) Abdullah, H.; Khan, M. M. R.; Ong, H. R.; Yaakob, Z. Modified TiO_2 Photocatalyst for CO2 Photocatalytic Reduction: An Overview. *J. CO_2 Util.* **2017**, *22*, 15–32.

(3) Behrens, M.; Studt, F.; Kasatkin, I.; Kühl, S.; Hävecker, M.; Abild-Pedersen, F.; Zander, S.; Girgsdies, F.; Kurr, P.; Kniep, B.-L.; Tovar, M.; Fischer, R. W.; Nørskov, J. K.; Schlögl, R. The Active Site of Methanol Synthesis over Cu/ZnO/Al_2O_3 Industrial Catalysts. *Science.* **2012**, *336*, 893–897.

(4) Huang, C.; Chen, S.; Fei, X.; Liu, D.; Zhang, Y. Catalytic Hydrogenation of CO_2 to Methanol: Study of Synergistic Effect on Adsorption Properties of CO_2 and H_2 in CuO/ZnO/ZrO_2 System. *Catalysts* **2015**, *5* (4), 1846–1861.

(5) Graciani, J.; Mudiyanselage, K.; Xu, F.; Baber, A. E.; Evans, J.; Senanayake, S. D.; Stacchiola, D. J.; Liu, P.; Hrbek, J.; Sanz, J. F.; Rodriguez, J. A. Highly Active Copper-Ceria and Copper-Ceria-Titania Catalysts for Methanol Synthesis from CO_2. *Science.* **2014**, *345* (6196), 546–550.

(6) Sheldon, D. Methanol Production – A Technical History. *Johnson Matthey Technol. Rev.* **2017**, *61* (3), 172–182.

(7) Behrens, M. Promoting the Synthesis of Methanol: Understanding the Requirements for an Industrial Catalyst for the Conversion of CO_2. *Angew. Chemie - Int. Ed.* **2016**, *55* (48), 14906–14908.

(8) Behrens, M. Heterogeneous Catalysis of CO_2 Conversion to Methanol on Copper Surfaces. *Angew. Chemie - Int. Ed.* **2014**, *53* (45), 12022–12024.

(9) Behrens, M.; Furche, A.; Kasatkin, I.; Trunschke, A.; Busser, W.; Muhler, M.; Kniep, B.; Fischer, R.; Schlögl, R. The Potential of Microstructural Optimization in Metal/Oxide Catalysts: Higher Intrinsic Activity of Copper by Partial Embedding of Copper Nanoparticles. *ChemCatChem* **2010**, *2*, 816–818.

(10) Kuld, S.; Conradsen, C.; Moses, P. G.; Chorkendorff, I.; Sehested, J. Quantification of Zinc Atoms in a Surface Alloy on Copper in an Industrial-Type Methanol Synthesis Catalyst. *Angew. Chemie - Int. Ed.* **2014**, *53*, 5941–5945.

(11) Denise, B.;Sneeden, R.P.A.;Beguin, B.; Cherifi, O. Supported Copper Catalysts in the Synthesis of Methanol: N_2O Titrations. *Appl. Catal.* **1987**, *30*, 353–363.

(12) Fleisch, T. H.; Mieville, R. L. Studies on the Chemical State of Cu during Methanol Synthesis. *J. Catal.* **1984**, *90* (1), 165–172.

(13) Pan, W. X.; Cao, R.; Roberts, D. L.; Griffin, G. L. Methanol Synthesis Activity of CuZnO Catalysts. *J. Catal.* **1988**, *114* (2), 440–446.

(14) Herman, R. G.; Klier, K.; Simmons, G. W.; Finn, B. P.; Bulko, J. B.; Kobylinski, T. P. Catalytic Synthesis of Methanol from COH_2. *J. Catal.* **1979**, *56* (3), 407–429.

(15) Sheffer, G. R.; King, T. S. Differences in the Promotional Effect of the Group IA Elements on Unsupported Copper Catalysts for Carbon Monoxide Hydrogenation. *J. Catal.* **1989**, *116* (2), 488–497.

(16) Gao, D.; Zegkinoglou, I.; Divins, N. J.; Scholten, F.; Sinev, I.; Grosse, P.; Cuenya, B. R. Plasma-Activated Copper Nanocube Catalysts for Efficient Carbon Dioxide Electroreduction to Hydrocarbons and Alcohols. *ACS Nano* **2017**, *11*, 4825–4831.

(17) Wang, Y.; Chen, Z.; Han, P.; Du, Y.; Gu, Z.; Xu, X.; Zheng, G. Single-Atomic Cu with Multiple Oxygen Vacancies on Ceria for Electrocatalytic CO_2 Reduction to CH_4. *ACS Catal.* **2018**, *8* (8), 7113–7119.
(18) Liu, X.-M.; Lu, G. Q.; Yan, Z.-F.; Beltramini, J. Recent Advances in Catalysts for Methanol Synthesis via Hydrogenation of CO and CO_2. *Ind. Eng. Chem. Res.* **2003**, *42* (25), 6518–6530.
(19) Alaba, P. A.; Abbas, A.; Mohd, W.; Daud, W. Insight into Catalytic Reduction of CO_2: Catalysis and Reactor Design. *J. Clean. Prod.* **2017**, *140*, 1298–1312.
(20) Bozzano, G.; Manenti, F. Efficient Methanol Synthesis: Perspectives, Technologies and Optimization Strategies. *Prog. Energy Combust. Sci.* **2016**, *56*, 71–105.
(21) Palomino, R. M.; Ramírez, P. J.; Liu, Z.; Hamlyn, R.; Waluyo, I.; Mahapatra, M.; Orozco, I.; Hunt, A.; Simonovis, J. P.; Senanayake, S. D.; Rodriguez, J. A. Hydrogenation of CO_2 on ZnO/Cu(100) and ZnO/Cu(111) Catalysts: Role of Copper Structure and Metal-Oxide Interface in Methanol Synthesis. *J. Phys. Chem. B* **2018**, *122* (2), 794–800.
(22) Arakawa, H.; Dubois, J.-L.; Sayama, K. Selective Conversion of CO_2 to Methanol By Catalytic Hydrogenation Over Promoted Copper Catalyst. *Energy Convers. Mgmt* **1992**, *33*, 521–528.
(23) Wang, W.; Wang, S.; Ma, X.; Gong, J. Recent Advances in Catalytic Hydrogenation of Carbon Dioxide. *Chem. Soc. Rev.* **2011**, *40*, 3703–3727.
(24) Lunkenbein, T.; Schumann, J.; Behrens, M.; Schlögl, R.; Willinger, M. G. Formation of a ZnO Overlayer in Industrial Cu/ZnO/Al_2O_3 Catalysts Induced by Strong Metal-Support Interactions. *Angew. Chemie - Int. Ed.* **2015**, *54* (15), 4544–4548.
(25) Studt, F.; Behrens, M.; Kunkes, E. L.; Thomas, N.; Zander, S.; Tarasov, A.; Schumann, J.; Frei, E.; Varley, J. B.; Abild-Pedersen, F.; Nørskov, J. K.; Schlögl, R. The Mechanism of CO and CO_2 Hydrogenation to Methanol over Cu-Based Catalysts. *ChemCatChem* **2015**, *7*, 1105–1111.
(26) Le Valant, A.; Comminges, C.; Tisseraud, C.; Canaff, C.; Pinard, L. The Cu–ZnO Synergy in Methanol Synthesis from CO_2, Part 1: Origin of Active Site Explained by Experimental Studies and a Sphere Contact Quantification Model on Cu^+ ZnO Mechanical Mixtures. *J. Catal.* **2015**, *324*, 41–49.
(27) Tisseraud, C.; Comminges, C.; Belin, T.; Ahouari, H.; Soualah, A.; Pouilloux, Y.; Le Valant, A. The Cu–ZnO Synergy in Methanol Synthesis from CO_2, Part 2: Origin of the Methanol and CO Selectivities Explained by Experimental Studies and a Sphere Contact Quantification Model in Randomly Packed Binary Mixtures on Cu–ZnO Coprecipitate Catalysts. *J. Catal.* **2015**, *330*, 533–544.
(28) Tisseraud, C.; Comminges, C.; Pronier, S.; Pouilloux, Y.; Le Valant, A. The Cu–ZnO Synergy in Methanol Synthesis Part 3 : Impact of the Composition of a Selective Cu@ZnO_x Core–Shell Catalyst on Methanol Rate Explained by Experimental Studies and a Concentric Spheres Model. *J. Catal.* **2016**, *343*, 106–114.
(29) van den Berg, R.; Prieto, G.; Korpershoek, G.; van der Wal, L. I.; van Bunningen, A. J.; Lægsgaard-Jørgensen, S.; de Jongh, P. E.; de Jong, K. P. Structure Sensitivity of Cu and CuZn Catalysts Relevant to Industrial Methanol Synthesis. *Nat. Commun.* **2016**, *7*, 1–7.
(30) Martin, O.; Mondelli, C.; Cervellino, A.; Ferri, D.; Curulla-Ferré, D.; Pérez-Ramírez, J. Operando Synchrotron X-Ray Powder Diffraction and Modulated- Excitation Infrared Spectroscopy Elucidate the CO_2 Promotion on a Commercial Methanol Synthesis Catalyst Angewandte. *Angew. Chemie - Int. Ed.* **2016**, *55*, 11031–11036.

(31) Nakamura, J.; Choi, Y.; Fujitani, T. On the Issue of the Active Site and the Role of ZnO in Cu/ZnO Methanol Synthesis Catalysts. *Top. Catal.* **2003**, *22*, 277–285.
(32) Kuld, S.; Thorhauge, M.; Falsig, H.; Elkjær, C. F.; Helveg, S.; Chorkendorff, I.; Sehested, J. Quantifying the Promotion of Cu Catalysts by ZnO for Methanol Synthesis. *Science.* **2016**, *352* (6288), 969–974.
(33) Burch, R.; Golunski, S. E.; Spencer, M. S. The Role of Hydrogen in Methanol Synthesis Over Copper Catalysts. *Catal. Letters* **1990**, *5*, 55–60.
(34) Rodriguez, J. A.; Liu, P.; Graciani, J.; Senanayake, S. D.; Grinter, D. C.; Stacchiola, D.; Hrbek, J.; Fernández-Sanz, J. Inverse Oxide/Metal Catalysts in Fundamental Studies and Practical Applications: A Perspective of Recent Developments. *J. Phys. Chem. Lett.* **2016**, *7* (13), 2627–2639.
(35) Schumann, J.; Eichelbaum, M.; Lunkenbein, T.; Thomas, N.; Álvarez Galván, M. C.; Schlögl, R.; Behrens, M. Promoting Strong Metal Support Interaction: Doping ZnO for Enhanced Activity of Cu/ZnO:M (M = Al, Ga, Mg) Catalysts. *ACS Catal.* **2015**, *5* (6), 3260–3270.
(36) Schwab, G. M. Electronics of Supported Catalysts. *Adv. Catal.* **1979**, *27*, 1–22.
(37) Jennison, D. R.; Dulub, O.; Hebenstreit, W.; Diebold, U. Structure of an Ultrathin TiO_x Film, Formed by the Strong Metal Support Interaction (SMSI), on Pt Nanocrystals on TiO_2 (110). *Surf. Sci.* **2001**, *492*, L677–L687.
(38) Hayek, K.; Fuchs, M.; Klötzer, B.; Reichl, W.; Rupprechter, G. Studies of Metal–Support Interactions with "Real" and "Inverted" Model Systems: Reactions of CO and Small Hydrocarbons with Hydrogen on Noble Metals in Contact with Oxides. *Top. Catal.* **2000**, *13*, 55–66.
(39) Demmin, R. A.; Ko, C. S.; Gorte, R. J. Effect of Titania on the Chemisorption and Reaction Properties of Pt. *J. Phys. Chem.* **1985**, *89*, 1151–1154.
(40) Braunschweig, E. J.; Logan, A. D.; Datye, A. K.; Smith, D. J. Reversibility of Strong Metal-Support Interactions on Rh/TiO_2. *J. Catal.* **1989**, *118*, 227–237.
(41) Vayssilov, G. N.; Lykhach, Y.; Migani, A.; Staudt, T.; Petrova, G. P.; Tsud, N.; Skála, T.; Bruix, A.; Illas, F.; Prince, K. C.; Matolín, V.; Neyman, K. M.; Libuda, J. Support Nanostructure Boosts Oxygen Transfer to Catalytically Active Platinum Nanoparticles. *Nat. Mater.* **2011**, *10*, 310–315.
(42) Matte, L. P.; Kilian, A. S.; Luza, L.; Alves, M. C. M.; Morais, J.; Baptista, D. L.; Dupont, J.; Bernardi, F. Influence of the CeO_2 Support on the Reduction Properties of Cu/CeO_2 and Ni/CeO_2 Nanoparticles. *J. Phys. Chem. C* **2015**, *119*, 26459–26470.
(43) Wen, W.; Jing, L.; White, M. G.; Marinkovic, N.; Hanson, J. C.; Rodriguez, J. A. In Situ Time-Resolved Characterization of Novel $Cu–MoO_2$ Catalysts during the Water–Gas Shift Reaction. *Catal. Letters* **2007**, *113*, 1–6.
(44) Tauster, S. J. Strong Metal-Support Interactions. *Acc. Chem. Res.* **1987**, *20*, 389–394.
(45) Wu, C. H.; Eren, B.; Bluhm, H.; Salmeron, M. B. Ambient-Pressure X-Ray Photoelectron Spectroscopy Study of Cobalt Foil Model Catalyst under CO, H_2, and Their Mixtures. *ACS Catal.* **2017**, *7* (2), 1150–1157.
(46) Kruse, N.; Chenakin, S. XPS Characterization of Au/TiO_2 Catalysts: Binding Energy Assessment and Irradiation Effects. *Appl. Catal. A Gen.* **2011**, *391*, 367–376.
(47) Favaro, M.; Xiao, H.; Cheng, T.; Goddard, W. A.; Yano, J.; Crumlin, E. J. Subsurface Oxide Plays a Critical Role in CO_2 Activation by Cu(111) Surfaces to Form Chemisorbed CO_2, the First Step in Reduction of CO_2. *Proc. Natl. Acad. Sci. U. S. A.* **2017**, *114* (26),

6706–6711.
(48) Deng, X.; Verdaguer, A.; Herranz, T.; Weis, C.; Bluhm, H.; Salmeron, M. Surface Chemistry of Cu in the Presence of CO_2 and H_2O. *Langmuir* **2008**, *24*, 9474–9478.
(49) Bluhm, H.; Hävecker, M.; Knop-Gericke, A.; Kleimenov, E.; Schlögl, R.; Teschner, D.; Bukhtiyarov, V. I.; Ogletree, D. F.; Salmeron, M. Methanol Oxidation on a Copper Catalyst Investigated Using in Situ X-Ray Photoelectron Spectroscopy †. *J. Phys. Chem. B* **2004**, *108* (38), 14340–14347.
(50) Tanaka, K.; Matsuzaki, S.; Toyoshima, I. Photodecomposition of Adsorbed Methoxy Species by UV Light and Formaldehyde Adsorption on Si (111) Studied by XPS and UPS. *J. Phys. Chem.* **1993**, *97*, 5673–5677.
(51) Eren, B.; Heine, C.; Bluhm, H.; Somorjai, G. A.; Salmeron, M. Catalyst Chemical State during CO Oxidation Reaction on Cu (111) Studied with Ambient-Pressure X-ray Photoelectron Spectroscopy and Near Edge X-ray Adsorption Fine Structure Spectroscopy. *J. Am. Chem. Soc.* **2015**, *137*, 11186–11190.
(52) Ferrah, D.; Haines, A. R.; Galhenage, R. P.; Bruce, J. P.; Babore, A. D.; Hunt, A.; Waluyo, I.; Hemminger, J. C. Wet Chemical Growth and Thermocatalytic Activity of Cu-Based Nanoparticles Supported on TiO_2 Nanoparticles/HOPG: In Situ Ambient Pressure XPS Study of the CO_2 Hydrogenation Reaction. *ACS Catal.* **2019**, *9*, 6783–6802.
(53) Guo, Q.; Zhou, C.; Ma, Z.; Ren, Z.; Fan, H.; Yang, X. Elementary Photocatalytic Chemistry on TiO_2 Surfaces. *Chem. Soc. Rev.* **2016**, *45*, 3701–3730.
(54) Biesinger, M. C. Advanced Analysis of Copper X-Ray Photoelectron Spectra. *Surf. Interface Anal.* **2017**, *49*, 1325–1334.
(55) Baber, A. E.; Yang, X.; Kim, H. Y.; Mudiyanselage, K.; Soldemo, M.; Weissenrieder, J.; Senanayake, S. D.; Al-mahboob, A.; Sadowski, J. T.; Evans, J.; Rodriguez, J. A.; Liu, P.; Hoffmann, F. M.; Chen, J. G.; Stacchiola, D. J. Stabilization of Catalytically Active Cu^+ Surface Sites on Titanium-Copper Mixed-Oxide Films. *Angew. Chemie - Int. Ed.* **2014**, *126*, 5440–5444.
(56) Zafeiratos, S.; Piccinin, S.; Teschner, D. Alloys in Catalysis: Phase Separation and Surface Segregation Phenomena in Response to the Reactive Environment. *Catal. Sci. Technol.* **2012**, *2* (9), 1787–1801.
(57) Kim, H. Y.; Liu, P. Complex Catalytic Behaviors of $CuTiO_x$ Mixed-Oxide during CO Oxidation. *J. Phys. Chem. C* **2015**, *119* (40), 22985–22991.

Chapter 3

Stability of CuO_x/TiO_2/HOPG Model Catalysts under Electrochemical CO_2 Reduction Conditions

3.1 Introduction

Electrochemical reduction of CO_2 has gained a lot of attention due to its capability of storing electrical energy, ability to operate under mild conditions, and reaction tunability, which enables the formation of different reaction products by adjusting the reaction conditions, i.e. applied potential or electrode material.[1–3] Presently, copper has been identified as the most effective catalyst capable of reducing CO_2 to multi-carbon hydrocarbons and alcohols at reasonable Faradaic efficiencies (FE). It has been suggested that this is due to its intermediate binding strength to CO.[4–8] However, this process requires overpotentials as high as 1 V to overcome the CO_2 activation barrier and further hydrogenate adsorbed CO.[4,9–11]

Research efforts have been focused on modifying Cu catalysts in order to tune their selectivity and achieve product formation at lower overpotentials.[2,12,13] It has been proposed that Cu^+ species and subsurface oxygen on polycrystalline Cu could affect the activity and selectivity of Cu catalysts. Gao et al.[12] studied copper nanocube catalysts with tunable Cu(100) facets and found that O_2 plasma treated Cu(100) nanocubes resulted in a higher activity and selectivity for ethylene compared to untreated Cu(100) nanocubes, highlighting the importance of the role of oxygen species. Li et al.[13] reported that the reduction of CO_2 on Cu_2O films results in the formation of ethylene and ethane whereas polycrystalline Cu produces ethylene and methane. They also found that the Cu_2O films were more resistant to deactivation compared to polycrystalline Cu electrodes.

Catalysts consisting of copper on various metal oxide supports, such as TiO_2, ZnO and CeO_x, have been extensively studied in the thermal reduction of CO_2 into methanol.[14–21] In this process, it has been shown that Cu/oxide catalysts are more active than Cu catalysts due to the ability of reducible metal oxides to bind and activate CO_2.[15,16,22,23] TiO_2 is also a widely used photo- and electrocatalyst for CO_2 reduction as it has been shown to enhance the catalytic and Faradaic efficiency and assist in CO_2 adsorption.[24–26] Studies of TiO_2 electrodes in aprotic solvents have shown that TiO_2 is capable of binding, reducing, and activating CO_2 at lower potentials than are currently required to reduce CO_2 on Cu metal.[27,28] Investigations of various metals (such as Cu, Au, and Ag) on CeO_x, a reducible metal oxide support, have reported an enhancement of the CO_2RR at higher Faradaic efficiencies and that the metal-metal oxide interface aids in the stabilization of reaction intermediates compared to the metals by themselves.[29,30] According to the Pourbaix diagram for copper in aqueous solutions[31], CuO_x substrates would reduce to copper metal under electrochemical CO_2 reduction conditions. The addition of a metal oxide support, such as TiO_2 or ZnO, may help to stabilize Cu^+ species which could aid in reducing the overpotential of this reaction and lead to better catalytic stability.

In order to be commercially viable, electrochemical reduction catalysts need to have high performance and stability for long-term operation as CO_2 hydrogenation catalysts are stable over multiple years.[32] It has been reported that polycrystalline Cu electrodes deactivate and undergo catalyst degradation over a short period of time under electrochemical CO_2 reduction conditions. However, it has also been reported that modified catalysts did not deactivate as quickly and showed improved stability over time.[2,24] While there have been numerous research efforts focused on improving the activity and selectivity of Cu catalysts for electrochemical CO_2 reduction, investigations into their structural and chemical stability has received less attention.[3,33]

Here, we studied the reactivity of model catalysts consisting of CuO_x/TiO_2/HOPG (discussed in Chapter 1) under electrochemical CO_2 reduction conditions in an effort to investigate its reactivity and stability. The reactivity was investigated using differential electrochemical mass spectrometry (DEMS) and chronoamperometry and cyclic voltammetry studies were carried out in order to investigate the catalyst stability. The particle stability studies on the model catalyst described here highlight the importance of investigations on structural stability of heterogeneous electrochemical catalysts as this could give insight into catalyst degradation mechanisms and help mitigate deactivation during CO_2 electrochemical reduction.

3.2 Experimental

3.2.1 Fabrication of TiO_2/HOPG and CuO_x/TiO_2/HOPG samples

The TiO_2 nanoparticles on HOPG were prepared by PVD on a commercial evaporator under high vacuum (10^{-6} Torr). The HOPG substrate was pretreated with either low energy Ar plasma or placed directly into the chamber in order to achieve high and low density TiO_2 nanoparticles on the substrate. The HOPG substrate was heated to 770 ^oC and held at this temperature throughout the deposition. The TiO_2/HOPG sample was then further annealed at this temperature for 2.5 hours. The CuO_x/TiO_2/HOPG samples were fabricated using a photodeposition solution of 3 mM $CuCl_2$ at a pH of 3 with the addition of 1% methanol. The sample was submerged in this solution and irradiated with UV light for 6 hours in order to selectively deposit CuO_x nanoparticles onto the TiO_2 nanoparticles. The Cu/HOPG samples were prepared by plasma treating the HOPG substrate and immersing it in a 3 mM $CuCl_2$ solution with 1% methanol at pH of 7 for 6 hours.

3.2.2 Electrochemical reactivity and characterization

The samples were characterized using X-ray photoelectron spectroscopy (XPS, Kratos Axis Supra), atomic force microscopy (AFM, Anton-Paar Tosca 400) and scanning electron microscopy (SEM, FEI Magellan 400 XHR). The cyclic voltammetry and chronoamperometry measurements were performed in a one compartment, three-electrode cell using a Gamry Series G 300 potentiostat in a 0.1 M $KHCO_3$ (ACS Reagent, ≥99.7%, Sigma-Aldrich) electrolyte solution saturated with CO_2 (99.999% purity, AirGas). This was obtained by bubbling CO_2 gas into the electrolyte solution for 15 minutes until a pH of 6.8 was achieved, indicative of saturation of CO_2. The CuO_x/TiO_2/HOPG sample was affixed to a sample holder that exposed a fixed area of 200 mm^2 of the sample surface to the solution and was used as the working electrode. A carbon rod was used as the counter electrode with a saturated calomel reference electrode. The CVs were run at a scan rate of 10 mV/s with 1 mV steps for 30 cycles ranging from 0 to -1.30 V vs SCE. All measured potentials vs SCE in this study have been converted into the reversible hydrogen electrode (RHE) scale using the Nernst equation where E^o_{SCE} has a value of 0.241 V at 25^{o}C.

3.2.3 Differential electrochemical mass spectrometry (DEMS)

The principles of DEMS and its applications to electrochemical surface science have been previously discussed and reviewed.[34,35] The instrumentation and setup used for DEMS analysis has also been recorded and detailed previously[36–38] and only aspects related to the analysis of the CuO_x/TiO_2 nanoparticles on HOPG samples is described here. A three electrode setup was used with Ag/AgCl (1 M KCl) as the reference electrode and a Pt wire counter

electrode. The working electrode consisted of Cu nanoparticles on TiO_2 nanoparticles oriented on a highly oriented pyrolytic graphite (HOPG) substrate.

Four samples were analyzed using DEMS: HOPG, TiO_2 nanoparticles on HOPG, CuO_x/TiO_2/HOPG and Cu/TiO_2/HOPG. The HOPG substrate was used as a control and the TiO_2 nanoparticles on HOPG was used to confirm no electrochemical reactivity in the absence of Cu nanoparticles. Initially the Cu-based nanoparticles on TiO_2 are CuO_x species so the Cu/TiO_2/HOPG sample was annealed prior to electrochemical analysis in order to reduce the copper oxide species to metallic copper. The annealing temperature ranged from 650-750 K but, since the heating was not in situ, it is presumed that some CuO_x species were present due to the exposure of Cu nanoparticles to atmosphere. The samples were submerged into a 0.1 M $KHCO_3$ solution saturated with CO_2 by purging with high-purity gas. The pH of the solutions was initially at 8.2 and dropped to 6.8 upon saturation of the CO_2 gas. The samples were then held at -1.2 V vs RHE for 600 s while the reaction products were monitored using an HPR-20 quadrupole mass spectrometer (Hidden Analytical, Warrington, England). The samples were held at -1.2 V vs RHE for 180 s prior to mass spectrometry collection in order to clean the sample of any hydrocarbon contamination.

3.3 Results and Discussion

As discussed in Chapter 2, these model catalysts are active for the thermal reduction of CO_2 to either methanol or methane, depending on the chemical state of the Cu metal or lack thereof (in the case of the TiO_2/HOPG sample which was active for the formation of methanol). The activity of these model catalysts was studied using DEMS in an effort to observe the products formed during electrochemical reduction of the CuO_x/TiO_2/HOPG and TiO_2/HOPG

catalysts. For DEMS analysis, methane (CH_4, m/z=15), ethylene (C_2H_4, m/z=26), and alcohols (m/z=31) were monitored using mass spectrometry and the ion currents were plotted as a function of time. It was found that both the $Cu/TiO_2/HOPG$ and $CuO_x/TiO_2/HOPG$ samples showed catalytic activity towards the formation of methane but not for the formation of ethylene or alcohols (Figure 3.1). This result is consistent with the expectation for Cu nanoparticle based catalysts with the small nanoparticle sizes that are present in these samples.[2] The HOPG sample was used as a control so product formation was not expected and the TiO2 nanoparticles by themselves were not shown to be active for CO_2 reduction under the conditions studied here.

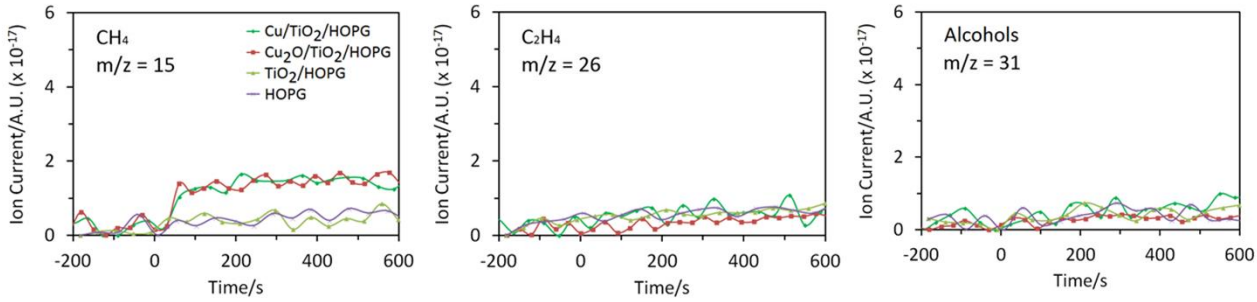

Figure 3.1: Differential electrochemical mass spectrometry (DEMS) preliminary data for $Cu/TiO_2/HOPG$, $CuO_x/TiO_2/HOPG$, $TiO_2/HOPG$ and HOPG samples during CO_2 reduction.

While these model catalysts have shown to be active for electrochemical and thermal reduction of CO_2, their stability during these processes differs as the $CuO_x/TiO_2/HOPG$ catalyst is stable under thermal reduction conditions but exhibited changes in the nanoparticle morphology under electrochemical reduction. Figure 3.2 shows SEM images of the $CuO_x/TiO_2/HOPG$ and $TiO_2/HOPG$ samples before and after DEMS analysis. From the SEM images, it is shown that after DEMS analysis (Figures 3.2B and D), it appears that the particles coalesce under strong reducing potentials and features of the individual particles become more

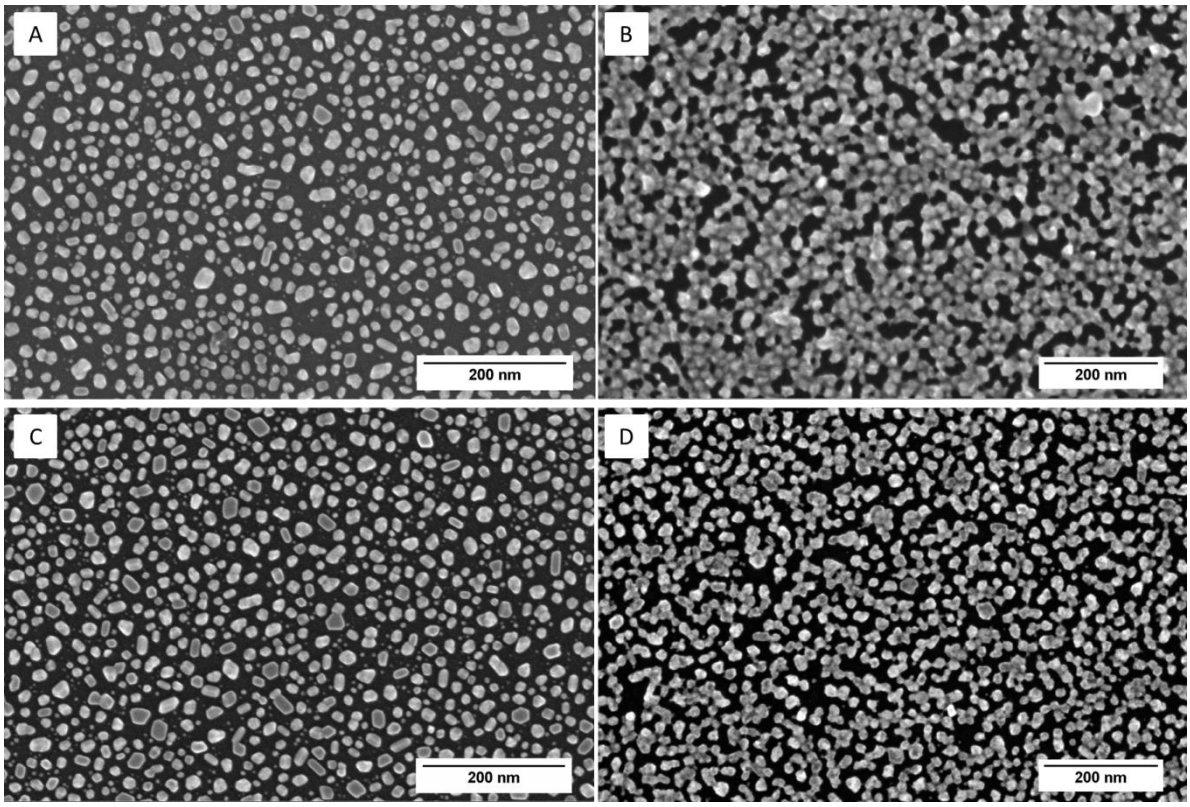

Figure 3.2: SEM images of TiO_2/HOPG initially (A) and after DEMS analysis (B). SEM images of CuO_x/TiO_2/HOPG sample initially (C) and after DEMS analysis (D).

Table 3.1: Description and experimental conditions of samples analyzed.

Sample No.	Description	Experiments performed
1	CuO_x/TiO_2 NPs	30 CV cycles in 0.1 M $KHCO_3$ with N_2
2	CuO_x/TiO_2 NPs	30 CV cycles in 0.1 M $KHCO_3$ with CO_2
3	CuO_x/TiO_2 NPs	Chronamperometry - increasing from -0.66 V to -0.91 V vs RHE
4	TiO_2 NPs	Chronamperometry - increasing from -0.66 V to -0.91 V vs RHE
5	TiO_2 NPs	Chronamperometry - held at -0.91 V vs RHE for 3 hours

difficult to distinguish. From these images, it is unclear whether the nanoparticles deform and coalesce or if the "webbing" features are a result of contamination.

In an effort to investigate the stability of this catalyst and determine the origin of the nanoparticle movement and deformation, electrochemical reactivity studies were performed. The prepared samples and the experimental conditions that were studied and reported are recorded in Table 3.1. After initial XPS analysis, which will be discussed next, the samples were exposed to a mild surface cleaning using the in situ plasma cleaner in the SEM and images were taken at multiple marked locations on the sample surface. Marking the sample with a scratch on the surface enables direct comparisons of specific nanoparticles before and after electrochemical treatment in order to identify particle movements and any change in particle shape. SEM images of the CuO_x/TiO_2 nanoparticles show a high density of nanoparticles on the HOPG surface, similar to those discussed in Chapter 1. The TiO_2 nanoparticles here are roughly 15 nm in diameter and the Cu-based nanoparticles supported on the TiO_2 nanoparticles are about 2-5 nm in diameter, as shown with TEM in previous work and discussed in Chapter 1.[14]

Table 3.2: XPS data for Samples 1 and 2 giving the approximate amounts of Cu and Ti species on TiO_2 nanoparticles and HOPG substrate.

Sample	Species	Ratio	Initial	After SEM imaging/before CV cycles	After CV cycles/ before SEM imaging	After both
1	Total amount	Cu2p/Ti2p	0.61	0.43	0.36	0.36
	Total amount	Ti2p/C1s	0.31	0.34	0.45	0.37
	Cu_2O	Cu2p/Ti2p	0.09	0.10		0.10
	$Cu(OH)_2$	Cu2p/Ti2p	0.52	0.34		0.26
2	Total amount	Cu2p/Ti2p	0.71	0.43	0.32	0.29
	Total amount	Ti2p/C1s	0.31	0.34	0.39	0.37
	Cu_2O	Cu2p/Ti2p	0.12	0.10		0.10
	$Cu(OH)_2$	Cu2p/Ti2p	0.59	0.33		0.19

Initial XPS analysis confirms the formation of stoichiometric TiO_2 nanoparticles with a $Ti2p_{3/2}$ peak at ~458.8 eV and the presence of Cu nanoparticles on TiO_2 nanoparticles with $Cu2p_{3/2}$ peaks at ~932.3, 934.5, 939.4, 943.4 eV which correspond to Cu_2O, $Cu(OH)_2$ and the two shake-up peaks characteristic of Cu^{2+} species.[39] From the high resolution XPS spectrum of each element, the ratio of the integrated peak areas was used to determine the approximate amount of material on the sample. As seen in Table 3.2, for Samples 1 and 2, the initial Cu2p/Ti2p ratios are 0.61 and 0.71 and the initial Ti2p/C1s ratios are 0.31 for both samples.

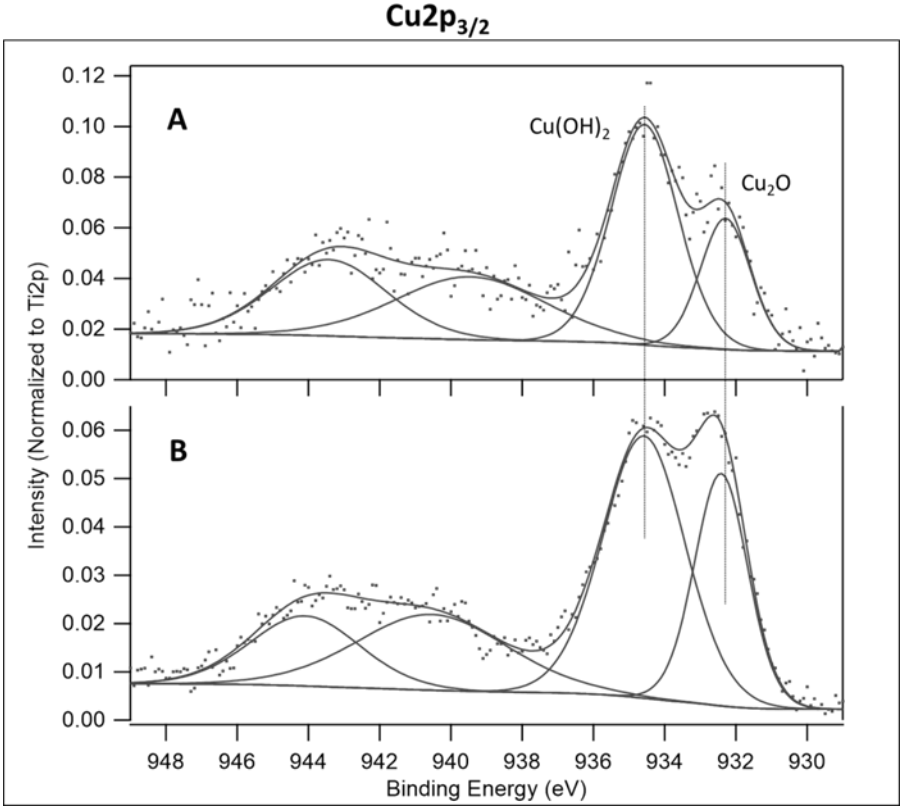

Figure 3.3: $Cu2p_{3/2}$ XPS spectra of CuO_x/TiO_2 NPs (A) initially and (B) after SEM imaging and in situ air plasma treatment. XPS spectra are normalized to the $Ti2p_{3/2}$ intensity.

Following SEM imaging, the samples were again analyzed via XPS to determine if the mild oxygen plasma treatment in the SEM resulted in any change in the amount or chemical species of the TiO_2 and CuO_x nanoparticles. Initially, XPS analysis of both samples showed that

there was more $Cu(OH)_2$ present compared to Cu_2O (Figure 3.3A). However, after SEM imaging, the distribution became more even between the two chemical species (Figure 3.3B).

It is also worth noting that the Cu2p/Ti2p ratios for Samples 1 and 2 have decreased after initial SEM imaging, as seen in Table 3.2. After the first XPS analysis and SEM imaging, the Cu2p/Ti2p ratio is 0.43 for both Samples 1 and 2, corresponding to a decrease of 29% and 39%, respectively. This decrease could be attributed to the loss of $Cu(OH)_2$ particles that were formed during the photodeposition process that were deposited on the HOPG substrate. Previous studies show that $Cu(OH)_2$ nanoparticles, formed through the dissolution of $CuCl_2$ in H_2O, are deposited onto the HOPG surface in the absence of TiO_2 nanoparticles.[14] These particles could be adhered to the HOPG surface by electrostatic interactions and may have been removed by the oxygen plasma treatment in the SEM or by the X-ray beam during XPS analysis.

The specific loss of $Cu(OH)_2$ nanoparticles is supported by the ratio between the $Cu2p_{3/2}$ peak for each Cu species, $Cu(OH)_2$ and Cu_2O, compared to the $Ti2p_{3/2}$ peak. As seen in Table 3.2, the initial Cu2p/Ti2p ratio for $Cu(OH)_2$ and Cu_2O was 0.25 and 0.09, respectively and after initial SEM imaging the Cu2p/Ti2p ratio for $Cu(OH)_2$ and Cu_2O was 0.18 and 0.10, respectively. The same trend is observed for Sample 2 where the approximate amount of $Cu(OH)_2$ decreases compared to the amount of Cu_2O, which stays fairly consistent before and after initial SEM imaging.

In an effort to observe chemical changes to the nanoparticles in situ, cyclic voltammetry studies were performed for various CuO_x/TiO_2/HOPG and TiO_2/HOPG samples. However, specific reduction events associated with TiO_2, Cu, and HOPG were difficult to distinguish as the reduction potentials for these events were similar or tended to overlap with the reduction of residual oxygen that may be present in solution. The plasma treatment on the HOPG substrate

also added another layer of complexity to the cyclic voltammetry analysis. For these reasons, individual reduction events were not able to be distinguished. However, the CV cycles did provide useful insight on the catalyst stability and ability to bind CO_2. Cyclic voltammetry scans were performed for the same sample in a 0.1 M $KHCO_3$ solution purged with N_2 gas and then with the addition of CO_2. The working electrode setup was shown to have slight variation in the current when changing between different samples so by keeping the same sample on the electrode, small variations in the CV cycles with and without CO_2 could be observed. Figure 3.4 shows the CV scans for the CuO_x/TiO_2/HOPG, Cu/HOPG, and TiO_2/HOPG samples. It is shown that, after the addition of CO_2, there is an observed increase in the current which is indicative of CO_2 activation on the catalyst surface.

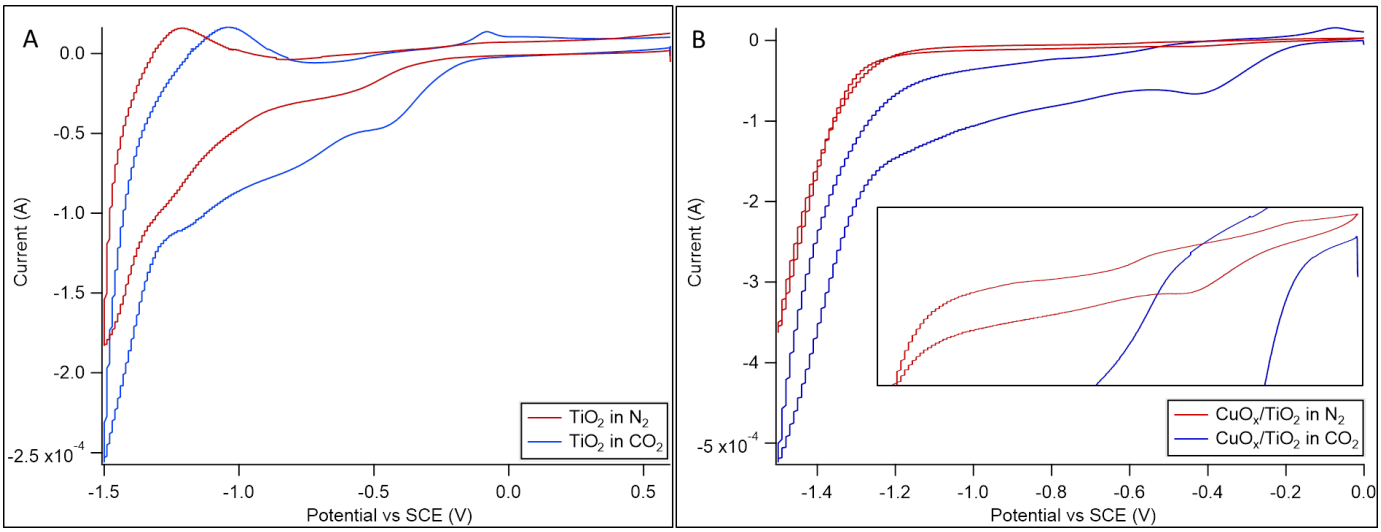

Figure 3.4: CV scans of the same samples of (A) TiO_2/HOPG and (B) CuO_x/TiO_2/HOPG in 0.1 M $KHCO_3$ solutions with N_2 and then with the addition of CO_2. Inset in (B) is CV trace for CuO_x/TiO_2/HOPG in N_2 enlarged for detail.

Cyclic voltammetry studies were then performed for Samples 1 and 2 in order to determine the stability of the catalyst after an extended period of time. The CVs were run for 30 cycles for a total time of ~2 hours (see Experimental Section for parameters) in a 0.1 M $KHCO_3$

solution purged with N_2 for Sample 1 and saturated with CO_2 for Sample 2. For Samples 1 and 2, the CV scans ranged from 0 to -0.57 V vs RHE and 0 to -0.66 V vs RHE, respectively, in order to avoid production of H_2 gas from the hydrogen evolution reaction, which is observed at more negative potentials (as seen by the sharp current decrease for the red trace in Figure 3.4B). The CV scans quickly stabilized after the 6th scan and 12th scan for the Sample 1 and 2, respectively (Figure 3.5). The changes in the current during the CV scans indicated that the surface of the sample was physically or chemically changing under these conditions.

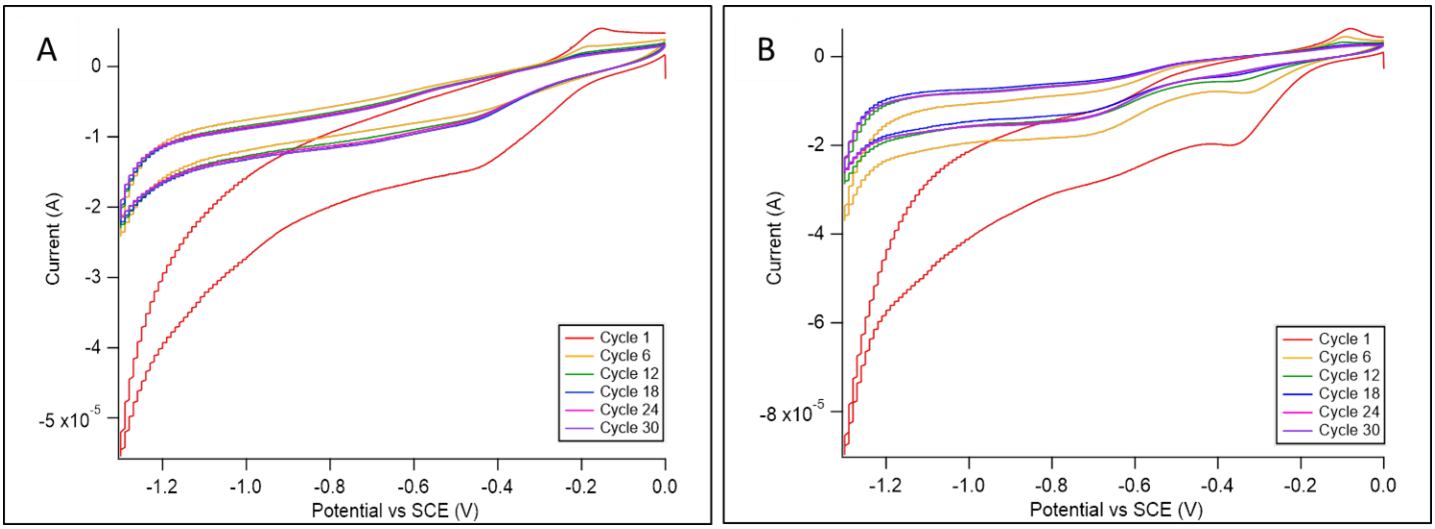

Figure 3.5: Cyclic voltammetry scans for CuO_x/TiO_2/HOPG samples in 0.1 M $KHCO_3$ solution (A) purged with N_2 gas for 20 minutes prior to scan and (B) saturated with CO_2 gas. Each sample was scanned for 30 cycles. The Figures selected cycles 1, 6, 12, 18, 24 and 30 as representative of the total cycles recorded.

After the 30 CV cycles, SEM analysis showed that there was no significant nanoparticle movement observed (Figure 3.6). XPS analysis showed that while the amount of TiO_2 nanoparticles did not change significantly after electrochemistry, the Cu2p/Ti2p ratio decreased by 16% and 26% for Samples 1 and 2, respectively, indicating a loss of copper signal for both of the samples. Table 3.2 shows that the Cu2p/Ti2p ratio before electrochemistry was 0.43 for both Samples 1 and 2 and after 30 CV cycles it was reduced to 0.36 and 0.32, respectively. Other

studies have shown that Cu-based nanocubes and nanoparticles undergo significant morphology and size changes under electrochemical CO_2 reduction conditions. It has been reported by Jung et al.[40] that 20 nm Cu_2O nanoparticles fragmented into 2-4 nm Cu-based particles under CO_2 reduction conditions after 10 hours and Grosse et al.[41] reported that Cu nanocubes underwent roughening and loss of crystal facets, loss of Cu atoms at edges and corners and reduction of CuO_x species under CO_2 reduction conditions. Based on these studies, it is likely that the CuO_x nanoparticles may be decreasing in size or undergoing particle loss during electrochemical reduction, which would account for the decrease in Cu2p/Ti2p ratio.

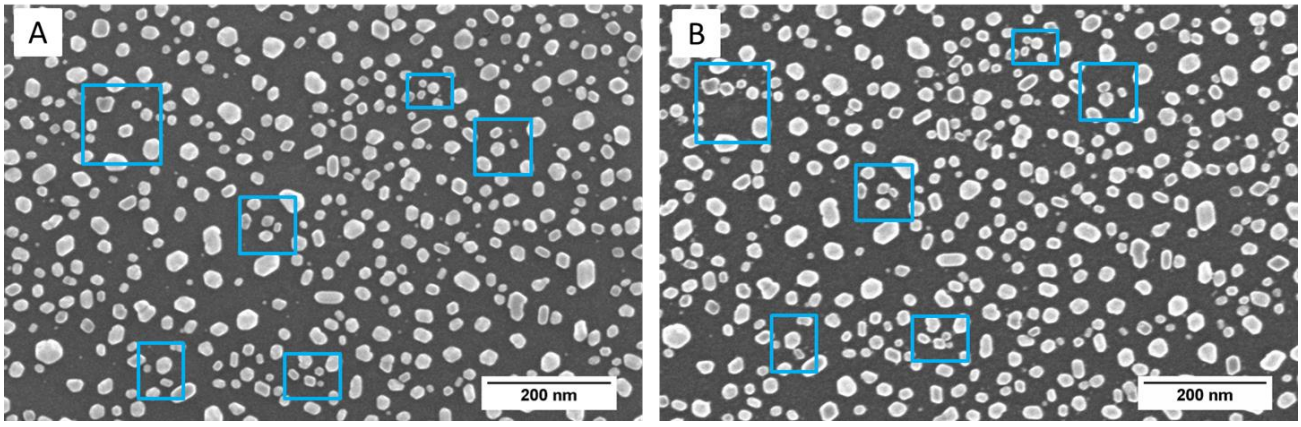

Figure 3.6: SEM images of Cu/TiO_2 NPs (A) before and (B) after 30 cyclic voltammetry cycles. The highlighted boxes represent movement of specific particles where, after cyclic voltammetry, the Cu/TiO_2 NPs start to agglomerate together.

After 30 CV cycles, there was an increase in the C1s species located at 284.9, 286.0, 288.7 eV which correspond to sp^3, C–O, and O–C=O species, respectively (Figure 3.7). The presence of these species on the sample surface is likely a result of either the deposition of bicarbonate (HCO_3^-) and/or CO_2 (aq) or a result of carbon corrosion. However, after SEM imaging, the carbon species are reduced and resembles the C1s spectrum before electrochemistry, indicating that the increase in the carbon species was a result of surface

contamination and was not chemically bound to the surface or the result of a change in the HOPG substrate.

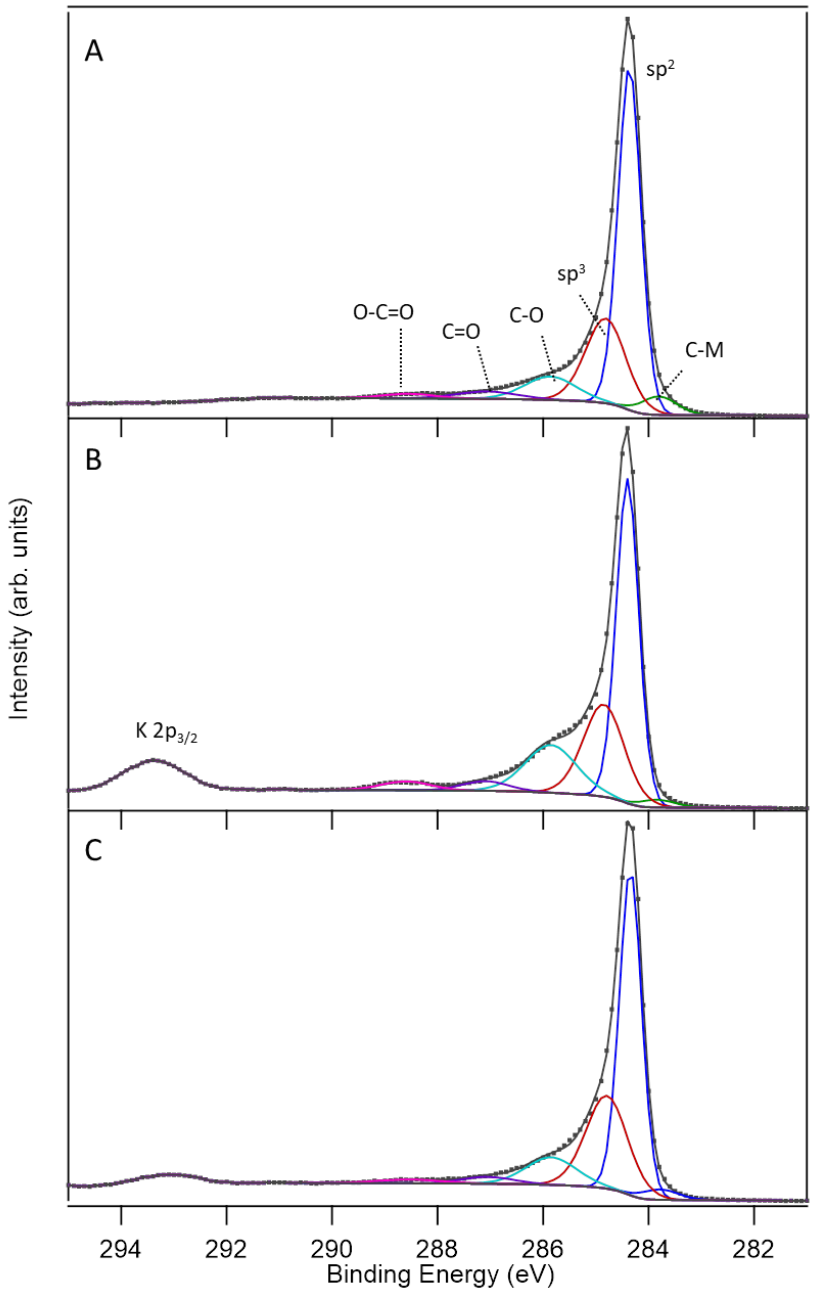

Figure 3.7: C1s spectra (A) initially, (B) after 30 cyclic voltammetry cycles, and (C) after SEM imaging with an in situ air plasma treatment of a CuO_x/TiO_2/HOPG sample highlighting the evolution of carbon contamination in the sample.

The Ti2p XPS spectrum did not indicate a significant change in the chemical species after cyclic voltammetry. A small amount of Ti^{3+} is observed at 457.5 eV which has previously been shown to be located on the surface of the TiO_2 nanoparticles.[14] It is noted that the amount of Ti^{3+} did not increase significantly after electrochemical reduction (Figure 3.8A and B). TiO_2 is readily oxidized in the atmosphere and the formation of Ti^{3+} after electrochemical reduction would likely not be observed since XPS analysis was performed ex situ.

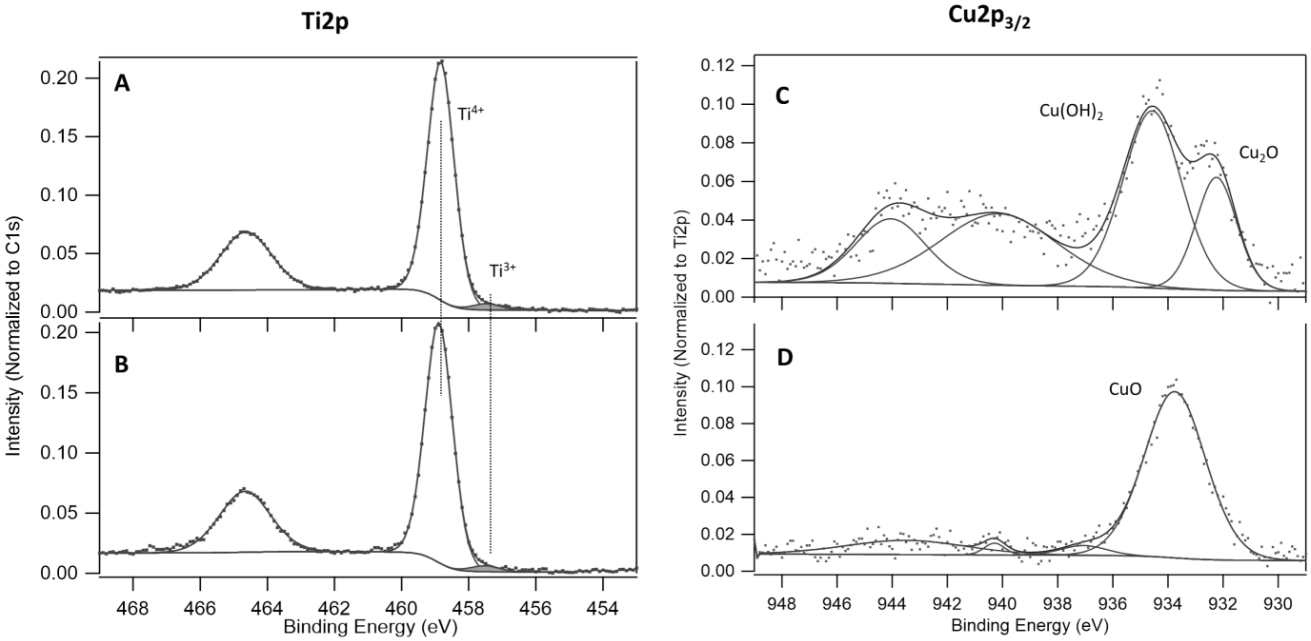

Figure 3.8: Ti2p and $Cu2p_{3/2}$ XPS spectra of CuO_x/TiO_2/HOPG nanoparticles (A, C) initially and (B, D) after 30 CV cycles.

On the other hand, the Cu2p XPS spectrum did show a change in the chemical species after 30 CV cycles where one main copper peak located at 933.8 eV was observed which corresponds to CuO (Figure 3.8D) indicating the oxidation of the Cu_2O and $Cu(OH)_2$ nanoparticles (Figure 3.8C). The samples were then analyzed via SEM and exposed to the in situ air plasma treatment. After SEM imaging, the Cu2p spectra for both samples showed a distribution between the Cu species with peaks at 932.7 and 934.5 eV, corresponding to Cu_2O

and $Cu(OH)_2$, respectively. The reduction of CuO to Cu_2O is likely due to the exposure to X-rays, electron beam or plasma treatment that would induce chemical reduction, as it has been shown that CuO is reduced to Cu_2O under sputtering conditions.[42] The total amount of Cu nanoparticles on TiO_2 nanoparticles remained relatively stable after SEM imaging as seen in the Cu2p/Ti2p ratio, which was 0.36 and 0.29 for Samples 1 and 2, respectively.

Electrochemical CO_2 reduction experiments performed in 0.1 M $KHCO_3$ solution saturated with CO_2 typically occur at more negative electrochemical potentials of around -1.1 V vs. RHE.[2,5] In an effort to investigate the threshold of nanoparticle stability, new CuO_x/TiO_2 nanoparticles and TiO_2 nanoparticle samples, Samples 3 and 4, respectively were held at constant potentials, in a 0.1 M $KHCO_3$ aqueous solution saturated with CO_2, for one hour starting at -0.66 V vs RHE and increasing in -0.05 V increments until it reached a final potential of -0.91 V vs RHE. After each -0.05 V increment, SEM images of specific nanoparticles on the samples were obtained in order to track movements in the nanoparticles or changes in morphology of the sample surface that occur at each potential. It has been reported that at lower potentials, as low as -0.75 V vs RHE, there is observed product formation during CO_2RR so investigating the stability of these particles over a range will help give insight into whether these particles would be stable for prolonged periods of time during CO_2RR.[40,43]

After electrochemical treatment, XPS analysis of Samples 3 and 4 showed a loss in the amount of Cu on the TiO_2 nanoparticles, consistent with what was observed for Samples 1 and 2, accompanied by a decrease in the number of TiO_2 nanoparticles on the HOPG substrate. As seen in Table 3.3, for Sample 3 the Cu2p ratio initially was 0.39 and after electrochemical processing was 0.25, accounting for a 36% loss in Cu amount with no change in the Cu chemical species. However, it appears that the Cu_2O nanoparticles had a larger decrease than the $Cu(OH)_2$

nanoparticles after electrochemical treatment with a decrease in amount of Cu by 67% for Cu_2O and 24% for $Cu(OH)_2$ based on the Cu2p/Ti2p ratios in Table 3.3.

Table 3.3: XPS data for Samples 3 and 4 giving the approximate amounts of Cu and Ti species on TiO_2 nanoparticles and HOPG substrate.

Sample	Species	Ratio	Initial	After chronoamperometry
3	Total amount	Cu2p/Ti2p	0.39	0.25
	Total amount	Ti2p/C1s	0.56	0.50
	Cu_2O	Cu2p/Ti2p	0.09	0.03
	$Cu(OH)_2$	Cu2p/Ti2p	0.29	0.22
4	Total amount	Ti2p/C1s	0.46	0.36

XPS analysis showed that, after electrochemical treatment, the Ti2p/C1s ratio decreased by approximately 10% and 20% for Samples 3 and 4, respectively. The loss in the amount of TiO_2 could be due to loss of material or could be a result of the particles agglomerating together and reducing the Ti2p signal in XPS, as SEM and AFM data show particle agglomeration and an increase in TiO_2 particle heights. It was also observed that the mobile TiO_2 nanoparticles are decreasing in size after electrochemical reduction. Diameter measurements of individual particles in SEM images show that some of the TiO_2 nanoparticles undergo a slight decrease in diameter upon agglomeration, as will be discussed later.

Figure 3.9 shows SEM images of Sample 4, consisting of TiO_2 nanoparticles, initially and after electrochemical treatment. Note that these images are of the same area of the sample, with the blue box highlighting one of the TiO_2 particles in each image for a frame of reference. The SEM images in Figure 3.9 show that, at more reducing electrochemical potentials, ~30% of the nanoparticles move and begin to agglomerate with neighboring particles. The particles that

move leave behind “shadow” features in the SEM images are where a moved nanoparticle was previously located. The particle agglomeration was unusual since previous studies have shown that these samples are thermally stable at temperatures up to 550 K in vacuum for extended periods of time and do not undergo agglomeration.[14] It is worth noting that the particle agglomeration occurs at electrochemical potentials where hydrogen production would occur. It is possible that the production of hydrogen may be dislodging some of the TiO_2 nanoparticles from the HOPG substrate resulting in agglomeration.

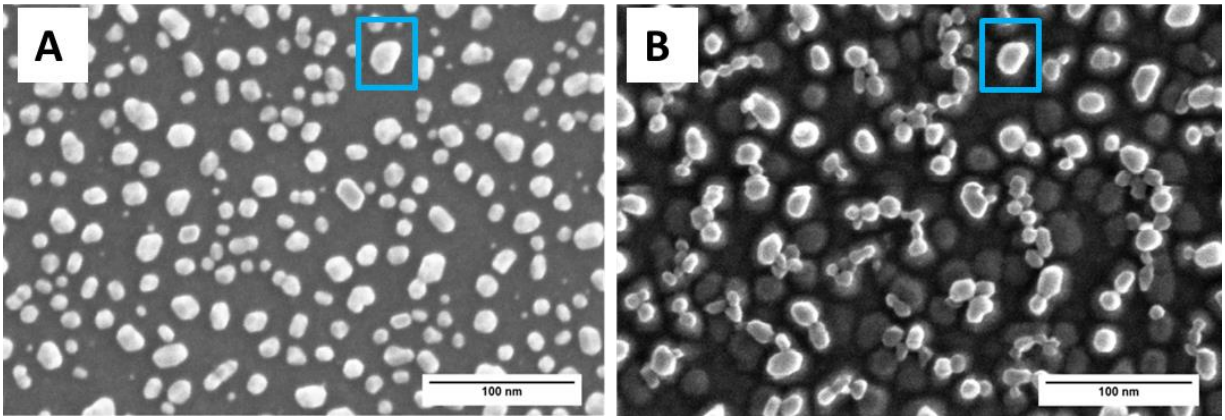

Figure 3.9: SEM comparison of the same location of TiO_2 nanoparticles (A) before and (B) after being held at reducing electrochemical potentials ranging from -0.66 V to -0.91 V vs RHE for 6 hours total. The blue box highlights the same particle in both SEM images as a frame of reference for comparison.

While agglomeration of TiO_2 nanoparticles under these conditions is not well known, Huang et. al.[44] has shown that 16 nm Cu-based nanocubes undergo nanoclustering into dendritic morphologies after exposure to reducing potentials of -1.1 V vs RHE for 1 hour, in the same solution studied here, where they report that the applied negative potential is the main driving force in the observed morphological changes. The applied negative potential could also induce mobility of the TiO_2 nanoparticles but the exact mechanism of the movement of some of the nanoparticles observed here is not well understood.

Figure 3.10 shows SEM images at a 45^o and 40^o tilt before (Figure 3.10A) and after electrochemical treatment (Figure 3.10B), respectively. Initially, the TiO_2 nanoparticles are attached to the surface of the HOPG substrate but after being held at reducing electrochemical potentials, it is apparent that the surface is covered in raised mounds that have a darker contrast in the SEM imaging compared to the TiO_2 nanoparticles. Based on this image, the "shadow" features in Figure 3.9B are attributed to these raised mounds and that the difference in contrast between the "shadows" and the HOPG substrate in the SEM image could be a result of a change in height.

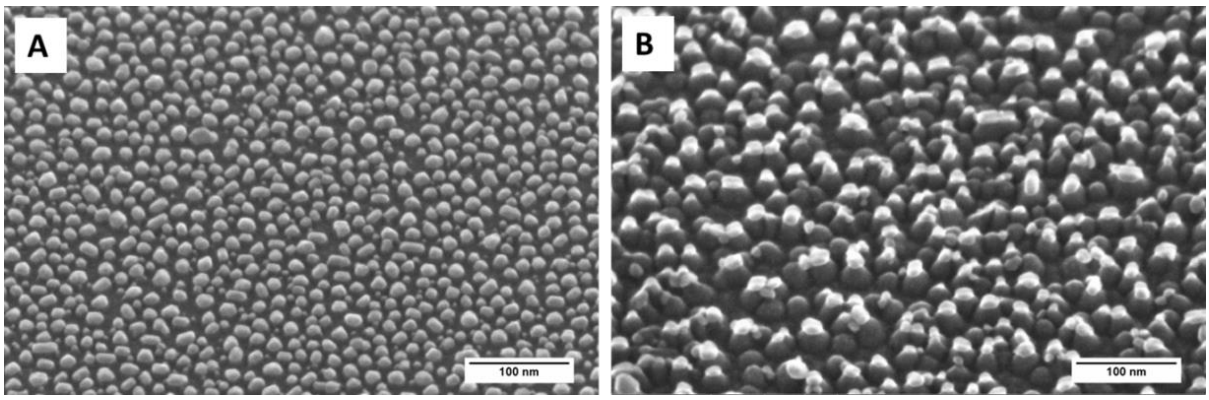

Figure 3.10: SEM images of TiO_2 nanoparticles (A) initially with the sample tilted and imaged at a 45^o angle. SEM images of TiO_2 nanoparticles (B) after electrochemical treatment with the sample tilted at a 40^o angle.

To gain more insight into the nature of the "shadow" particles in the SEM images, we have obtained AFM images of the nanoparticles on samples with high densities of nanoparticles (such as those associated with the SEM images in Figure 3.9). However, with the high density of nanoparticles, it is difficult to fully resolve individual nanoparticles in the AFM images. In an effort to investigate the "shadow" features, a sample with a lower density of TiO_2 nanoparticles, grown only along the step edges of HOPG, was held at a constant potential of -1.01 V vs RHE in 0.1 M $KHCO_3$ solution saturated with CO_2 for 2 hours and analyzed via SEM and AFM. TiO_2

nanoparticles grown along the step edges of HOPG have a much lower particle density, compared to particle growth on a plasma treated HOPG substrate, which allows for better separation of the particles in the AFM imaging. The lower density of TiO_2 nanoparticles also makes it possible to differentiate between the TiO_2 nanoparticles and "shadow" features in the AFM scans by analysis of the height differences and comparison with SEM images.

Line profile scans of the AFM images in Figure 3.11 shows that the as prepared TiO_2 nanoparticles were ~15-20 nm in height initially. After electrochemical treatment, some of the TiO_2 nanoparticles measured ~5 nm in height while most of the others were in the 20-30 nm range. Figure 3.11D shows the AFM scan of the TiO_2 nanoparticles after electrochemical treatment and Figure 3.11B shows the SEM image of the same area scanned in the AFM image for comparison. The inset in Figure 3.11B is of a select area where the contrast and brightness of the image was enhanced in order to better observe the "shadow" features. The very small bright spots in the SEM image and inset in 3.11B are a result of damage to the HOPG substrate by the cantilever tip as a result of AFM imaging. Studies we have done on bare HOPG have shown these AFM damage features as well. SEM imaging shows that the ~5 nm high particles observed in AFM, as seen in the line scan of Figure 3.11F, actually correspond to "shadow" features that have been previously observed in the SEM images shown in Figure 3.9. This indicates that these "shadows" are indeed raised features on the HOPG substrate surface that have been substantially reduced in height from the particle that was in the same spot prior to the electrochemistry. However, it is unclear whether these "shadows" are a result of deformation of the HOPG substrate or a result of a thin layer of TiO_2 that remains on the HOPG substrate when the TiO_2 nanoparticle has moved to attach to a neighboring particle. The TiO_2 nanoparticles are grown by PVD but it is not well understood exactly how the nanoparticles are attached to the HOPG

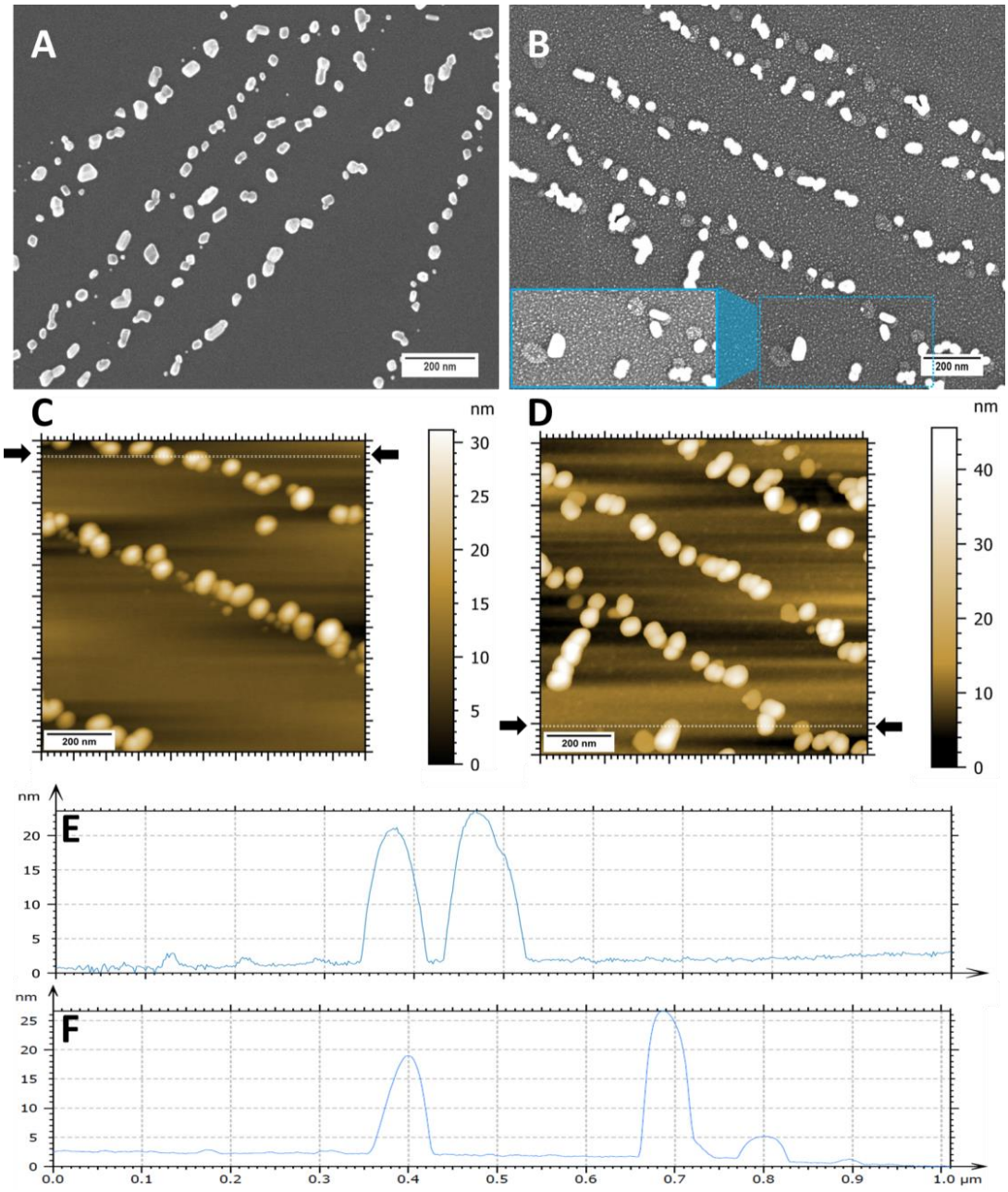

Figure 3.11: SEM and AFM images of TiO_2 nanoparticles grown along the step edges of HOPG (A,C) initially and (B, D) after being held at -1.01 V vs RHE for 2 hours. The SEM image shown in (B) is of the area scanned in the AFM image (D). Inset in (B) enhanced the brightness and contrast in order to better distinguish between the "shadow" features and nanoparticles. The arrows in (C) correspond to the location of the line scan (E) that shows the TiO_2 nanoparticles are ~20 nm in height. The arrows in (D) correspond to the location of the line scan (F) where the 5 nm high feature at 0.8 µm represents the height of the "shadow" feature seen in the inset in (B).

surface. More specifically, while it is likely, it is not known for certain if the Ti impinging on the surface bonds with carbon at defects in the HOPG substrate and forms a Ti-C layer before the TiO_2 nanoparticle grows. If an interfacial layer of Ti-C forms at the HOPG/nanoparticle interface, it is possible that the "shadow" that remains behind when a TiO_2 nanoparticle moves is the Ti-C interfacial layer.

The SEM images seen in Figure 3.9 show that, in the same area, there are about ~200 TiO_2 nanoparticles initially and, after electrochemical reduction, there are ~170 distinguishable nanoparticles, per manual counting. The observed loss of ~15% of TiO_2 nanoparticles may explain the decrease in the Ti2p/C1s ratio in the XPS analysis however, individual diameter measurements of various particles shows that the particles that moved have slightly decreased in diameter. The decrease in the amount of TiO_2 on the HOPG substrate could be a combination of some particle loss, agglomeration and decrease in diameter of the particles that have moved. The individual diameter measurements also show that the size of the particles that don't move remains roughly the same before and after electrochemical treatment.

Figure 3.12 shows SEM images of the same area of Sample 4, TiO_2 nanoparticles, initially and after electrochemical treatment. Various particles are numbered in the Figure and individual diameter measurements of these particles and "shadows" are recorded in Table 3.4. These measurements show that the particles that do not move, such as particles 1 and 2, remain roughly the same size after electrochemical treatment with a 1.8% and 1.5% decrease in diameter, respectively. However, particles that do move, such as particles 7 or 8, show a slight decrease in size after electrochemical treatment with a 19.7% and 17.3% decrease in diameter, respectively. It is also worth noting that the "shadow" left behind by a moved particle is larger in lateral dimension than the particle that occupied that space originally. Specifically, the shadow

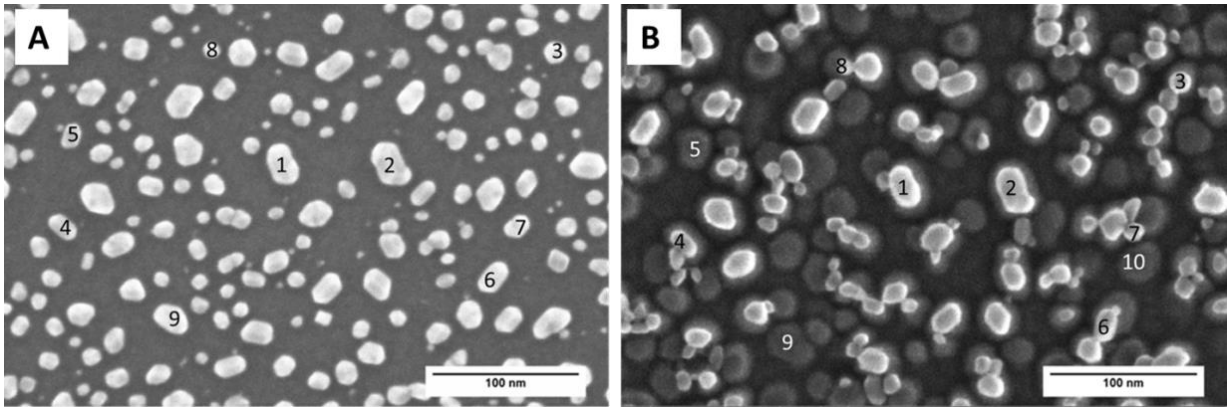

Figure 3.12: SEM imaged of TiO_2 nanoparticles (A) before and (B) after electrochemical treatment. Individual particles are numbered and their diameter measurements are recorded in Table 3.4.

Table 3.4: Individual particle diameter measurements taken from Figure 3.12.

	Initial		After electrochemical treatment	
Location	Description	Diameter (nm)	Description	Diameter (nm)
1	TiO_2 particle	28.3	TiO_2 particle	27.8
2	TiO_2 particle	33.5	TiO_2 particle	33.0
3	TiO_2 particle	15.7	TiO_2 particle	15.8
4	TiO_2 particle	20.5	TiO_2 particle	21.6
5	TiO_2 particle	16.5	Shadow	25.9
6	TiO_2 particle	23.8	TiO_2 particle	22.8
7	TiO_2 particle	17.8	TiO_2 particle	14.3
8	TiO_2 particle	12.7	TiO_2 particle	10.5
9	TiO_2 particle	24.4	Shadow	31.6
10			Shadow	29.3

left behind when particle 5 moved has an area 1.6 times larger than the original particle and the shadow of particle 9 has an area 1.3 times larger than the original particle. While it is possible that the "shadows" could be attributed to the deformation of the carbon substrate under electrochemical conditions, the HOPG substrate itself was stable at the reducing electrochemical potentials used, as seen in AFM analysis. Both a freshly cleaved HOPG substrate and an HOPG substrate exposed to Ar plasma treatment were held at -0.91 V vs RHE for 3 hours and subsequent AFM analysis indicated no obvious changes in the height or morphology of the surface. Thus it is most likely that the "shadows" observed in the SEM images taken after electrochemical reduction are the residual of the particle that moved or the Ti-C interfacial layer, as described previously.

AFM analysis on Sample 5, consisting of a high density of TiO_2 nanoparticles, initially showed an average particle height of approximately 6 nm, as seen in Figure 3.13. After being held at -0.91 V vs RHE for 3 hours, SEM images revealed formation of "shadow" features and the particles underwent significant movement. It is important to note that Sample 5 was held at -0.91 V vs RHE initially, unlike Samples 3 and 4 that were ramped up to achieve a final voltage of -0.91 V vs RHE from a starting point of -0.66 V vs RHE. This distinction is noteworthy because the movement of nanoparticles does depend on a combination of the strength of the potential applied and the time held at those potentials. Sample 5 was initially held at -0.91 V vs RHE for 1 hour whereupon slight particle movement was observed but not as significant as was expected based on the SEM images of Samples 3 and 4 at that potential. Sample 5 was then subsequently held at -0.91 V vs RHE for an additional 2 hours where significant particle movement was observed after this total time, as seen in Figure 3.13B.

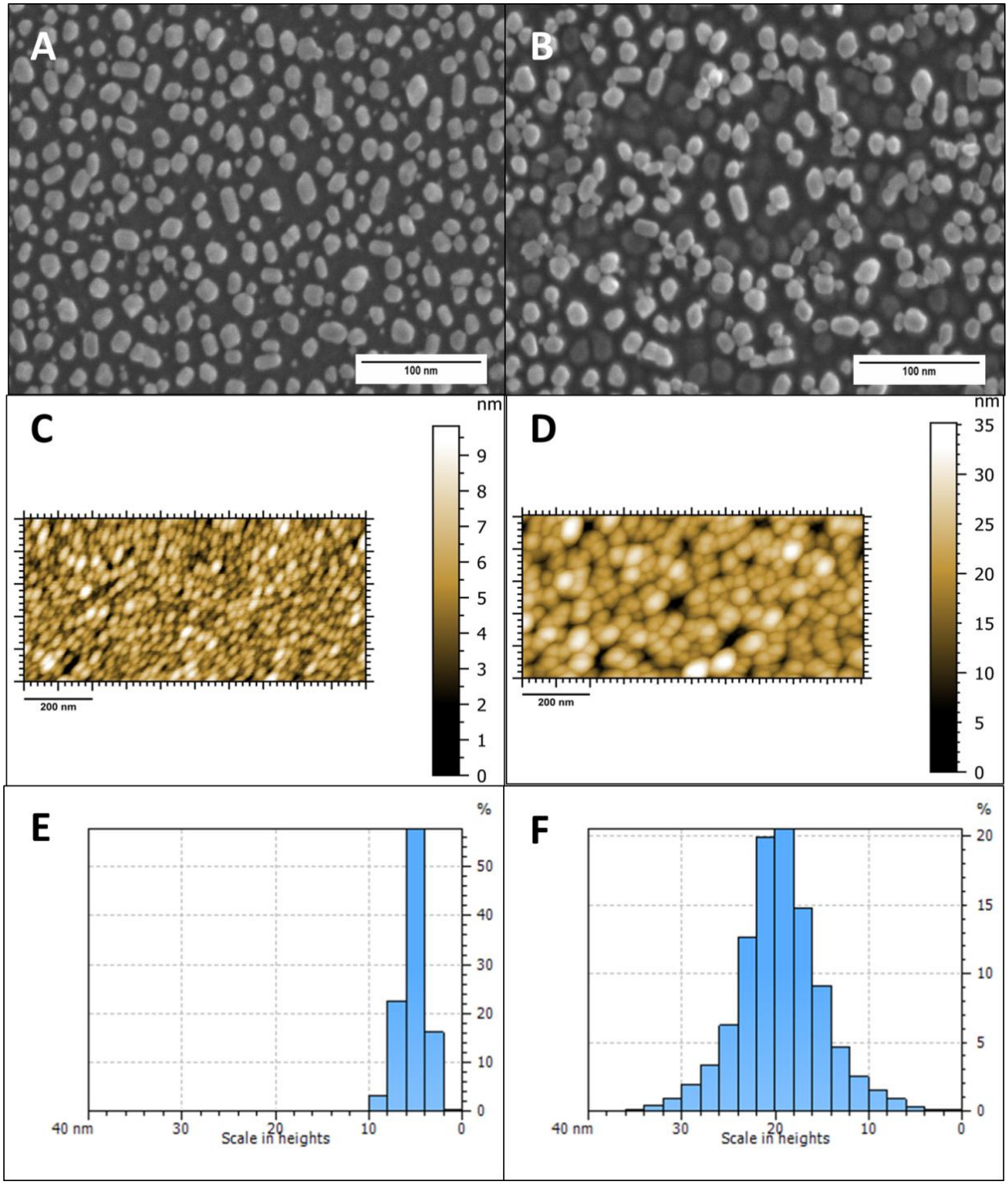

Figure 3.13: SEM and AFM images of TiO_2 nanoparticles (A, C) before and (B, D) after being held at -0.91 V vs RHE for 3 hours. Histograms show the particle height distribution of the AFM images for the TiO_2 nanoparticles (E) initially and (F) after electrochemical treatment.

AFM analysis of this sample after electrochemical treatment gave an average particle height of approximately 20 nm. Figure 3.13 shows the AFM height view images before and after electrochemical treatment and it is apparent that, after being held at a reducing electrochemical potential, fewer particles are observed in the same size area. This is likely a result of the inability of the cantilever to distinguish individual nanoparticles that have agglomerated together, as the tip is not sharp enough to differentiate between particles at such close distances.

The histograms in Figures 3.13E and 3.13F show the distribution in heights for each AFM image. Initially, the histogram shows that the heights of the nanoparticles exhibit a relatively narrow height distribution with about 56% of the nanoparticles being approximately 6 nm in height with some particles being slightly larger or smaller by about 2 nm. However, the histogram of the AFM image after electrochemical treatment indicates significant growth in the particle heights and a much broader height distribution after electrochemical reduction. About 40% of the particles are either 20 or 22 nm in height with the remaining nanoparticles varying in size from 6 to 34 nm. The lack of uniformity in the sample heights is consistent with what is visually observed in the SEM images where areas of particle agglomeration appear after being electrochemically reduced.

Based on the SEM and AFM data, it is apparent that the particle agglomeration that occurs during electrochemical reduction results predominantly in vertical growth of the particles as opposed to horizontal growth. The SEM images in Figure 3.13 clearly show particles stacked on top of one another as well as “shadow” features that are seen across the surface. This is also supported by the change in the heights as seen in AFM analysis where, initially, the average particle height was 6 nm which increased to approximately 20 nm after electrochemical treatment. The histogram after electrochemical treatment showed a small amount of particles

with 6 nm in height. This implies that the heights of all of the particles have increased as opposed to just the particles that have agglomerated together. However, it is difficult to look at height changes in individual particles in order to get a clearer idea of what may be attributing to the height difference. From Figure 3.10, we see that, after electrochemical treatment, raised mounds appear across the surface of the sample. The AFM and SEM images in Figure 3.11 show that these raised mounds can be assigned to the "shadow" features that are observed in the un-tilted SEM images after electrochemical treatment. However, Figure 3.10 also shows raised mounds with particles situated atop of them which would differ from the "shadow" features but result in an increase in the height of all the particles after electrochemical treatment.

3.4 Conclusion

The investigation of nanoparticle stability of this CuO_x/TiO_2/HOPG model catalyst is crucial to understand its viability in the electrochemical reduction of CO_2. At reducing electrochemical potentials, lateral movement of a small number of the nanoparticles (~30%) results in vertical growth of the neighboring nanoparticles. The potentials applied are in the range where hydrogen production is expected to occur and it is possible that the production of hydrogen bubbles would lead to an increase in the mobility of TiO_2 nanoparticles on the HOPG surface, but the detailed mechanism remains unclear. The stability of the nanoparticles is influenced by a combination of total time of exposure and the strength (more negative) of reducing potential applied where the nanoparticles may be stable at more negative potentials but would undergo agglomeration over time. XPS analysis shows that the amount of copper on the TiO_2 nanoparticles decreases after electrochemical reduction but it is expected that it would remain a viable catalyst despite the reduction in the amount of copper. The DEMS preliminary

studies show that these model catalysts are active for the electrochemical reduction of CO_2 and merit further investigation into their reactivity to see if any product formation is observed at lower potentials, as the TiO_2 nanoparticles are expected to help reduce the overpotential currently required for CO_2 reduction on copper metal.

3.5 References

(1) Whipple, D. T.; Kenis, P. J. A. Prospects of CO_2 Utilization via Direct Heterogeneous Electrochemical Reduction. *J. Phys. Chem. Lett.* **2010**, *1*, 3451–3458.

(2) Reske, R.; Mistry, H.; Behafarid, F.; Roldan Cuenya, B.; Strasser, P. Particle Size Effects in the Catalytic Electroreduction of CO_2 on Cu Nanoparticles. *J. Am. Chem. Soc.* **2014**, *136*, 6978–6986.

(3) Popovic, S.; Smiljanic, M.; Jovanovic, P.; Vavra, J.; Buonsanti, R.; Hodnik, N. Stability and Degradation Mechanisms of Copper-Based Catalysts for Electrochemical CO_2 Reduction. *Angew. Chemie - Int. Ed.* **2020**, *132*, 2–13.

(4) Raciti, D.; Wang, C. Recent Advances in CO_2 Reduction Electrocatalysis on Copper. *ACS Energy Lett.* **2018**, *3* (7), 1545–1556.

(5) Kas, R.; Kortlever, R.; Milbrat, A.; Koper, M. T. M.; Mul, G.; Baltrusaitis, J. Electrochemical CO_2 Reduction on Cu_2O-Derived Copper Nanoparticles: Controlling the Catalytic Selectivity of Hydrocarbons. *Phys. Chem. Chem. Phys.* **2014**, *16*, 12194–12201.

(6) Liu, X.; Xiao, J.; Peng, H.; Hong, X.; Chan, K.; Nørskov, J. K. Understanding Trends in Electrochemical Carbon Dioxide Reduction Rates. *Nat. Commun.* **2017**, *8*, 1–7.

(7) Kuhl, K. P.; Hatsukade, T.; Cave, E. R.; Abram, D. N.; Kibsgaard, J.; Jaramillo, T. F. Electrocatalytic Conversion of Carbon Dioxide to Methane and Methanol on Transition Metal Surfaces. *J. Am. Chem. Soc.* **2014**, No. 136, 14107–14113.

(8) Peterson, A. A.; Nørskov, J. K. Activity Descriptors for CO_2 Electroreduction to Methane on Transition-Metal Catalysts. *J. Phys. Chem. Lett.* **2012**, *3*, 251–258.

(9) Umeda, M.; Niitsuma, Y.; Horikawa, T.; Matsuda, S.; Osawa, M. Electrochemical Reduction of CO_2 to Methane on Platinum Catalysts without Overpotentials: Strategies for Improving Conversion Efficiency. *ACS Appl. Energy Mater.* **2020**, *3*, 1119–1127.

(10) Hori, Y.; Murata, A.; Takahashi, R. Formation of Hydrocarbons in the Electrochemical Reduction of Carbon Dioxide at a Copper Electrode in Aqueous Solution. *J. Chem. Soc., Faraday Trans. 1* **1989**, *85* (8), 2309–2326.

(11) Kuhl, K. P.; Cave, E. R.; Abram, D. N.; Jaramillo, T. F. New Insights into the Electrochemical Reduction of Carbon Dioxide on Metallic Copper Surfaces. *Energy Environ. Sci.* **2012**, *5*, 7050–7059.

(12) Gao, D.; Zegkinoglou, I.; Divins, N. J.; Scholten, F.; Sinev, I.; Grosse, P.; Cuenya, B. R. Plasma-Activated Copper Nanocube Catalysts for Efficient Carbon Dioxide Electroreduction to Hydrocarbons and Alcohols. *ACS Nano* **2017**, *11*, 4825–4831.

(13) Li, C. W.; Kanan, M. W. CO_2 Reduction at Low Overpotential on Cu Electrodes Resulting from the Reduction of Thick Cu_2O Films. *J. Am. Chem. Soc.* **2012**, *134* (17), 7231–7234.

(14) Ferrah, D.; Haines, A. R.; Galhenage, R. P.; Bruce, J. P.; Babore, A. D.; Hunt, A.; Waluyo, I.; Hemminger, J. C. Wet Chemical Growth and Thermocatalytic Activity of Cu-Based Nanoparticles Supported on TiO_2 Nanoparticles/HOPG: In Situ Ambient Pressure XPS Study of the CO_2 Hydrogenation Reaction. *ACS Catal.* **2019**, *9*, 6783–6802.

(15) Kattel, S.; Liu, P.; Chen, J. G. Tuning Selectivity of CO_2 Hydrogenation Reactions at the Metal/Oxide Interface. *J. Am. Chem. Soc.* **2017**, *139*, 9739–9754.

(16) Rodriguez, J. A.; Liu, P.; Stacchiola, D. J.; Senanayake, S. D.; White, M. G.; Chen, J. G. Hydrogenation of CO_2 to Methanol: Importance of Metal-Oxide and Metal-Carbide Interfaces in the Activation of CO_2. *ACS Catal.* **2015**, *5* (11), 6696–6706.

(17) Jadhav, S. G.; Vaidya, P. D.; Bhanage, B. M.; Joshi, J. B. Catalytic Carbon Dioxide

Hydrogenation to Methanol: A Review of Recent Studies. *Chem. Eng. Res. Des.* **2014**, *92* (11), 2557–2567.
(18) Graciani, J.; Mudiyanselage, K.; Xu, F.; Baber, A. E.; Evans, J.; Senanayake, S. D.; Stacchiola, D. J.; Liu, P.; Hrbek, J.; Sanz, J. F.; Rodriguez, J. A. Highly Active Copper-Ceria and Copper-Ceria-Titania Catalysts for Methanol Synthesis from CO_2. *Science.* **2014**, *345* (6196), 546–550.
(19) Nomura, N.; Tagawa, T.; Goto, S. Titania Supported Copper Catalysts for Methanol Synthesis from Carbon Dioxide. *React. Kinet. Catal. Lett.* **1998**, *63* (1), 9–13.
(20) Saeidi, S.; Amin, N. A. S.; Rahimpour, M. R. Hydrogenation of CO_2 to Value-Added Products - A Review and Potential Future Developments. *J. CO_2 Util.* **2014**, *5*, 66–81.
(21) Porosoff, M. D.; Yan, B.; Chen, J. G. Catalytic Reduction of CO_2 by H_2 for Synthesis of CO, Methanol and Hydrocarbons: Challenges and Opportunities. *Energy Environ. Sci.* **2016**, *9*, 62–73.
(22) Behrens, M.; Studt, F.; Kasatkin, I.; Kühl, S.; Hävecker, M.; Abild-Pedersen, F.; Zander, S.; Girgsdies, F.; Kurr, P.; Kniep, B.-L.; Tovar, M.; Fischer, R. W.; Nørskov, J. K.; Schlögl, R. The Active Site of Methanol Synthesis over $Cu/ZnO/Al_2O_3$ Industrial Catalysts. *Science.* **2012**, *336*, 893–897.
(23) Kattel, S.; Yu, W.; Yang, X.; Yan, B.; Huang, Y.; Wan, W.; Liu, P.; Chen, J. G. CO_2 Hydrogenation over Oxide-Supported PtCo Catalysts: The Role of the Oxide Support in Determining the Product Selectivity. *Angew. Chemie - Int. Ed.* **2016**, *55*, 7968–7973.
(24) Yuan, J.; Zhang, J.-J.; Yang, M.-P.; Meng, W.-J.; Wang, H.; Lu, J.-X. CuO Nanoparticles Supported on TiO_2 with High Efficiency for CO_2 Electrochemical Reduction to Ethanol. *Catalysts* **2018**, *8*, 171.
(25) Qu, J.; Zhang, X.; Wang, Y.; Xie, C. Electrochemical Reduction of CO_2 on RuO_2/TiO_2 Nanotubes Composite Modified Pt Electrode. *Electrochim. Acta* **2005**, *50*, 3576–3580.
(26) Li, T.-T.; Shan, B.; Xu, W.; Meyer, T. J. Electrocatalytic CO_2 Reduction with a Ruthenium Catalyst in Solution and on Nanocrystalline TiO_2. *ChemSusChem* **2019**, *12*, 2402–2408.
(27) Mendieta-Reyes, N. E.; Cheuquepan, W.; Rodes, A.; Gomez, R. Spectroelectrochemical Study of CO_2 Reduction on TiO_2 Electrodes in Acetonitrile. *ACS Catal.* **2020**, *10*, 103–113.
(28) Ramesha, G. K.; Brennecke, J. F.; Kamat, P. V. Origin of Catalytic Effect in the Reduction of CO_2 at Nanostructured TiO_2 Films. *ACS Catal.* **2014**, *4*, 3249–3254.
(29) Gao, D.; Zhang, Y.; Zhou, Z.; Cai, F.; Zhao, X.; Huang, W.; Li, Y.; Zhu, J.; Liu, P.; Yang, F.; Wang, G.; Bao, X. Enhancing CO_2 Electroreduction with the Metal − Oxide Interface. *J. Am. Chem. Soc.* **2017**, *139*, 5652–5655.
(30) Varandili, S. B.; Huang, J.; Oveisi, E.; Gregorio, G. L. De; Mensi, M.; Strach, M.; Vavra, J.; Gadiyar, C.; Bhowmik, A.; Buonsanti, R. Synthesis of Cu/CeO_{2-x} Nanocrystalline Heterodimers with Interfacial Active Sites To Promote CO_2 Electroreduction. *ACS Catal.* **2019**, *9*, 5035–5046.
(31) Beverskog, B.; Puigdomenech, I. Revised Pourbaix Diagrams for Copper at 25 to 300 °C. *J. Electrochem. Soc.* **1997**, *144* (10), 3476–3483.
(32) Sheldon, D. Methanol Production – A Technical History. *Johnson Matthey Technol. Rev.* **2017**, *61* (3), 172–182.
(33) Kas, R.; Yang, K.; Bohra, D.; Kortlever, R.; Burdyny, T.; Smith, W. A. Electrochemical CO_2 Reduction on Nanostructured Metal Electrodes: Fact or Defect? *Chem. Sci.* **2020**, *11*,

1738–1749.
(34) Baltruschat, H. Differential Electrochemical Mass Spectrometry. *J. Am. Soc. Mass Spectrom.* **2004**, *15*, 1693–1706.
(35) Abd-El-Latif, A. A.; Bondue, C. J.; Ernst, S.; Hegemann, M.; Kaul, J. K.; Khodayari, M.; Mostafa, E.; Stefanova, A.; Baltruschat, H. Insights into Electrochemical Reactions by Differential Electrochemical Mass Spectrometry. *Trends Anal. Chem.* **2015**, *70*, 4–13.
(36) Javier, A.; Chmielowiec, B.; Sanabria-Chinchilla, J.; Kim, Y.; Baricuatro, J. H.; Soriaga, M. P. A DEMS Study of the Reduction of CO_2, CO, and HCHO Pre-Adsorbed on Cu Electrodes: Empirical Inferences on the CO_2RR Mechanism. *Electrocatalysis* **2015**, *6*, 127–131.
(37) Javier, A.; Baricuatro, J. H.; Kim, Y.; Soriaga, M. P. Overlayer Au-on-W Near-Surface Alloy for the Selective Electrochemical Reduction of CO_2 to Methanol : Empirical (DEMS) Corroboration of a Computational (DFT) Prediction. *Electrocatalysis* **2015**, *6*, 493–497.
(38) Javier, A.; Baricuatro, J. H.; Kim, Y.-G.; Soriaga, M. P. Electrocatalytic Reduction of CO_2 on Cu and Au/W Electrode Surfaces: Empirical (DEMS) Confirmation of Computational (DFT) Predictions. *ECS Trans.* **2017**, *75*, 1–17.
(39) Biesinger, M. C. Advanced Analysis of Copper X-Ray Photoelectron Spectra. *Surf. Interface Anal.* **2017**.
(40) Jung, H.; Lee, S. Y.; Lee, C. W.; Cho, M. K.; Won, D. H.; Kim, C.; Oh, H.; Min, B. K.; Hwang, Y. J. Electrochemical Fragmentation of Cu_2O Nanoparticles Enhancing Selective C−C Coupling from CO_2 Reduction Reaction. *J. Am. Chem. Soc.* **2019**, *141*, 4624–4633.
(41) Grosse, P.; Gao, D.; Scholten, F.; Sinev, I.; Mistry, H.; Cuenya, B. R. Dynamic Changes in the Structure, Chemical State and Catalytic Selectivity of Cu Nanocubes during CO_2 Electroreduction: Size and Support Effects. *Angew. Chemie - Int. Ed.* **2018**, *57*, 6192–6197.
(42) Panzner, G.; Egert, B.; Schmidt, H. P. The Stability of CuO and Cu_2O Surfaces During Argon Sputtering Studied by XPS and AES. *Surf. Sci.* **1985**, *151*, 400–408.
(43) Kim, D.; Kley, C. S.; Li, Y.; Yang, P. Copper Nanoparticle Ensembles for Selective Electroreduction of CO_2 to C_2–C_3 Products. *PNAS* **2017**, *114* (40), 10560–10565.
(44) Huang, J.; Hörmann, N.; Oveisi, E.; Loiudice, A.; De Gregorio, G. L.; Andreussi, O.; Marzari, N.; Buonsanti, R. Potential-Induced Nanoclustering of Metallic Catalysts during Electrochemical CO_2 Reduction. *Nat. Commun.* **2018**, *9* (3117).

Chapter 4

Synthesis and Characterization of ZnO Nanoparticles Supported on HOPG and Silicon

4.1 Introduction

Heterogeneous catalysts have been widely investigated for the conversion of CO_2 into value adding chemicals, such as methanol (MeOH) or methane (CH_4). Industrially, thermal reduction of CO_2 is used on a larger scale to produce methanol.[1–3] This process requires a mixture of synthesis gases ($H_2/CO_2/CO$) to be passed over a $Cu/ZnO/Al_2O_3$ catalyst at elevated pressures (50 to 100 bar) and temperatures (200 to 300 ^oC).[2,4–6] However, the active site of this catalyst has been a subject of debate as researchers seek to understand the role of ZnO in the promotion of methanol production.

Some reports claim that ZnO acts as a physical spacer between the copper nanoparticles in order to help disperse the Cu phase and results in a high surface area of Cu in industrial catalysts.[2] Other studies suggest a synergistic effect between the ZnO and Cu nanoparticles that would result in catalyst stabilization through strong metal support interactions (SMSI).[7] With this synergy, ZnO could act as a structural modifier, hydrogen reservoir, direct promoter for bond activation, or form a ZnCu alloy.[2,7–14] Kattel et al. has shown that ZnCu alloy undergoes surface oxidation under thermal CO_2 reduction reaction conditions which results in the formation of ZnO and Cu which facilitates methanol synthesis via formate intermediates.[8]

The debate of the role of ZnO in this process highlights the need for fundamental investigations on the reaction mechanism for CO_2 hydrogenation. This could be achieved by studying a model catalyst system consisting of Cu/ZnO nanoparticles, similar to the studies performed for the Cu/TiO_2 system discussed in Chapters 1 and 2. The two common approaches

to preparing Cu/ZnO catalysts are either: 1) wet chemistry techniques such as sol-gel or coprecipitation or 2) vacuum-based techniques such as atomic layer deposition (ALD) or chemical vapor deposition (CVD).[15–20] However these techniques have their drawbacks as wet chemistry techniques result in samples that have a wide range of surface sites making characterization difficult and CVD processes often result in surface contamination problems through reactions with the precursor ligands.

In this Chapter, the synthesis of ZnO nanoparticles has been attempted using physical vapor deposition (PVD) as this process has resulted in the formation of well-defined and crystalline TiO_2 nanoparticles in past studies.[21,22] The growth of ZnO by PVD has been reported and typically results in the formation of a thin film or nanowires/rods of ZnO.[23–25] In this study, we have attempted to deposit ZnO nanoparticles on an HOPG or Si substrate and subsequent photodeposition and stability studies have been carried out. The growth of ZnO nanostructures is reported as well as the various conditions used to optimized the PVD process in order to achieve small (5-10 nm) ZnO nanoparticles with a high density on the substrate surface for fundamental CO_2 reduction studies.

4.2 Experimental

ZnO nanoparticles were grown on either an HOPG or silicon (Si) substrate by PVD on a commercial evaporator (Edwards 306A Coating System) under vacuum. The HOPG and Si substrate were either placed into the chamber as is or pre-treated using oxygen (O_2) or argon (Ar) plasma. The HOPG substrate was resistively heated between two copper rods and held at various substrate temperatures. The Si substrate was placed on a stainless steel heater that is heated resistively using copper rods and tungsten wire.

The ZnO nanoparticles were prepared by thermal evaporation of a zinc (Zn) metal shot (1-6 mm, Puratronic, 99.9999% metals basis, Alfa Aesar) in an alumina ceramic coated tungsten crucible. The ceramic coated tungsten crucible was resistively heated above the evaporation temperature of Zn in order to sublimate to the vapor phase. The oxidation of the ZnO particles was performed either in vacuum or with the addition of O_2 gas to the PVD chamber. The amount of ZnO deposited is monitored using a quartz crystal microbalance (QCM). The samples were characterized using scanning electron microscopy (SEM) and X-ray photoelectron spectroscopy (XPS) using an FEI Magellan 400 XHR SEM and Kratos Axis Supra photoelectron spectrometer (Kratos Analytical), respectively.

4.3 Results and Discussion

4.3.1 Argon plasma on HOPG

For the deposition of ZnO nanoparticles, the HOPG substrate was placed directly into the PVD chamber without plasma pre-treatment to determine if ZnO_x nanoparticles would form along the step edges of HOPG, similar to what was observed for PVD of TiO_2 nanoparticles. The HOPG substrate was heated to 60 ^oC due to the high mobility of the ZnO_x nanoparticles, as will be discussed later. The Zn metal was deposited for 10 minutes and the sample was further annealed at 60 ^oC for 30 minutes after deposition. SEM imaging showed the formation of square and hexagonal structures that were ~200-350 nm in diameter (Figure 4.1A). Figure 4.1B shows an area where it appears the ZnO_x nanoparticles are aligned along the step edges of HOPG. Synthesis of ZnO by PVD has been shown to result in the formation of nanowires or nanorods with a hexagonal shape.[23–28] This is similar to what is observed here although the ZnO_x deposited does not result in long nanowires or rods, compared to literature reports of ZnO nanowires that

vary from 20-80 μm in length.[29–31] From Figure 4.1C and D, the SEM image of a separate sample with a large agglomeration of ZnO nanoparticles is taken at a 45^{o} tilt. The formed ZnO_x structures are roughly 150-250 nm in height, as measured using ImageJ, and some nanostructures appear plate-like.

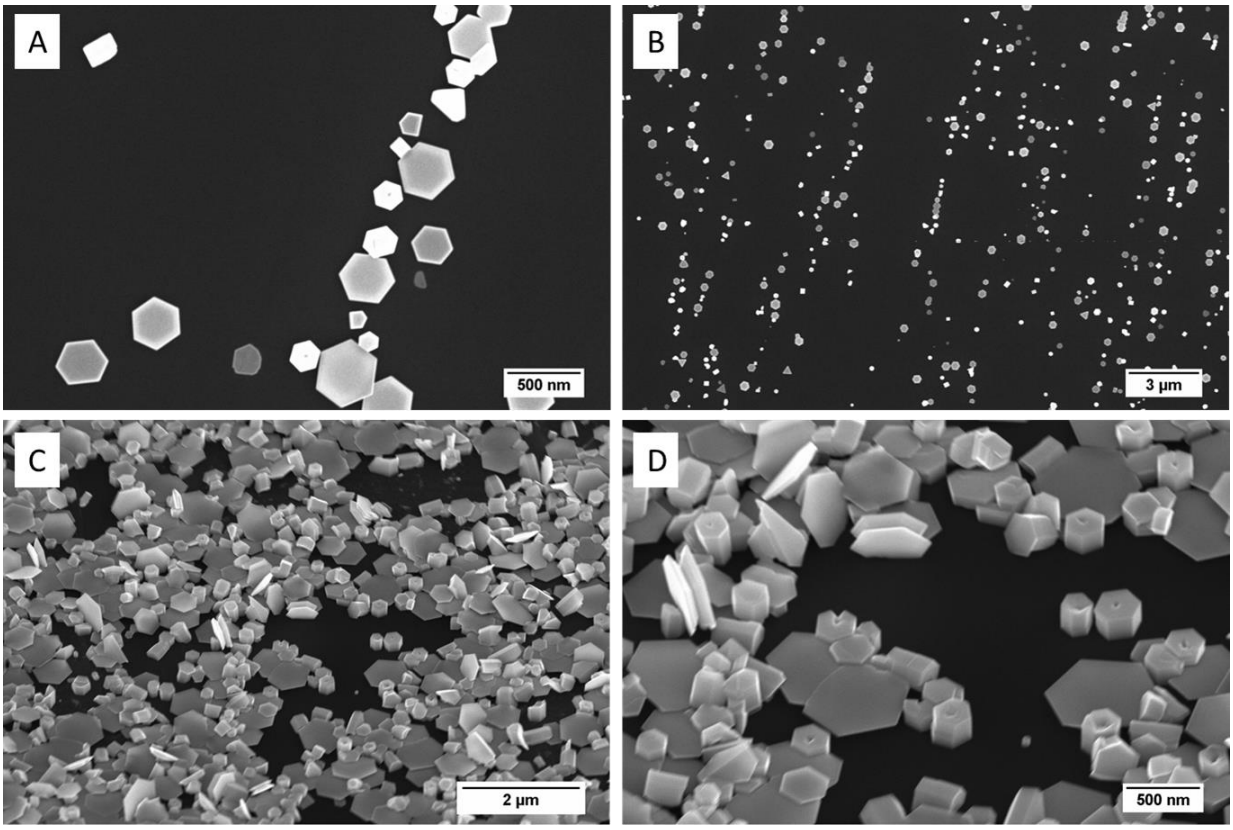

Figure 4.1: SEM images of (A, B) ZnO nanoparticles aligned along the step edge of HOPG and (C,D) a large agglomeration of ZnO nanoparticles taken at a 45^{o} tilt.

Figure 4.2A and B shows the Zn2p and Zn LMM XPS spectra that confirms the presence of ZnO species with a $Zn2p_{3/2}$ binding energy of 1022.12 eV and Zn LMM kinetic energy of 987.5 eV. The binding energy difference between ZnO and Zn metal in the Zn2p spectrum is less than 1 eV so the Zn LMM X-ray induced Auger peak is used for assigning information about the oxidation state of the Zn species.[32] ZnO and Zn metal have a difference of 4 eV in the Zn LMM spectrum. XPS analysis on single crystal ZnO was performed for comparison purposes and

shown in Figure 4.2C and D with a $Zn2p_{3/2}$ peak at 1022.22 eV and Zn LMM peak at kinetic energy of 988 eV. It is shown that the line shape of the Zn LMM peak of the synthesized sample is representative of ZnO, as seen in Figure 4.2B and D.

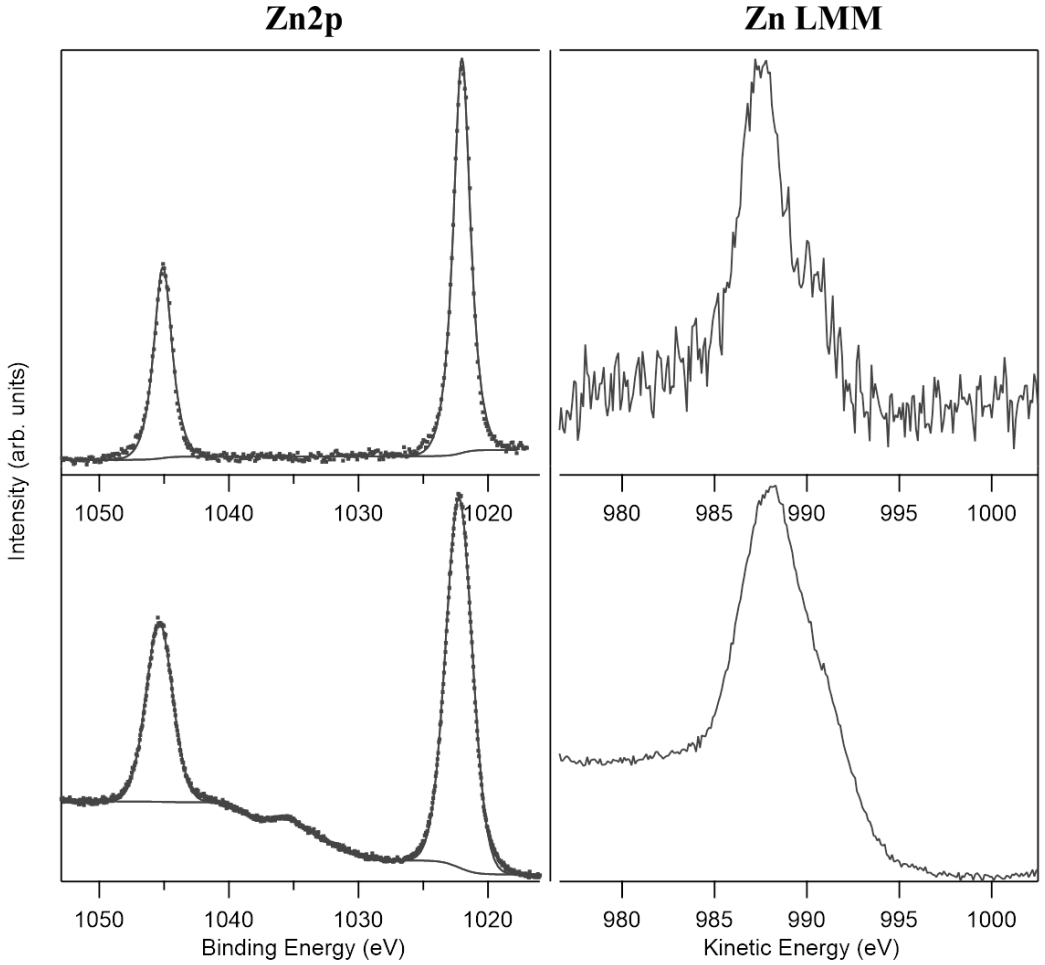

Figure 4.2: High resolution Zn2p and Zn LMM XPS spectra of (A, B) ZnO nanoparticles on HOPG and (C, D) single crystal ZnO.

However, the formation of ZnO_x along the step edges of HOPG under these conditions could not be replicated as subsequent samples prepared using these conditions did not show any ZnO_x formation via XPS. Survey spectrum of three separate samples prepared under these conditions did not show the presence of ZnO as there were no Zn2p or Zn LMM peaks detected.

For TiO_2/HOPG samples, the HOPG substrate is pretreated with low energy Ar plasma, which creates defect nucleation sites on the HOPG surface and results in the formation of a high density of TiO_2 nanoparticles. With this in mind, the HOPG substrate was treated with low energy Ar plasma prior to PVD in an effort to create high density ZnO nanoparticles.

Initially, the HOPG substrate was treated with low energy Ar plasma at 9 W with a pressure of 200 mTorr for 25 minutes which resulted in the formation of large agglomerations of hexagonal ZnO nanostructures that are 250-350 nm in diameter and small ZnO nanoparticles that are 3-4 nm in diameter (Figure 4.3A and B). This sample also had a distinct blue coloring on the substrate surface, seen in the inset of Figure 4.3B, indicating the formation of large amounts of

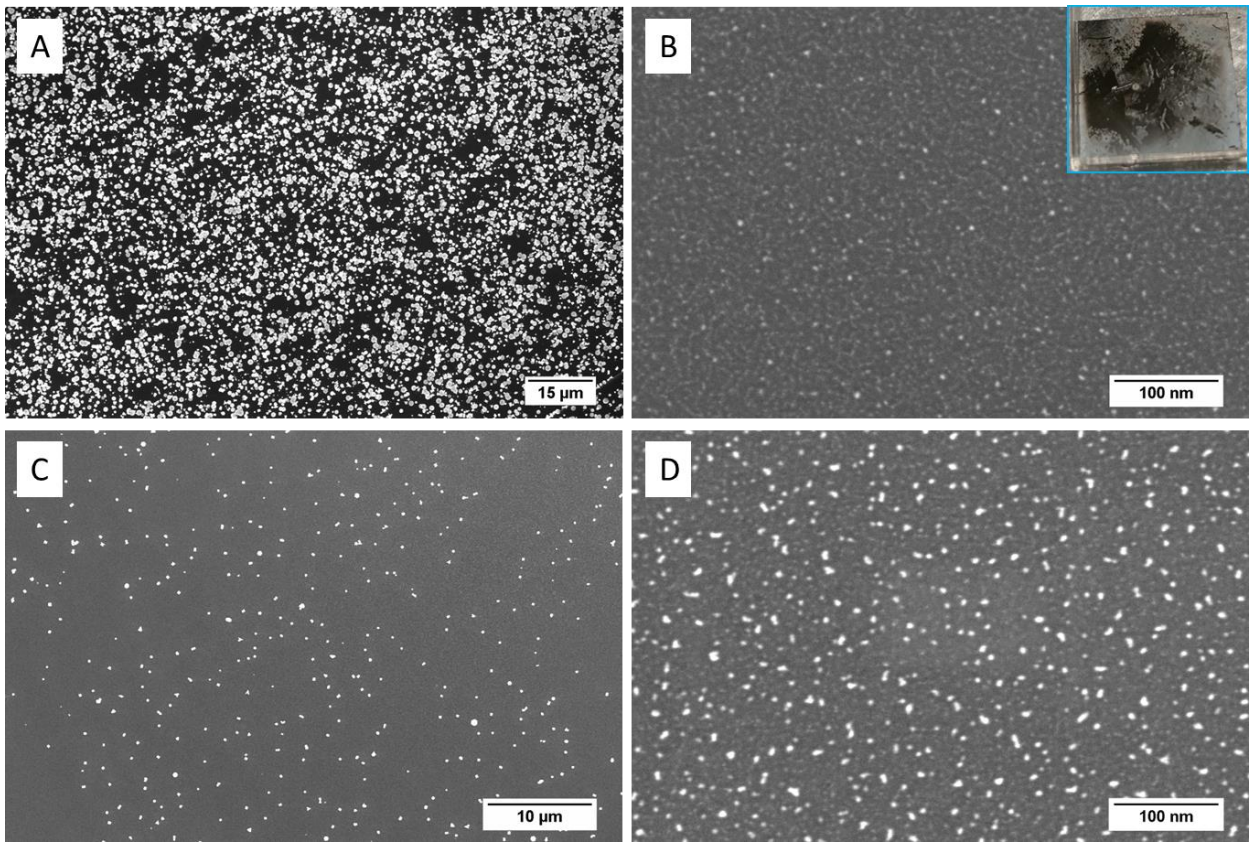

Figure 4.3: SEM images of ZnO nanoparticles on HOPG (A) on a sample that had deposition of large amounts of ZnO resulting in a blue coloring on the sample surface (seen in the inset) and (B) formation of 3-4 nm ZnO nanoparticles. SEM images of a separate sample prepared under the same conditions that had (C) less hexagonal ZnO structures on the surface and (D) deposition of 5 nm diameter ZnO nanoparticles.

ZnO as ZnO is blue gray in color. Indeed, Figure 4.3A shows the formation of clusters of large ZnO nanostructures across the surface of the HOPG substrate, which is likely causing the observed blue gray color observed on the sample. However, another sample under the same PVD and plasma treatment conditions also showed the formation of the hexagonal ZnO structures but at a much lower density on the surface (Figure 4.3C). This sample also had ZnO nanoparticles that were 5-10 in diameter deposited on the surface (Figure 4.3D). The inconsistency in the two depositions is in stark contrast to what is observed for the deposition of TiO_2 nanoparticles. The melting point for zinc metal (420 ^{o}C) is much lower than Ti metal (1,660 ^{o}C) which results in a rapid deposition. The time for the deposition of zinc is about 10 minutes whereas the Ti deposition is 1.5 hours. The rapid deposition of zinc makes it difficult to control the size and amount of nanoparticles that are deposited.

The Ar plasma treatment was varied for longer and shorter time periods to determine if the time of exposure to the plasma influences the size of the nanoparticles grown on HOPG. HOPG substrates were exposed to Ar plasma at 9 W and 200 mTorr for 10, 35, and 60 minutes and the zinc deposition was carried out under the same PVD parameters described above with a substrate temperature of 60 ^{o}C and subsequent 30 minute anneal after deposition. Figure 4.4 shows the various samples under these plasma conditions where all samples showed the formation of large, hexagonal ZnO structures across the sample surface as well as the formation of small ZnO nanoparticles, which varied in diameter according to the time of plasma exposure. The samples exposed to Ar plasma for 10 and 60 minutes had less nanoparticle density and small particle sizes (3-4 nm) compared to the samples exposure to Ar plasma for 25 and 35 minutes, which had nanoparticles that were 5 nm in diameter. This indicates the plasma treatment of the substrate has an effect on the size of the nanoparticles deposited.

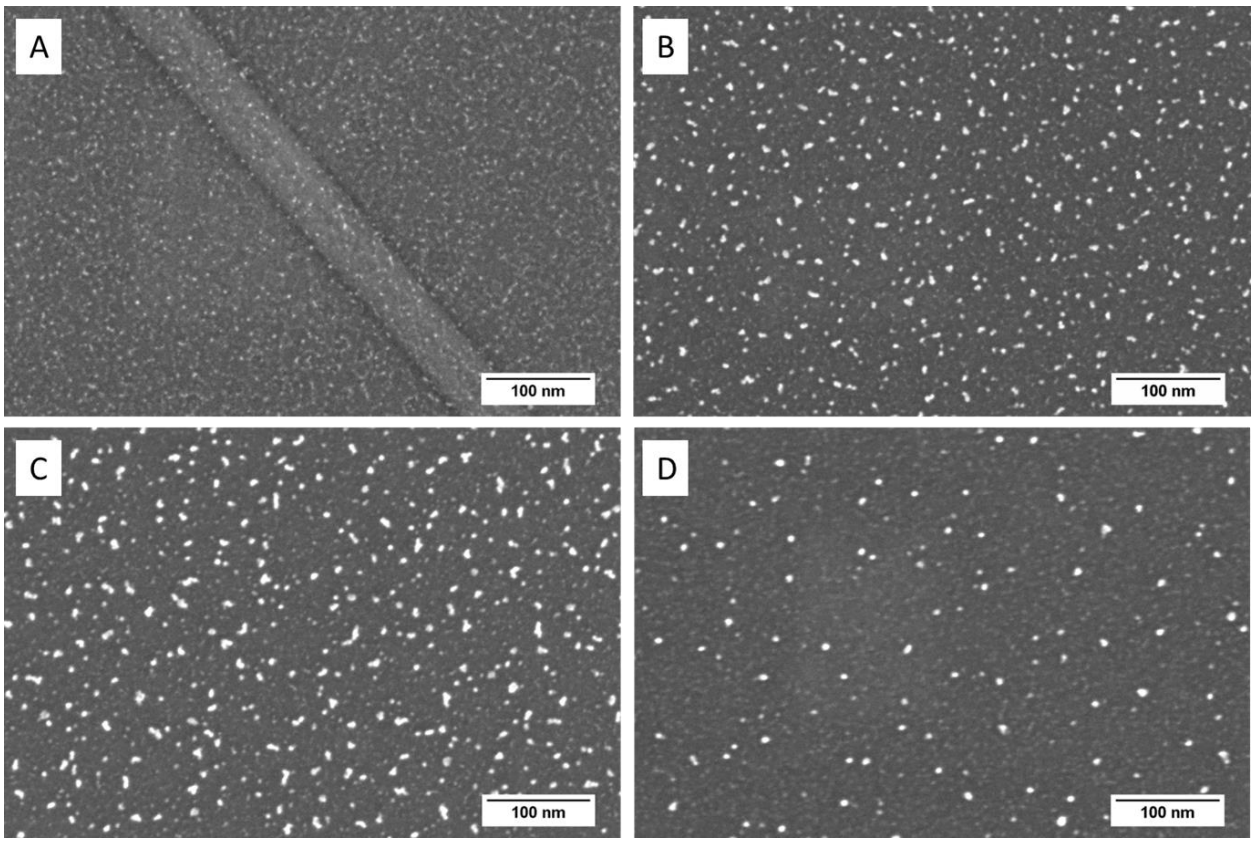

Figure 4.4: SEM images of ZnO nanoparticles on HOPG that was plasma treated with low energy Ar plasma for (A) 10 min, (B) 25 min, (C) 35 min, and (D) 60 min.

4.3.2 Substrate temperature on HOPG

It was found in the previous section that the exposure to low energy Ar plasma for 25 minutes resulted in the formation of large, hexagonal ZnO structures but also smaller nanoparticles on the surface that are 5 nm in diameter. In an effort to form larger particles, the temperature of the substrate during deposition was varied in order to determine if the ZnO nanoparticle mobility would increase with increasing substrate temperature and result in the formation of larger nanoparticles. The substrate temperatures studied were: 25 (room temperature, no heating), 100, 200, 600, and 800 ^{o}C. Table 4.1 details the substrate temperatures used and the XPS Zn2p/C1s ratio of these samples.

Table 4.1: XPS analysis detailing the Zn2p/C1s ratio of ZnO nanoparticles on HOPG deposited at various substrate temperatures.

Substrate Temperature (^{o}C)	$Zn2p_{3/2}$ area	C1s area	Ratio Zn2p/C1s
25 (room)	473.56	5710.20	0.0829
60	4996.62	6035.49	0.8279
100	49914.13	60446.31	0.8258
200	751.10	6197.45	0.1212
600	248.37	57177.72	0.0043
800	319.95	68924.33	0.0046

The samples with substrate temperatures of 600 and 800 ^{o}C had a very small $Zn2p_{3/2}$ peak which resulted in a low Zn2p/C1s ratio of 0.004 for both samples. The XPS data shows that the amount of ZnO deposited on the HOPG substrate at temperatures over 100 ^{o}C is very low. During PVD, it is not clear whether zinc is initially deposited as a metal and oxidized on the HOPG substrate to form ZnO nanoparticles or whether ZnO nanoparticles are deposited onto the substrate directly after being oxidized in the PVD chamber. The melting temperature for zinc is 420 ^{o}C whereas the melting temperature of ZnO is 1,975 ^{o}C. Therefore, the substrate temperatures here would not result in desorption of ZnO nanoparticles. It is possible that zinc metal is formed on the HOPG substrate initially and oxidized during annealing as there is very little to no zinc observed with substrate temperatures higher than 400 ^{o}C. The sample with a substrate temperature of 200 ^{o}C showed a small amount of ZnO formed with a Zn2p/C1s ratio of 0.1212 but substrate temperatures lower than 100 ^{o}C were shown to have the largest amount of ZnO nanoparticles. However, the substrate that was not heated during deposition showed little ZnO formation with a Zn2p/C1s ratio of 0.0829 indicating the importance of substrate heating for the nanoparticle mobility.

SEM imaging of the samples with substrate temperatures less than 100 ^{o}C reveals the formation of very small ZnO_x nanoparticles that are $\leq$5 nm in diamter (Figure 4.5A-C). Most of

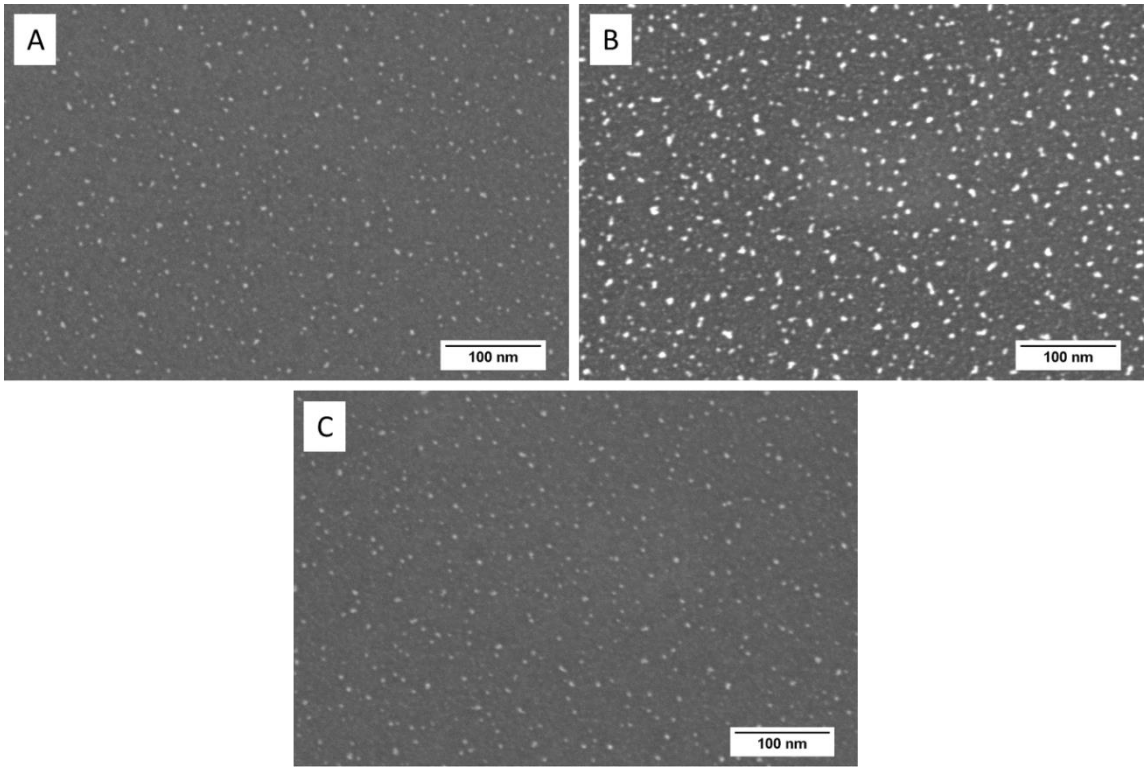

Figure 4.5: SEM images of ZnO nanoparticles deposited on Ar plasma treated HOPG with substrate temperatures of (A) room temperature with no heating, (B) 60 ^{o}C, and (C) 100 ^{o}C.

the samples revealed the formation of the larger, hexagonal ZnO nanostructures on the surface which is likely formed during the agglomeration of small ZnO nanoparticles or are zinc metal flakes deposited on the substrate surface. EDS analysis on the larger hexagonal structures revealed the presence of zinc with Kα and Lα peaks located at 8.6 and 1.0 keV, respectively (Figure 4.6). In contrast with the XPS results, XRD analysis shows the presence of mainly Zn peaks at 36.33^{o}, 39.06^{o}, 43.23^{o}, and 54.51^{o} diffraction angles which correspond to the (0,0,2), (1,0,0), (1.0.1) and (1,0,2) planes of the hexagonal close packed structure of zinc metal, respectively (Figure 4.7). The peak at 36.33^{o} also corresponds to the (1,0,1) plane of ZnO but as this overlaps with the peak for zinc metal and no other ZnO peaks were observed, it was determined the nanoparticles were metallic zinc. Since XRD is more of a bulk technique compared to XPS, it is possible that only the surface of the Zn nanoparticles is oxidized to ZnO.

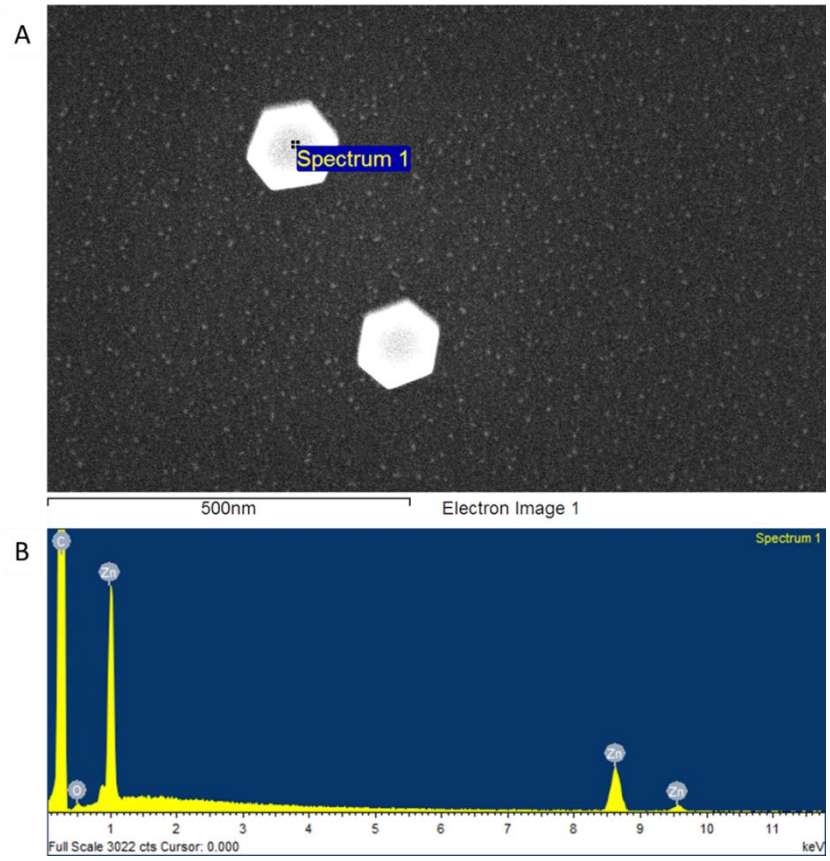

Figure 4.6: (A) SEM images of ZnO nanoparticles on HOPG showing the formation of large, hexagonal structures and (B) EDS analysis of the hexagonal structures confirming the presence of zinc material.

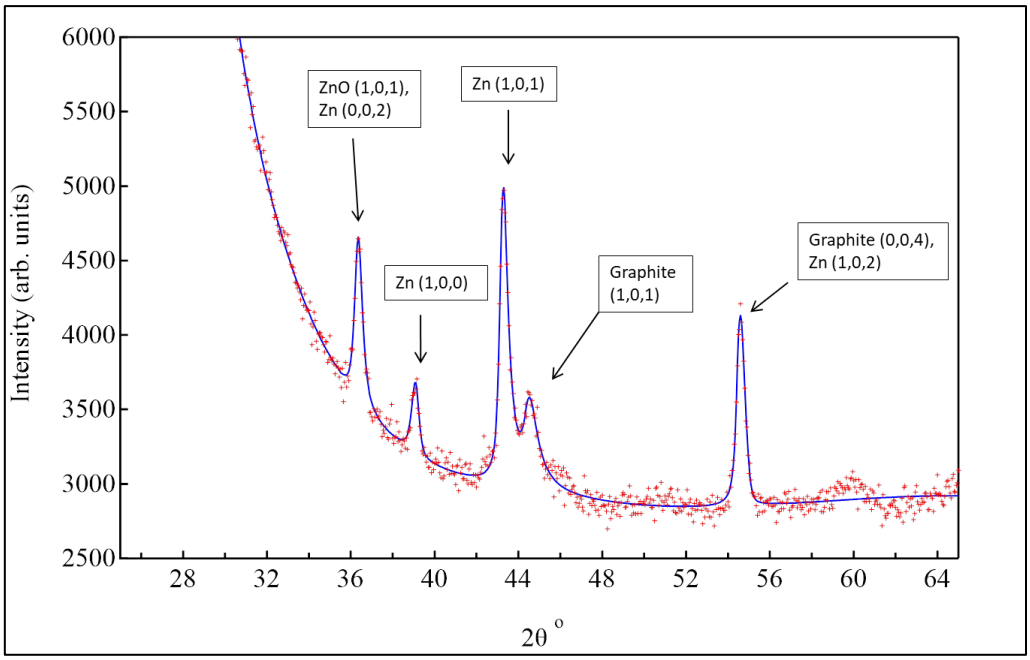

Figure 4.7: XRD analysis of a ZnO/HOPG sample showing the phases of zinc metal present in the sample.

This could explain the lack of ZnO formation observed during deposition of substrates with higher temperatures where Zn would not adhere to the HOPG substrate above 420 ^{o}C.

It was found that the deposition of zinc with a substrate temperature of 60 ^{o}C resulted in the formation of large amounts of ZnO material and the amount of ZnO deposited decreases with increasing substrate temperature (Table 4.1). The Zn metal and ZnO species appear to be more mobile compared to TiO_2 nanoparticles and crystallize at lower temperatures. While the HOPG substrate needed to be held at temperatures of 770 ^{o}C for rutile TiO_2 formation, the crystalline ZnO nanoparticles formed at lower substrate temperatures. It is possible that the mobility of the ZnO nanoparticles is so great at higher temperatures that the nanoparticles do not bind as well to the HOPG substrate or move off of the substrate and attach to the copper rods that are used for substrate heating. It was determined from this study that a substrate temperature of 60 ^{o}C would work best for the resulting ZnO depositions.

4.3.3 Oxygen plasma on HOPG

Varying the Ar plasma treatment times and the substrate temperature did not have a large effect on the size of the ZnO nanoparticles deposited as expected. Since Ar plasma is inert, pre-treating the HOPG substrate with more reactive plasma, such as oxygen, may result in better binding and nucleation of the deposited Zn material. The use of oxygen plasma on HOPG may result in reactive defect sites that have some residual oxygen located on the surface which may change the size and shape of the ZnO nanoparticles deposited.[33] Before deposition, the HOPG substrate was exposed to the in situ plasma cleaner in the Magellan SEM that uses air plasma. Initially, three substrate temperatures of 25, 60, and 140 ^{o}C were tested in order to confirm that 60 ^{o}C is the optimum substrate temperature. It was found that, after deposition, the 25 ^{o}C

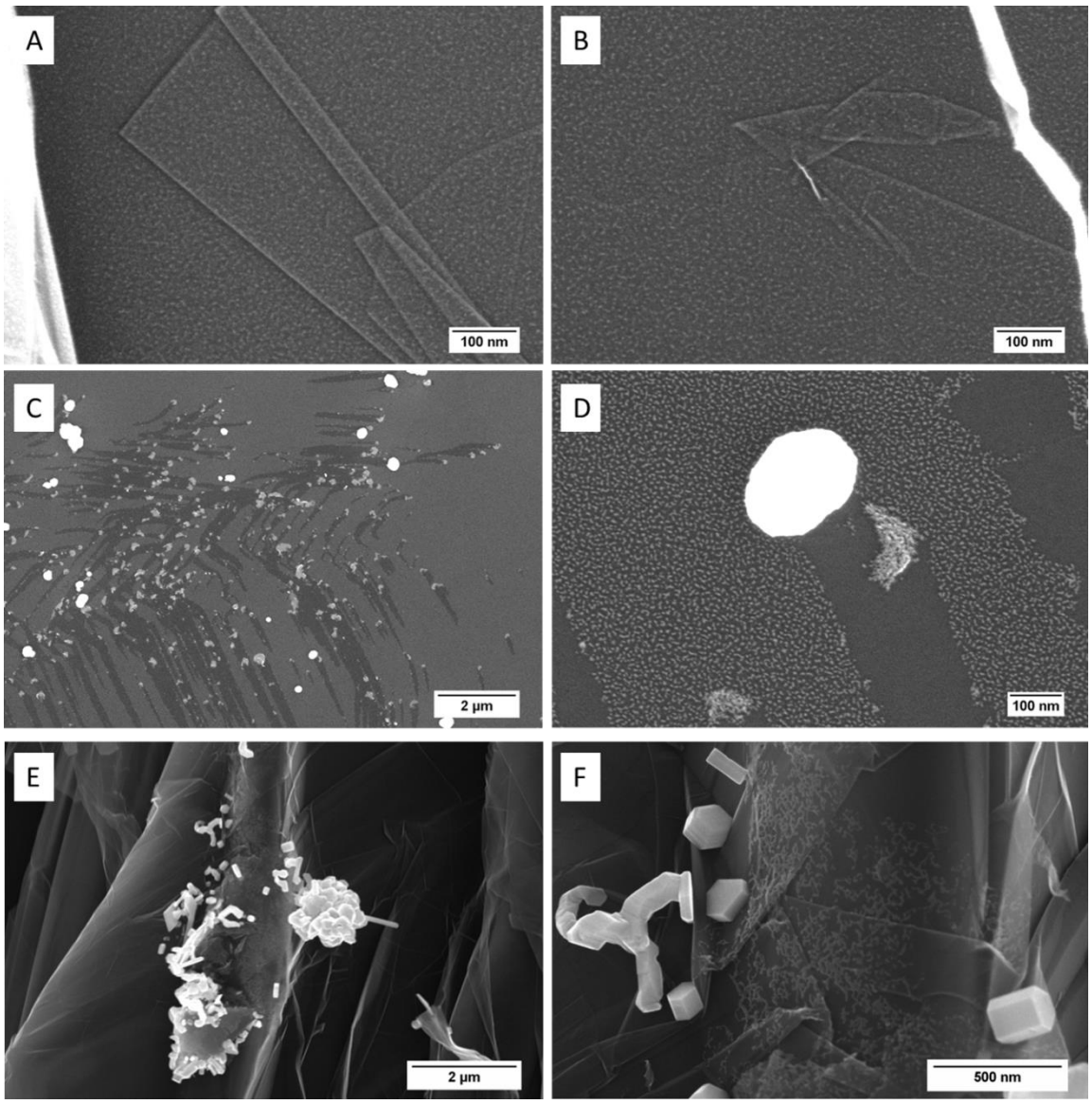

Figure 4.8: SEM images of ZnO nanoparticles on HOPG that was treated with O_2 plasma prior to deposition. ZnO deposition was performed with substrate temperatures of (A, B) 25 ^{o}C, (C, D) 60 ^{o}C, and (E, F) 140 ^{o}C.

substrate had very small ZnO nanoparticles (Figure 4.8 A, B) while the 140 ^{o}C sample did not have any small nanoparticles but rather had groupings of large particles that oriented on defects (Figure 4.8 E, F). This indicates that the ZnO nanoparticles have high mobility and resulted in the formation of small nanorods. The 60 ^{o}C substrate showed the formation of both small and larger nanoparticles but also showed signs of the high nanoparticle mobility. From Figure 4.8C

and D, it is shown that the larger nanoparticles move across the surface and form through the agglomeration of the smaller nanoparticles, as seen by the drag marks devoid of nanoparticles. This further supports the high mobility of the nanoparticles on the surface of HOPG with a substrate temperature of 60 ^{o}C.

The in situ plasma cleaner in the SEM has a fixed power and exposure time so subsequent oxygen plasma studies were carried out on a different plasma cleaner (South Bay Technology) in an oxygen gas atmosphere, as opposed to ambient air. In order to determine the optimum plasma parameters, powers of 20, 50, and 100 W were tested at a pressure of 200 mTorr O_2 for 2 minutes. Since oxygen plasma is more reactive than argon plasma, the time of exposure to the plasma was significantly shorter in comparison. The HOPG substrate was held at 60 ^{o}C during deposition and further annealed for 30 minutes, as previously discussed. The SEM images of these samples shows that, at 50 W, the ZnO nanoparticles were 5-10 nm in diameter and had a high density of nanoparticles across the HOPG surface (Figure 4.9B). The 20 W sample (Figure 4.9C) had small, dendritic like nanoparticles whereas the 100 W sample had better defined nanoparticles that were 3-4 nm in diameter (Figure 4.9A).

The O_2 plasma at 50 W produced slightly larger, 5-10 nm nanoparticles compared to the argon plasma, which resulted in nanoparticles that were ≤5 nm in diameter. The time of exposure to the plasma treatment was then investigated with O_2 plasma at 50 W and 200 mTorr and exposure for 15 seconds, 2 minutes, and 5 minutes. The 15 s plasma treatment resulted in the formation of very small nanoparticles on the HOPG surface whereas the 5 minute exposure produced larger but more dendritic like nanoparticles at the longer exposure time (Figure 4.9D, E). From this, it was determined that pre-treating the HOPG surface with O_2 plasma at 50 W in a

pressure of 200 mTorr for 2 minutes would result in the formation of well-defined ZnO nanoparticles with a high density.

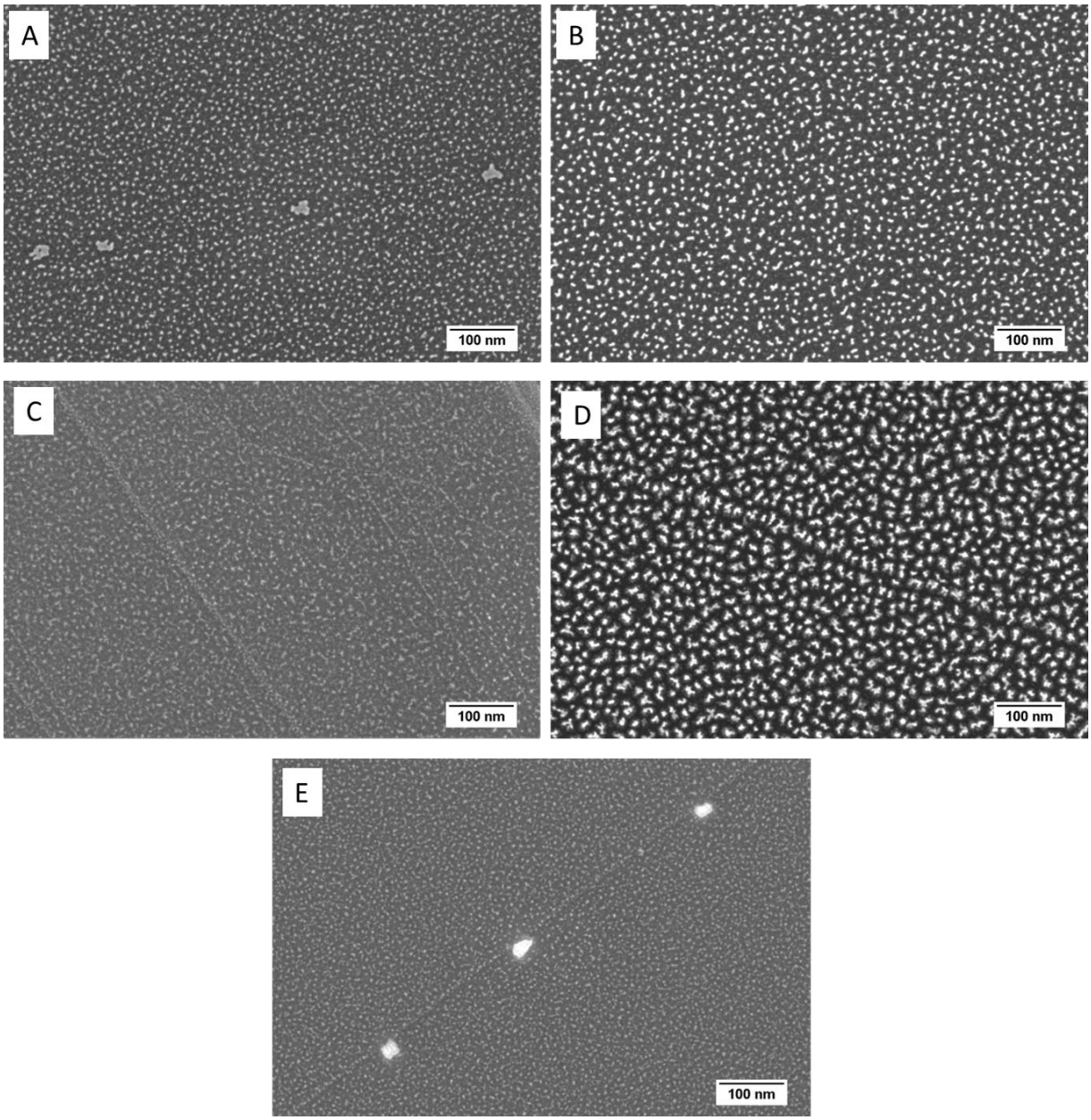

Figure 4.9: SEM images of ZnO nanoparticles deposited on HOPG treated with O_2 plasma with a pressure of 200 mTorr for 2 minutes at (A) 100 W, (B) 50 W, (C) 20 W. SEM images of ZnO nanoparticles deposited on HOPG treated with O_2 plasma at 200 mTorr and 50 W for (D) 5 min and (E) 15 s.

4.3.4 Annealing conditions

Adjusting the substrate temperature during deposition did not lead to a significant change in the ZnO nanoparticle size and shape even with the oxygen plasma treatment. The annealing conditions of the sample were then investigated to determine the effect on the nanoparticle size and shape and in an effort to obtain highly oxidized ZnO nanoparticles. The depositions for each sample were carried out at a substrate temperature of 60 ^{o}C with either no anneal or a 30 minute anneal at substrate temperatures of 60, 70, or 90 ^{o}C (Figure 4.10). The sample with no anneal had nanoparticles that were similar in size to the sample annealed at 60 ^{o}C but the nanoparticles were not as well defined and appeared more dendritic like. The samples that were annealed for 30

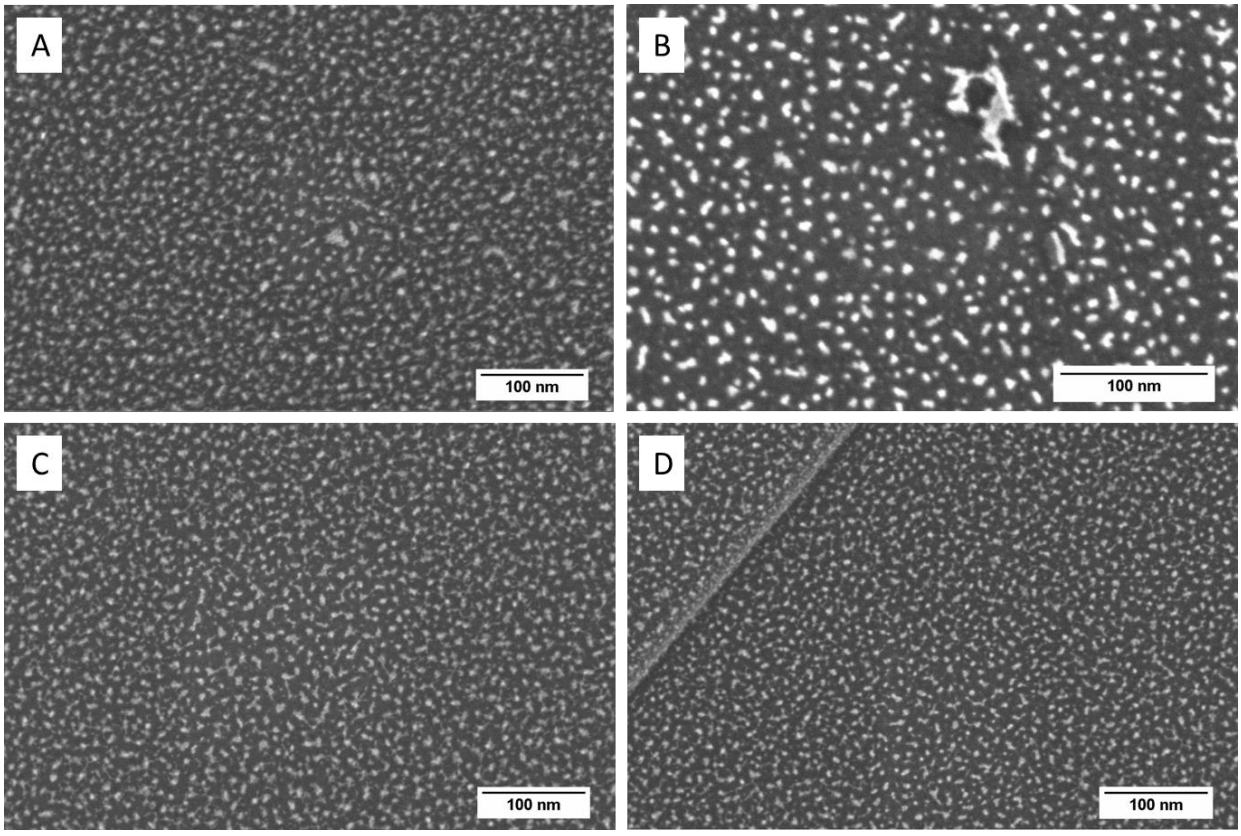

Figure 4.10: ZnO nanoparticles deposited on HOPG with (A) no anneal and 30 minute anneal at (B) 60 ^{o}C, (C) 70 ^{o}C, and (D) 90 ^{o}C.

minutes at 70 and 90 ^{o}C looked similar to the sample annealed at 60 ^{o}C and there were no major differences in the nanoparticle size which shows that the substrate temperature adjustment during anneal did not have a significant effect.

Reports on the synthesis of ZnO nanoparticles typically use an oxygen rich environment for deposition as opposed to the vacuum conditions used here.[23,25] In order to see the effect the atmosphere had on the deposition and annealing conditions, various studies looked at annealing in either air or oxygen. In one instance, the HOPG substrate was not annealed in vacuum after deposition but annealed for 40 minutes at 60 ^{o}C after the chamber had been vented (and reached atmospheric pressure of 760 Torr). Another sample had a 30 minute anneal in vacuum followed by a 40 minute anneal after the PVD chamber had been vented with a substrate temperature of 60 ^{o}C. Both of these instances did not yield any significant visual or chemical changes to the nanoparticles.

An oxygen gas line was then affixed to the PVD chamber in order to add high purity oxygen gas during the deposition or annealing steps. In one instance, the sample substrate was heated to 60 ^{o}C in an oxygen atmosphere with a chamber pressure of 0.18 Torr, as opposed to $2x10^{-6}$ Torr, during the deposition. However, this did not result in any deposition of ZnO material which may be due to the increased pressure in the PVD chamber. The oxygen gas line did not have a precise valve to input the O_2 gas which resulted in a high chamber pressure during deposition. It is possible that Zn metal or ZnO in the vapor phase may not have reached the HOPG substrate due to the inelastic collisions with the oxygen atoms. At this pressure, the inelastic mean free path may have been shorter than the distance between the crucible and sample substrate. Typical deposition methods with an oxygen atmosphere have a steady flow of an inert carrier gas through a tube furnace where the sample distance is close to the crucible. It is

possible that for our PVD process, the substrate may need to be moved closed to the crucible to achieve successful depositions in an oxygen environment.

4.3.5 Deposition on Si wafer

The ZnO nanoparticles on the HOPG substrate did not undergo significant changes despite all of the adjustments during deposition and anneal. Deposition on a silicon (Si) substrate was then investigated in an effort to determine substrate effects on ZnO nanoparticle formation. The silicon wafer was cut using a diamond scribe into 10 x 10 mm pieces and sonicated in separate solutions of acetone and isopropyl alcochol for 10 minutes prior to being placed into the PVD chamber. Both n- and p-type silicon wafers were used although this did not seem to impact the nanoparticle deposition. The Si wafers were heated on a stainless steel heater to 60 ^{o}C during deposition and then further annealed for 30 minutes. The Si wafers were pretreated with either argon or oxygen plasma in order to determine the effect of plasma on the deposition.

The Si substrate was exposed to low energy argon plasma of 9 W with a pressure of 200 mTorr for 25 minutes, as previously discussed. This led to a deposition of large, hexagonal ZnO structures across the Si surface. With HOPG as a substrate, the ZnO material formed small nanoparticles on the surface with large, hexagonal structures deposited irregularly across the surface. With the Si substrate, there is no observed small particle formation and there are large, hexagonal ZnO structures on the surface, as seen in Figure 4.11A and B. However, these particles have a low density on the surface compared to the high density of TiO_2 nanoparticles on HOPG. The ZnO nanoparticles formed range between 120-300 nm in diameter. As can be seen in Figure 4.11A, there are also areas on the Si substrate that resulted in agglomeration of the ZnO

nanoparticles, indicating the high mobility of the nanoparticles on the Si substrate, similar to what was observed on HOPG.

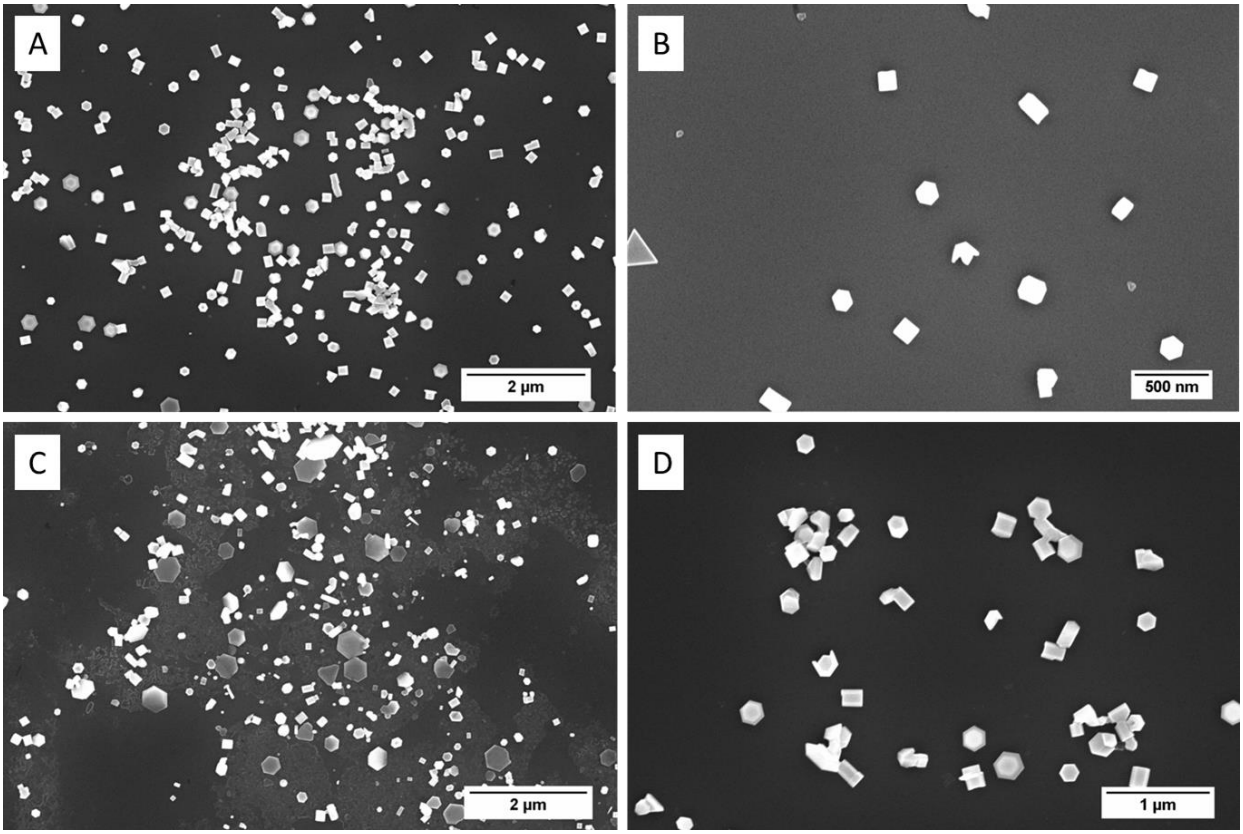

Figure 4.11: SEM images of ZnO nanoparticles on a Si substrate with (A, B) Ar plasma at 200 mTorr and 9 W for 25 minutes and (C, D) O_2 plasma at 200 mTorr and 50 W for 2 minutes.

The oxygen plasma on Si yielded similar results to the argon plasma with no major notable differences (Figure 4.11C, D). The oxygen plasma used was 50 W with a pressure of 200 mTorr for 2 minutes, as was previously discussed. The Si substrates with the oxygen and argon plasma treatment were able to be reproduced multiple times which indicates that these conditions are optimal to produce ZnO nanoparticles with the current PVD setup. However, the ZnO nanoparticles were much larger than desired so methods to control the nanoparticle size and density would need to be developed in the future. XPS analysis confirmed the presence of ZnO with a Zn2p peaks located at 1022.40 and 1045.56 eV corresponding to a ΔBE of ~23 eV which

is characteristic of ZnO.[28] EDS analysis of the hexagonal structures on the Si substrate show the presence of zinc Kα and Lα peaks located at 8.6 and 1.0 keV, as seen in Figure 4.12.

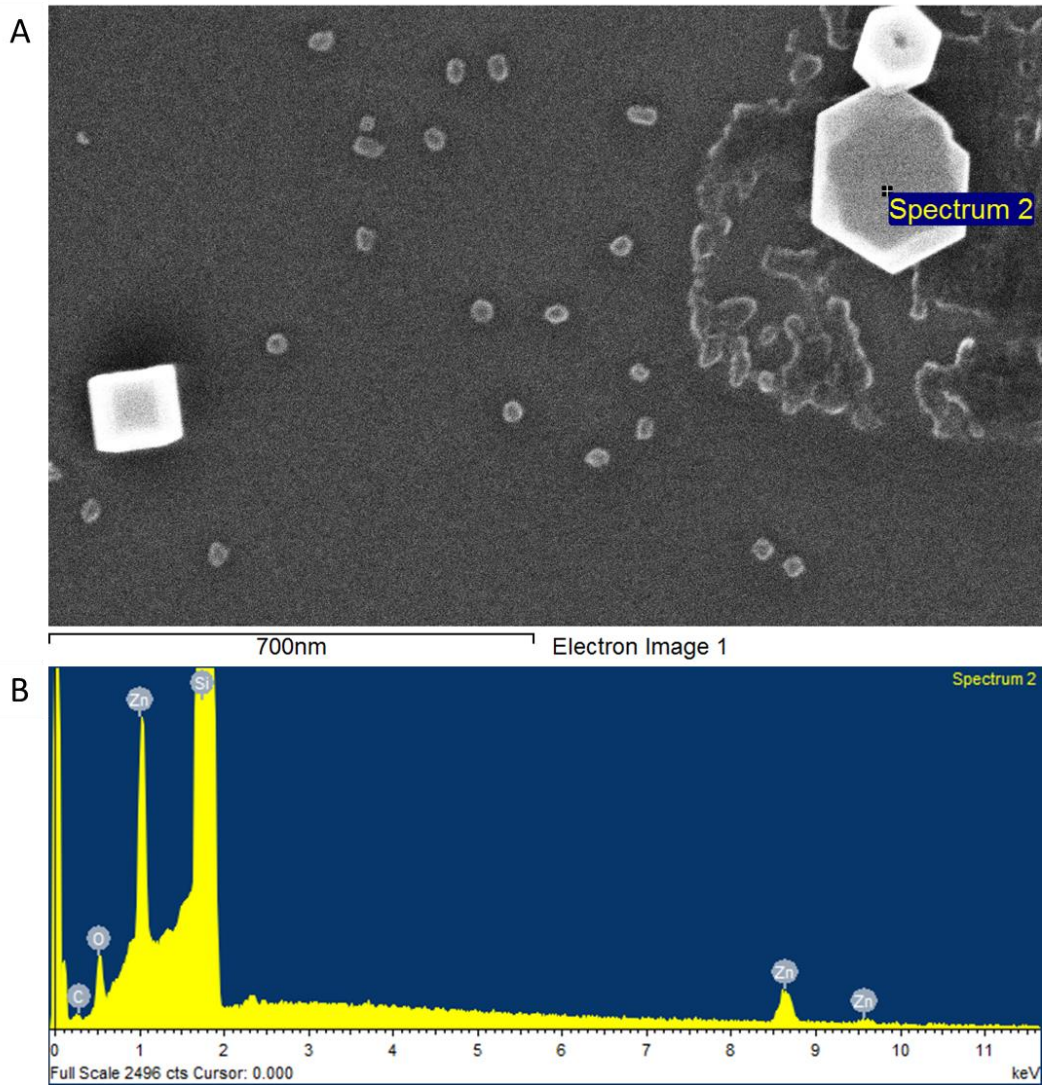

Figure 4.12: (A) SEM image of hexagonal ZnO nanoparticles on a Si substrate with (B) EDS analysis confirming the presence of zinc on the hexagonal structure.

4.3.6 Photodeposition and Stability Studies

As discussed in Chapter 1, photodeposition is used to selectively deposit metal nanoparticles onto metal oxide nanoparticles. This is achieved by submerging the metal oxide nanoparticles in a metal salt solution and irradiating the solution with UV light at a wavelength greater than the band gap of the metal oxide, in this case ZnO. The band gap of ZnO is reported

to be ~3.37 eV, similar to the band gap of TiO_2 of 3.0 eV.[34] The photodeposition of various metals on the ZnO nanoparticles on HOPG was investigated by submerging the ZnO/HOPG samples in an aqueous solution of 1.0 μM K_2PtCl_4 for 4 hours. However, XPS analysis after photodeposition did not reveal any Pt or Zn species present, as seen in Figure 4.13. As can be seen in the Figure, prior to photodeposition, there was a large Zn2p peaks which are not present after photodeposition. The $Pt4f_{7/2}$ peak is located at 74 eV which shows no significant increase after photodeposition (Figure 4.13B).

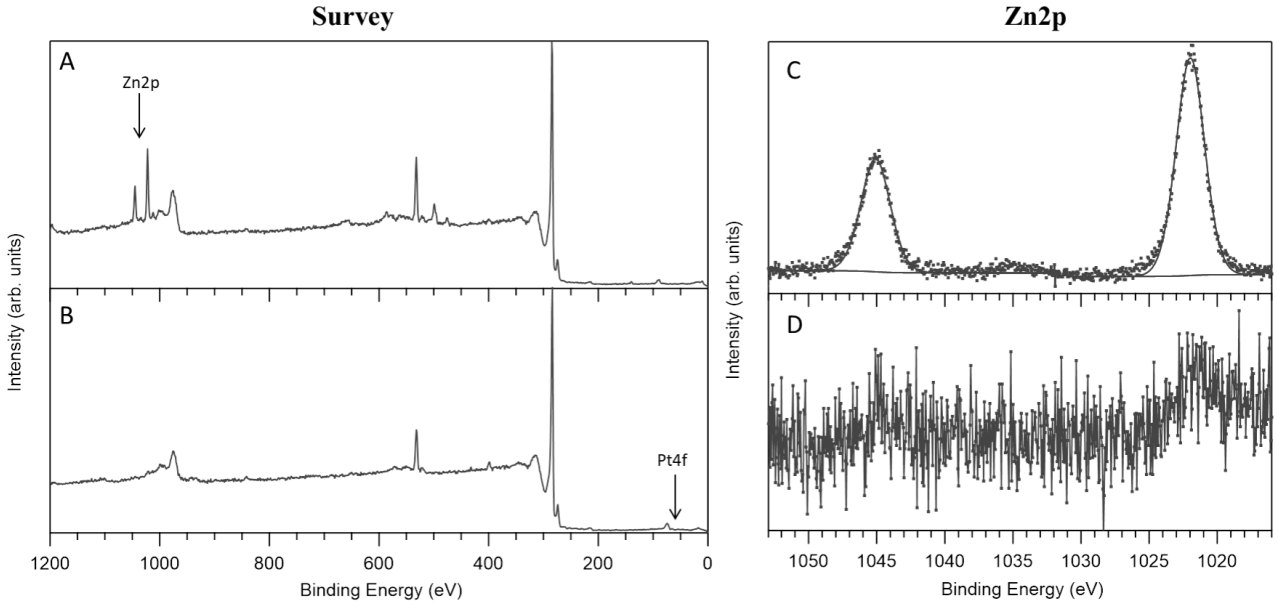

Figure 4.13: Survey and Zn2p XPS spectra of ZnO on HOPG (A, C) before and (B, D) after Pt photodeposition showing the removal of ZnO material.

In order to determine the stability of the hexagonal ZnO structures under UV light, a new ZnO sample was submerged in deionized water and irradiated with UV light for 4 hours. After this allotted time, SEM images showed that the ZnO nanoparticles appeared to be coated with another substance (Figure 4.14B-D). However, point identification with EDS confirmed that only zinc was present, indicating that the ZnO nanoparticles are likely decomposing under these conditions (Figure 4.14E).

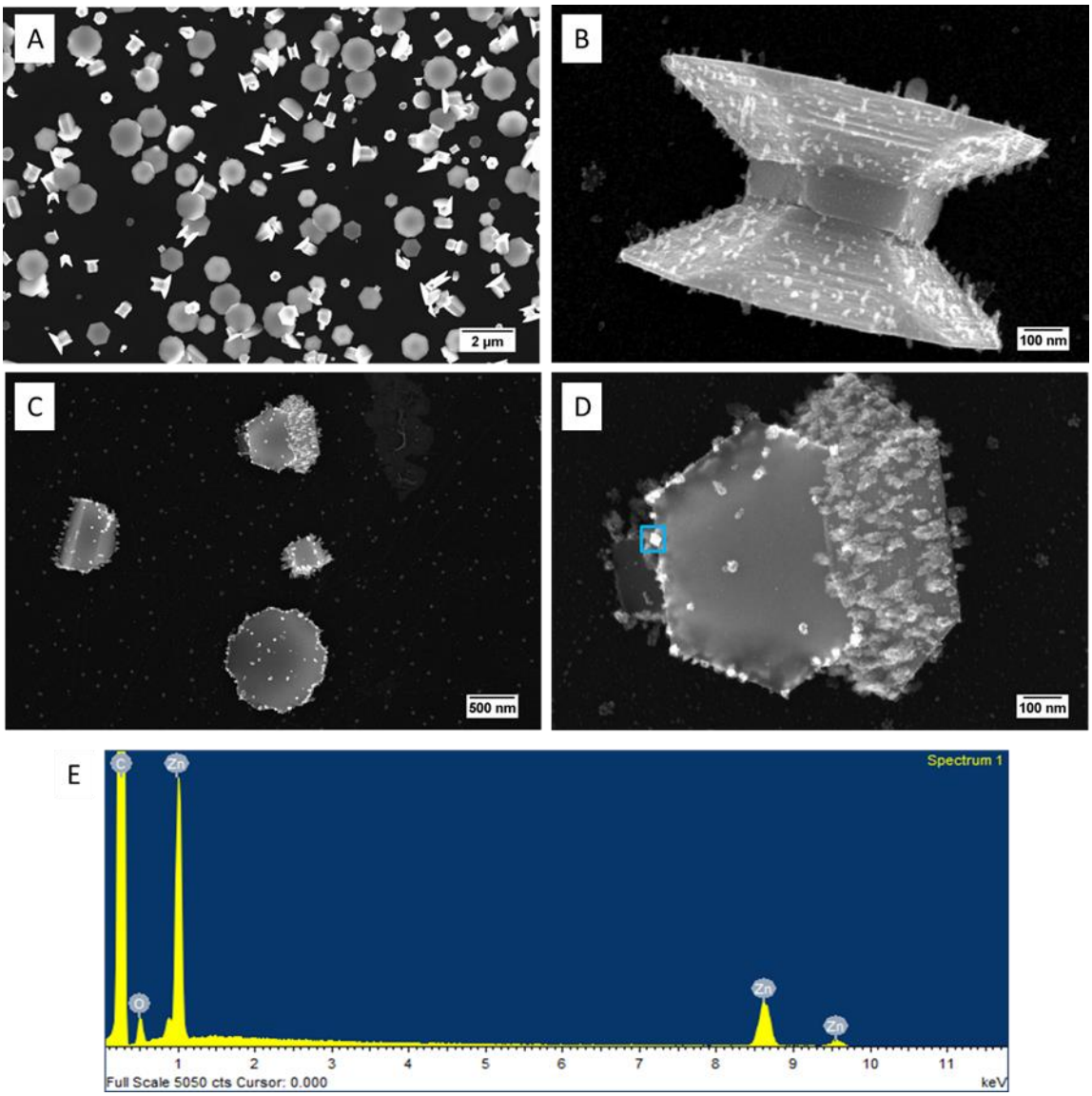

Figure 4.14: SEM images of large ZnO nanostructures (A) initially and (B-D) after photodeposition of 1.0 µM aqueous K_2PtCl_4 solution. (E) Subsequent EDS analysis of the blue box highlighted in (D) shows that the particles on the ZnO hexagonal structure consists of only zinc material indicating the decomposition of this structure.

As the nanoparticles were unstable in aqueous solutions, another photodeposition attempt was carried out by submerging the sample in a 0.14 mM K_2PtCl_4 solution in ethanol and irradiated with UV light for 1 hour. XPS analysis did not show the deposition of a significant amount of Pt species but some of the ZnO species remained on the surface. The Zn2p/C1s ratio before photodeposition was 0.87 and was 0.35 after photodeposition. This decrease may be

attributed to the removal of the larger hexagonal structures as SEM imaging did now show significant changes to the smaller ZnO nanoparticles on the surface. SEM imaging showed that the smaller nanoparticles were stable after photodeposition and EDS confirmed small amounts of Pt deposited (Figure 4.15C) and stability of ZnO species (Figure 4.15D). It is shown that the small nanoparticles on the HOPG surface are stable when ethanol is used as a solvent although a

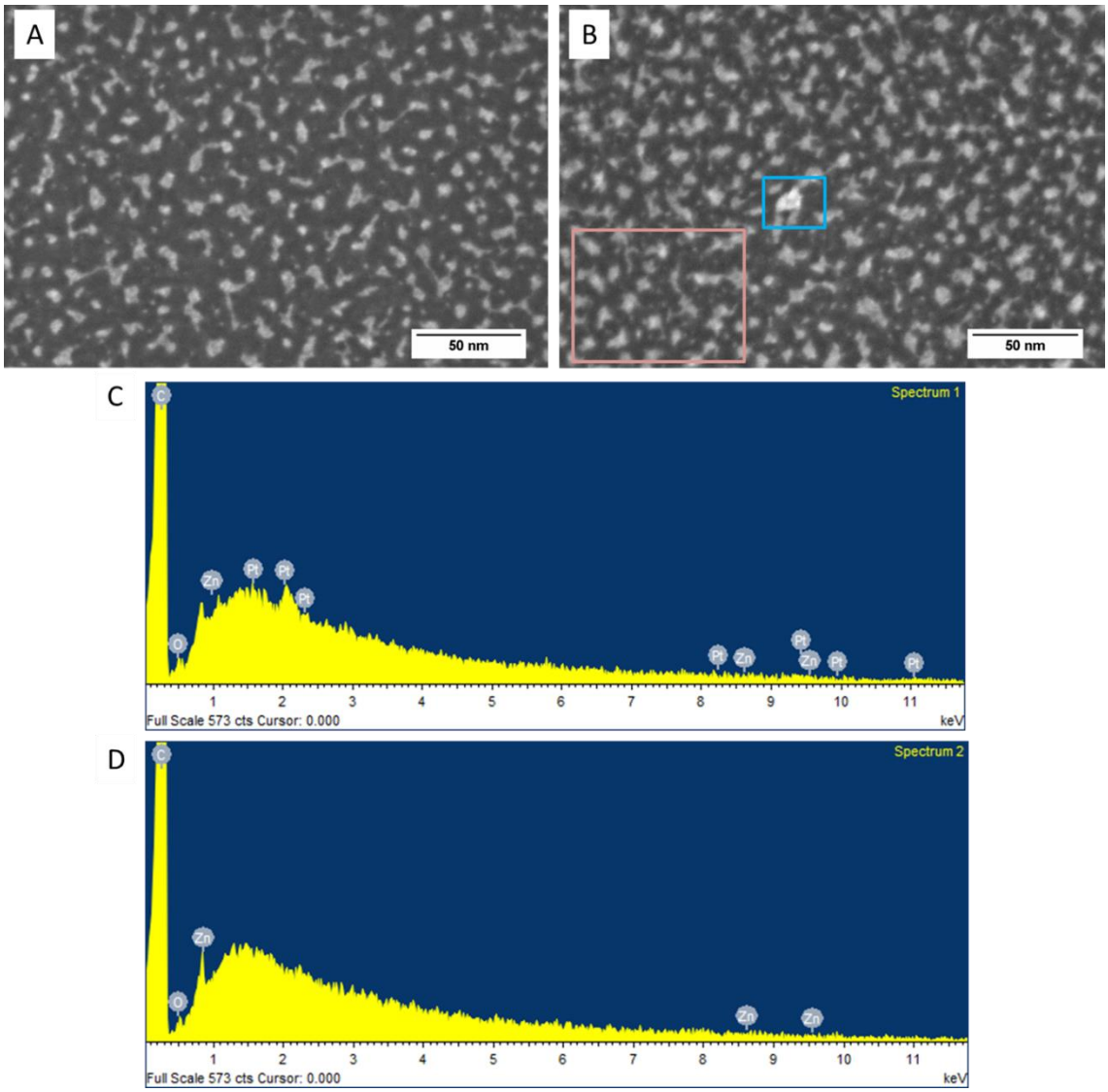

Figure 4.15: SEM images of ZnO nanoparticles on HOPG (A) initially and (B) after photodeposition in 0.14 mM K_2PtCl_4 solution with ethanol as a solvent. (C) Subsequent EDS analysis of the area highlighted in the blue box in (B) that shows the formation of Pt species. (D) EDS analysis of the area highlighted in the pink box in (B) that shows the presence of zinc species and no Pt deposition.

significant amount of Pt species was not deposited. The parameters for photodeposition on these samples would need to be further investigated and may benefit from using a non-aqueous solvent.

Table 4.2: XPS analysis of a sample of ZnO nanoparticles on an HOPG substrate that was heated in a temperature ramp from 60 to 350 ^{o}C. The sample was held at each temperature for 1 hour in order to determine the stability of the samples with increasing temperature.

Anneal Temperature (^{o}C)	**Zn2p$_{3/2}$ area**	**C1s area**	**Ratio Zn2p/C1s**
60	4996.62	6035.49	0.8279
120	4224.44	7342.86	0.5753
215	4793.65	7171.93	0.6684
260	4565.91	7239.65	0.6307
300	3948.85	7757.02	0.5091
350	1757.65	8107.09	0.2168

The larger ZnO nanoparticles were also not stable when annealed at higher temperatures. Some of the ZnO nanoparticle samples were annealed in an oxygen atmosphere or vacuum at high temperatures after deposition in order to observe the effect on the ZnO chemical species and nanoparticle size and shape. While this did not result in significant changes to the small nanoparticles, it was observed that the large, hexagonal ZnO nanostructuress appeared to degrade at higher temperatures. For one of these samples, a temperature ramp was performed where the substrate was heated in a temperature range of 60-350 ^{o}C and held at each temperature for 1 hour. Table 4.2 shows the Zn2p/C1s ratio taken from XPS data which shows a decrease in the amount of zinc with increasing substrate temperatures. SEM images shown in Figure 4.16C shows that the hexagonal ZnO nanoparticles appear to be more transparent and the formation of holes in the nanoparticles is observed. However, there was no obvious change to the smaller nanoparticle size or shape (Figure 4.16B, D). The PVD parameters for ZnO nanoparticles would

need to be modified in order to control the size and shape of the smaller nanoparticles that are observed on the HOPG substrate and hinder the formation of the large, hexagonal ZnO nanoparticles, as these are not stable at higher temperatures or in aqueous solution/UV light.

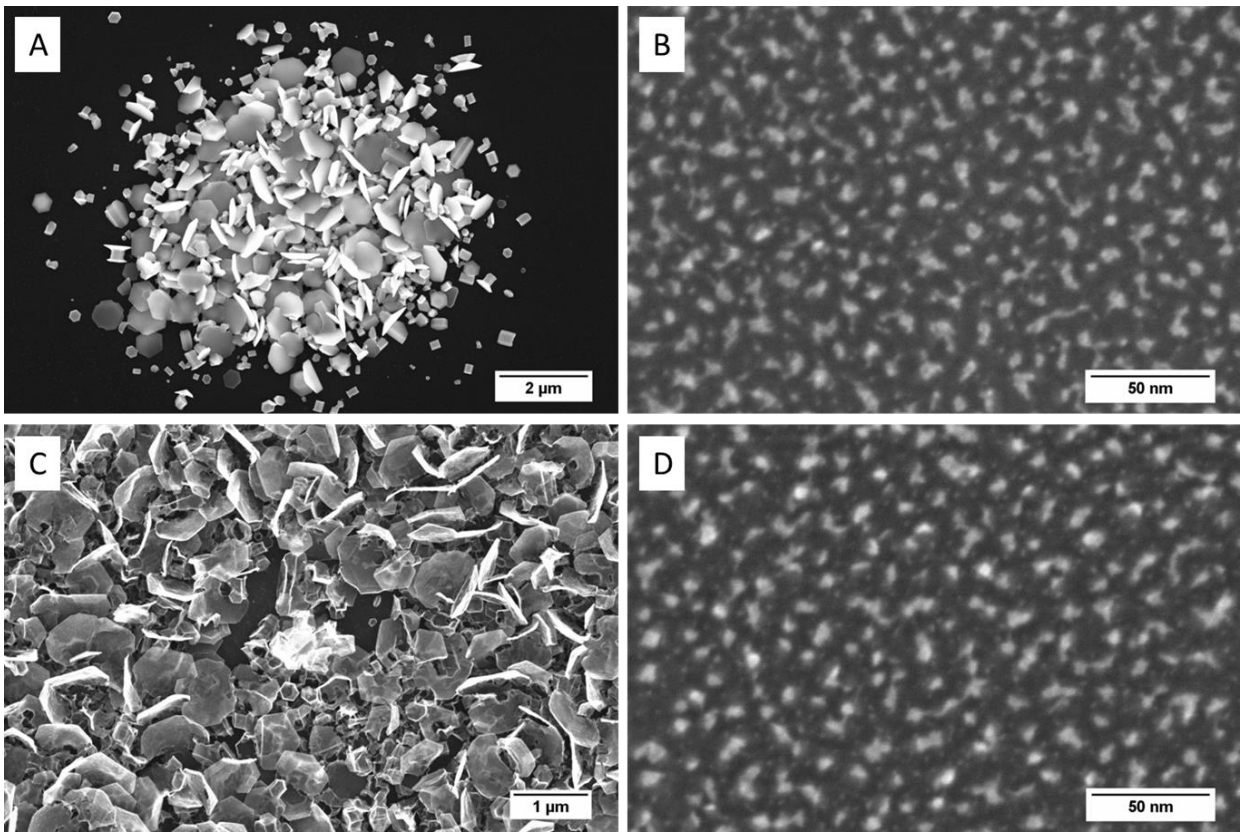

Figure 4.16: SEM images of ZnO nanoparticles (A, B) initially and (C, D) after the temperature ramp and final substrate heating to 350 ^{o}C showing the instability of the hexagonal ZnO nanoparticles.

4.4 Conclusion

The deposition of ZnO nanoparticles on either an HOPG or Si substrate was attempted in this Chapter. Investigations on the substrate temperature during deposition, plasma treatment, annealing conditions, and different substrates were carried out and resulted in the formation of both small nanoparticles and large nanostructures of ZnO. XRD analysis showed that Zn was the predominant species while XPS analysis revealed ZnO was the main species present on the

samples indicating the surface oxidation of these nanoparticles. Photodeposition on ZnO/HOPG samples showed that the large, hexagonal ZnO nanostructures were not stable in aqueous solution or under UV irradiation. However, the smaller nanoparticles formed on HOPG were stable although a significant amount of Pt was not deposited on the nanoparticles. The hexagonal nanostructures were also shown to be unstable at higher temperatures and the degradation of these structures was observed in SEM and XPS. Future synthesis parameters for the ZnO nanoparticles would need to be modified in order to obtain nanoparticles with a more uniform size, shape, and density.

4.5 Future Directions

The oxygen gas line that was equipped to the PVD chamber was not capable of being pumped out, meaning that there was likely air getting into the chamber instead of pure oxygen gas. The gas valve was a needle valve which is not ideal for regulating small amounts of gas. In the future, a stainless steel oxygen gas line that is capable of being pumped out and baked with a more precise leak valve, could be beneficial in the attempts to deposit ZnO nanoparticles in an oxygen atmosphere, aiding in nanoparticle oxidation. The distance between the substrate and the crucible should also be altered as this has shown to result in significant changes in the deposition of TiO_2 nanoparticles and could help to deposit more ZnO nanoparticles or a thin film.

The Si substrate did not show the formation of small nanoparticles on the surface but there were numerous larger ZnO nanostructures that may be useful for future studies. Cleaning the Si substrate with HF and annealing at high temperature would result in a well ordered 7x7 Si surface, which may be useful in controlling the density of the ZnO nanoparticles as opposed to

the plasma treatment on the substrate. Different plasma treatments than the ones studied here could also be investigated in order to determine its effect.

It may be possible to use metal oxide nanoparticles as a base for the ZnO nanoparticle growth. Specifically, perform the ZnO PVD on a sample of TiO_2 nanoparticles on HOPG where the TiO_2 nanoparticles may act as sites for particle nucleation, similar to the defects on the HOPG substrate formed from the plasma treatment. TiO_2 nanoparticles may be useful as seeding particles in order to control the size and density of the ZnO nanoparticles deposited. This could be achieved through deposition of (1) a thin film of TiO_2 using an e-beam evaporator or (2) TiO_2 nanoparticles using PVD as described in Chapter 1. The above suggestions may be helpful in the future synthesis of ZnO nanoparticles.

During photodeposition, it was shown that the large ZnO nanostructures were not stable under UV light or in aqueous solutions. Future attempts may benefit from the use of a non-aqueous solvent in order to selectively deposit metal nanoparticles on the metal oxide nanoparticles. The UV light parameters could also be adjusted by shining the light at a shorter wavelength than was used here in order to be significantly higher in energy than the band gap of ZnO. The wavelength used here was greater than the band gap of ZnO but was close enough that the successful promotion of the electron from the valence to the conduction band may not have occurred.

4.6 References

(1) Porosoff, M. D.; Yan, B.; Chen, J. G. Catalytic Reduction of CO_2 by H_2 for Synthesis of CO, Methanol and Hydrocarbons: Challenges and Opportunities. *Energy Environ. Sci.* **2016**, *9*, 62–73.

(2) Behrens, M.; Studt, F.; Kasatkin, I.; Kühl, S.; Hävecker, M.; Abild-Pedersen, F.; Zander, S.; Girgsdies, F.; Kurr, P.; Kniep, B.-L.; Tovar, M.; Fischer, R. W.; Nørskov, J. K.; Schlögl, R. The Active Site of Methanol Synthesis over $Cu/ZnO/Al_2O_3$ Industrial Catalysts. *Science.* **2012**, *336*, 893–897.

(3) Van Den Berg, R.; Zečević, J.; Sehested, J.; Helveg, S.; De Jongh, P. E.; De Jong, K. P. Impact of the Synthesis Route of Supported Copper Catalysts on the Performance in the Methanol Synthesis Reaction. *Catal. Today* **2016**, *272*, 87–93.

(4) Schumann, J.; Eichelbaum, M.; Lunkenbein, T.; Thomas, N.; Álvarez Galván, M. C.; Schlögl, R.; Behrens, M. Promoting Strong Metal Support Interaction: Doping ZnO for Enhanced Activity of Cu/ZnO:M (M = Al, Ga, Mg) Catalysts. *ACS Catal.* **2015**, *5* (6), 3260–3270.

(5) Huang, C.; Chen, S.; Fei, X.; Liu, D.; Zhang, Y. Catalytic Hydrogenation of CO_2 to Methanol: Study of Synergistic Effect on Adsorption Properties of CO_2 and H_2 in $CuO/ZnO/ZrO_2$ System. *Catalysts* **2015**, *5* (4), 1846–1861.

(6) Graciani, J.; Mudiyanselage, K.; Xu, F.; Baber, A. E.; Evans, J.; Senanayake, S. D.; Stacchiola, D. J.; Liu, P.; Hrbek, J.; Sanz, J. F.; Rodriguez, J. A. Highly Active Copper-Ceria and Copper-Ceria-Titania Catalysts for Methanol Synthesis from CO_2. *Science.* **2014**, *345* (6196), 546–550.

(7) Lunkenbein, T.; Schumann, J.; Behrens, M.; Schlögl, R.; Willinger, M. G. Formation of a ZnO Overlayer in Industrial $Cu/ZnO/Al_2O_3$ Catalysts Induced by Strong Metal-Support Interactions. *Angew. Chemie - Int. Ed.* **2015**, *54* (15), 4544–4548.

(8) Kattel, S.; Ramírez, P. J.; Chen, J. G.; Rodriguez, J. A.; Liu, P. Active Sites for CO_2 Hydrogenation to Methanol on Cu/ZnO Catalysts. *Science.* **2017**, *355*, 1296–1299.

(9) Behrens, M.; Furche, A.; Kasatkin, I.; Trunschke, A.; Busser, W.; Muhler, M.; Kniep, B.; Fischer, R.; Schlögl, R. The Potential of Microstructural Optimization in Metal/Oxide Catalysts: Higher Intrinsic Activity of Copper by Partial Embedding of Copper Nanoparticles. *ChemCatChem* **2010**, *2*, 816–818.

(10) Martin, O.; Mondelli, C.; Cervellino, A.; Ferri, D.; Curulla-Ferré, D.; Pérez-Ramírez, J. Operando Synchrotron X-Ray Powder Diffraction and Modulated- Excitation Infrared Spectroscopy Elucidate the CO_2 Promotion on a Commercial Methanol Synthesis Catalyst Angewandte. *Angew. Chemie - Int. Ed.* **2016**, *55*, 11031–11036.

(11) Kondrat, S. A.; Smith, P. J.; Lu, L.; Bartley, J. K.; Taylor, S. H.; Spencer, M. S.; Kelly, G. J.; Park, C. W.; Kiely, C. J.; Hutchings, G. J. Preparation of a Highly Active Ternary Cu-Zn-Al Oxide Methanol Synthesis Catalyst by Supercritical CO_2 Anti-Solvent Precipitation. *Catal. Today* **2018**, *317*, 12–20.

(12) Kuld, S.; Thorhauge, M.; Falsig, H.; Elkjær, C. F.; Helveg, S.; Chorkendorff, I.; Sehested, J. Quantifying the Promotion of Cu Catalysts by ZnO for Methanol Synthesis. *Science.* **2016**, *352* (6288), 969–974.

(13) Kuld, S.; Conradsen, C.; Moses, P. G.; Chorkendorff, I.; Sehested, J. Quantification of Zinc Atoms in a Surface Alloy on Copper in an Industrial-Type Methanol Synthesis Catalyst. *Angew. Chemie - Int. Ed.* **2014**, *53*, 5941–5945.

(14) Nakamura, J.; Choi, Y.; Fujitani, T. On the Issue of the Active Site and the Role of ZnO in Cu/ZnO Methanol Synthesis Catalysts. *Top. Catal.* **2003**, *22*, 277–285.
(15) Bao, J.; Liu, Z.; Zhang, Y.; Tsubaki, N. Preparation of Mesoporous Cu/ZnO Catalyst and Its Application in Low-Temperature Methanol Synthesis. *Catal. Commun.* **2008**, *9*, 913–918.
(16) Kroll, M.; Löber, T.; Schott, V.; Wöll, C.; Köhler, U. Thermal Behavior of MOCVD-Grown Cu-Clusters on ZnO (1010). *Phys. Chem. Chem. Phys.* **2012**, *14*, 1654–1659.
(17) Kung, H.; Teplyakov, A. V. Formation of Copper Nanoparticles on ZnO Powder by a Surface- Limited Reaction. *J. Phys. Chem. C* **2014**, *118*, 1990–1998.
(18) Fujita, S.; Moribe, S.; Kanamori, Y.; Kakudate, M.; Takezawa, N. Preparation of a Coprecipitated Cu / ZnO Catalyst for the Methanol Synthesis from CO_2 — Effects of the Calcination and Reduction Conditions on the Catalytic Performance. *Appl. Catal. A Gen.* **2001**, *207*, 121–128.
(19) Becker, R.; Parala, H.; Hipler, F.; Tkachenko, O. P.; Klementiev, K. V; Grünert, W.; Wilmer, H.; Hinrichsen, O.; Muhler, M.; Birkner, A.; Wöll, C.; Schäfer, S.; Fischer, R. A. MOCVD-Loading of Mesoporous Siliceous Matrices with Cu/ZnO: Supported Catalysts for Methanol Synthesis. *Angew. Chemie - Int. Ed.* **2004**, *43*, 2839–2842.
(20) Znaidi, L.; Chauveau, T.; Tallaire, A.; Liu, F.; Rahmani, M.; Bockelee, V.; Vrel, D.; Doppelt, P. Textured ZnO Thin Fi Lms by Sol – Gel Process:Synthesis and Characterizations. *Thin Solid Films* **2016**, *617*, 156–160.
(21) Taing, J.; Cheng, M. H.; Hemminger, J. C. Photodeposition of Ag or Pt onto TiO_2 Nanoparticles Decorated on Step Edges of HOPG. *ACS Nano* **2011**, *5* (8), 6325–6333.
(22) Ferrah, D.; Haines, A. R.; Galhenage, R. P.; Bruce, J. P.; Babore, A. D.; Hunt, A.; Waluyo, I.; Hemminger, J. C. Wet Chemical Growth and Thermocatalytic Activity of Cu-Based Nanoparticles Supported on TiO_2 Nanoparticles/HOPG: In Situ Ambient Pressure XPS Study of the CO_2 Hydrogenation Reaction. *ACS Catal.* **2019**, *9*, 6783–6802.
(23) Garcia-Gutierrez, R.; Barboza-Flores, M.; Berman-Mendoza, D.; Rangel-Segura, R.; Contreras-Lopez, O. E. Luminescence and Structure of ZnO Grown by Physical Vapor Deposition. *Adv. Mater. Sci. Eng.* **2012**, *2012*.
(24) Yan, Y.; Zhang, Y.; Meng, G.; Zhang, L. Synthesis of ZnO Nanocrystals with Novel Hierarchical Structures via Atmosphere Pressure Physical Vapor Deposition Method. *J. Cryst. Growth* **2006**, *294* (2), 184–190.
(25) Wang, L.; Zhang, X.; Zhao, S.; Zhou, G.; Zhou, Y.; Qi, J. Synthesis of Well-Aligned Nanowires by Simple Physical Vapor Deposition on - Oriented Thin Films without Catalysts or Additives Synthesis of Well-Aligned ZnO Nanowires by Simple Physical Vapor Deposition on c-Oriented ZnO Thin Films without Catalysts or A. *Appl. Phys. Lett.* **2005**, *86*, 86–87.
(26) Kushwaha, A.; Aslam, M. Hydrogen-Incorporated ZnO Nanowire Films : Stable and High Electrical Conductivity. *J. Phys. D. Appl. Phys.* **2013**, *46*, 1–8.
(27) Djurisic, A. B.; Leung, Y. H. Optical Properties of ZnO Nanostructures. *Small* **2006**, *2*, 944–961.
(28) Al-Gaashani, R.; Radiman, S.; Daud, A. R.; Tabet, N.; Al-Douri, Y. XPS and Optical Studies of Different Morphologies of ZnO Nanostructures Prepared by Microwave Methods. *Ceram. Int.* **2013**, *39* (3), 2283–2292.
(29) Voss, T.; Svacha, G. T.; Mazur, E.; Muller, S.; Ronning, C.; Konjhodzic, D.; Marlow, F. High-Order Waveguide Modes in ZnO Nanowires. *Nano Lett.* **2007**, *7*, 3675–3680.

(30) Campos, A. C.; Paes, S. C.; Correa, B. S.; Cabrera-pasca, G. A.; Costa, M. S.; Costa, C. S.; Otubo, L.; Carbonari, A. W. Growth of Long ZnO Nanowires with High Density on the ZnO Surface for Gas Sensors. *ACS Appl. Nano Mater.* **2020**, *3*, 175–185.
(31) Yang, P.; Yan, H.; Mao, S.; Russo, R.; Johnson, J.; Saykally, R.; Morris, N.; Pham, J.; He, R.; Choi, H. Controlled Growth of ZnO Nanowires and Their Optical Properties. *Adv. Funtional Mater.* **2002**, *12*, 323–331.
(32) Abd Aziz, S. N. Q. A.; Pung, S.-Y.; Ramli, N. N.; Lockman, Z. Growth of ZnO Nanorods on Stainless Steel Wire Using Chemical Vapour Deposition and Their Photocatalytic Activity. *Sci. World J.* **2014**, *2014*, 252851.
(33) Levesque, T.; Leckenby, J. Application of Plasma Cleaning Technology in Microscopy. XEI Scientific, Inc.
(34) Özgür, Ü.; Alivov, Y. I.; Liu, C.; Teke, A.; Reshchikov, M. A.; Do, S.; Avrutin, V. A Comprehensive Review of ZnO Materials and Devices. *J. Appl. Phys.* **2005**, *98*.

Chapter 5

Depth and pH Dependent Changes in the Solvation of Various Solutes in Aqueous Solution at the Liquid/Vapor Interface Probed by Liquid-Jet X-ray Photoelectron Spectroscopy

5.1 Introduction

Solvation effects in aqueous solutions can have a significant effect on the chemical reactivity, particularly for hydrogen bonding solutes. Recent experimental developments have enabled the analysis of the electronic structure of aqueous solutions through the use of liquid-jet X-ray photoelectron spectroscopy (LJ-XPS).[1–6] Liquid-jet XPS is used to probe the local chemical environment, electronic structure and local hydrogen bonding structure of solutes in solution by analyzing core-level chemical shifts and changes in peak profiles due to intermolecular interactions with surrounding water molecules.[3,7,8] In particular, the shifts in the core-level binding energies can be related to changes in the solvent configuration which can vary between the liquid/vapor interface and the bulk of the solution.[9,10]

Detailed information on the electronic properties of liquids can provide an important benchmark for molecular dynamics (MD) simulations. Computational modeling of liquid solutions has a high computational complexity and often requires hundreds of atoms in order to account for the dynamic structure of the liquid environment.[11] The combination of MD simulations, electronic structure calculations (e.g. *ab initio* MD) and experimental liquid-jet XPS data, can be used to understand, in detail, the solute/solvent interactions that lead to measured changes in the solute electronic structure.[8,12–14] This detailed information can provide insight into many chemical processes, as has been demonstrated in the case of the reactivity of atmospheric aerosols and hydrogen bonding at the molecular level.[9,15–17]

Acetic acid, sodium acetate, and acetamide are C_2 solutes that have two distinct carbon bonding environments which lead to distinct C1s binding energies. Glycinamide and 4-aminopyridine are organic solutes that have distinct carbon and nitrogen bonding environments, leading to well separated N1s and C1s peaks. The change in the difference in binding energy (ΔBE) for these carbon and nitrogen environments is related to the distribution of electrons in the molecule and can be related to the interactions with the water solvent. For example, by studying the ΔBE between the carboxyl and methyl carbons from the interface to the bulk of the solution, information about changes to the solvation and electronic structure of these solutes as a function of depth into the solution can be elucidated. The pH dependence of these organic solutes was also investigated to observe changes in the solvation interactions for the protonated and deprotonated solutions.

In this Chapter, various concentrations of these solutes in aqueous solutions are investigated using liquid-jet XPS in order to study the solvation induced changes in the electronic structure of these solutes from the surface to the bulk and as a function of pH using synchrotron radiation. These investigations will give insight into solvent effects for molecular solutes that reside at or near the liquid/vapor interface of the solution. The studies here provide experimental data that, coupled with MD and electronic structure calculations, can provide information of the hydrogen bonding of water molecules to these solutes.

5.2 Experimental

Photoemission measurements were performed from a 25 μm diameter liquid vacuum jet on the SOL^{3}PES experimental setup[7] at the soft X-ray U49-2-PGM-1 beamline at the BESSY II synchrotron facility in Berlin, Germany. The flow rate of the jet was 0.6 mL/min with a jet

temperature of 15 ^{o}C. Under operating conditions, the pressure in the analysis chamber was ~2x10^{-4} mbar. The high resolution C1s, N1s and O1s spectra were recorded at 50 eV pass energy and 25 meV step size. The exit slit size was varied with each change in photon energy to maintain a beamline resolution of ~300 meV. This allows for the observation of small binding energy shifts as the FWHM and shape of the C1s peaks at different photon energies did not vary greatly. For one of the 1.0 M aqueous acetic acid solutions (denoted as 'run 2'), the exit slit was kept at 80 μm for the recorded spectra so the energy resolution of the beamline fluctuated with increasing photon energy which resulted in a fluctuation of the FWHM values. However, this fluctuation did not seem significant as the ΔBE values for the solution measured here were similar to the 1.0 M acetic acid solution with the beamline resolution kept at 300 meV.

The photon energies used were varied for each subshell to obtain information at photoelectron kinetic energies (KE) ranging from 140-700 eV.[9,15–17] Investigating the range of kinetic energies gives depth profile information of the solution going from the surface (140 eV) to the bulk (700 eV). For most of the C1s spectra reported here, photon energies of 430, 610, and 820 eV (photoelectron kinetic energies of 140, 320, and 530 eV) were studied. The N1s spectra were recorded at photon energies of 550, 725, and 100 eV (photoelectron kinetic energies of 145, 320, and 595 eV). All spectra were calibrated to the O1s peak of liquid water at 538.0 eV. Details on the electronic structure of the solute were obtained through analysis of the difference in the change in binding energy (ΔBE) values for the C1s and N1s spectra. By using the experimental difference in binding energy value as a measure of the impact of the solvent interactions on the solute electronic structure, we avoid the need to determine the absolute binding energy at high accuracy as that may be impacted by small amounts of charging of the liquid.

The aqueous solutions were prepared from sodium acetate, acetic acid, acetamide, 4-aminopyridine (Sigma Aldrich), and glycinamide hydrochloride (Alfa Aesar) diluted in deionized water. Various solution concentrations were prepared and the pH adjustments were made with either sodium hydroxide (NaOH) or hydrochloric acid (HCl). The pH measurements were done using a calibrated pH meter (Greisinger GPH 114, calibrated with buffers of pH 4.0, 7.0 and 10.0 accordingly) equipped with a GE 114 electrode.

5.3 Results and Discussion

The following studies were carried out by tuning the X-ray wavelength (photon energy) in order to obtain depth profile information for these solutions. Increasing the excitation photon energy (hν or PE) results in an increase of the kinetic energy (KE) of the emitted photoelectrons.[2] This is related through the equation: KE = hν – BE, where BE corresponds to the binding energy of the orbital. For instance, XPS measurements of the C1s orbital taken at a photon energy of 430 eV results in the emission of C1s photoelectrons with kinetic energies of 140 eV. The probe depth of the experiment is related to the inelastic mean free path (IMFP) of the ejected electrons as they leave the sample. Figure 5.1A illustrates that at lower kinetic energies, the inelastic mean free path (IMFP) is shorter meaning that only electrons that are closer to the interface could escape into vacuum whereas at higher kinetic energies, electrons from the bulk of the solution are able to be analyzed.[2]

Olivieri et al. performed studies using the NIST database for the Simulation of Electron Spectra for Surface Analysis (SESSA) in order to determine quantitative estimates on the XPS experimental probe depth as a function of photoelectron KE for various solutions. The information depth (ID) of XPS measurements is directly related to the IMFP by the following

equation: $ID = \lambda \cos\alpha \ (1 - 0.787\omega) \ln\left[\frac{1}{1-\left(\frac{P}{100}\right)}\right]$, where λ is the IMFP, α is the photoelectron emission angle with respect to surface normal, P is a percentage of the detected signal and ω is the measure of the strength of elastic-scattering effects on photoelectron trajectories.[18] Through their calculations, it was found that at kinetic energies of 65 eV, the information depth of the XPS measurements is ~1.50 nm whereas at kinetic energies of 800 eV, the information depth is ~7.90 nm for a solution of pure water (Figure 5.1B).[19] From this study, it is shown that by changing the X-ray wavelength (photon energy), XPS information of the solution at the interface and bulk can be obtained. In the experiments described here, XPS spectra were obtained for various solutions with in the kinetic energy range of 140 to 700 eV, with IDs that are roughly 2.4 and 6.8 nm[19], respectively, in order to obtain depth profile information on the electronic structure changes in solution.

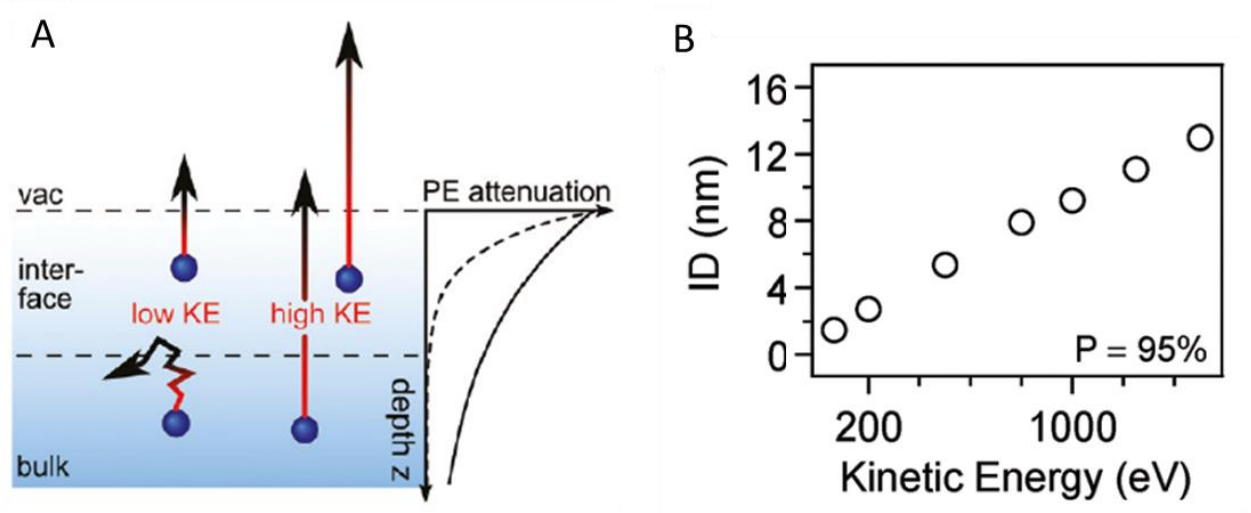

Figure 5.1: (A) Depiction of escape of electrons from the solution at both low and high kinetic energies illustrating the elastic and inelastic scattering effects. Reprinted with permission from Reference 2. Copyright 2011 American Chemical Society. (B) Information depth with kinetic energy for 95% of the detected XPS signal. Reprinted with permission from Reference 19. Copyright 2017 Royal Society of Chemistry.

5.3.1 Acetic acid

Figure 5.2 shows the C1s spectra of 3.0 M aqueous acetic acid and gas phase acetic acid taken at a photon energy of 430 eV (KE = 140 eV) which corresponds to the surface of the solution. For the gas phase spectrum, the liquid jet is retracted away from the synchrotron beam so only the surrounding gas phase is ionized. The gas phase peak is easily distinguishable in the aqueous spectrum at 430 eV but the gas phase shoulder becomes less pronounced when probing

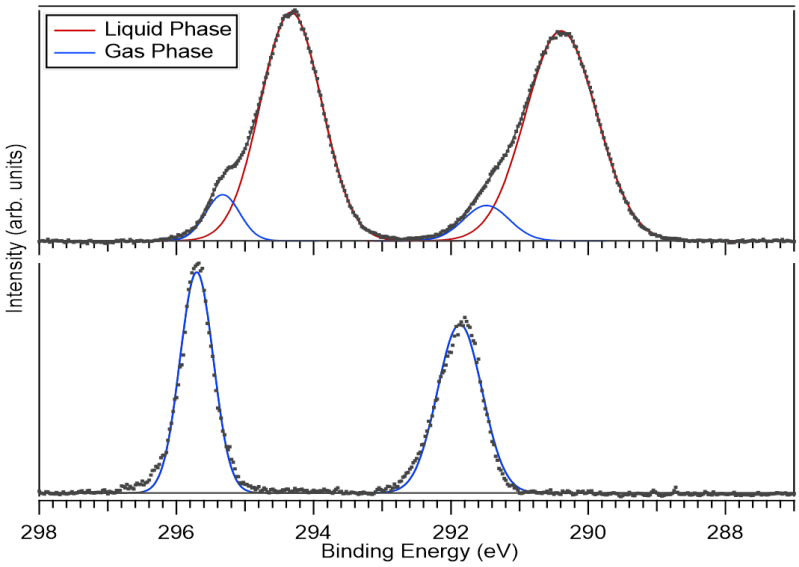

Figure 5.2: C1s photoelectron spectra of 3.0 M aqueous acetic acid and corresponding gas phase.

deeper into the solution, at photon energy of 820 eV (KE = 530 eV). The binding energies and ΔBE values for the acetic acid solutions are recorded in Table 5.1. In the gas phase spectrum, the methyl and carboxyl peaks are located at 291.869 and 295.705 eV, respectively, for the 3.0 M aqueous acetic acid solution. The C1s liquid peaks at 290.394 and 294.329 eV correspond to the methyl and carboxyl carbons, respectively. The separation between the methyl and carboxyl C1s liquid peaks (ΔBE) at 430 eV, was 3.935 and 3.896 eV for the 3.0 and 1.0 M acetic acid solutions, respectively which is consistent with the separation of 3.88 eV seen by Ottosson et al.

for 1.0 M aqueous acetic acid.[20] The gas phase peaks that are seen in the liquid acetic acid spectrum are slightly shifted to ~291.483 and ~295.327 eV for the methyl and carboxyl peaks.

Table 5.1: Binding energy and ΔBE values for the liquid and gas phase C1s peaks of various acetic acid solutions over a range of photon energies.

		Liquid			Gas		
Solution	**Photon energy (eV)**	**BE carboxyl (eV)**	**BE methyl (eV)**	**ΔBE**	**BE carboxyl (eV)**	**BE methyl (eV)**	**ΔBE**
3.0 M	430	294.329	290.394	3.935	295.327	291.483	3.844
	610	294.359	290.385	3.974	295.459	291.633	3.826
	820	294.148	290.144	4.004	295.214	291.306	3.908
	gas phase				295.705	291.869	3.836
1.0 M run 1	430	294.395	290.499	3.896	295.319	291.519	3.800
	610	294.720	290.794	3.926	295.619	291.972	3.647
	820	294.542	290.610	3.932	295.501	291.715	3.786
	gas phase				295.555	291.725	3.830
1.0 M run 2	430	294.359	290.469	3.890	295.244	291.493	3.751
	570	294.432	290.521	3.911	295.346	291.612	3.734
	700	294.425	290.491	3.934	295.479	291.582	3.897
	840	294.114	290.178	3.936	295.078	291.392	3.686
	990	294.275	290.311	3.964	295.318	291.547	3.771

The ΔBE values for the liquid phase, gas phase (aq) and gas phase peaks for the 1.0 and 3.0 M solutions are plotted as a function of photon energy in Figure 5.3. The aqueous gas phase spectra for the 3.0 M solution varies with the change in photon energy. This is likely a result of the fit of the aqueous gas phase peaks as it is more difficult to discern these peaks in the liquid spectrum at higher photon energies. It is not expected that the gas phase spectra would exhibit a ΔBE as a function of increasing photon energy. As seen in Figure 5.3, at a photon energy of 430 eV, the ΔBE value for the 3.0 M aqueous gas phase peaks aligns with the gas phase spectra for both the 1.0 and 3.0 M solutions, which is expected.

Figure 5.3 also shows that the ΔBE for the 3.0 M liquid phase peaks follows a linear trend and the ΔBE values are increasing by ~35 meV with increasing photon energy. The increase in ΔBE values for the 3.0 M aqueous solution from the surface to the bulk implies that

the electronic structure changes as a function of depth of the solution. However, the 1.0 M liquid phase peaks have a ΔBE value of 30 meV initially and increases by 6 meV going further into the bulk of the solution. The magnitude of the ΔBE difference going further into the bulk of the solution for the 1.0 M aqueous acetic acid solution varies between two different runs. LJ-XPS measurements of a different 1.0 M aqueous acetic acid solution exhibited a linear increase in the ΔBE going from the surface to the bulk of the solution with a larger magnitude.

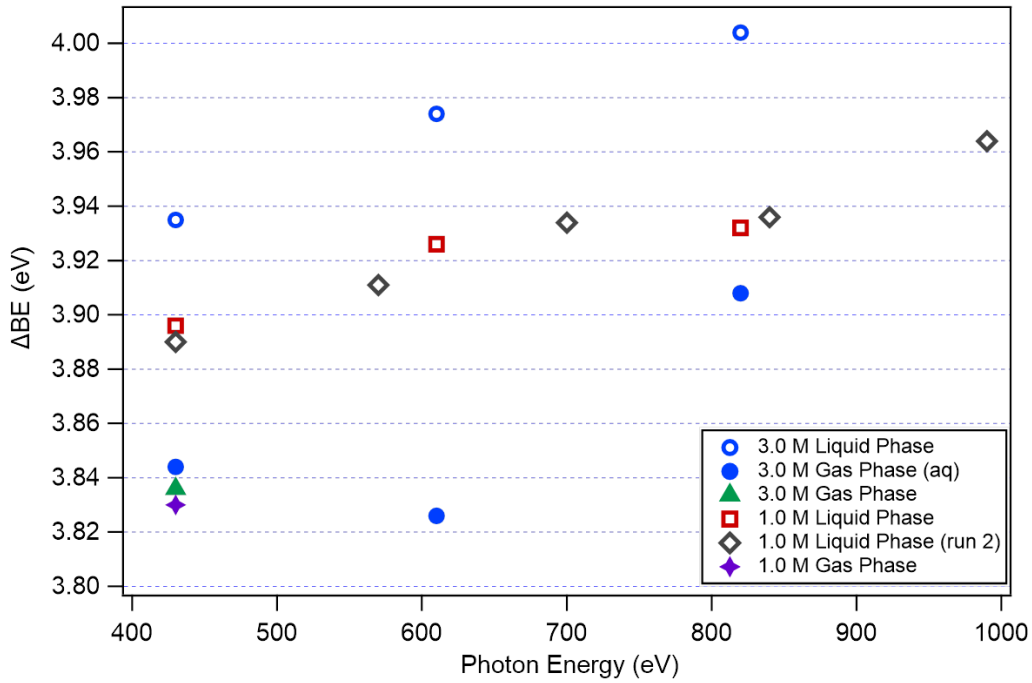

Figure 5.3: Recorded C1s change in binding energy (ΔBE) values shown as a function of photon energy for the various acetic acid solutions.

The '1.0 M Liquid Phase run 2' trace in Figure 5.3 shows a linear increase of the ΔBE values with increasing photon energy and the binding energy and ΔBE values for this solution are recorded in Table 5.1. Specifically, this solution shows an increase of 25 meV going from a photon energy of 570 eV to a photon energy of 840 eV, compared to the 6 meV increase seen at similar photon energies for a different 1.0 M aqueous acetic acid solution. This difference in magnitude may be attributed to the slight fluctuations of the liquid jet that would lead to a shift in

the binding energy spectrum or could be a result of the dynamic nature of the solvation of the acetic acid molecule. As will be discussed later, it is shown that the 1.0 M acetic acid solution acts more 'bulk-like' at kinetic energies of 280 eV (or photon energy of 570 eV) or higher.

The change in magnitude of the ΔBE values may be a result of the different solvation configurations that are occurring and averaged over the time of measurement. The magnitude difference of the increase in the ΔBE is unclear but the increase in the ΔBE values as we probe deeper into the solution is important to note as this is representative of a change in the solvation configuration that occurs from the surface to the bulk of the solution. It is interesting to note that the ΔBE values at photon energies of 430, 610 and 820 eV of the 3.0 M solution are larger compared to those of the 1.0 M solution (Table 5.1). This indicates a concentration dependence of the electronic structure changes which would need to be investigated further with theoretical calculations.

In order to obtain depth profile information of a 1.0 M aqueous acetic acid solution, C1s and O1s spectra were recorded at the same kinetic energies. The C/O ratio was obtained by fitting the C1s and O1s XPS spectra at different photoelectron kinetic energies (140-700 eV) and was corrected for the energy-dependent electron analyzer sensitivity, photon flux, and the photoionization cross section.[21] The C/O ratio was calculated using the following equation: $\frac{C}{O} = \frac{\frac{C1s\ area}{C1s\ flux * C1s\ cross\ section}}{\frac{O1s\ area}{O1s\ flux * O1s\ cross\ section}}$ where the $flux = \frac{mirror\ current\ (nA) * exit\ slit\ (\mu m)}{10}$ and the photoionization cross section values were obtained from literature.[21] The O1s area was calculated from the O1s peak of water.

Figure 5.4 shows the measured C/O ratios as a function of kinetic energy for a 1.0 M acetic acid solution. From these calculations, the C/O ratio at 140 eV photoelectron kinetic energy (KE) is ~2.5 which is due to surface segregation of the acetic acid molecules. The surface

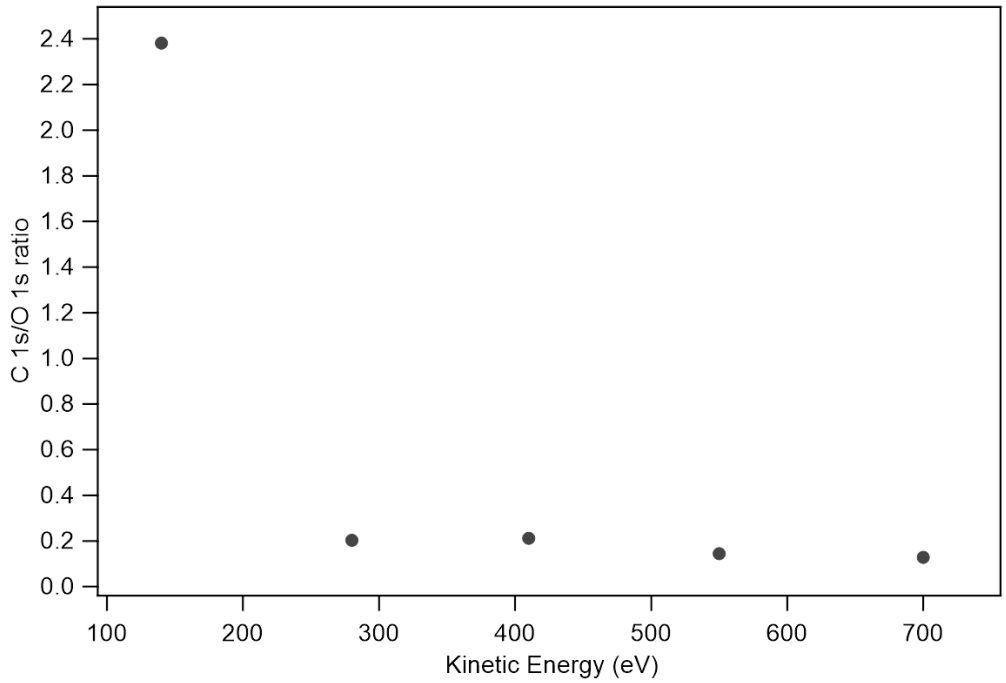

Figure 5.4: Measured C1s and O1s photoemission signals as a function of kinetic energy for 1.0 M aqueous acetic acid.

segregation of acetic acid molecules has been seen in other studies and it has been shown that the degree of protonation of acetic acid at the surface of a liquid solution is near complete.[20] At 280 eV KE, the C/O ratio drops to ~0.20 which is similar to the ratio in the bulk of 0.12, taken at 700 eV KE. This suggests that the acetic acid solution becomes more bulk like at kinetic energies of 280 eV and higher. Since the calculated C/O ratio includes both the methyl and carboxyl carbon, the carbon behaves as a 2.0 M solution (two carbon molecules for each acetic acid molecule) and the oxygen would correspond to 55.5 M solution (the concentration of water). This would give an expected bulk ratio of 0.036 which is a factor of about 3.5 lower than the measured C/O ratio of 0.12 in the bulk of the solution. However, this difference may be due to the photoionization cross section values as the data was extrapolated from literature and may not be accurate values for the photon energies used in this study.

From these results, it is shown that the solvation of acetic acid is changing going from the surface to the bulk of the solution. The surface segregation of acetic acid molecules may result in less solvation at the surface whereas the acetic acid molecule would become more hydrated in the bulk of the solution, which would result in the changes in the electronic structure we observe in the ΔBE values. Acetic acid has three locations where hydrogen bonding can occur where water would act as a donor at the carboxyl oxygen and hydroxyl oxygen or an acceptor at the hydroxyl hydrogen. Theoretical calculations have shown that the hydrogen bonding of acetic acid with water molecules is likely to occur through the carboxyl oxygen and hydroxyl hydrogen where water acts as both a donor and acceptor.[22–24] Previous studies by our group on the electronic structure change of acetic acid using liquid jet AP-XPS and theoretical calculations show that the number of solvent molecules needed to reproduce an experimental ΔBE shift of 3.76±0.17 eV is only one water molecule which is hydrogen bonded through the hydroxyl hydrogen. The addition of more water molecules leads to an increase in the ΔBE so it is likely that the acetic acid molecules are becoming more solvated in the bulk of the solution compared to the surface.

5.3.2 Sodium acetate

The binding energy and ΔBE values for the sodium acetate solutions are recorded in Table 5.2. From this Table, it is shown that the C1s spectrum for 2.5 M aqueous sodium acetate solution at photon energy of 430 eV has the methyl and carboxyl carbon peaks located at 290.013 and 293.458 eV, respectively. At 430 eV, the ΔBE between the methyl and carboxyl peaks is about 3.445 eV, consistent with the separation of 3.46 eV in acetate seen by Ottosson et al.[20] Figure 5.5 shows the ΔBE of the 2.5 and 1.0 M solutions and their duplicate runs that were

Table 5.2: Binding energy and ΔBE values for various concentrations of aqueous sodium acetate and their duplicate runs over a range of photon energies.

Solution	Photon energy (eV)	BE carboxyl (eV)	BE methyl (eV)	ΔBE
2.5 M run 1	430	293.458	290.013	3.445
	610	293.623	290.149	3.474
	820	293.575	290.070	3.505
2.5 M run 2	430	293.458	290.016	3.442
	610	293.483	290.008	3.475
	820	293.513	290.031	3.482
1.0 M run 1	430	293.384	289.925	3.459
	610	293.565	290.069	3.496
	820	293.482	289.957	3.525
1.0 M run 2	430	293.529	290.076	3.453
	610	293.528	290.043	3.485
	820	293.602	290.096	3.506

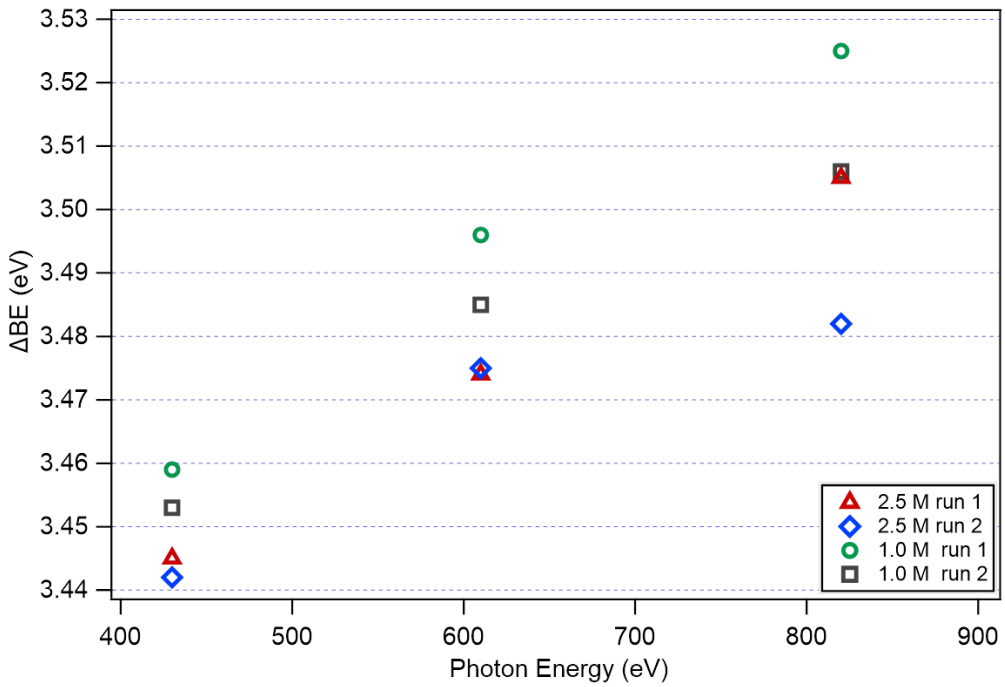

Figure 5.5: Recorded C1s change in binding energy (ΔBE) values shown as a function of photon energy for the various aqueous sodium acetate solutions.

plotted as a function of photon energy. As seen in the Figure and Table, the C1s ΔBE values increases by about 30 meV with increasing photon energy, i.e. when probing further into the bulk of the solution. The 2.5 M sodium acetate solution second run had an initial increase in the ΔBE of 30 meV but did not increase significantly going from 610 to 820 eV.

Similar to the case with acetic acid, this change in magnitude may be a result of fluctuations of the liquid jet or a consequence of the dynamic nature of the solvation since a separate run for 2.5 M sodium acetate showed an increase of 31 meV going from photon energy of 610 eV to 820 eV. While the difference in magnitude would need to be further explored, it is important to note that the ΔBE is increasing going from the surface to the bulk of the solution. This increase in separation is representative of perturbations in the electronic structure of the carbons going from the surface to the bulk of the solution which indicates changes in the solvation configuration at the interface versus the bulk.

Theoretical calculations have suggested that acetate forms around 3 or 4 hydrogen bonds on each oxygen atom, where water acts a donor, which would require upwards of 6 water molecules to achieve the first hydration shell.[25–27] Previous studies by our group on the electronic structure change of acetate using liquid jet AP-XPS and theoretical calculations show that the number of solvent molecules needed to reproduce the observed experimental binding shift of ~3.45 eV is closer to 20 water molecules. The higher number of solvent molecules required in the first solvation shell may be attributed to the electrostatic interactions in the ionic system.

Zhang et. al. performed *ab initio* molecular dynamics simulations on the effect the rotation of the methyl group in acetate has on the solvation shell formation and found that the rotation of the methyl group controls the structure and dynamics of the first hydration shell of

acetate.[28] It was shown that the change in the dihedral angle of acetate directly affects the hydrogen bonding that occurs at the oxygen species in the carboxylate group.[28] The rotation of the methyl group could affect the amount of water molecules required for the first solvation shell in acetate. While our results cannot detail the exact mechanism of hydrogen bonding, it is clear from our results that the solvation configuration of acetate changes from the surface to the bulk of the solution.

5.3.3 Acetamide

Acetamide, derived from acetic acid, contains an amide group and previous liquid-jet XPS studies on nitric acid solutions[9,15] have shown that the liquid N1s spectra is sensitive to changes in its chemical environment. Studying the changes in both the C1s and N1s spectrum of aqueous acetamide solutions would enable further insight into the solvation and hydrogen binding of this solute. Figure 5.6A shows the C1s spectrum for 2.0 M aqueous acetamide solution at pH of 4.78 at photon energy of 430 eV. The C1s peaks at ~290.710 and ~293.899 eV corresponds to the methyl and amide carbon. Figure 5.6B shows the 2.0 M N1s spectrum at

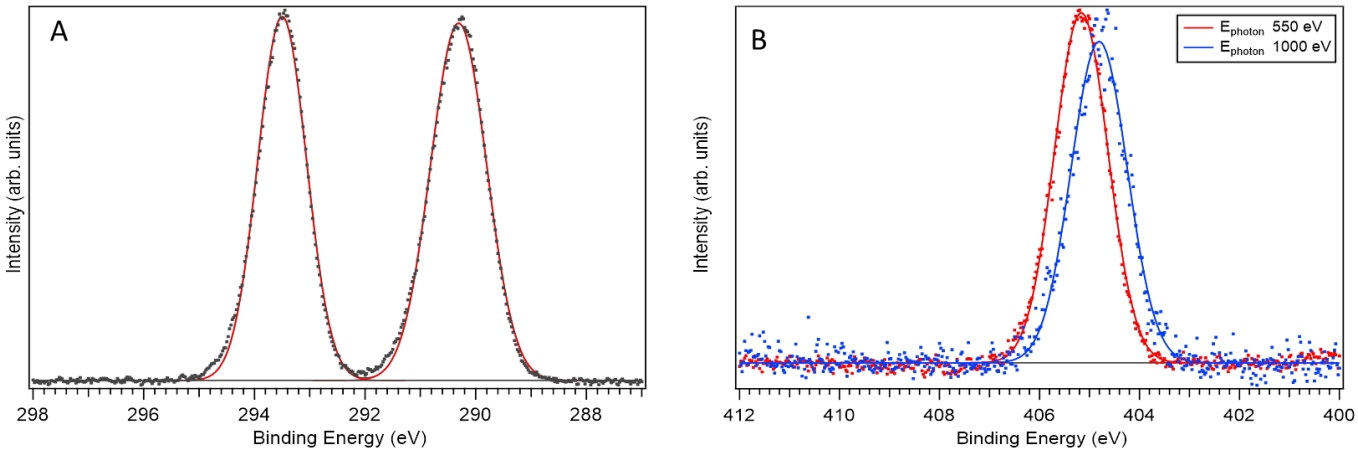

Figure 5.6: (A) C1s XPS spectrum recorded with 430 eV photon energy and (B) N1s XPS spectrum at various photon energies for 2.0 M aqueous acetamide solution.

different photon energies where the nitrogen peak appears at 405.565 and 405.206 eV at 550 and 1000 eV photon energy, respectively. It is worth noting that this shift in N1s binding energies occurs for both acetamide solutions at low pH where the ΔBE between 550 and 1000 eV was 359 and 303 meV for the 2.0 and 1.0 M solutions, respectively, as seen in Table 5.3.

Table 5.3: Recorded C1s and N1s binding energy and ΔBE values over a range of photon energies for the acetamide solutions at various concentrations and with a change in pH.

	C1s				N1s	
Solution	**Photon energy (eV)**	**BE amide (eV)**	**BE methyl (eV)**	**ΔBE**	**Photon energy (eV)**	**BE NH_2 (eV)**
2.0 M pH 4.78	430	293.499	290.310	3.189	550	405.165
	610	293.519	290.306	3.213		
	820	293.487	290.245	3.242	1000	404.806
1.0 M pH 4.79	430	293.381	290.191	3.190	550	405.081
	610	293.469	290.257	3.212		
	820	293.423	290.181	3.242	1000	404.778
2.0 M pH 11.07	430	293.931	290.746	3.185	550	405.579
	610	293.932	290.722	3.210		
	820	294.039	290.828	3.211	1000	405.340

This binding energy shift suggests a change in the solvation at the interface and the bulk of the solution for the nitrogen species. Previous studies have shown that similar binding energy shifts from the interface to the bulk occur for the HNO_3 species in nitric acid and MD simulations have shown that this is a result of a change in the solvent configuration, specifically increased hydrogen bonding of HNO_3 at the surface versus the bulk.[15] However in the case of HNO_3, the hydrogen bonding would occur at the oxygen site and not the nitrogen species. In the case of acetamide, theoretical calculations have shown that the oxygen site is preferable for hydrogen bonding but hydrogen bonding also occurs at the nitrogen species where water acts as an acceptor and bonds through the proton on the nitrogen species, not directly on the nitrogen atom itself.[29–33] The binding energy shift to a lower value in the bulk of the solution is likely a

result of the increase in electron density on the nitrogen species as a result of hydrogen bonding with water.

For the 2.0 M aqueous acetamide solution at pH of 11.07, the C1s peaks for the methyl and amide carbon are located at 290.726 and 293.931 eV, respectively, at photon energy of 430 eV. It is notable that, at high pH, the amide carbon shifts to a higher binding energy by about 32 meV. The amide carbon in the low pH solution is resonance stabilized between the oxygen and amine species which increases its electron density and results in a shift to lower binding energy. The amide carbon at high pH is not resonance stabilized so the binding energy is shifted higher as a result of less electron density around the carbon species. The N1s spectrum for the 2.0 M aqueous acetamide solution at pH 11.07 has peaks located at 405.579 and 405.340 eV at photon energies of 550 and 1000 eV, respectively. As seen in the solutions at low pH, the nitrogen species experiences a shift to a lower binding energy from the surface to the bulk of the solution of about 239 meV. This shift is less pronounced in the high pH solution but it is still a large decrease in binding energy which may be a result of the increase in hydrogen bonding interactions that might occur in the bulk of the solution for the $–NH_2$ group.

The ΔBE values between the C1s peaks for the acetamide solutions are plotted as a function of photon energy in Figure 5.7 and recorded in Table 5.3. As shown in the Figure and Table, for the 1.0 and 2.0 M acetamide solutions at pH of ~4.8, the ΔBE values are essentially the same and increase linearly by about 25 meV with increasing photon energy. The 2.0 M acetamide solution at pH 11.07 did not follow this same linear trend, with the ΔBE increasing by 25 meV going from 430 to 610 eV but remains constant at 820 eV. However, it is unclear if this is due to a change in the solvation with an increase in the pH of the solution. As seen in the ΔBE values for acetic acid and sodium acetate, some runs experienced a small increase in magnitude

going from 610 to 820 eV photon energies of 6-7 meV. The changes in magnitude may be a result of fluctuations of the liquid jet or a consequence of the dynamic nature of the solvent interactions. Since only one run was recorded for the 2.0 M acetamide at a high pH, we cannot comment on whether a greater increase in magnitude would be observed for duplicate runs.

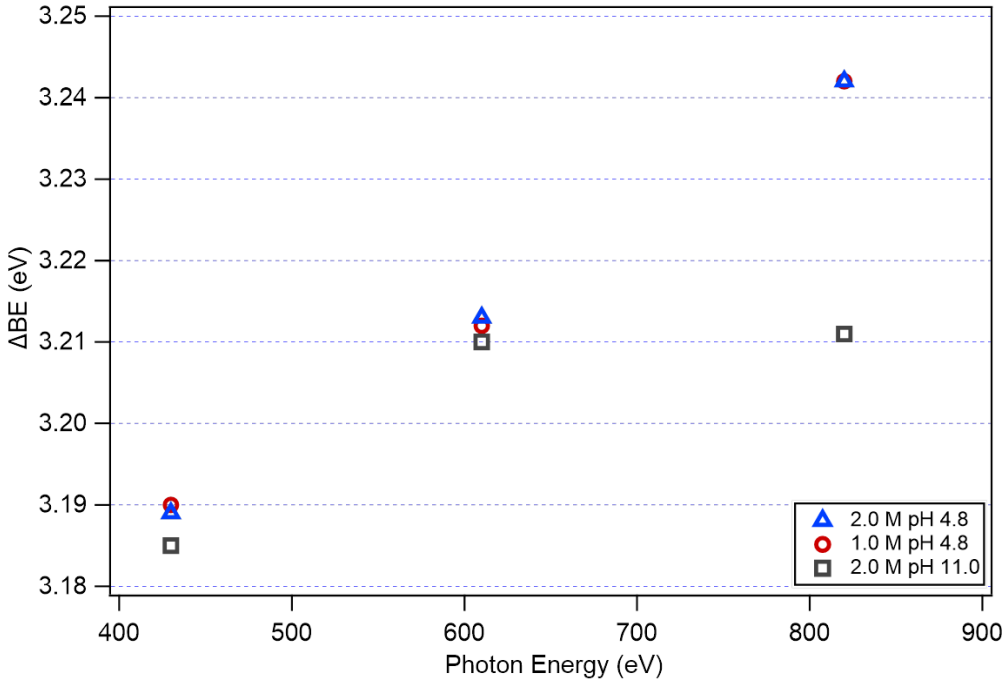

Figure 5.7: Recorded C1s change in binding energy (ΔBE) values shown as a function of photon energy for the various aqueous acetamide solutions.

It is interesting to note that the change in pH did not significantly affect the ΔBE values at 430 and 610 eV photon energies. As can be seen in Figure 5.7 and Table 5.3, the ΔBE values for all three solutions at these photon energies are relatively consistent. From this information, it can be deduced that the solvation configuration of acetamide is changing as a function of depth for the solutions at low pH and the solution at high pH exhibits a change in solvation from the surface further into the solution. The N1s spectrum for the three solutions shows a shift to lower binding energy going from the surface to the bulk of the solution which implies a change in

solvation configuration for the nitrogen species. This observed shift is lower in magnitude for the high pH solution with a shift to lower BE of ~240 meV whereas the low pH solutions recorded a shift to lower BE of 359 and 303 meV for the 2.0 and 1.0 M solutions, respectively.

5.3.4 Glycinamide hydrochloride

The chemical structure of glycinamide hydrochloride in acidic and basic solutions is shown in Figure 5.8. The protonated nitrogen species is found on the amine end of the molecule

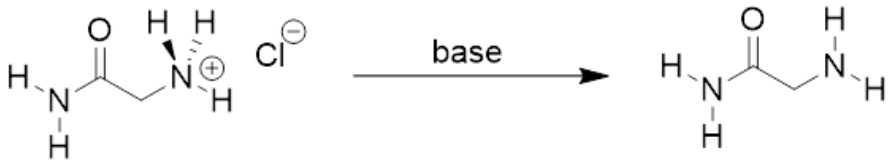

Figure 5.8: Glycinamide hydrochloride structure in acidic and basic aqueous solutions.

due to its higher basicity and the hydrogen bonding of the water molecule is expected to occur on the amide oxygen. Figure 5.9 shows the C1s spectra for both the protonated (pH 4.98) and deprotonated (pH 10.2) aqueous glycinamide solutions. For the deprotonated C1s spectra, the C1s peaks located at 291.345 and 293.621 eV correspond to the amine (C_2) and amide (C_1) carbon, respectively. The binding energy and ΔBE values for both the protonated and deprotonated aqueous glycinamide C1s spectra are recorded in Table 5.4. At photon energy of 430 eV the separation between the C1s peaks is 2.276 eV for the deprotonated solution. Going further into the bulk of the solution, or higher photon energy, the ΔBE increases to 2.313 eV. This 37 meV increase indicates a change in the solvation configuration going from the surface to the bulk of the solution.

In the protonated solution, the C1s peaks are located at 291.680 and 293.586 eV for the amine and amide carbon, respectively. As seen in Figure 5.9, the amine C1s peak shifts to a

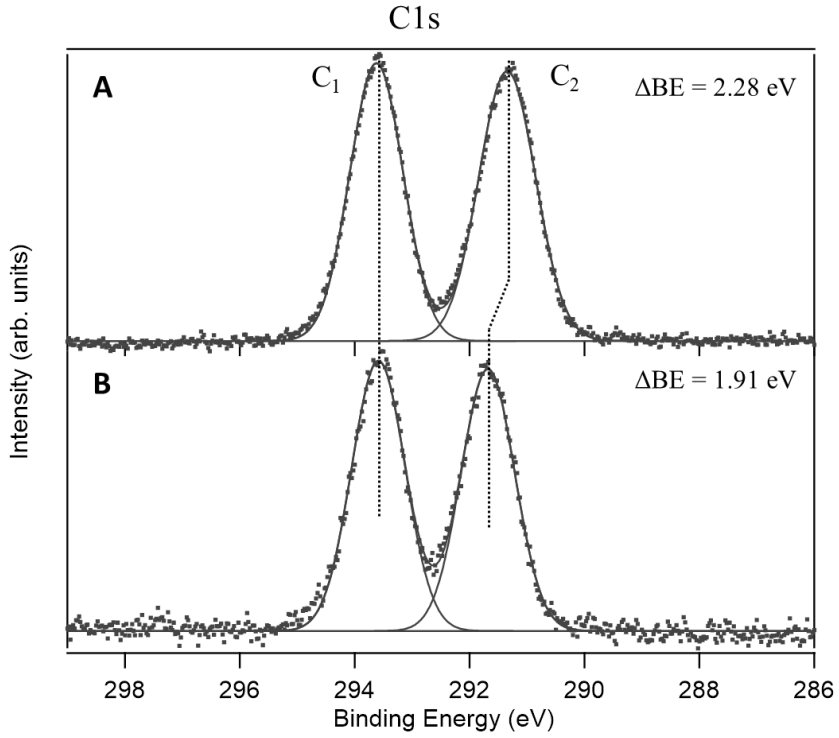

Figure 5.9: C1s spectra of (A) deprotonated and (B) protonated aqueous glycinamide solutions. The deprotonated and protonated solutions have a pH of 10.2 and 4.98, respectively.

Table 5.4: Recorded C1s binding energy and ΔBE values at various photon energies for the protonated and deprotonated aqueous glycinamide solutions.

Solution	Photon energy (eV)	BE C_1 (eV)	BE C_2 (eV)	ΔBE
0.5 M pH 4.98	430	293.586	291.680	1.906
	610	293.691	291.764	1.927
	820	293.573	291.664	1.909
1.0 M pH 10.20	430	293.621	291.345	2.276
	820	293.569	291.256	2.313

higher binding energy of 291.680 eV, which is likely a result of the positively charged nitrogen species pulling electron density away from the carbon species and resulting in a shift to higher binding energy. The shift to higher binding energy results in a ~400 meV decrease in the separation of the C1s peaks. The binding energy of the amide carbon does not change with pH

which is expected since the amide nitrogen species is not thought to protonate at high pH. Figure 5.10 shows the ΔBE of the C1s and N1s peaks as a function of photon energy for the protonated aqueous glycinamide solutions. For the 0.5 M solution at photon energy of 430 eV, the ΔBE of the C1s peaks is 1.906 eV (Table 5.4 and Figure 5.10). This separation increases by 21 meV at photon energy of 610 eV and then decreases in the bulk of the solution (photon energy 820 eV) by 18 meV.

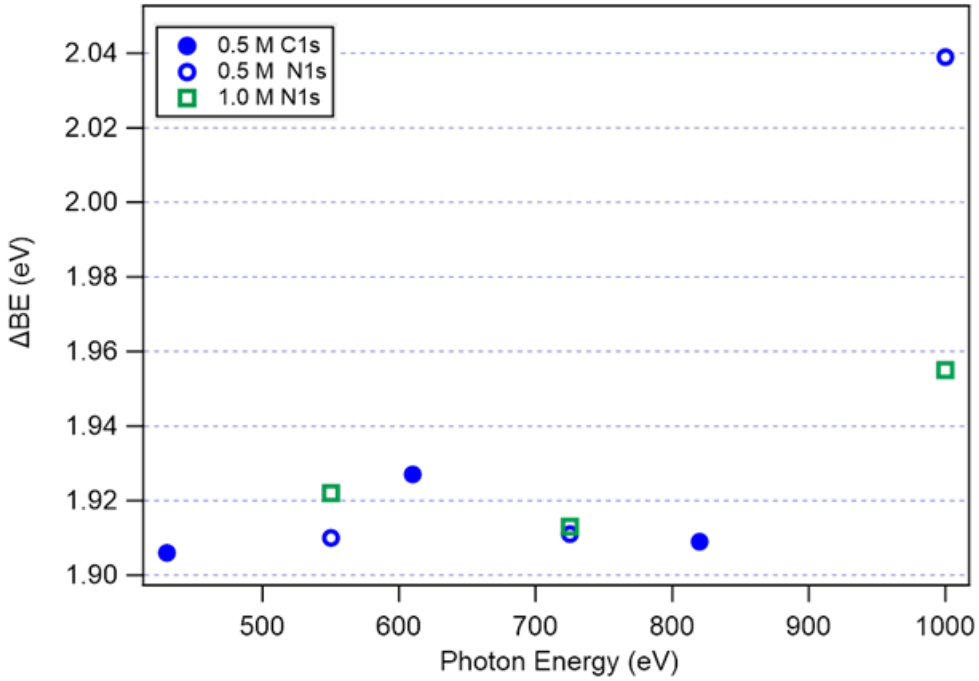

Figure 5.10: Change in binding energy (ΔBE) values as a function of photon energy for the N1s and C1s XPS spectra for the protonated aqueous glycinamide solutions.

The differences in the peak separation with photon energy may be a result of the conformational changes of protonated glycinamide in solution. Kinser et al. performed *ab initio* studies on protonated glycinamide and found that isomer IA, shown in Figure 5.11, is the most stable.[34] This stabilization is due to the intramolecular hydrogen bond from the protonated amine group to the oxygen atom, which is a better hydrogen bond acceptor than the amide nitrogen.[34] It

is possible that the conformation of protonated glycinamide is changing in the solution which would lead to the observation of the increase and decrease in the ΔBE between the two C1s peaks in the XPS spectra. The hydrogen bonding between the amine and oxygen atom would draw electron density away from the two carbon species and result in a shift to higher binding energy, which is observed at 610 eV photon energy (Table 5.4).

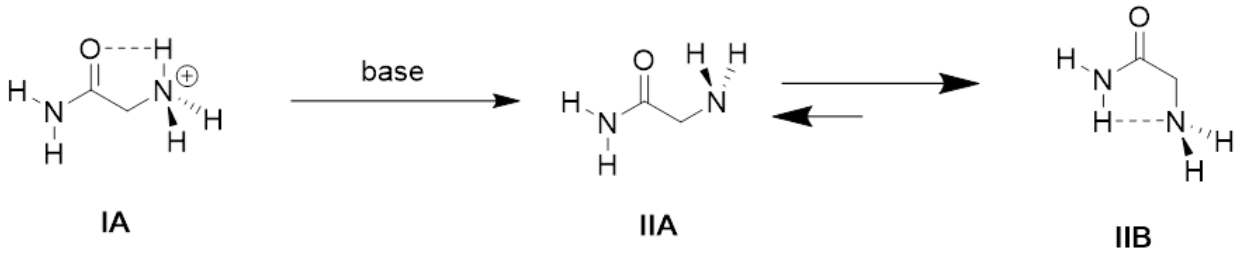

Figure 5.11: Reported conformers of glycinamide in acidic and basic solutions. Conformer IIB is considered the stable conformer in basic solutions.

However, the switching of the conformers in solution is happening on a time scale that is faster than the XPS analysis would be able to capture. With this in mind, the change in binding energy observed may be a result of intermolecular hydrogen bonding, as opposed to intramolecular bonding. The intermolecular hydrogen bonding may be a result of a change in solvation configuration with solution depth as the binding of water molecules to the solute may differ at the surface versus the bulk. Hydrogen bonding with water molecules is preferred at the amide oxygen species but could also bond with the NH_2 or NH_3^+ groups, which would result in binding energy shifts of the C1s spectrum.[35,36] For the results reported here, the C1s spectrum has similar ΔBE at the surface and bulk (photon energies of 430 and 820 eV) but varies in between (photon energy of 610 eV). The differences in the binding energy changes may also be a result of fluctuations of the liquid jet during analysis. Further analysis with theoretical

calculations would be required in order to elucidate the origin of the binding energy changes observed here.

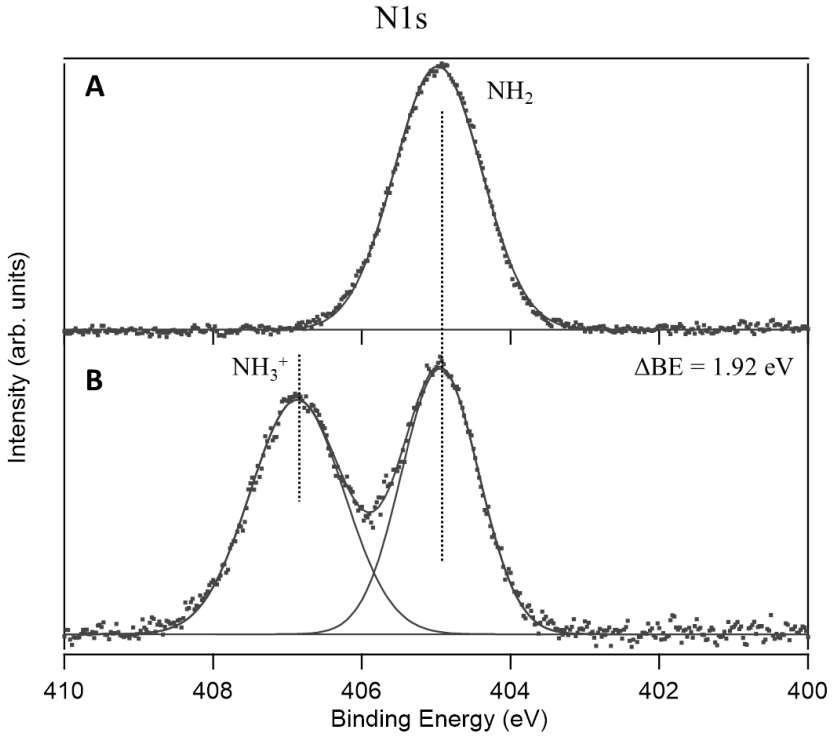

Figure 5.12: N1s spectra of (A) deprotonated and (B) protonated aqueous glycinamide solutions. The deprotonated and protonated solutions have a pH of 10.2 and 4.98, respectively.

Table 5.5: Recorded binding energy and ΔBE values at various photon energies for the N1s XPS spectra in both the protonated and deprotonated aqueous glycinamide solutions.

Solution	**Photon energy (eV)**	**BE NH_3^+ (eV)**	**BE NH_2 (eV)**	**ΔBE**
0.5 M pH 4.98	550	406.972	405.062	1.910
	725	406.990	405.079	1.911
	1000	406.743	404.704	2.039
1.0 M pH 4.98	550	406.869	404.947	1.922
	725	406.728	404.815	1.913
	1000	406.842	404.887	1.955
1.0 M pH 10.20	550		404.976	
	1000		404.865	

Figure 5.12 shows the N1s spectra for the 1.0 M protonated and deprotonated solutions. Table 5.5 details the binding energy and ΔBE for the N1s spectra of the protonated and deprotonated glycinamide solutions. For the protonated solution, there are two distinct N1s peaks that occur at 404.947 and 406.869 eV which correspond to the amine and amide nitrogen species, respectively. Figure 5.10 shows the separation of the nitrogen peaks in the protonated solution as a function of photon energy. For both the 0.5 and 1.0 M protonated solution, the ΔBE at 550 and 725 eV remains constant and then increases significantly at 1000 eV. When the photon energy is increased from 725 to 1000 eV, an increase in the ΔBE of 128 and 42 meV for the 0.5 and 1.0 M protonated solutions, respectively, is observed. The deprotonated solution shows a single nitrogen peak in the N1s spectrum that occurs at 404.865 eV, consistent with the amine nitrogen. The oxygen atom on the amide nitrogen is expected to draw electron density away from the amide nitrogen species which would result in a higher binding energy shift for the N1s peak. However, we only observe one nitrogen peak in the XPS spectrum. Since the amide nitrogen is resonance stabilized, the electron density increases which would result in a shift to lower binding energy. It is possible that the resonance effect offsets the pull of electron density towards the oxygen species which would result in a single nitrogen peak. This may also be due to the change in conformation that occurs for the deprotonated glycinamide in aqueous solution.

The two stable conformers of glycinamide discussed in literature are shown in Figure 5.11.[37–39] DFT studies performed by Li et al. have shown that the IIB conformer is the more stable conformer in the aqueous and gas phase.[38,40] The hydrogen bonding that occurs between the amide and amine nitrogen species may result in an increase in their electron density and result in a shift to higher binding energy. It is possible that, due to this intramolecular bonding, there is only one peak visible for the nitrogen species in the N1s XPS spectra. However, the

binding energy change as a result of the intramolecular binding may not be as significant as what is observed experimentally. The observation of one N1s peak in the deprotonated solution is interesting as the amide NH_2 group is resonance stabilized and is not expected to have the same binding energy as the amine group. Further investigations with theoretical calculations would need to be performed in order to determine the origin of the binding energy shift.

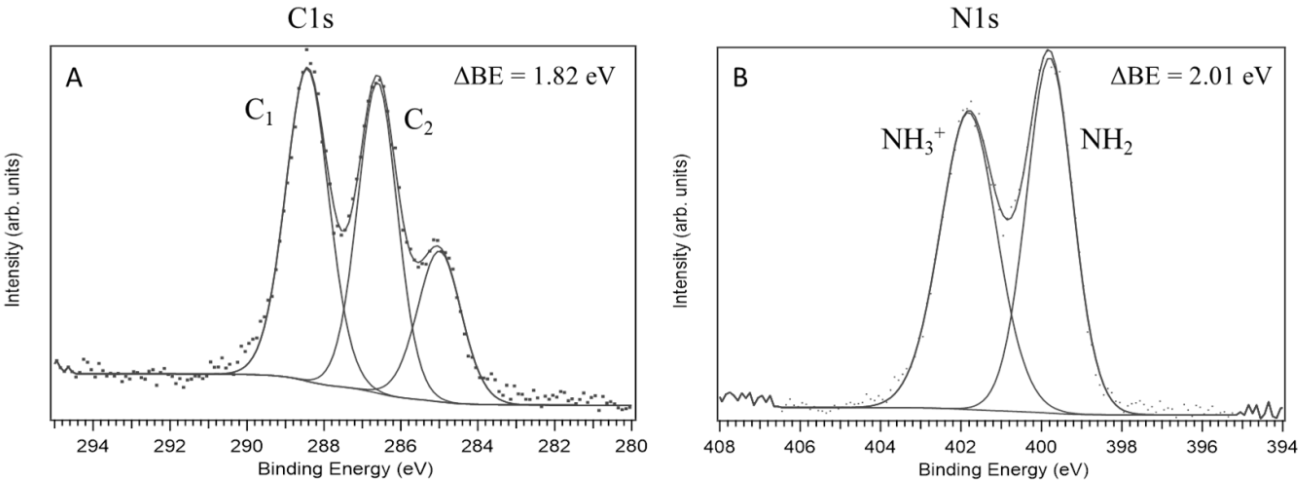

Figure 5.13: (A) C1s and (B) N1s XPS spectra of solid glycinamide hydrochloride powder. C_1 and C_2 refer to the amine and amide carbon species, respectively.

Solid glycinamide hydrochloride powder was analyzed in a UHV XPS system in order to compare the BE differences in solid and aqueous phase. The C1s and N1s XPS spectrum and binding energy values for the glycinamide hydrochloride powder are shown in Figure 5.13 and Table 5.6. The C1s peak separation in the solid sample was 1.82 eV, which is an 86 meV decrease compared to the separation of the 0.5 M protonated solution with a ΔBE of 1.906 eV. The opposite effect was observed for the N1s spectra where the solid sample had a separation of 2.01 eV, about a 100 meV increase compared to the protonated aqueous phase ΔBE of 1.910 eV at the interface of the solution. The separation between the nitrogen peaks in the powder sample is comparable to the separation that is seen in the bulk of the 0.5 M protonated solution where, at

photon energy of 1000 eV, the ΔBE of the two N1s peaks is 2.039 eV. The difference in the separation of the C1s and N1s peaks is likely due to the solvation changes that occur in aqueous solution.

Table 5.6: Recorded C1s and N1s XPS binding energy and ΔBE values for glycinamide hydrochloride powder. The ΔBE between the liquid and solid phase peaks is shown for comparison.

	C1s		**N1s**	
	BE (eV)	**$\Delta BE_{(liquid-solid)}$ (eV)**	**BE (eV)**	**$\Delta BE_{(liquid-solid)}$ (eV)**
	286.61	5.09	399.80	5.15
	288.43	5.18	401.81	5.09
ΔBE	1.82		2.01	

The C1s peaks for the amine and amide carbons were found at 286.61 and 288.43 eV for the solid sample and at ~291.7 and ~293.6 eV for the aqueous solution, respectively. The C1s peaks in the aqueous phase were located 5.09 and 5.19 eV higher for the amine and amide carbons, respectively, compared to the solid sample. The same trend was observed for the nitrogen peaks where the N1s peaks for the amine and amide nitrogen species were found at 399.80 and 401.81 eV for the solid sample and ~405.0 and ~406.8 eV for the aqueous phase, respectively. In the aqueous phase, the N1s peaks were located at 5.15 and 5.09 eV higher for the amine and amide nitrogen species, respectively, compared to the solid sample.

The difference in the locations of the binding energy peaks between the solid and aqueous phases is expected since the reference points differ between the two phases. For solid and liquid samples, the binding energy values are referenced with respect to the Fermi level and vacuum level, respectively. The difference between the Fermi and vacuum levels is the work function of the solid material. The ΔBE for the liquid and solid C1s and N1s XPS peaks are

recorded in Table 5.6 and have an average value of 5.13 eV, which would be characteristic of the work function of the glycinamide hydrochloride powder.

5.3.5 4-aminopyridine

The chemical structure of 4-aminopyridine is shown in Figure 5.14. Studies have shown that the mono-protonation of 4-aminopyridine occurs on the ring nitrogen species and di-protonated species are only stable in strongly acidic solutions.[41–43] The carbon species are labeled as C_1, C_2 and C_3 which correspond to the benzene, amine and pyridine carbons, respectively. Figure 5.15 shows the C1s spectrum for 0.5 M aqueous 4-aminopyridine for both the protonated (pH 2.17) and deprotonated (pH 11.31) solutions. The binding energy and ΔBE values for the deprotonated and protonated solutions are recorded in Tables 5.7 and 5.8, respectively. The deprotonated C1s spectra peaks located at 289.686, 290.575 and 291.297 eV correspond to the C_1, C_2 and C_3 carbons, respectively. For the protonated solution, the peaks in the C1s spectra located at 289.887, 291.126 and 291.652 eV correspond to the C_1, C_2, and C_3 carbons, respectively.

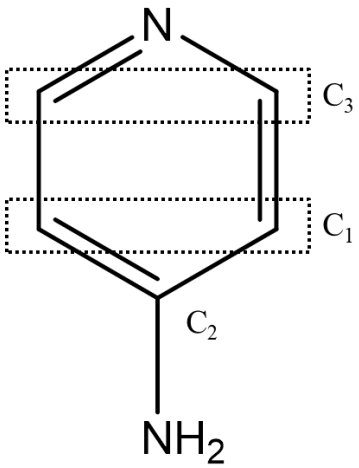

Figure 5.14: Structure of 4-aminopyridine with benzene (C_1), amine (C_2), and pyridine (C_3) carbon species labeled.

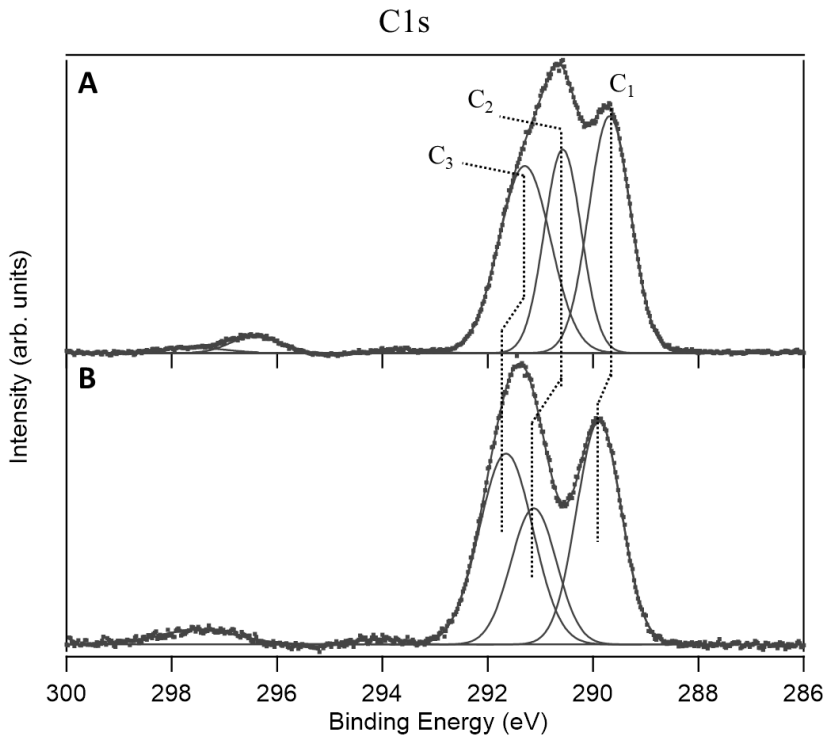

Figure 5:15: C1s spectra of (A) deprotonated and (B) protonated aqueous 4-aminopyridine solutions. The deprotonated and protonated solutions have a pH of 11.3 and 2.17, respectively. C_1, C_2, and C_3 refer to the benzene, amine, and pyridine carbons, respectively.

Upon protonation, the C_1 carbon experiences a slight shift of about 100 meV to higher binding energy. Due to the resonance stabilization of the C_1 carbon, it is not expected that this species would have a significant binding energy shift upon protonation, especially since the protonation would affect the nitrogen species. On the other hand, the amine (C_2) and pyridine (C_3) carbon species exhibit a shift of about 500 and 300 meV, respectively, to a higher binding energy upon protonation. This could be due to the di-protonation of the nitrogen species, which would pull electron density away from the carbons and result in a shift to higher binding energy. It is also possible that the mono-protonated 4-aminopyridine could be resonance stabilized where both nitrogen species would carry some charge.[42] This stabilization of the mono-protonated species could also result in the observed shifts seen in the C1s spectra.

Figure 5.15 shows that there are 3 peaks in the C1s spectra located at 293.617, 296.430, and 497.601 eV corresponding to the shake-up peaks associated with the C_1, C_2, and C_3 carbons, respectively, in the deprotonated solution. The shake-ups peaks shift with respect to the binding energy shifts of their carbon counterparts with a change in pH. In other words, the ΔBE between the shake-up peaks and its associated carbon species does not significantly change with a change in pH (seen in Tables 5.7 and 5.8). The shake-up peaks for the C_2 and C_3 carbons in the protonated solution became difficult to distinguish as these peaks overlap (Figure 5.15B).

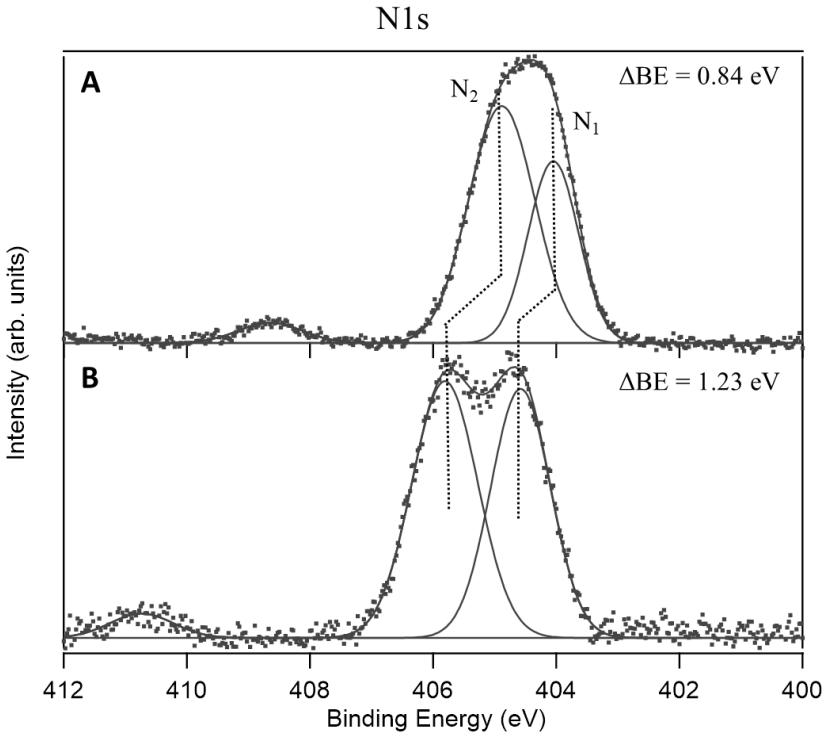

Figure 5.16: N1s spectra of (A) deprotonated and (B) protonated aqueous 4-aminopyridine solutions. The deprotonated and protonated solutions have a pH of 11.3 and 2.17, respectively. N_1 and N_2 refer to the pyridine and amine nitrogen species, respectively.

The binding energy shift upon protonation is also observed for the nitrogen species. Figure 5.16 shows the N1s spectra for the 0.5 M aqueous 4-aminopyridine for both the protonated and deprotonated solutions. The deprotonated solution has N1s peaks located closer

together at 404.048 and 404.886 eV which correspond to the pyridine (N_1) and amine (N_2) nitrogen species, respectively. The protonated solution has two distinct nitrogen peaks located at 404.579 and 405.810 eV which are attributed to the pyridine and amine nitrogen species, respectively. Upon protonation, the pyridine and amine nitrogen species exhibit a shift to higher binding energy of about 500 and 900 meV, respectively. While the mono-protonated structure would have some charge on the NH_2 group through resonance, it would be a minor resonance structure and would not be as easy to distinguish by binding energy shifts in the XPS spectrum since it would occur on too fast of a time scale. Therefore, the distinct binding energy shifts for both of the nitrogen species observed here indicates the di-protonation of 4-aminopyridine in the acidic solution.

The shake-up peak associated with the $\pi \rightarrow \pi^*$ transition of the pyridine nitrogen species is located at 408.644 eV for the deprotonated solution, which is 4.596 eV higher in binding energy than the N1s pyridine peak located at 404.048 eV. Upon protonation, the pyridine shake-up peak is shifted to a binding energy of 410.735 eV, which is at a binding energy that is 6.156 eV higher than the pyridine N1s peak located at 404.579 eV. This shift can be explained by the change in electron density with protonation. The electron donating NH_2 group in the deprotonated structure adds electron density to the ring structure and is also resonance stabilized. Since this molecule is di-protonated in the solution used here, the NH_3^+ group would pull electron density away from the ring structure and can no longer take part in resonance stabilization. This loss of electron density to the ring structure results in a shift of the $\pi \rightarrow \pi^*$ transition shake-up peak to higher binding energy, which is observed here.

The C1s and N1s spectra were taken at various photon energies in order to obtain depth profile information. The ΔBE between the carbon and nitrogen peaks at various photon energies

for the deprotonated solution is recorded in Table 5.7. As can be seen in the Table, for the deprotonated solution, the ΔBE for the carbon species at 610 eV was higher than at the interface

Table 5.7: Recorded binding energy and ΔBE values at various photon energies for the C1s and N1s XPS spectra of the deprotonated (pH 11.3) aqueous 4-aminopyridine solution.

	C1s				N1s			
Photon Energy (eV)		**430**	**610**	**820**		**550**	**725**	**1000**
Binding Energy (eV)	C_1	289.686	289.804	289.724	N_1	404.048	404.059	403.830
	C_2	290.575	290.697	290.606	N_2	404.886	404.904	404.664
	C_3	291.297	291.467	291.333				
	shake-up C_1	293.617		293.721	shake up N_1	408.64	408.77	408.37
	shake-up C_2	296.430	296.360	296.428				
	shake-up C_3	297.601	296.979	297.545				
ΔBE (eV)	(C_1 & C_2)	0.889	0.893	0.882	(N_1 & N_2)	0.838	0.845	0.834
ΔBE (eV)	(C_2 & C_3)	0.722	0.770	0.727	(N_1 & shake up)	4.596	4.708	4.544
ΔBE (eV)	(C_1 & C_3)	1.611	1.663	1.609				

or bulk of the solution. This may indicate a change in solvation configuration or could be fluctuations that are a result of the resonance stabilized structured. The N1s species in the deprotonated solution also exhibits this trend where the ΔBE is higher at 725 eV compared to 550 or 1000 eV photon energies. Theoretical and experimental studies have investigated the solvation of 2- and 3-aminopyridine and it was found that water molecules are likely to bond at the pyridine nitrogen species and form a water dimer structure around the ring.[44–47] The change in solvation as a function of depth may reflect changes in the binding of the water molecules to 4-aminopyridine, whether through the nitrogen or carbon species; however, theoretical calculations would need to be performed in order to elucidate the solvation mechanism.

The depth profile measurements for the protonated solution exhibits a more linear trend. Table 5.8 shows that for the C1s spectra, the ΔBE is increasing going from the surface to the bulk when comparing the ΔBE between the amide and pyridine carbons and between the benzene and pyridine carbons. The ΔBE for the N1s species is slightly increasing going from the

surface to the bulk of the solution which indicates a change in the solvation configuration, which may be similar to the solvation as discussed above, although molecular dynamics simulations would need to be carried out in order to understand how the protonated species influences the solvation.

Table 5.8: Recorded binding energy and ΔBE values at various photon energies for the C1s and N1s XPS spectra of the protonated (pH 2.17) aqueous 4-aminopyridine solution.

	C1s				N1s			
Photon Energy (eV)		**430**	**610**	**820**		**550**	**725**	**1000**
Binding Energy (eV)	C_1	289.887	289.828	289.852	N_1	404.579	404.554	404.312
	C_2	291.126	291.059	291.082	N_2	405.810	405.789	405.551
	C_3	291.652	291.624	291.691				
	shake-up C_1	294.042	293.712	293.692	shake up N_1	410.735	410.639	410.680
	shake-up C_2	296.949	296.878	296.944				
	shake-up C_3	297.731	297.860	297.794				
ΔBE (eV)	(C_1 & C_2)	1.239	1.231	1.230	(N_1 & N_2)	1.231	1.235	1.239
ΔBE (eV)	(C_2 & C_3)	0.526	0.565	0.609	(N_1 & shake up)	6.156	6.085	6.368
ΔBE (eV)	(C_1 & C_3)	1.765	1.796	1.839				

5.4 Conclusion

Liquid-jet XPS was used to study the change in solvation configuration as a function of depth and pH for various solutes in aqueous solutions. The ΔBE value between the carbon or nitrogen peaks provides insight into perturbations in the electronic structure of these solutes in solution. The photon energy was varied using synchrotron radiation in order to obtain information on the ΔBE at the interface versus the bulk of the solution and with a change in solution pH. It was found that for almost all of the solutes studied, there were observed changes in the ΔBE values at the interface compared to the bulk, indicating a change in the solvation configuration presumably due to the hydrogen bonding with water. While the ΔBE values can show that the solvation is changing, molecular dynamics and electronic structure calculations are

needed in order to fully understand the hydrogen bonding mechanism and elucidate the number of water molecules in the solvation shells.

5.5 References

(1) Gozem, S.; Seidel, R.; Hergenhahn, U.; Lugovoy, E.; Abel, B.; Winter, B.; Krylov, A. I.; Bradforth, S. E. Probing the Electronic Structure of Bulk Water at the Molecular Length Scale with Angle-Resolved Photoelectron Spectroscopy. *J. Phys. Chem. Lett.* **2020**, *11*, 5162–5170.

(2) Seidel, R.; Thürmer, S.; Winter, B. Photoelectron Spectroscopy Meets Aqueous Solution: Studies from a Vacuum Liquid Microjet. *J. Phys. Chem. Lett.* **2011**, *2*, 633–641.

(3) Fransson, T.; Harada, Y.; Kosugi, N.; Besley, N. A.; Winter, B.; Rehr, J. J.; Pettersson, L. G. M.; Nilsson, A. X-ray and Electron Spectroscopy of Water. *Chem. Rev.* **2016**, *116*, 7551–7569.

(4) Salmeron, M.; Schlögl, R. Ambient Pressure Photoelectron Spectroscopy: A New Tool for Surface Science and Nanotechnology. *Surf. Sci. Rep.* **2008**, *63*, 169–199.

(5) Seidel, R.; Winter, B.; Bradforth, S. E. Valence Electronic Structure of Aqueous Solutions: Insights from Photoelectron Spectroscopy. *Annu. Rev. Phys. Chem.* **2016**, *67*, 283–305.

(6) Bruce, J. P.; Hemminger, J. C. Characterization of Fe^{2+} Aqueous Solutions with Liquid Jet X-ray Photoelectron Spectroscopy: Chloride Depletion at the Liquid/ Vapor Interface Due to Complexation with Fe^{2+}. *J. Phys. Chem. B* **2019**, *123*, 8285–8290.

(7) Seidel, R.; Pohl, M. N.; Ali, H.; Winter, B.; Aziz, E. F. Advances in Liquid Phase Soft-X-

Ray Photoemission Spectroscopy: A New Experimental Setup at BESSY II. *Rev. Sci. Instrum.* **2017**, *88*.

(8) Ottosson, N.; Børve, K. J.; Spangberg, D.; Bergersen, H.; Sæthre, L. J.; Faubel, M.; Pokapanich, W.; Öhrwall, G.; Björneholm, O.; Winter, B. On the Origins of Core-Electron Chemical Shifts of Small Biomolecules in Aqueous Solution: Insights from Photoemission and Ab Initio Calculations of Glycineaq. *J. Am. Chem. Soc.* **2011**, *133*, 3120–3130.

(9) Lewis, T.; Winter, B.; Stern, A. C.; Baer, M. D.; Mundy, C. J.; Tobias, D. J.; Hemminger, J. C. Dissociation of Strong Acid Revisited: X-Ray Photoelectron Spectroscopy and Molecular Dynamics Simulations of HNO_3 in Water. *J. Phys. Chem. B* **2011**, *115*, 9445–9451.

(10) Lewis, T.; Faubel, M.; Winter, B.; Hemminger, J. C. CO_2 Capture in Amine-Based Aqueous Solution: Role of the Gas–Solution Interface. *Angew. Chemie - Int. Ed.* **2011**, *50*, 10178–10181.

(11) Pham, T. A.; Govoni, M.; Seidel, R.; Bradforth, S. E.; Schwegler, E.; Galli, G. Electronic Structure of Aqueous Solutions : Bridging the Gap between Theory and Experiments. *Sci. Adv.* **2017**, *3*, 1–8.

(12) Makowski, M. J.; Stern, A. C.; Hemminger, J. C.; Tobias, D. J. Orientation and Structure of Acetonitrile in Water at the Liquid − Vapor Interface: A Molecular Dynamics Simulation Study. *J. Phys. Chem. C* **2016**, *120*, 17555–17563.

(13) Gaiduk, A. P.; Govoni, M.; Seidel, R.; Skone, J. H.; Winter, B.; Galli, G. Photoelectron Spectra of Aqueous Solutions from First Principles. *J. Am. Chem. Soc.* **2016**, *138*, 6912–6915.

(14) Brown, M. A.; Vila, F.; Sterrer, M.; Thürmer, S.; Winter, B.; Ammann, M.; Rehr, J. J.; van Bokhoven, J. A. Electronic Structures of Formic Acid (HCOOH) and Formate ($HCOO^-$) in Aqueous Solutions. *J. Phys. Chem. Lett.* **2012**, *3*, 1754–1759.

(15) Lewis, T.; Winter, B.; Stern, A. C.; Baer, M. D.; Mundy, C. J.; Tobias, D. J.; Hemminger, J. C. Does Nitric Acid Dissociate at the Aqueous Solution Surface? *J. Phys. Chem. C* **2011**, *115*, 21183–21190.

(16) Perrine, K. A.; Parry, K. M.; Stern, A. C.; Van Spyk, M. H. C.; Makowski, M. J.; Freites, J. A.; Winter, B.; Tobias, D. J.; Hemminger, J. C. Specific Cation Effects at Aqueous Solution−vapor Interfaces: Surfactant-like Behavior of Li^+ Revealed by Experiments and Simulations. *PNAS* **2017**, *114* (51), 13363–13368.

(17) Perrine, K. A.; Spyk, M. H. C. Van; Margarella, A. M.; Winter, B.; Faubel, M.; Bluhm, H.; Hemminger, J. C. Characterization of the Acetonitrile Aqueous Solution/Vapor Interface by Liquid-Jet X-Ray Photoelectron Spectroscopy. *J. Phys. Chem. C* **2014**, *118*, 29378–29388.

(18) Olivieri, G.; Parry, K. M.; Powell, C. J.; Tobias, D. J.; Brown, M. A. Quantitative Interpretation of Molecular Dynamics Simulations for X-Ray Photoelectron Spectroscopy of Aqueous Solutions for X-Ray Photoelectron Spectroscopy of Aqueous Solutions. *J. Chem. Phys.* **2016**, *144*, *1-9*.

(19) Olivieri, G.; Parry, K. M.; Powell, C. J.; Tobias, D. J.; Brown, M. A. Simulated Photoelectron Intensities at the Aqueous Solution-Air Interface for Flat and Cylindrical (Microjet) Geometries. *Phys. Chem. Chem. Phys.* **2017**, *19*, 6330–6333.

(20) Ottosson, N.; Wernersson, E.; Söderström, J.; Pokapanich, W.; Kaufmann, S.; Svensson, S.; Persson, I.; Öhrwall, G.; Björneholm, O. The Protonation State of Small Carboxylic Acids at the Water Surface from Photoelectron Spectroscopy. *Phys. Chem. Chem. Phys.*

2011, *13*, 12261–12267.
(21) Yeh, J. J.; Lindau, I. Atomic Subshell Photoionization Cross Sections and Asymmetry Parameters: 1 ⩽ Z ⩽ 103. *At. Data Nucl. Tables* **1985**, *32* (1), 1–155.
(22) Chocholoušová, J.; Vacek, J.; Hobza, P. Acetic Acid Dimer in the Gas Phase, Nonpolar Solvent , Microhydrated Environment, and Dilute and Concentrated Acetic Acid: Ab Initio Quantum Chemical and Molecular Dynamics Simulations. *J. Phys. Chem. A* **2003**, *107*, 3086–3092.
(23) Gu, W.; Frigato, T.; Straatsma, T. P.; Helms, V. Dynamic Protonation Equilibrium of Solvated Acetic Acid. *Angew. Chemie - Int. Ed.* **2007**, *46*, 2939–2943.
(24) Krishnakumar, P.; Maity, D. K. Microhydration of Neutral and Charged Acetic Acid. *J. Phys. Chem. A* **2017**, *121*, 493–504.
(25) Wang, G.; Zhou, Y.; Lin, H.; Jing, Z.; Liu, H.; Zhu, F. Structure of Aqueous Sodium Acetate Solutions by X-Ray Scattering and Density Functional Theory. *Pure Appl. Chem.* **2020**, *92* (10), 1627–1641.
(26) Houriez, C.; Meot-Ner (Mautner), M.; Masella, M. Simulated Solvation of Organic Ions II: Study of Linear Alkylated Carboxylate Ions in Water Nanodrops and in Liquid Water. Propensity for Air/Water Interface and Convergence to Bulk Solvation Properties. *J. Phys. Chem. B* **2015**, *119*, 12094–12107.
(27) Fedotova, M. V.; Kruchinin, S. E. Hydration of Acetic Acid and Acetate Ion in Water Studied by 1D-RISM Theory. *J. Mol. Liq.* **2011**, *164*, 201–206.
(28) Zhang, X.; Kumar, R.; Kuroda, D. G. Acetate Ion and Its Interesting Solvation Shell Structure and Dynamics. *J. Chem. Phys.* **2018**, *148* (094506).
(29) Aparicio-Martínez, S.; Balbuena, P. B. On the Properties of Aqueous Amide Solutions through Classical Molecular Dynamics Simulations. *Mol. Simul.* **2007**, *33* (11), 925–938.
(30) Krestyaninov, M. A.; Odintsova, E. G.; Kolker, A. M.; Kiselev, M. G. The Structure of Water – Acetamide Hydrogen Bonded Complexes. Quantum Chemical Analysis. *J. Mol. Liq.* **2018**, *264*, 343–351.
(31) Tolosa Arroyo, S.; Sansón Martín, J. A.; Hidalgo García, A. Molecular Dynamics Simulation of Acetamide Solvation Using Interaction Energy Components: Application to Structural and Energy Properties. *Chem. Phys.* **2006**, *327*, 187–192.
(32) Spencer, J. N.; Berger, S. K.; Powell, C. R.; Henning, B. D.; Furman, G. S.; Loffredo, W. M.; Rydberg, E. M.; Neubert, R. A.; Shoop, C. E.; Blauch, D. N. Amide Interactions in Aqueous and Organic Medium. *J. Phys. Chem.* **1981**, *85*, 1236–1241.
(33) Panuszko, A.; Gojło, E.; Zielkiewicz, J.; Maciej, Ś.; Krakowiak, J.; Stangret, J. Hydration of Simple Amides. FTIR Spectra of HDO and Theoretical Studies. *J. Phys. Chem. B* **2008**, *112*, 2483–2493.
(34) Kinser, R. D.; Ridge, D. P.; Hvistendahl, G.; Rasmussen, B.; Uggerud, E. The Unimolecular Chemistry of Protonated Glycinamide and the Proton Affinity of Glycinamide-Mass Spectrometric Experiments and Theoretical Model. *Chem. Eur. J.* **1996**, *2* (9), 1143–1149.
(35) Schemer, S.; Wang, L. Hydrogen Bonding and Proton Transfers of the Amide Group. *J. Am. Chem. Soc.* **1993**, *115*, 1958–1963.
(36) Venkata Ramiah, K.; Puranik, P. G. Hydrogen Bonding in Amides. *Proc. Indian Acad. Sci.* **1962**, *56*, 96–102.
(37) Sulzbach, H. M.; Schleyer, P. R.; Schaefer III, H. F. Interrelationship between Conformation and Theoretical Chemical Shifts. Case Study on Glycine and Glycine

Amide. *J. Am. Chem. Soc.* **1994**, *116*, 3967–3972.
(38) Li, P.; Bu, Y.; Ai, H. Conformational Study of Glycine Amide Using Density Functional Theory. *J. Phys. Chem. A* **2003**, *107* (33), 6419–6428.
(39) Ganguly, B.; Kesharwani, M. K.; Basaric, N.; Suresh, E.; Biswas, A. K.; Mlinaric-Majerski, K. Conformational Preference of Glycinamide in Solution: An Answer Derived from Combined Experimental and Computational Studies. *J. Mol. Graph. Model.* **2013**, *46*, 52–58.
(40) Li, P.; Bu, Y.; Ai, H. Density Functional Studies on Conformational Behaviors of Glycinamide in Solution. *J. Phys. Chem. B* **2004**, *108*, 1405–1413.
(41) Pittman, C. U.; Attallah, O. M.; Kispert, L. D. INDO Theoretical Studies of 4-Aminopyridine and Protonated 4-Aminopyridine. *J.C.S. Perkin II* **1975**, 1776–1778.
(42) Dega-Szafran, Z.; Kania, A.; Nowak-wydra, B.; Szafran, M. UV, ^{1}H and ^{13}C NMR Spectra, and AM1 Studies of Protonation Aminopyridines. *J. Mol. Struct.* **1994**, *322*, 223–232.
(43) Fossey, J.; Loupy, A.; Strzelecka, H. An Ab Initio Study of Protonation and Alkylation of Aminopyridine. *Tetrahedron* **1981**, *37*, 1935–1941.
(44) Hager, J.; Wallace, S. C. Solvation Effects In Jet-Cooled 2-Aminopyridine Clusters : Excited-State Dynamics and Two-Color Threshold Photoionization Spectroscopy. *J. Phys. Chem.* **1985**, *89* (18), 3833–3841.
(45) Wu, R.; Nachtigall, P.; Brutschy, B. Structure and Hydrogen Bonding of 2-Aminopyridine*$(H_2O)_n$ (n = 1, 2) Studied by Infrared Ion Depletion Spectroscopy. *Phys. Chem. Chem. Phys.* **2004**, *6*, 515–521.
(46) Yamada, Y.; Goto, Y.; Higuchi, S.; Nibu, Y. Drastic Change in Electronic Transition upon Hydrogen Bond Network Switching in 3 - Aminopyridine−$(H_2O)_n$ Clusters. *J. Phys. Chem. A* **2019**, *123*, 3728–3734.
(47) Zhao, J.; Song, P.; Cui, Y.; Liu, X.; Sun, S.; Hou, S.; Ma, F. Effects of Hydrogen Bond on 2-Aminopyridine and Its Derivatives Complexes in Methanol Solvent. *Spectrochim. Acta Part A Mol. Biomol. Spectrosc.* **2014**, *131*, 282–287.

APPENDIX A

Solid State Sample Holder with Heating Capabilities for AP-XPS

The lab-based ambient pressure X-ray photoelectron spectrometer (AP-XPS) instrument is used for the studies of liquid solutions. The current set up uses a liquid jet that is generated by an HPLC pump and passed through a 20 μm glass capillary. In order to perform AP-XPS experiments similar to the model catalyst reactivity studies conducted at the synchrotron, where gas is added to the chamber and the sample is heated in a temperature ramp, a gas manifold was set up on the main chamber. A solid sample holder was designed and fabricated in order to heat the nanoparticle (either TiO_2 or ZnO) samples and conduct AP-XPS experiments in the lab.

Detailed images of the sample holder are shown in Figures A.1 and A.2. The sample holder consists of a 304 stainless steel block with dimensions of 13L x 14W x 20H mm. Oxygen free high conductivity copper was used to create the copper bar and plate. The copper braiding for heating was silver soldered onto the fabricated copper plate. Macor spacers were placed between the copper plate and stainless steel block connections for thermal insulation (Figure A.2 A). Tungsten wire is placed through two slits on the macor front plate (that holds the sample) and the wires are bent and positioned between the copper plate and bar (Figure A.2 B). The sample is placed on the macor plate and fastened with molybdenum bars and screws across the top and bottom. A K type thermocouple is placed between the sample and macor plate in order to record the substrate temperature.

The block set up is screwed into a stainless steel rod that is attached to a rotary manipulator in order to rotate the sample in the chamber (Figure A.3 C). The braided heating wires are attached to a copper rod (Figure A.4 A) with a copper tube and screws. The copper rod extends outside the vacuum setup in order to attach connections to the voltage supply box for

substrate heating (Figure A.3 A). The thermocouple attachments located next to the copper rod also extend outside the vacuum set up and are connected to a thermocouple thermometer.

The braided heating wire connected to the copper rod is the length of the rotary attachment (Figure A.3 C). The smaller section of braided heating wire soldered to the copper plate was connected to the longer heating wire using a copper tube and screws in order for easier removal of the block for sample exchange (Figure A.4 B). The sample is then able to be heated in the AP-XPS chamber with the introduction of reactant gases in order to obtain reactivity data for thermal reduction in the lab. Blueprints and dimensions of the sample holder are included in Figures A.5, A.6, and A.7.

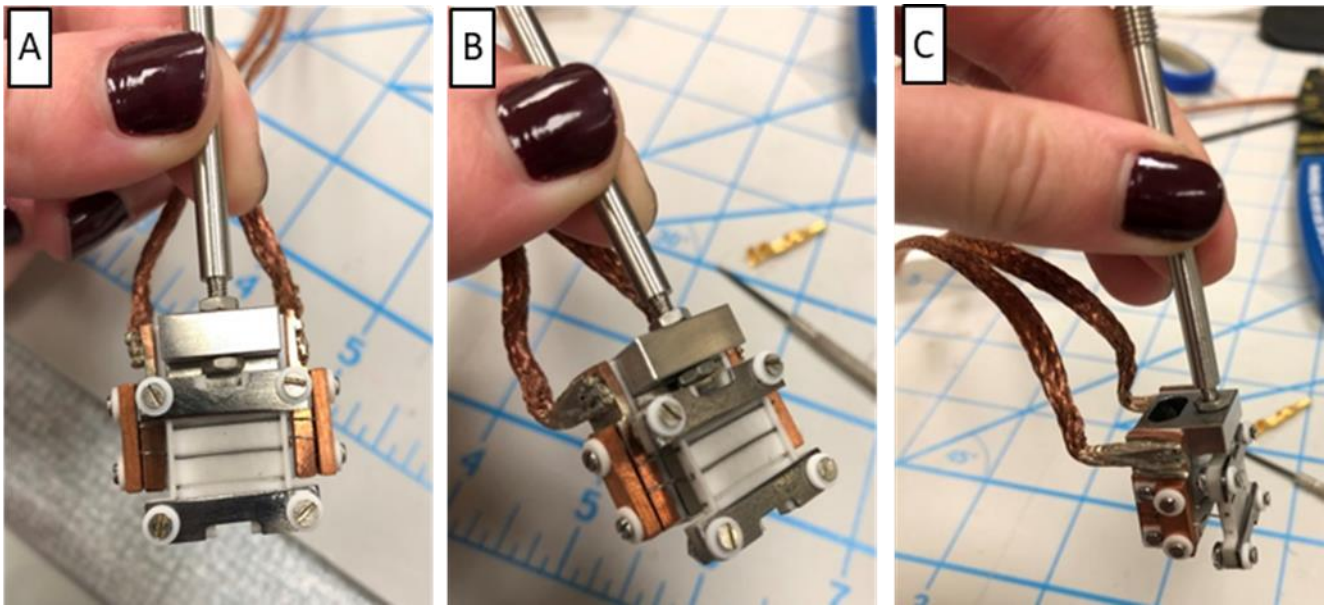

Figure A.1: (A) Front, (B) side angled, (C) top angled view of the stainless steel block with the copper plate and bars attached. Image (A) and (B) show the two tungsten wires that are located on the white, macor plate that are responsible for substrate heating.

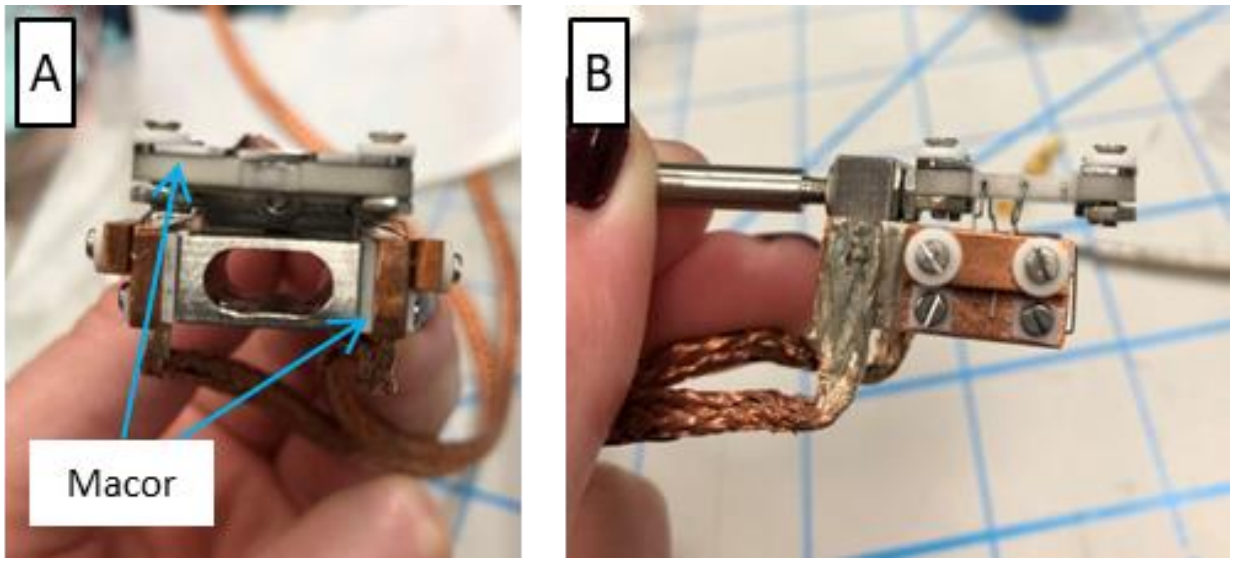

Figure A.2: (A) Bottom and (B) side view of the stainless steel block with the copper plate and bars attached. Image (A) highlights the macor plate that is situated between the copper plate and stainless steel block and the macor front plate where the sample is held between the molybdenum bars and heated with the tungsten wires.

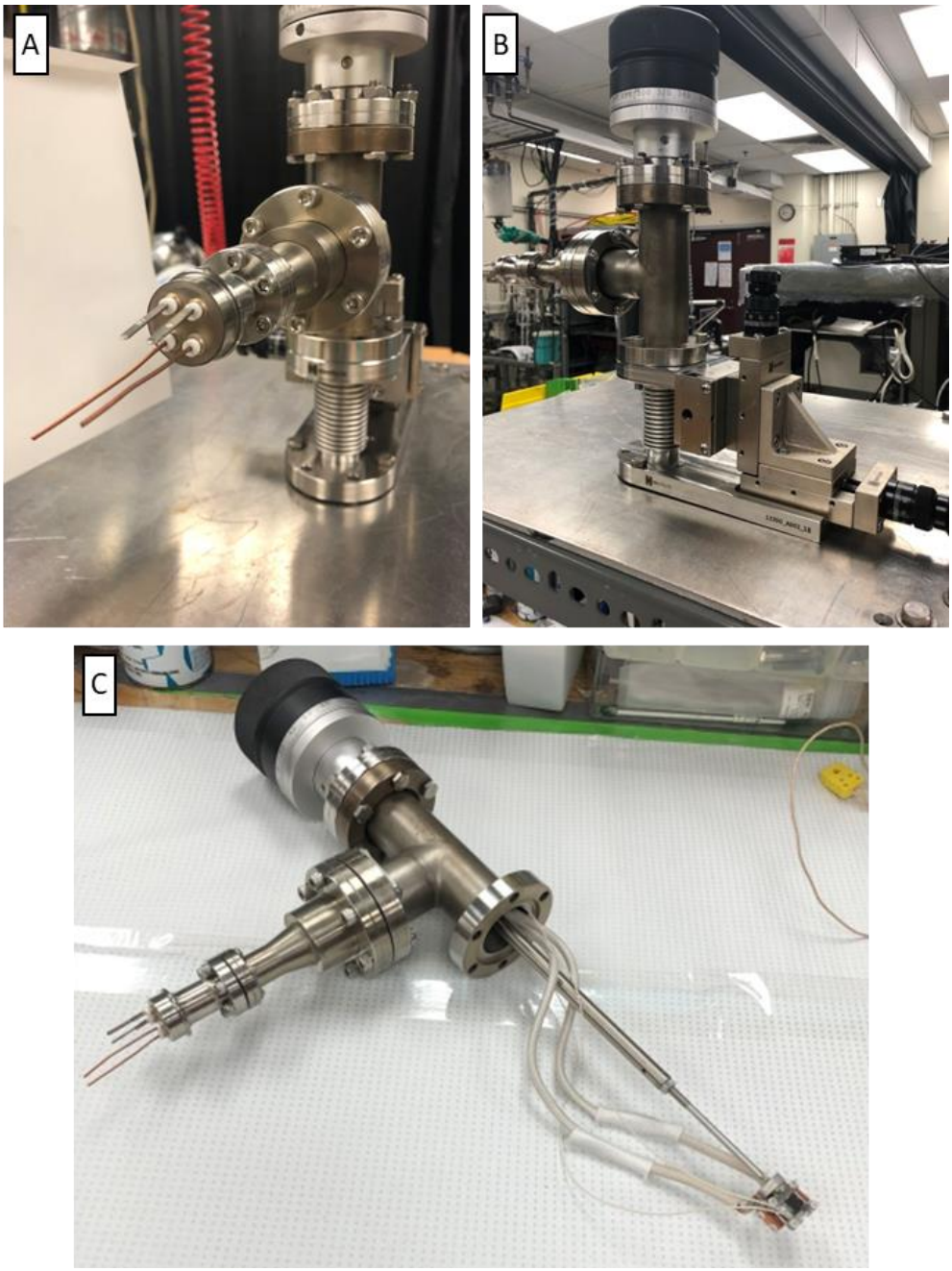

Figure A.3: (A) Side view of the set up with the copper heating rods and thermocouple attachments. (B) View of the components outside the vacuum chamber with the manipulator, T-shaped attachment and the rotary manipulator. (C) Full set up of the T-shaped attachment and rotary arm with block and heating and thermocouple wires attached.

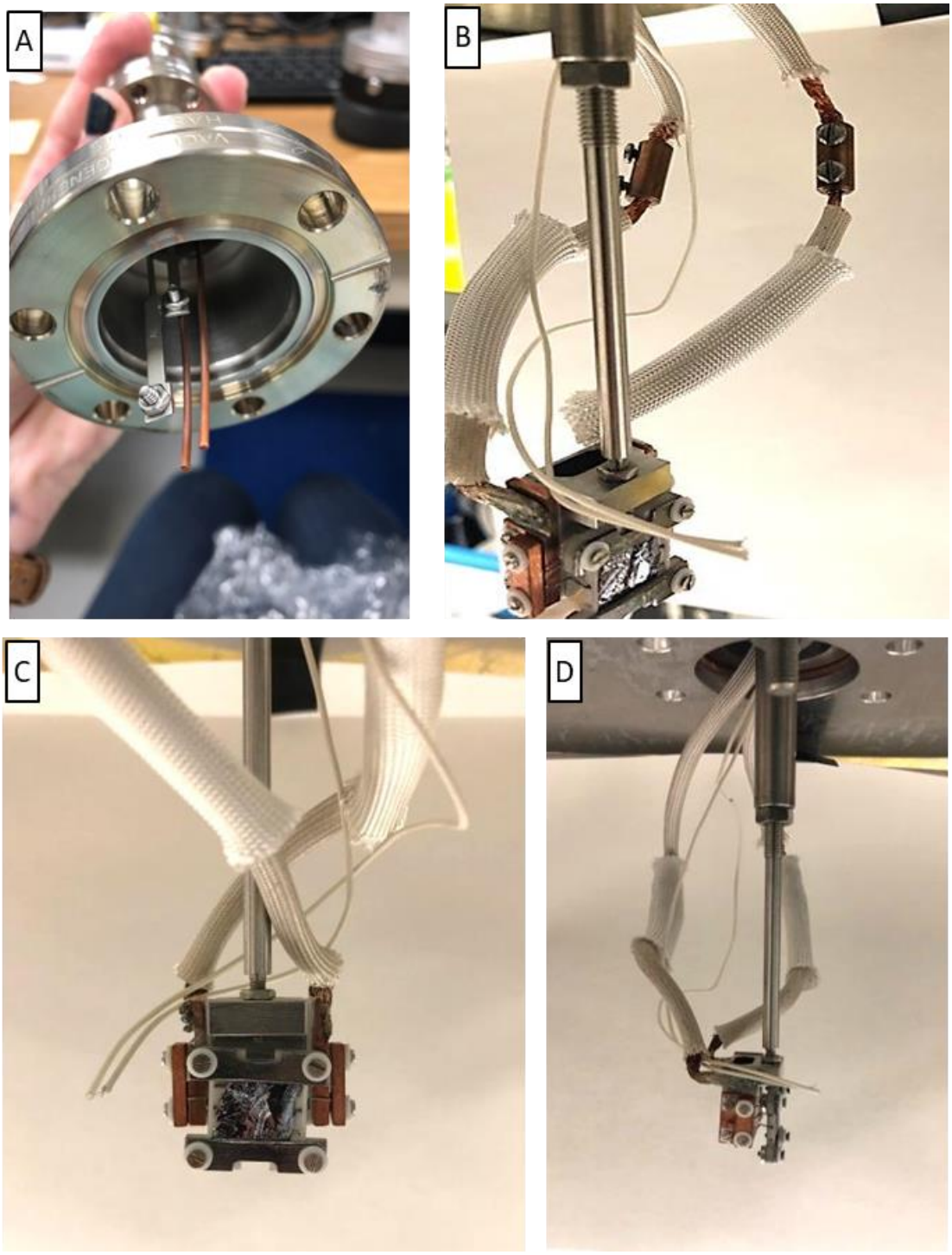

Figure A.4: (A) Thermocouple and heating wire attachment. (B) Detailed image showing the copper wire heating attachments. The heating wires are screwed into a copper tube for easy removal. (C) Front and (D) side views of the sample heater attached to the rotary manipulator with a sample affixed on the macor plate. The thin wires in (C) are the K type thermocouple wires that will go between the sample and the macor plate in order to read the temperature.

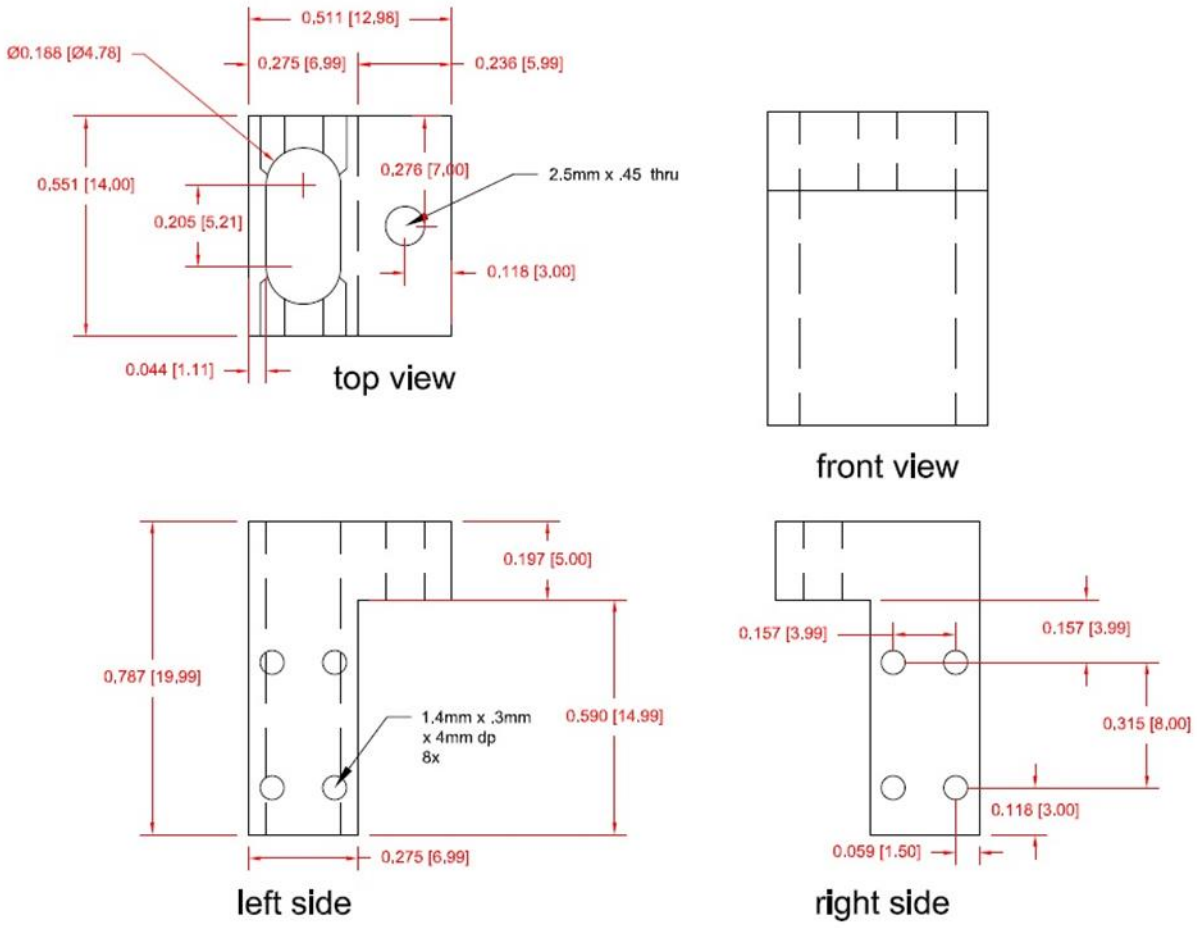

Figure A.5: Blueprint and dimensions of the stainless steel block designed using AutoCAD Mechanical software.

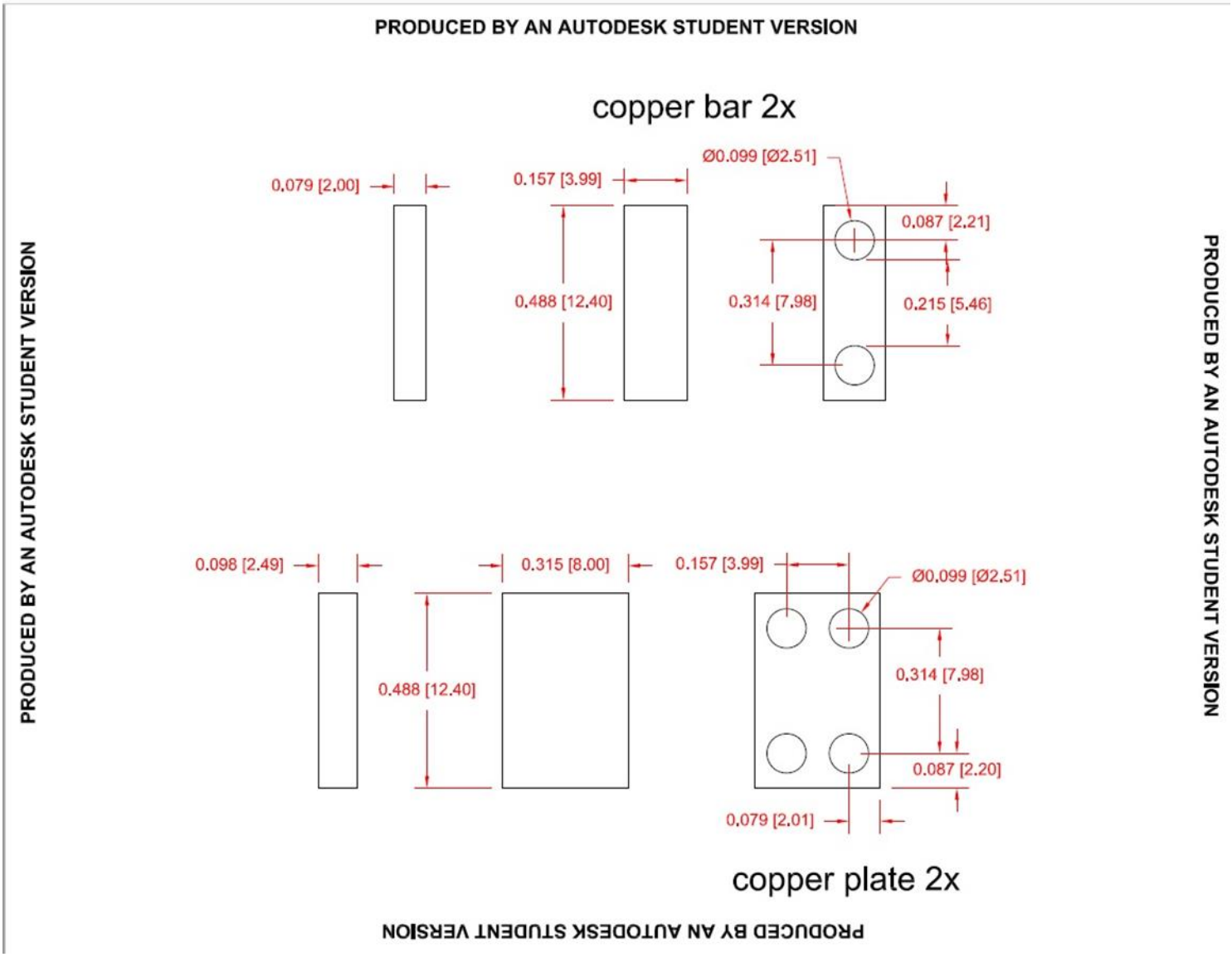

Figure A.6: Blueprint and dimensions of the copper plates and bars designed using AutoCAD Mechanical software.

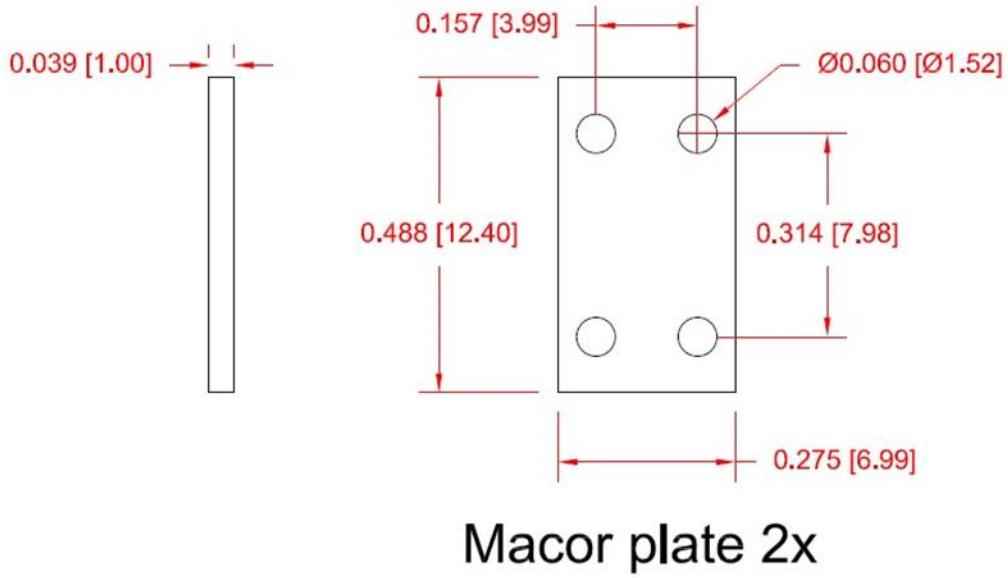

Figure A.7: Blueprint and dimensions of the macor plates designed using AutoCAD Mechanical software.